Understanding Freshwater Changes in the Arctic Ocean



Sam Cornish

University College

University of Oxford

A thesis submitted for the degree of

Doctor of Philosophy

Trinity Term 2021

To my grandfather, Dr John Earle, who encouraged me to be curious

List of Publications

This thesis is comprised of work that has been published in or submitted to the following peer-reviewed journals:

- **Johnson, Cornish, Kostov, Beer, and Lique, 2018**, Arctic Ocean Freshwater Content and its Decadal Memory of Sea-Level Pressure. *Geophysical Research Letters*.
- **Cornish, Kostov, Johnson, and Lique, 2020**, Response of Arctic Freshwater to the Arctic Oscillation in Coupled Climate Models. *Journal of Climate*.

Other publications that are partly related to the work in this thesis are:

- **Muilwijk, Ilicak, Cornish et al. 2019**, Arctic Ocean Response to Greenland Sea Wind Anomalies in a Suite of Model Simulations. *Journal of Geophysical Research—Oceans*.
- **Mallett, Stroeve, Cornish et al.**, Record winter winds in 2020/21 drove exceptional Arctic sea ice transport. *Communications Earth and Environment*.

Manuscripts led by myself are in preparation based on chapters 3, 4 and 5, with the co-authors listed in the Apportion of Credit.

Acknowledgements

I feel incredibly privileged to have had such fantastic supervisors in Prof. Helen Johnson and Dr Yavor Kostov, who always found time and enthusiasm in their busy schedules to guide me. I have benefited not only from their significant expertise, but also from their example: to aim to 'do good science', with an open mind, and to enjoy doing so.

Next, I want to acknowledge and thank my parents, Joe and Jenny, and my sister, Chloe. My parents fostered my interest in the natural world from an early age, and supported me in every endeavour as I grew up. My sister blazed a trail through school and beyond; her tenacity and character have been inspirational. A portion of the enclosed work was completed at home in North Yorkshire during the first COVID lockdown. I am particularly grateful to my parents, and dog (Coco), for providing unwavering support and encouragement—and food—at that time. Though in truth, they always have done.

The senior members of my family deserve special thanks. My grandmother Caroline, for being a wellspring of positivity; my late grandfather George for music. My step-grandmother, Fiona, for always taking an interest in my work alongside my grandfather John. My grandmother Anne for Yorkshire spirit.

I've struck up some great friendships during the DPhil. Deserving special thanks are my various housemates over the years: James, Nick, Maj, Ed, Emilie, Vicky, and Barclay, all of whom are also wonderful friends. James has been a near-constant throughout, and got me out cycling on the Oxfordshire lanes. Robbie and Morven have been great collaborators with whom it has been exciting to share science. And my old friends—Stu and JH, Adam and Nic—have kept me smiling. María has been a constant source of encouragement, and has helped me to see things in ways I could have never imagined before. I'm deeply grateful.

Apportion of Credit

I am grateful to the following authors who assisted or collaborated with me on the work presented in the enclosed chapters. Their contributions are detailed below. Helen Johnson and Yavor Kostov additionally provided guidance and comment on all of the enclosed chapters.

Chapter 1

Helen L. Johnson, Yavor Kostov, Emma Beer and Camille Lique

HLJ conceived of the study and EB performed initial analysis. YK provided methodological expertise. I undertook the analysis for the *GRL* paper and the work presented here, and developed the reconstruction of observations. HLJ wrote the *GRL* manuscript with input from myself, YK, CL and EB. The chapter is based on the *GRL* paper, with modifications and additions.

Chapter 2

Helen L. Johnson, Yavor Kostov and Camille Lique

HLJ, CL and myself together conceived of the study. I performed the analysis with support from YK and wrote the *J. Climate* manuscript with assistance from authors HLJ, YK and CL. The chapter is based on the *J. Climate* paper, with modifications and additions.

Chapter 3

Helen L. Johnson, Yavor Kostov, Camille Lique, Claude Talandier and Morven Muilwijk

I developed the hypothesis and performed the analysis. CT undertook model runs with CREG025 planned by myself, YK, HLJ, CL and CT. MM also provided thoughtful discussion and model data that helped to shape the study. YK and I performed MITgcm runs. I collected additional data and wrote the chapter.

Chapter 4

Helen L. Johnson, Yavor Kostov, Robbie Mallett, Jakob Dörr, Alice Richards

I conceived of the study with input from JD. AR downloaded and organised CESM-LE model data. RM analysed and provided data from SNOW-LG. YK and HLJ provided intellectual input. I undertook the analysis and wrote the chapter.

Chapter 5

Morven Muilwijk, Jeff Scott, John Marshall, Qiang Wang, Wenhao Zhang, Juliana Marson, Paul Myers, Helen L. Johnson, Yavor Kostov

I conceived of the study with input from MM after reviewing model experiments contributing to the larger project led by JM. MM and I requested model data, which was processed and provided by authors QW, WZ, PM, JM, MM, and JS. JS provided intellectual input and performed the turning angle experiments with the MITgcm. I performed the analysis and wrote a manuscript with assistance from HLJ, YK, JS and MM, which I have added to and modified for this chapter.

Abstract

By enforcing a strong stratification at the ocean surface, freshwater is a key determiner of the physical and biogeochemical dynamics of the Arctic Ocean. In addition, fluxes of Arctic freshwater to the Atlantic have the potential to impact the Atlantic Meridional Overturning Circulation, with global implications for climate. The Arctic Ocean is understood to be freshening, but our grasp of its freshwater variability—in time and space—is hampered by the short duration and sparsity of observations.

We seek to explore the causes of recent changes in Arctic liquid freshwater content (FWC) and interpret the processes underpinning its variability on Arctic-wide and regional scales. We focus on the interactions between wind patterns, sea ice dynamics and thermodynamics, and FWC.

Through the application of linear response theory to a suite of coupled climate models, we demonstrate that Arctic FWC has a decadal memory of wind forcing, and that recent changes in FWC can be largely explained by variability in the leading modes of atmospheric circulation. Using forced ice-ocean model experiments, we show that—via dynamic thinning of sea ice in the interior Arctic basins—Fram Strait sea ice export can impact seasonal ice growth and melt, in a manner sensitive to wind forcing and ice dynamics. By constructing a linear model using data from a large ensemble of climate model simulations, we determine controls on forced changes in ice production in the Kara and Laptev seas with anthropogenic climate change, and highlight a pivotal role for September sea ice area changes. Relying on a series of coordinated model experiments, we demonstrate that sea ice import into the Beaufort gyre influences wind-driven FWC accumulation/flushing.

Our results emphasise the central importance of winds in controlling Arctic FWC variability, and elucidate significant roles for wind-driven sea ice dynamics in affecting liquid FWC via the thermodynamic growth and melt of sea ice.

Contents

Acronyms **xx**

0 Introduction **1**
0.1 Amplified warming in the Arctic . . . 1
0.2 Freshwater in the Arctic Ocean . . . 6
0.2.1 Characteristics of Arctic Ocean freshwater . . . 6
0.2.2 Significance of Arctic Ocean freshwater . . . 11
0.3 Guide to the thesis . . . 13

1 Arctic Ocean Freshwater Content and its Decadal Memory of Sea Level Pressure **16**
1.1 Introduction . . . 17
1.1.1 Freshwater adjustment in the Arctic's largest freshwater reservoir: the Beaufort Gyre . . . 19
1.2 Model details and methodology . . . 20
1.3 FWC variability in HiGEM . . . 23
1.4 Relationship between sea-level pressure and FWC . . . 27
1.5 Reconstructing freshwater variability . . . 31
1.5.1 Model FWC variability . . . 31
1.5.2 Historical freshwater changes . . . 33
1.5.3 Predictability of freshwater changes . . . 36
1.6 Discussion . . . 36
1.7 Concluding summary . . . 40

2 Response of Arctic Freshwater to the Arctic Oscillation in Coupled Climate Models **41**
2.1 Introduction . . . 42
2.1.1 Arctic FWC and the Arctic Oscillation . . . 44
2.2 Materials and methods . . . 46
2.2.1 Models used . . . 46
2.2.2 Representation of Arctic freshwater . . . 47
2.2.3 Representation of atmospheric variability . . . 50

2.2.4 Linear response function method . . . 52
2.2.5 Monte Carlo methods . . . 56
2.3 FWC step response functions in pre-industrial control runs . . . 59
2.3.1 Results . . . 59
2.3.2 Spectral properties and sources of uncertainty . . . 63
2.3.3 Reducing error with high-pass filtered FWC timeseries . . . 67
2.4 Investigating CMIP5 historical runs . . . 71
2.4.1 Methods . . . 72
2.4.2 Results . . . 73
2.5 Reconstructing historical FWC changes . . . 77
2.5.1 Selected response functions . . . 77
2.5.2 Reconstructions with selected response functions . . . 78
2.6 Discussion . . . 81
2.7 Concluding summary . . . 86

3 Wind-Driven Export: a 'Sea Ice Conveyor' of Arctic Freshwater? 87
3.1 Introduction . . . 88
3.1.1 Fram Strait sea ice export . . . 89
3.2 The 'sea ice conveyor' hypothesis . . . 93
3.2.1 Motivation: HiGEM experiments . . . 93
3.2.2 Proposed mechanism . . . 97
3.3 Contribution of sea ice export to open water in the Arctic Ocean . . . 99
3.3.1 Materials and methods . . . 99
3.3.2 Results and discussion . . . 102
3.4 Forced Fram Strait export model experiments . . . 105
3.4.1 Models used . . . 106
3.4.2 Experimental design and rationale . . . 107
3.4.3 Results . . . 112
3.5 Discussion . . . 125
3.6 Concluding summary . . . 130

4 Rise and Fall of Sea Ice Production in Arctic 'Ice Factories' 132
4.1 Introduction . . . 133
4.1.1 Arctic sea ice in decline, winter growth in ascendance? . . . 134
4.1.2 The Kara and Laptev seas . . . 138
4.2 Materials and Methods . . . 144
4.2.1 Climate model . . . 144
4.2.2 Observation-based estimates . . . 146
4.3 Understanding changes in the Kara and Laptev 'ice factories' using CESM-LE . 148
4.3.1 Shrinking growth season, rising growth rate . . . 148
4.3.2 A linear model for ice factory production . . . 156
4.3.3 Explaining forced changes in ice production . . . 165
4.3.4 Application to the observable Arctic . . . 167

4.3.5 Shifting patterns of winter ice production . . . 173
4.4 Discussion . . . 176
4.5 Conclusions . . . 178

5 Effect of Wind-Driven Sea Ice Import/Export on Beaufort Gyre Adjustment 180
5.1 Introduction . . . 181
5.1.1 The Beaufort Gyre and its freshwater content . . . 184
5.1.2 Sea ice motion and freshwater redistribution . . . 186
5.2 Coordinated Climate Response Function (CRF) experiments . . . 189
5.2.1 CRF experiments: background . . . 189
5.2.2 Experimental setup . . . 191
5.2.3 Models used . . . 192
5.2.4 Coordinated CRF experiment results . . . 193
5.3 MITgcm modified wind experiments . . . 196
5.3.1 Method . . . 196
5.3.2 Results . . . 197
5.3.3 A simple source/sink balance . . . 201
5.4 Discussion . . . 205
5.5 Concluding summary . . . 208

6 Concluding Discussion 210
6.1 Summary of key results . . . 210
6.2 Arctic-wide freshwater changes . . . 212
6.3 Sea ice export variability and upstream effects . . . 219
6.4 Shifting patterns of ice production . . . 222
6.5 Sea ice thermodynamic growth rate and Beaufort Gyre freshwater . . . 224
6.6 Evaluation of materials and methods . . . 227
6.6.1 Linear response functions from coupled climate models . . . 227
6.6.2 Model perturbation experiments with ice-ocean models . . . 229
6.6.3 Large ensembles of coupled climate models . . . 230
6.6.4 Satellite products . . . 230
6.7 Related research frontiers . . . 231
6.7.1 Satellite estimates of sea ice thickness . . . 232
6.7.2 Modelling the (coupled) climate system . . . 233
6.7.3 Effect of sea ice changes on ocean-atmosphere coupling . . . 235
6.7.4 Atlantification . . . 235
6.7.5 Increasing ocean heat from the Pacific . . . 236
6.7.6 Impact of Arctic Ocean changes on mid-latitude weather . . . 237
6.7.7 Arctic freshwater export and the AMOC . . . 238
6.8 Concluding remarks . . . 239

References 242

Glossary **286**

List of Figures

0.1 a) CMIP5 multi-model zonal mean surface temperature change for the last 30 years of the 150 year long CMIP5 $4\times CO_2$ experiment compared with the last 30 years of the pre-industrial control run. In the $4\times CO_2$ experiment, the atmospheric concentration of CO_2 is instantaneously quadrupled relative to pre-industrial values as a step-change perturbation. Box and whisker plots show the median (lines), 25th to 75th percentiles (boxes) and full spread (whiskers) of temperature change averaged over the tropics (30 °S–30 °N) and the Arctic (60 °S–90 °N). b) Multi-model mean Arctic warming across different seasons. Arctic warming is 15.9 K in winter and 6.5 K in summer. Figure from Pithan and Mauritsen (2014). 2

0.2 Bathymetric map of the Arctic Ocean, showing the major basins, seas, straits, topographic features, islands and landmasses. Bathymetric basemap is the International Bathymetric Chart of the Arctic Ocean (IBCAO), available at: https://www.gebco.net/data_and_products/gridded_bathymetry_data/arctic_ocean/ . . . 7

0.3 a) Annual mean sea-level pressure from ERA5 reanalysis data (Hersbach et al., 2020). Mean taken over the years 1979–2018. b) Depth of the 34.45 isohaline, which lies near the base of the halocline. Figure taken from Carmack et al. (2016). c) Schematic showing the dominant circulation of the upper ocean (blue arrows) and underlying Atlantic Water (red-pink arrows). Figure taken from Carmack et al. (2015). 10

1.1 Conceptual summary of linear response methodology. Terms explained in the text. 21

1.2 (a) Time series of Arctic FWC. Monthly mean values are plotted in blue, and the time series with mean seasonal cycle removed is shown in red. (b) Mean seasonal cycle in Arctic liquid FWC (solid blue line) and sea-ice (dashed blue line); freshwater fluxes from snowfall plus precipitation minus evaporation (red dashed line) and river runoff (solid red line). Spatial distribution of the (c) mean FWC, (d) amplitude of the mean seasonal cycle, and (e) standard deviation after mean seasonal cycle removed. 24

1.3 Freshwater fluxes through the straits that define the gateways to our Arctic domain. Upper panel shows liquid freshwater fluxes (FWF), lower panel shows freshwater fluxes as sea ice (IVOLF stands for ice volume fluxes). Straight grey line indicates the time mean of the sum of all straits in both cases. Transparent lines are the complete timeseries, heavier lines show the same data after removal of a seasonal cycle. 26

1.4 HiGEM pre-industrial control run FWC timeseries after removal of time-mean (109,000 km^3), compared with: upper panel—accumulated liquid freshwater fluxes (FWF) and sea ice volume fluxes (IVOLF); lower panel—accumulated ice-to-ocean freshwater fluxes due to freezing and melting (I2O) and accumulated precipitation plus runoff minus evaporation (P+R-E). 27

1.5 (a–c) First three empirical orthogonal functions (EOFs) of the sea-level pressure north of 70 °N. (d) Change in Arctic freshwater content (FWC) in response to a step change of one standard deviation in each of the three principal components of sea-level pressure: PC1 (orange), PC2 (green), and PC3 (grey). Black lines show the mean estimate and shaded envelopes the uncertainty. A step change in sea-level pressure of the magnitude and sign shown in (a)–(c) would result in the change in FWC shown in (d). 28

1.6 Reconstructed time series of Arctic freshwater content (orange line) in the control run, based on a convolution of the impulse response function with the model SLP field using (a) PC1 only; (b) PC1 and PC2; and (c) PC1, PC2, and PC3. The model's (detrended) Arctic FWC is shown in black. Plotted in (d) is the fraction of FWC variance explained (R^2) when the convolution excludes SLP data from the most recent time period (the forecast horizon). 32

1.7 Reconstructed time series of Arctic FWC (orange line) using reanalysis (ERA-20C and ERA-Interim) and impulse response functions derived from HiGEM. Black stars: observational data from Rabe et al. (2014). Blue line: best fit line through Polyakov et al. (2013) observational data. Cyan arrow: flux of freshwater proposed by R. Curry and Mauritzen (2005). Blue line in (b), (c), and (d): projections of the ERA-20C sea-level pressure variability onto EOF1, EOF2, and EOF3, respectively (36-month running means); contribution to the FWC shown in orange. Time series in (a) sums the orange lines in (b), (c), and (d). Shaded windows (a): periods in which the convolution uses less than full 30-year response functions. 35

2.1 De-seasonalised Arctic FWC timeseries in 12 CMIP5 pre-industrial control runs. Model simulations are categorised into lengths of 3,600, 6,000 and 9,600 months (see text). Mean FWC is given beneath the name of each simulation. Magnitude of variability can be seen by comparison with y-axis spacing of 10,000 km^3. The timeseries are positioned on the y-axis such that the first value is anchored to this spacing. 49

2.2 Mean freshwater distribution, in metres, over the Arctic Ocean domain considered here. Mean taken over a 50 year period selected randomly from within the pre-industrial control runs. 51

2.3 The negative AO as represented by ERA-Interim (Berrisford et al., 2001). Calculated as the first EOF of SLP variability north of 70 °N, this mode explains 53% of the variance in ERA-Interim SLP data spanning 1979–2018. 52

2.4 Pre-industrial control run reconstruction of Arctic FWC in CCSM4 using SLP and estimated response functions. R denotes the correlation of the reconstructed timeseries with the original FWC timeseries. R_S denotes the correlation after removal of the FWC contributions from the other components. 55

2.5 Flow chart illustrating our Monte Carlo method for calculating the uncertainty on the response functions. Repeated boxes and ellipses indicate the presence of 1,000 versions of the given timeseries. $\mathrm{PC1}^{rand}$ and $\mathrm{FWC}^{RandRes}$ are generated through randomisation of PC1 and FWC^{res}, respectively. The randomisation process is described in Section 2.2.5. The $\times$ symbol indicates convolution (first term on the RHS of Equation 2.3); + refers to the addition and rescaling process that completes the RHS of Equation 2.3; $\backslash$ is shorthand for the multiple lagged regression used to estimate impulse responses. 58

2.6 Response of Arctic FWC to a step change to a more anticyclonic (more negative) AO in 12 CMIP5 pre-industrial control runs. Shaded areas show the one standard deviation uncertainty, calculated using Monte Carlo method in Section 2.2.5. Black dotted line in all panels is the ensemble mean step response across all 12 models. Response functions are divided into four panels for legibility. 60

2.7 Reconstruction skill of response functions, pre-industrial control run. Bars indicate what reconstruction skill would be significant at the 95% confidence level; blue and red shading mark the significance thresholds for PC1 and all three PCs, respectively. Significance levels are derived using the Monte Carlo technique. Blue crosses indicate the R value from the correlation of reconstructed FWC using PC1 and the actual FWC timeseries, after removal of the reconstructions using PC2 and PC3. Red crosses give the R value for the timeseries correlation of FWC and the reconstruction using all three PCs. 62

2.8 Mean sea ice volume and extent in pre-industrial control runs of 12 CMIP5 model simulations. 63

2.9 Mean synthetic response function error (n = 500) associated with the synthetic test outlined in the text. Legend heading *variance* refers to the variance explained by the predictable part of the signal. The other part of the 'target' FWC timeseries is comprised of 'residual noise' with the decorrelation timescale specified. As the variance explained decreases, the residual noise becomes increasingly dominant. Error is integrated through time and given relative to the size of the FWC reservoir. The PC1 response function for ACCESS 1-0 is used as the initial response function for these synthetic tests. 66

2.10 a) Power spectra of Arctic FWC in all models, before (dashed line), and after (solid line) filtering with a 40 year high-pass filter. b) Autocorrelation functions for original FWC timeseries. c) Autocorrelation functions for filtered FWC timeseries. Horizontal black line indicates the $1/e$ value. Curves intersect this value at the e-folding decorrelation timescale. 68

2.11 Step responses of Arctic FWC to a step increase in the strength of the anticyclonic AO-, using high-pass filtered FWC timeseries. Dashed line shows the ensemble mean response of all 12 models. Shaded envelopes show the one standard deviation uncertainty. 69

2.12 Reconstruction skill of response functions computed using filtered pre-industrial control run FWC timeseries. Bars indicate what reconstruction skill would be significant at the 95% confidence level; blue and red shading mark the significance thresholds for PC1 and all three PCs, respectively. Significance levels are derived using the Monte Carlo technique. Blue crosses indicate the R value from the correlation of reconstructed FWC using PC1 and the actual FWC timeseries, after removal of the reconstructions using PC2 and PC3. Red crosses give the R value for the correlation of the actual FWC timeseries and the reconstruction using all three PCs. 70

2.13 Monte Carlo evaluation of historical runs. Blue bars indicate the significance levels for a single forcing component. Crosses show the reconstruction skill using linear response functions derived from the pre-industrial control run, calculated after removal of the FWC contributions from PC2 and PC3. Squares represent the 95th percentile reconstruction skill using a Monte Carlo ensemble of synthetic response functions—an *upper* estimate of possible reconstruction skill with linear responses. 74

2.14 Selected response functions: response of Arctic FWC to a step change to a more negative AO in pre-industrial control runs. Selected based on performance in both pre-industrial and historical runs. Black dashed line shows mean of selected response functions, grey dashed line shows mean of all 12 response functions presented in this chapter. 78

2.15 Reconstruction of historical FWC changes from 1980. Calculated using SLP from reanalysis and response functions estimated from pre-industrial control runs of each model, and compared against FWC data from Rabe et al. (2014). The upper panels show the negative AO in ERA-20C (1960–1978) and ERA-Interim (1979–2018) reanalysis SLP data, normalised to one standard deviation in the monthly data. Note that positive values indicate a more negative AO. Grey line: monthly timeseries; blue line: three-year moving mean. Solid line in lower panel denotes reconstruction using PC1 alone while dotted line is for all three PCs. 79

3.1 Components of the liquid Arctic FWC responses to PC2 (upper panel) and PC3 (lower panel) in coupled climate model HiGEM. Corresponding empirical orthogonal functions (EOFs) of SLP are shown on the right, flipped in sign from those presented in Chapter 1, such that the responses (left) describe freshwater export. 'H' indicates high pressure, while 'L' indicates low pressure. Note that a positive export is a loss of FWC from the Arctic Ocean, while negative ice-to-ocean fluxes are a loss of FWC from ocean to sea ice. 94

3.2 Components of the Arctic solid freshwater responses to PC2 (upper panel) and PC3 (lower panel) in coupled climate model HiGEM. Corresponding EOFs of SLP are shown on the right, flipped in sign from those presented in Chapter 1. 'H' indicates high pressure, while 'L' indicates low pressure. Note that a positive export is a loss of sea ice from the Arctic Ocean, while negative ice-to-ocean fluxes drain the liquid freshwater reservoir and add to the solid reservoir. 95

3.3 Illustration of hypothetical responses of sea ice export (upper row) and liquid freshwater fluxes (bottom row) to a step change in atmospheric forcing. The panels on the left show the time-instantaneous fluxes, whereas the panels on the right show the accumulated fluxes. The difference in scales is schematically indicated by cyan dashed lines. 96

3.4 Schematic illustrating the 'sea ice conveyor' mechanism: depletion of liquid FWC by freezing and wind-driven ice export to the North Atlantic. Note that there is no 'return flow' included in the conveyor mechanism (i.e. no lower branch). . . . 98

3.5 Contributions to open water area available for freezing during winter. Winters are labelled such that the winter of 2010/2011 lies at 2011 on the x-axis. Sources of data are described in Section 3.3.1. 103

3.6 Possible contributions to winter sea ice growth from each of the sources of open water in Figure 3.5, compared to the volume change from PIOMAS. Different thickness contributions are assumed based on the reasoning given in Section 3.3.1. . . . 104

3.7 Wind perturbations applied. a) Local Fram Strait wind forcing; b) Arctic Dipole pattern. Shown here on the CREG025 grid. 108

3.8 a) Empirical orthogonal functions (EOFs) of SLP from ERA5 calculated north of 60N. Red indicates higher pressure, blue indicates lower pressure. b) Regression of principal components (PCs) of SLP on to Fram Strait sea ice area export record of Smedsrud et al. (2017). Polarity of PCs matches that shown in (a). Regressions with a P value of more than 0.05 are greyed out and deemed insignificant at the 95% confidence level. P values for each PC are shown in each subplot. Steepness of regression line (orange) represents the magnitude of the regression coefficient. 109

3.9 Mean sea ice thickness in March and September in the control runs of CREG025 (left) and the ECCO configuration of the MITgcm (right), during the year the experiments are performed. 111

3.10 Response to local Fram Strait wind forcing in the ECCO configuration of the MITgcm (a,b) and CREG025 (c,d), over the Arctic region shown in Figure 3.11. (Liquid) FWC is relative to a reference salinity of 34.8, IVOL is sea ice volume, SIA is sea ice area in units 1,000 km^2, I2O is cumulative ice-to-ocean freshwater flux due to melting (positive) or freezing (negative), IVOLF is cumulative ice volume flux across all edges of region, Fram is IVOLF only through Fram Strait, Div is cumulative net divergence in units 1,000 km^2, FWF is cumulative freshwater flux across all edges of region. FWF was not available from CREG025. Export from the region is negative. Vertical dashed line in (a) and (c) shows when wind perturbation is switched off. Ice volume fluxes through Fram Strait are compared to control run fluxes in (b) and (d). 113

3.11 Wintertime anomaly maps in the MITgcm and CREG025 to the local Fram Strait perturbation pattern. Variables are integrated over the masked region in order to construct timeseries in Figure 3.10. SIT stands for sea ice thickness. 114

3.12 Summertime maps of the MITgcm and CREG025 responses to the local Fram Strait perturbation pattern. Ice-to-ocean fluxes are given here in terms of a melting anomaly. For maps (c) and (d), the accumulation of the melting anomaly begins at the start of June (there is no explicit imprint of the prior winter in these maps). . . 116

3.13 Response to Arctic Dipole wind forcing in the ECCO configuration of the MITgcm (a,b) and CREG025 (c,d), over Arctic region shown in Figure 3.11. (Liquid) FWC is relative to a reference salinity of 34.8, IVOL is sea ice volume, SIA is sea ice area in units 1,000 km^2, I2O is cumulative ice-to-ocean freshwater flux due to melting (positive) or freezing (negative), IVOLF is cumulative ice volume fluxes across all edges of region, Fram is IVOLF only through Fram Strait, Div is cumulative net divergence in units 1,000 km^2, FWF is cumulative liquid freshwater flux across all edges of region. FWF was not available from CREG025. Export from the region is negative. Vertical dashed line in (a) and (c) shows when wind perturbation is switched off. Ice volume fluxes through Fram Strait are compared to control run fluxes in (b) and (d). 118

3.14 Wintertime anomaly maps in the MITgcm and CREG025 to the Arctic Dipole wind perturbation pattern. 120

3.15 Summertime maps of the MITgcm and CREG025 responses to the Arctic Dipole wind forcing perturbation. Ice-to-ocean fluxes are given here in terms of a melting anomaly. For maps (c) and (d), the accumulation of the melting anomaly begins at the start of June (there is no explicit imprint of the prior winter in these maps). . . 122

4.1 Arctic sea ice volume trends from satellite retrievals. Figure from Kwok (2018) . . 136

4.2 Mean Arctic sea ice velocities 2000–2018 from the Polar Pathfinder sea ice drift product (Tschudi et al., 2019), which is based on satellite retrievals. Kara-Laptev study region outlined by blue box. 140

4.3 Decadal ensemble mean changes in early winter sea ice extent edges in CESM-LE from 1970–2080. Figure prepared by co-author of manuscript in preparation, J. Dörr. Study region indicated by black box. 150

4.4 Decadal mean changes in sea ice production across winter months in CESM-LE. Inset panel shows changes in the timing of peak sea ice production and changes in the amplitude of the peak value. 151

4.5 Ensemble mean of changes from one year to the next in monthly surface air temperature and sea ice area in CESM-LE. The plots indicate the change in air temperature (left) and sea ice area (right) in a given month and year from that same month the prior year. The yearly trends for each month are smoothed using a 10-year moving average. 152

4.6 Winter ice production (top) and decomposition into growth rate (left) and freezing area days (right). Note that the freezing area days is rescaled in terms of the total KL area, such that the upper limit is 210 on the y scale: the duration of our seven month winter period in days. 155

4.7 3D histogram showing divergence and ice-to-ocean fluxes in all grid cells within the KL seas during winters 1990–1999 from CESM-LE. First 10 million such grid points shown. 160

4.8 Timeseries comparison of key parameters in CESM-LE and real-world estimates (red line): a) surface air temperatures, b) September sea ice area, c) net area diverged, d) compensated area diverged, e) September 10 m T in CESM-LE and SST in NOAA OI SSTv2, f) snow depth on ice. 20C is shown in blue and RCP8.5 in orange; ensemble mean indicated by darker line. 163

4.9 Winter ice production regression coefficients for key parameters, standardised by one standard deviation in 20C. Regressions calculated using internal variability, with the ensemble mean removed. Variance explained is shown. 164

4.10 a) Ensemble mean winter sea ice production (black line), and reconstruction of ensemble mean using regressions trained on internal variability over the 20C (light blue line), RCP8.5 (light orange line) and full 1920–2080 timeseries (heavy blue line). Lower panel shows the contribution to the summed reconstruction made by different components of the linear model, plotted relative to the first winter (1920/1921). 166

4.11 Mean ocean-to-ice heat flux in the Kara-Laptev seas during the freezing season (values retrieved from grid cells showing net ice growth). 20C shown in blue, RCP8.5 shown in orange. Ensemble mean shown by darker lines. 168

4.12 Comparison of the spatial pattern of ensemble mean changes in CESM-LE between 1980–1999 and 2000-2019 to changes in observation-based estimates over approximately the same time period. (See Section 4.2 for exact time periods covered.) . . 170

4.13 Reconstruction of historical changes up to 2016/2017 in the winter ice production in the KL seas relative to the first winter of the reconstruction: 1982/1983. Reconstruction uses climate variables from observation-based estimates and the linear model trained on CESM-LE internal variability. 172

4.14 Shifting patterns of ensemble mean winter ice production in CESM-LE relative to a reference period 1980-1999 (a). b) shows the changing share of total Arctic ice production contributed by the KL seas. The Arctic region in question is enclosed by the magenta line in (a) and Bering Strait. Ensemble mean in (b) shown as darker line. Plots (c-f) show the spatial changes in ice production during sequential two-decade periods. Blue colour indicates more ice production; red indicates less. Ice production does not consider melting. 174

5.1 Possible mechanisms leading to sea ice export or import into the BG region (black box) under a stationary SLP anomaly. Blue arrows indicate ice motion. In (a), grey circles represents isobars, 'H' or 'L' indicate high or low SLP. Note that divergence corresponds to export and convergence to import in case (a). However in case (b) there may be confounding correlations with thickness advection. Dashed magenta line indicates the scenarios we attempt to induce in Section 5.3. 183

5.2 Plan-view schematic to illustrate the angular relationships between geostrophic winds, surface winds, sea ice motion and Ekman layer ocean velocities, in the absence of surface geostrophic ocean currents. The modified wind is used to trigger different sea ice export scenarios in Section 5.3. 188

5.3 BGP and BGM CRFs for each model. Upper row: liquid FWC responses. Lower row: cumulative sea ice flux responses. Dotted lines correspond to sea ice volume responses. Lower panel: corresponding anomaly patterns, BGP on left and BGM on right. 194

5.4 CRFs for different FWC budget terms in the regular CRF experiment (left side) and after +10° wind forcing modification (right side). Fluxes are positive when directed into the gyre. The FWC curves are coloured for compatibility with Figure 5.5. BGM and BGP FWC curves are overlain on BGM10 and BGP10 plots as dashed dark grey lines for ease of comparison. FWF = cumulative liquid freshwater flux across boundaries; FWC = liquid freshwater content; IOF = cumulative ice-to-ocean freshwater fluxes (positive into ocean); IVOL = sea ice volume; IVOLF = cumulative volume fluxes of sea ice across boundaries (import/export). 198

5.5 Maps showing sea ice thickness and velocity fields. Panels on the left show mean CTRL and CTRL10 conditions; panels on the right show the 30-year mean responses in those fields versus respective control periods. 199

5.6 Difference between the ice volume fluxes through each gate of the BG region (upper panel; positive into gyre region), and velocity and thickness fields (lower panels) between the BGP and BGP10 responses, and BGM and BGM10 responses, respectively. 200

5.7 Comparison of liquid freshwater CRFs from the BGP, BGP10, BGM and BGM10 experiments (heavy lines), and time-evolving solutions for FWC from Equation 5.3 (thin solid/dashed/dotted lines). 203

5.8 Multiple regression of the first three EOFs of SLP against ice divergence in the Beaufort gyre region from Polar Pathfinder. Comparison is on a weekly timescale. Upper panels show the EOF patterns, multiplied by 1 standard deviation of the corresponding principal component timeseries. The lower panels show the regressions. 207

Acronyms

20C The 20th Century, or 'historical' run of CESM-LE, spanning 1920–2005. xvii, xviii, 144, 151, 152, 155, 156, 162–168, 177, 178

AMOC Atlantic Meridional Overturning Circulation. 235, 238

AO Arctic Oscillation. 77, 225

AOMIP Arctic Ocean Model Intercomparison Project. 190

AWI Alfred Wegener Institute. 192

CAA Canadian Arctic Archipelago. 119, 120, 169, 171, 187, 198, 207

CESM-LE Large Ensemble of the Community Earth System Model. xx, 14, 84, 85, 133, 138, 144, 211, 213, 222, 224, 230

CGRF Canadian Meteorological Centre's global deterministic prediction system re-forecasts. 193

CMIP3 Coupled Model Intercomparison Project Phase 3. 49

CMIP5 Coupled Model Intercomparison Project Phase 5. xi, 2, 14, 24, 59, 82, 125, 212, 228

CMIP6 Coupled Model Intercomparison Project Phase 6. 49, 92, 239

ECMWF European Centre for Medium Term Weather Forecasting. 146

EOF Emprical orthogonal function. 215

FAMOS Forum for Arctic Modelling and Observational Synthesis. 190

FWC Freshwater content; unless otherwise stated, this refers to liquid freshwater. 43, 212

GSA Great Salinity Anomaly. 40

KL Kara and Laptev (seas). xvii, xviii, 134, 144, 146, 155, 156, 160, 169, 171–176, 178

MERRA-2 NASA's Modern Era Retrospective-Analysis for Research and Applications-Version 2. 147

MOSAiC Multidisciplinary Drifting Observatory for the Study of Arctic Climate. 231, 234, 235

NASA GSFC NASA Goddard Space Flight Centre. 147, 169, 171

NOAA OI SST v2 NOAA Optimum Interpolation Sea Surface Temperature Version 2. 148, 171

NSIDC National Snow and Ice Data Center. 100, 147

OE Observation-based Estimate (this includes e.g. satellite retrievals and reanalyses). 134, 156, 168, 169, 171

OSNAP Overturning in the Subpolar North Atlantic Program. 238

PIOMAS Pan-Arctic Ice Ocean Modeling and Assimilation System. xv, 101, 103, 104, 127, 135, 145

RAPID-MOCHA Rapid Climate Change Meridional Overturning Circulation and Heatflux Array. 238

RCP8.5 Representative Concentration Pathway to an increase in radiative forcing value on pre-industrial levels of 8.5 Wm^{-2}. xvii, xviii, 140, 144, 152, 155, 156, 162–168, 176, 177, 217

SHEBA Surface Heat Budget of the Arctic Ocean. 234, 235

SLP Sea-level pressure. 43, 212

SSM/I Special Sensor Microwave/Imager. 140

TOA Top-of-atmosphere. 3

ULS Upward-looking sonar. 126

Chapter 0

Introduction

This chapter provides a broad introduction to the thesis: its subject matter, its relevance and relation to active research questions, and its structure. Topic-specific introductions are given at the beginning of each respective chapter.

0.1 Amplified warming in the Arctic

The idea that climate changes in the Arctic are amplified relative to the global mean has existed since Arrhenius (1896). So-called Arctic Amplification is a robust feature of climate model simulations of the planet's response to increasing greenhouse gas concentrations (Figure 0.1; e.g. Holland & Bitz, 2003; Manabe & Stouffer, 1980; Manabe & Wetherald, 1975; Winton, 2006), and is also evident in palaeoclimate proxy records (G. H. Miller et al., 2010). Observations over the last century have clearly detected an amplified Arctic warming signal (Bekryaev et al., 2010; Box et al., 2019) that is most intense during autumn and winter periods (Serreze et al., 2009; Serreze & Barry, 2011), as predicted by climate models (e.g. Manabe & Stouffer, 1980).

The stark decline of Arctic sea ice (e.g. Cavalieri & Martin, 1994; Kwok, 2018; Maslanik et al., 2007; Stroeve et al., 2007) is both a vivid expression of anthropogenic climate change (Notz & Stroeve, 2016; Stroeve & Notz, 2018), and a driver of amplified Arctic warming (e.g. Dai

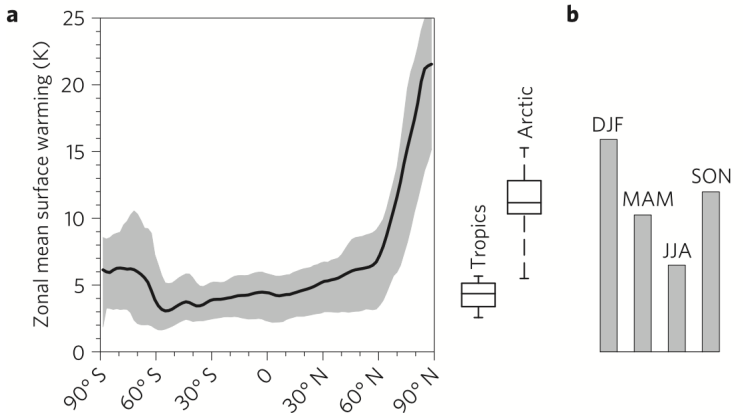


Figure 0.1: a) CMIP5 multi-model zonal mean surface temperature change for the last 30 years of the 150 year long CMIP5 $4\times CO_2$ experiment compared with the last 30 years of the pre-industrial control run. In the $4\times CO_2$ experiment, the atmospheric concentration of CO_2 is instantaneously quadrupled relative to pre-industrial values as a step-change perturbation. Box and whisker plots show the median (lines), 25th to 75th percentiles (boxes) and full spread (whiskers) of temperature change averaged over the tropics (30 °S–30 °N) and the Arctic (60 °S–90 °N). b) Multi-model mean Arctic warming across different seasons. Arctic warming is 15.9 K in winter and 6.5 K in summer. Figure from Pithan and Mauritsen (2014).

et al., 2019; Screen & Simmonds, 2010). The positive feedback associated with the loss of high albedo sea ice and snow cover has long been considered to be a key part of Arctic Amplification (Arrhenius, 1896; Manabe & Wetherald, 1975). As presently understood, however, Arctic Amplification is a multi-faceted phenomenon with a suite of inter-related processes operating on different timescales (Block et al., 2020; Payne et al., 2015; Serreze & Barry, 2011). The processes at play can be divided on a basic level into: a) shortwave radiative feedbacks, b) longwave (both upwards and downwards) radiative feedbacks, c) atmospheric transports of heat and moisture from lower latitudes and d) fluxes of heat from the ocean, whether driven by increased meridional heat convergence or increased vertical fluxes.

Primary among the shortwave radiative feedbacks is the positive feedback associated with the loss of reflective sea ice and its highly reflective snow cover: the 'ice-albedo feedback'. The effect of sea ice decline is not just limited to the summertime, when it enables increased absorption of shortwave solar radiation, but persists into the autumn and winter. Increased

heat fluxes from the (comparatively warm) ocean to atmosphere during the freezing season occur due to: a) additional heat sequestered in the ocean during summer, b) delayed onset of freezing and c) a thinner ice and snow cover (Screen & Simmonds, 2010; Serreze et al., 2009). However, models with a fixed snow and ice cover still show substantial Arctic Amplification under greenhouse gas forcing (Graversen & Wang, 2009; Hall, 2004), forcing us to consider other mechanisms.

The longwave radiative feedbacks comprise the effects of water vapour (Graversen & Wang, 2009) and clouds (Vavrus, 2004) on downwards longwave radiation, and longwave temperature feedbacks (Pithan & Mauritsen, 2014). Longwave temperature feedbacks concern the impact of rising surface air temperatures on the outgoing top-of-atmosphere (TOA) longwave radiation, and can be further subdivided into the Planck feedback and lapse-rate feedback (Payne et al., 2015). The Planck feedback is determined by the Stefan-Boltzmann law, in which the radiation from a substance at a temperature T and emissivity ϵ is given by $R = \epsilon\ \sigma\ T^4$, where σ is the Stefan-Boltzmann constant. The change in emitted radiation with respect to temperature ($\frac{dR}{dT}$) therefore goes with the cube of temperature. As such, in order to balance a radiative perturbation (ie. from greenhouse gas forcing), a larger temperature increase is required at higher latitudes, where the initial temperature is colder, than at lower latitudes (Pithan & Mauritsen, 2014). The importance of the Planck feedback is debated, however (Block et al., 2020).

The Planck feedback is related to vertically uniform changes in atmospheric temperature, whereas the Lapse-rate feedback concerns changes in the outgoing radiation due to deviations from vertically uniform warming (Pithan & Mauritsen, 2014). At low and mid-latitudes, deep convective mixing in the atmosphere means that surface warming is efficiently transmitted to the top of the troposphere by the rising of air parcels. These rising air parcels furthermore release additional latent heat high in the atmosphere in a warming climate, causing greater warming at the TOA than at the surface. This 'top-heavy' warming means that a smaller increase in warming is required to offset a given TOA radiative perturbation: the lapse-rate

feedback is a negative feedback at low latitudes (e.g. Block et al., 2020). In the Arctic, by comparison, the winter atmosphere is generally characterised by a stable temperature inversion, in which surface warming is relatively decoupled from the lighter air aloft; the 'bottom-heavy' warming that results requires a greater degree of surface warming to offset a given TOA radiative imbalance. Some studies suggest that the lapse-rate feedback is the leading cause of Arctic Amplification (Bintanja et al., 2011; Payne et al., 2015; Pithan & Mauritsen, 2014).

In the Barents and Kara seas, warming is partially explained by a positive trend of moist air intrusions from lower latitudes (Woods & Caballero, 2016). On a longer timescale, oceanic heat convergence is implicated in Arctic warming by a correlation between multi-decadal variations in Atlantic Ocean temperatures and Arctic surface air temperatures (Chylek et al., 2009). Indeed, increased Atlantic heat transport has been linked to the warming and decline of sea ice in the Barents Sea (Årthun et al., 2012; Årthun et al., 2019).

A vigorous debate continues about the relative roles of different climate feedbacks in explaining the magnitude of Arctic Amplification and spread between different coupled climate models (e.g. Block et al., 2020; Dai et al., 2019; Pithan & Mauritsen, 2014). It is a debate that is complicated by the interaction between different processes, and the multiple effects associated with a single phenomenon (e.g. the decline of sea ice).

The observed expression of Arctic Amplification in surface air temperatures, regardless of its cause, has been a warming of 2.7 °C during 1971–2017; 2.4 times stronger than the Northern Hemisphere mean (Box et al., 2019). Sea ice extent and thickness are declining in all seasons, but most strongly in the late summer (Kwok, 2018; Stroeve & Notz, 2018). September sea ice extent declined by 45% over 1979–2018 relative to the 1979–1989 mean (Stroeve & Notz, 2018), and September thickness has fallen by 66% between 1958–1976 and 2011–2018 (Kwok, 2018). As more Arctic sea ice melts in the summer, the ice pack is becoming increasingly seasonal and its age is declining (Maslanik et al., 2007; Maslanik et al., 2011). The area fraction of Arctic sea ice 5 years old or more has decreased from 30% in 1984 to 2% in 2018 (Stroeve & Notz, 2018). The increasing length of the melt season and reduced summer sea ice concentrations allow for

increased solar heating of the upper ocean, which, alongside a secondary contribution from lateral ocean heat convergence (Steele et al., 2010), has driven increasing late summer upper ocean temperatures during the satellite era (Steele et al., 2008; Timmermans & Labe, 2020).

In addition to these thermal changes, the Arctic Ocean freshened over the observational period between 1992–2014 (Rabe et al., 2014) and indeed is widely predicted to see increased freshwater storage, inflow and outflow fluxes under warming scenarios in coupled climate models (Haine et al., 2015; Holland et al., 2007; Jahn & Laiho, 2020; Shu et al., 2018; Zanowski et al., 2021). However, this freshening is not uniform and there is evidence linking episodic collapses in the stratification in the Eurasian Basin and northern Barents Sea to declines in freshwater delivery to those regions (Lind et al., 2018; Polyakov et al., 2017). The collapse, or weakening of the halocline makes those regions more susceptible to heat carried by water masses coming from the Atlantic Ocean, with significant implications for sea ice stability (Polyakov et al., 2020).

This phenomenon, of parts of the Arctic Ocean becoming more influenced by Atlantic inflows—and hydrographically more similar to the N. Atlantic—is referred to as 'Atlantification'. The term was coined (to our knowledge, by Simmonds et al., 2008) to describe the increased transport of Atlantic heat into the Arctic Ocean (Polyakov et al., 2005; Walczowski & Piechura, 2006). While long-term trends in volume transport are difficult to infer from limited observations, the temperature of the Atlantic inflow at Fram Strait and the Barents Sea Opening has warmed by about 1 °C between 1980 and 2012 (Muilwijk et al., 2018). Atlantification has been further investigated in terms of its influence on ice retreat/growth reductions in the Barents Sea (Årthun et al., 2012; Barton et al., 2018) and beyond (Årthun et al., 2019; Polyakov et al., 2017). Atlantic inflows, heat fluxes, atmospheric circulation, freshwater distribution and patterns of sea ice cover and sea ice-mediated freshwater redistribution are all interconnected, and their interactions in a warming climate is an urgent topic of critical interest (e.g. Asbjørnsen et al., 2020; Barton et al., 2018; Muilwijk et al., 2019; Polyakov et al., 2020; Skagseth et al., 2020).

Arctic warming appears to be changing certain pan-Arctic and synoptic scale patterns of atmo-

spheric circulation in the Arctic region (Moore et al., 2018; Overland & Wang, 2010; Simmonds et al., 2008). Less clear are the potential impacts on mid-latitude weather. Various hypotheses tie Arctic Amplification to extreme mid-latitude wintertime weather, in which cold air spills down from the Arctic to mid-latitudes (e.g. Cohen et al., 2014; Francis & Vavrus, 2012). However, this is a debate that is hotly contested (e.g. Blackport & Screen, 2020; Cohen et al., 2014; Cohen et al., 2018; Dai & Song, 2020; Francis & Skific, 2015; Mori et al., 2019).

The variety, complexity and speed of Arctic changes (Overland et al., 2019) demands concerted research efforts to understand and anticipate those changes. In this thesis, we focus on understanding changes in Arctic liquid freshwater. Freshwater, primarily by virtue of its role in enforcing a strong stratification at the surface of the Arctic Ocean, plays a core and dynamic role in the Arctic climate and biogeochemical system, with direct and indirect implications for global climate (e.g. Carmack, 2007; Carmack et al., 2016; Rudels, 2015).

0.2 Freshwater in the Arctic Ocean

0.2.1 Characteristics of Arctic Ocean freshwater

The Arctic Ocean (Figure 0.2), almost fully enclosed by land masses, receives river runoff from an area of over 22 million km^2, more than 1.5 times the size of the Arctic Ocean itself (Lammers et al., 2001; Peterson et al., 2002). These high latitude landmasses are net precipitation regions. Indeed the Arctic Ocean receives 11% of the world's river flow, while only comprising 4% of global ocean area, and—as the shallowest ocean—only 1% of global ocean volume (Dai & Trenberth, 2002; Lammers et al., 2001). The Arctic Ocean also receives inflow of relatively fresh waters from the Pacific through the shallow Bering Strait. Combined, these freshwater fluxes into the Arctic Ocean are approximately 9,000 km^3/yr (Haine et al., 2015), which is on the order of 10% of the total amount of freshwater stored in the Arctic Ocean (the value depends on the definition of the area encompassed by the Arctic Ocean; Haine et al., 2015; Serreze et al., 2006). These freshwater inflows are approximately balanced by outflows of freshwater—as

liquid and as sea ice—into the North Atlantic.

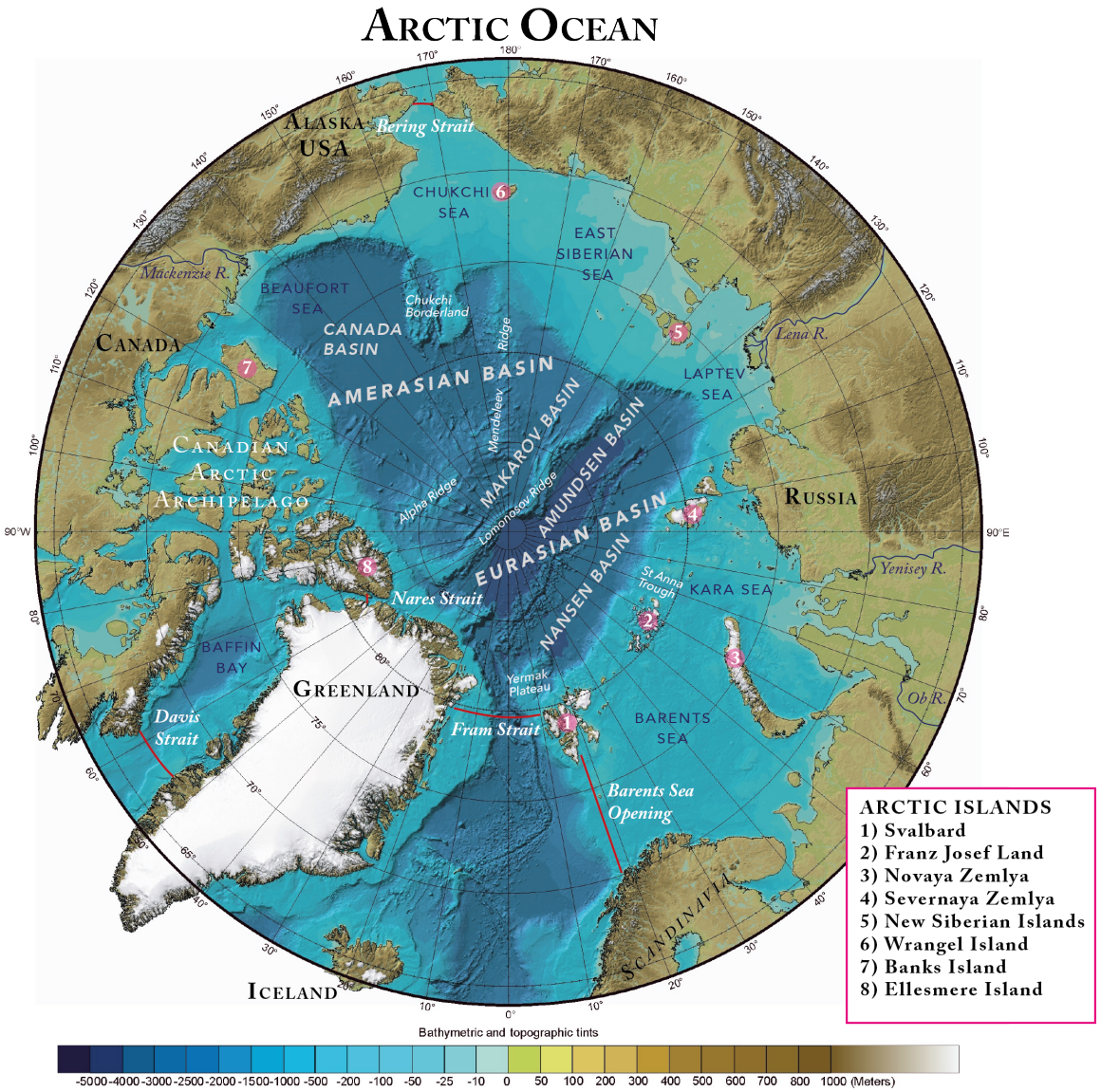


Figure 0.2: Bathymetric map of the Arctic Ocean, showing the major basins, seas, straits, topographic features, islands and landmasses. Bathymetric basemap is the International Bathymetric Chart of the Arctic Ocean (IBCAO), available at: https://www.gebco.net/data_and_products/gridded_bathymetry_data/arctic_ocean/

In the cold and relatively fresh waters above the base of the Arctic halocline, the density of seawater—and therefore the vertical structure of the ocean—is primarily determined by salinity rather than temperature (e.g. Carmack, 2007). As a result, the freshest waters reside in the uppermost part of the ocean, separated from more saline waters from the Atlantic below by

a cold halocline (the depth of the halocline base is approximated by the depth of the 34.45 isohaline, Figure 0.3b). The density difference across the halocline is sufficiently strong that vertical mixing and heat fluxes from the Atlantic Water into the fresh upper ocean are limited, generally less than 1 W/m^2 (e.g. Fer, 2009; Lenn et al., 2009; Shaw & Stanton, 2014).

As a result of its polar position, diurnal and seasonal cycles in the Arctic are unlike those at midlatitudes. North of the Arctic circle, the sun does not rise in midwinter; in midsummer, it does not set. The further north one goes, the longer these periods of polar night and polar day become. This distinctive seasonal cycle of solar radiation has important implications for radiative dynamics in the Arctic. Clouds, for instance, reduce incoming shortwave radiation in the summer but trap outgoing longwave radiation in the winter (J. A. Curry et al., 1996).

In summer, during polar day, the pack ice breaks up and partially melts, and solar radiation can penetrate into and warm the upper ocean (e.g. Perovich et al., 2008). The heat sequestered in the upper ocean is usually released to the atmosphere during the freezing season, when the mixed layer expands downwards towards the halocline. Mixing is primarily driven by strengthened winds and convection due to brine rejection: as sea ice forms it only accommodates a limited amount of salt into its crystalline lattice, the rest is rejected. The depth of the ocean that is cooled in this manner is limited by the halocline, which also suppresses the delivery of heat from the Atlantic Waters to the ice; in this way the abundance of Arctic freshwater stabilises sea ice (Bulgakov, 1962). Once the upper ocean is cooled to the freezing temperature of seawater (about -1.8 °C in the Arctic Ocean), sea ice growth can proceed apace, and freezing acts as a distillation process that salinifies the mixed layer (e.g. Aagaard & Carmack, 1989). With the return of sunlight in the summertime, sea ice thaws, releasing freshwater into the upper ocean. This seasonal melt and thaw of sea ice drives an exchange of freshwater of roughly 13,000 km^3 between the liquid and solid phases, and through its distillation effect helps to keep the uppermost ocean fresh (Haine et al., 2015). The motion of sea ice between sites of growth and thaw furthermore acts to redistribute freshwater around the Arctic Ocean (Aagaard & Carmack, 1989; Steele & Flato, 2000).

Wind-driven ocean currents also shape the distribution of freshwater in the Arctic Ocean. As shown in Figure 0.3c, the time-mean surface circulation can be simplified into three main components: cyclonic circulation in the Eurasian shelf seas and parts of the Makarov and Eurasian basins; anticyclonic circulation in the Beaufort Gyre, centred in the Canada Basin; with these two circulation centres separated by the Transpolar drift (e.g. Armitage et al., 2018; Morison et al., 2021). This pattern of ocean circulation is related to the time-mean sea-level pressure patterns over the Arctic region (Figure 0.3a), which features an anticyclone over the Beaufort Gyre (known as the Beaufort Sea High; Serreze & Barrett, 2011) and a trough of low pressure extending from the Icelandic Low northeastwards into the Kara Sea, associated with the northerly node of the North Atlantic Oscillation, which shows mobility along an axis towards the north east (Hilmer & Jung, 2000; Moore et al., 2013). This time-mean trough of low pressure is also characterised by the passage of synoptic-scale cyclones into the Barents and Kara seas from the North Atlantic (e.g. Simmonds et al., 2008). Changes in the atmospheric circulation modulate the position and size of these three features of the surface ocean circulation (e.g. Armitage et al., 2018; Morison et al., 2021; Proshutinsky et al., 2009). The depth of the halocline (Figure 0.3b)—influenced by Ekman convergence in anticyclonic regions and Ekman divergence in cyclonic regions—largely mirrors these circulation features (Carmack et al., 2016; Ma et al., 2017). Indeed, the slope of the halocline itself is associated with the surface circulation (Figure 0.3c) via thermal wind.

It is the combination of these patterns of surface circulation—in concert with the pathways of river plumes and the Bering Strait inflow, the patterns of ice growth, drift and melt, and the intensity of freshwater outflows—that help to establish the distribution of freshwater within the Arctic. The quantity of freshwater is established by the balance (or lack thereof) between inflows and outflows (e.g. Dickson et al., 2007; Haine et al., 2015). The dominant freshwater outflows from the Arctic run either side of Greenland: freshwater flow through Fram Strait joins the East Greenland Coastal Current, which wraps around the southern tip of Greenland before joining with fresh currents from Nares Strait and the Canadian Arctic Archipelago in the Labrador Sea and Baffin Bay. The flows define a cold boundary current directed south-

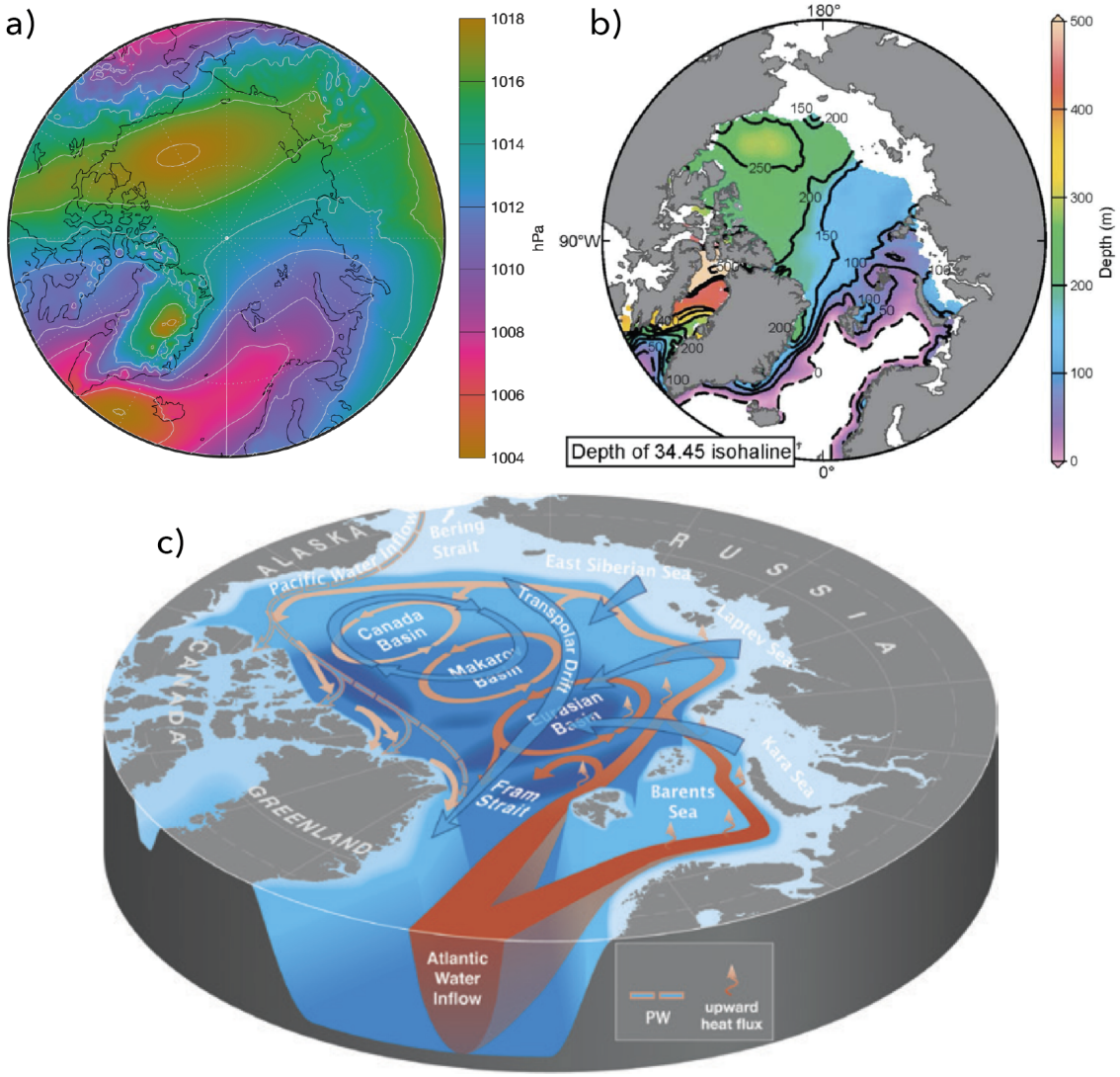


Figure 0.3: a) Annual mean sea-level pressure from ERA5 reanalysis data (Hersbach et al., 2020). Mean taken over the years 1979–2018. b) Depth of the 34.45 isohaline, which lies near the base of the halocline. Figure taken from Carmack et al. (2016). c) Schematic showing the dominant circulation of the upper ocean (blue arrows) and underlying Atlantic Water (red-pink arrows). Figure taken from Carmack et al. (2015).

wards along the North American continental margin towards the subpolar/subtropical gyre boundary. In addition to these fresh oceanic currents, roughly 2,000 km^3 of freshwater locked up in sea ice is exported into the N. Atlantic each year through Fram Strait (Spreen et al., 2020).

The circulation in the relatively fresh upper ocean (sometimes referred to as the Polar Water)

is relatively decoupled from the circulation of Atlantic Water below (Figure 0.3c), which enters the Arctic through two gateways: the Barents Sea Opening and Fram Strait (Aagaard & Carmack, 1989; Rudels et al., 1994). The Atlantic Water loses heat on its path into the Arctic Ocean, particularly in the Barents Sea (Smedsrud et al., 2010), before descending beneath the fresh Polar Water along the Polar Front, the position of which is topographically controlled (Gawarkiewicz & Plueddemann, 1995). The Atlantic Water, relatively warm at 0–4 °C (Carmack et al., 2016), proceeds to circulate beneath the Polar Water cyclonically in boundary currents around the Arctic basins, and spread into basin interiors via eddies and intrusions (Pnyushkov et al., 2015; Rudels et al., 1999; Woodgate et al., 2001). There is relatively little interaction between the Atlantic Water the Polar Water above, except for over steep topography and in the vicinity of the inflow regions (e.g. Padman & Dillon, 1991; Shaw et al., 2009; Sirevaag & Fer, 2009). The Atlantic Water is modified to some degree on its transit: in the inflow corridor of the St Anna Trough (Rudels, 2015) where winter mixing penetrates into the Atlantic layer, Atlantic Waters become more saline due to brine rejection; in the basin interior there is evidence for the entrainment of dense saline overflows from freezing on the shelves (Aagaard et al., 1985; Rudels, 1986). After exiting the Arctic through Fram Strait, these modified Atlantic Waters provide c. 40% of the North Atlantic Deep Water (Rudels et al., 1999).

0.2.2 Significance of Arctic Ocean freshwater

The abundance of freshwater maintains the strong stratification that reduces upwards heat fluxes from the Atlantic Water below to the ice and atmosphere (e.g. Aagaard & Carmack, 1989; Carmack, 2007), making the Arctic ocean a uniquely low upwards heat flux environment in the high latitude oceans. Where freshwater supply to a region becomes limited, this stratification is prone to weaken or collapse, permitting increased heat fluxes and limiting winter sea ice growth (Lind et al., 2018; Polyakov et al., 2017; Polyakov et al., 2020; Steele & Boyd, 1998). By stabilising sea ice, freshwater plays a key indirect role in the local and global radiative budget. The strong stratification freshwater enforces also limits the depth of wind-driven and convective mixing, limiting the re-supply of nutrients from the deep ocean, decreasing primary

production (McLaughlin & Carmack, 2010). In addition, different riverine freshwater sources play different biogeochemical roles in the Arctic Ocean, carrying nutrients and dissolved and particulate matter (Carmack et al., 2016). Increasing freshwater decreases alkalinity, which increases vulnerability to ocean acidification (caused by increasing anthropogenic CO_2 uptake), with potential harmful consequences for calcifying organisms (Yamamoto-Kawai et al., 2013).

Arctic freshwater places constraints on the limits of winter sea ice extent (Barton et al., 2018) and deep convection in the ocean (Lique et al., 2018). Indeed, high salinity in the subpolar North Atlantic is a prerequisite for the overturning circulation. Large fluxes of freshwater from the Arctic Ocean are of key scientific interest for their potential to disrupt deepwater formation in the subpolar North Atlantic, thereby potentially slowing the Atlantic Meridional Overturning Circulation (AMOC; e.g. Holliday et al., 2020; Jahn & Holland, 2013; Stouffer et al., 2006; M. Wang et al., 2018; Q. Yang et al., 2016). The AMOC plays a major role in global ocean circulation and climate, and may exhibit multiple stable states (e.g. Broecker, 1997; Broecker et al., 1985). The potential slowing of the AMOC (e.g. Rahmstorf et al., 2015) is therefore of key concern and interest. Large fluxes of freshwater in the past (Belkin et al., 1998; R. Curry & Mauritzen, 2005) are thought to have affected the overturning (Ionita et al., 2016). In tandem with the predicted freshening of the Arctic Ocean in a warming world, fluxes of freshwater to the subpolar North Atlantic are expected to increase (Haine et al., 2015; Jahn & Laiho, 2020). Coupled climate models indicate that Arctic freshwater content, and freshwater fluxes to the North Atlantic, also exhibit strong internal variability in addition to forced changes (e.g. Cornish et al., 2020). Understanding the dynamics of this internal variability, and its interplay with expected forced changes, is crucial for making links to potential downstream effects on the AMOC.

The local and far-field functions and effects of Arctic Ocean freshwater described above are, naturally, prone to change as the distribution and abundance of that freshwater changes. It is therefore a key scientific challenge to improve observational and model-based representations of Arctic freshwater variability (Haine, 2020; Ilicak et al., 2016; Lique et al., 2016), understand

the mechanisms underlying changes (e.g. Giles et al., 2012; Morison et al., 2012; Stewart & Haine, 2013; Timmermans et al., 2011; Q. Wang et al., 2019), anticipate future changes (Haine, 2020; Holland et al., 2006; Jahn & Laiho, 2020; Shu et al., 2018) and interpret their role in the interconnected climate system on local, regional and global scales (Carmack et al., 2015; Polyakov et al., 2018; Timmermans & Marshall, 2020).

Some of the key research questions that we are concerned with in this thesis are as follows. What has driven observed changes in Arctic FWC? In what manner are atmospheric circulation and FWC related? What is the role of sea ice export in Arctic FWC changes? We understand that sea ice production is important for liquid freshwater distribution: what are the processes underpinning it? How, and why, can we expect patterns of sea ice production to shift? Are the dynamics of the Arctic's largest freshwater reservoir, the Beaufort Gyre, sensitive to exchanges of freshwater with ice?

Our questions—and findings—have important implications for a number of other research areas, namely: the stability of the cold halocline, and 'Atlantification'; the nature, and effect, of Arctic freshwater fluxes to the subpolar N. Atlantic; the bioegeochemical effects of freshwater variability; the prediction of the sea ice state on seasonal timescales; the prediction of long-term sea ice stability; and the role of ocean heat in winter sea ice decline.

0.3 Guide to the thesis

Compelling evidence has emerged from forced model experiments tying various aspects of freshwater storage and distribution to wind-driven changes (e.g. Stewart & Haine, 2013; Timmermans et al., 2011). However, theory and idealised models also suggest that freshwater storage responds to changes in wind forcing over a multi-year timescale (Davis et al., 2014; Manucharyan & Spall, 2016), making attribution of freshwater changes to atmospheric forcing more challenging in the contexts of both coupled climate models and observations. In the first two chapters, we aim to bridge this gap by using linear response theory (e.g. Hassel-

mann et al., 1993) to isolate the relationship between Arctic freshwater content and sea-level pressure (SLP) patterns in coupled climate models. Our method captures the time-evolving response of freshwater content to an abrupt change in sea-level pressure forcing, enabling us to find the sign, magnitude and timescale of the freshwater response to a change in a given SLP pattern. (Because these are coupled models, this abrupt change is purely hypothetical: it is derived from statistical analysis.) We use these derived responses, together with SLP from atmospheric reanalysis to reconstruct historical variability in Arctic Ocean FWC. In Chapter 1, we undertake a detailed study using one model, before assessing 12 models from the CMIP5 ensemble and developing the method further in Chapter 2. The first two chapters are based on H. L. Johnson et al. (2018) and Cornish et al. (2020), with additions and modifications.

Chapter 3 begins the shift in focus to the mechanisms by which sea-level pressure patterns can excite a response in the liquid freshwater content and distribution of the Arctic Ocean. In Chapter 3, based on statistical results from the coupled model HiGEM, we develop a hypothesis that states that wind-driven sea ice export variability can drive changes in the total Arctic Ocean liquid FWC. We test the assumptions underpinning this hypothesis, with reference to a range of observational-based data, and through the design and application of forced model experiments.

In Chapter 4 we delve into a key process in the redistribution of freshwater content in the Arctic Ocean: sea ice production in the Kara and Laptev seas. Previous work has shown that ice production in these regions has been increasing due to negative feedbacks, but that this trend might change as atmospheric and oceanic warming begin to dominate (Petty et al., 2018; Stroeve et al., 2018). However, consistent physical mechanisms that could explain the identified forced changes have not been identified. The fate of ice production in the region has important implications for halocline stability in the Eurasian Basin and northern Barents Sea (e.g. Lind et al., 2018; Polyakov et al., 2018). In Chapter 4 we analyse ice production and its changing seasonal characteristics in the Kara and Laptev seas in the Large Ensemble of the Community Earth System Model. We develop an idealised linear model with insight from the

physics of sea ice growth. The model relies on climate variables that are readily accessible from observation-based estimates over the satellite era. We then use these estimates to reconstruct changes over the last few decades based on the linear model.

In Chapter 5 we turn to the Arctic Ocean's largest freshwater reservoir: the Beaufort Gyre. This region has been the focus of in-situ observational efforts (e.g. Proshutinsky et al., 2009; Proshutinsky et al., 2019) and coordinated modelling experiments (e.g. J. Marshall et al., 2017). Furthermore, significant advancements of our understanding of its basic dynamics have been made through the application of theory (e.g. Doddridge et al., 2019; Manucharyan et al., 2016), idealised models (e.g. Davis et al., 2014; Manucharyan & Spall, 2016) and high-resolution regional models (e.g. Regan, Lique, Talandier, et al., 2019). Satellite observations have provided another view into its behaviour and interactions with topography, sea ice cover and ocean dynamics (e.g. Petty et al., 2016; Regan, Lique, & Armitage, 2019). Unexplored so far, however, is the role that thermodynamic exchanges of freshwater between ice and ocean might play in the wind-driven adjustment of the gyre. We capitalise on a set of existing coordinated model experiments to investigate whether differences in wind-driven sea ice import/export in the region can explain differences in modelled freshwater changes, via interplay between the dynamic thickness of ice and net thermodynamic growth rate.

Chapter 6 provides a concluding discussion that synthesises the findings of the thesis. We discuss the implications of the work, with a particular focus on future changes in the Arctic climate system. Finally, we offer thoughts on research priorities to tackle further pressing questions regarding the Arctic climate system.

Chapter 1

Arctic Ocean Freshwater Content and its Decadal Memory of Sea Level Pressure

Abstract

Arctic freshwater content (FWC) has increased significantly since the mid-1990s, with potential future implications for the Atlantic meridional overturning circulation downstream. The origin of these changes is contested, however. Here, we investigate the potential role for winds in driving this accumulation, by extracting via linear response theory the response of Arctic FWC to step changes in the principal components of sea-level pressure in a coupled climate model. The results demonstrate that Arctic FWC adjusts on a decadal timescale, consistent with the idea that wind-driven ocean dynamics and eddies determine the response of Arctic Ocean circulation and properties to a change in surface forcing, as suggested by idealised models and theory. This decadal memory affords some degree of predictability to FWC evolution. Convolving the response of FWC to a change in sea-level pressure with historical sea-level pressure variations from reanalysis produces a reconstruction of freshwater changes that matches closely the recently observed accumulation of Arctic FWC. This suggests that the recent Arctic freshening has been driven in large part by variations in atmospheric circulation.

Based on work published in *Geophysical Research Letters* (https://doi.org/10.1029/2017GL076870)

1.1 Introduction

Between 1992–2012, the Arctic Ocean accumulated an additional c. 10,000 km^3 of liquid freshwater (Polyakov et al., 2013; Rabe et al., 2014), largely in the Beaufort Gyre (Haine et al., 2015; McPhee et al., 2009; Proshutinsky et al., 2009; Proshutinsky et al., 2019).

The current relatively elevated state of freshwater content (FWC) in the Arctic Ocean raises questions about the possibility of large fluxes of freshwater to the North Atlantic in the future. Large freshwater export events are thought to have happened at least once before: a freshwater pulse of Arctic origin is proposed to explain the observed low-salinity anomaly that circulated the subpolar North Atlantic in the 1970s (known as the Great Salinity Anomaly of the 1970s; Belkin et al., 1998; R. Curry & Mauritzen, 2005; Dickson et al., 1988). The prospect of similar, or larger, such events in the future is of wide interest due to the potential for freshwater anomalies in the subpolar North Atlantic to affect deepwater formation and consequently the strength of the Atlantic Meridional Overturning Circulation (AMOC; e.g. Jahn & Holland, 2013; Stouffer et al., 2006; H. Wang et al., 2018). This is one of several reasons we seek to understand the causes behind Arctic FWC variability, which is intimately related to freshwater fluxes to the North Atlantic (Haine et al., 2015; Jahn et al., 2010; Lique et al., 2009). We offer further introduction to the importance of Arctic FWC variability in Section 0.2.2.

Several mechanisms may have contributed to the recent increase in Arctic FWC: increased hydrological cycle and enhanced river runoff; increased glacial discharge from Greenland; a net flux of freshwater to the ocean from net melting of sea ice; changes in ocean circulation and river routing due to both changes in atmospheric circulation and also changing sea ice cover, which modulates the surface stresses (Giles et al., 2012; Jahn & Laiho, 2020; Q. Wang et al., 2018; Q. Wang et al., 2019). In this chapter, we investigate the role of atmospheric circulation in driving FWC changes. Note that a separate, but connected, question is how much of the influence of any of these mechanisms can be attributed to climate change. Recent work with the Large Ensemble of the Community Earth System Model by Jahn et al. (2010) shows that—in this model—forced changes in Arctic FWC should already be discernible from the range of

internal variability in a pre-industrial control run of the model.

We isolate the time-dependent response of Arctic FWC to abrupt changes in atmospheric circulation in a fully coupled climate model simulation, which includes complex bathymetry, sea-ice and coupled air-sea processes. We expect the amplitude and timescale of this response to be in large part governed by changes in the Beaufort Gyre, as the Arctic's largest freshwater reservoir. However, variability in total Arctic FWC also depends on processes of storage and redistribution over the rest of the Arctic basin and surrounding shelves; processes that are not yet well understood (e.g. Carmack et al., 2016).

Because we utilise a coupled climate model, we must extract the response of Arctic FWC to atmospheric circulation using multiple lagged regression between the variables in question in the model's control run. A distinct, but complementary approach, is to actively perturb the atmospheric forcing in a step-change manner, using an ice-ocean only model (J. Marshall et al., 2017; Muilwijk et al., 2019, see also Chapter 5,). We can then use this response to reconstruct historical changes in Arctic FWC through convolution with SLP data from atmospheric reanalysis.

In this chapter we make the case that changes in atmospheric circulation are the dominant drivers of Arctic-wide freshwater changes. Chapter 2 extends on this work by developing the linear response methodology and applying it to 12 different coupled climate models. The remaining chapters in this thesis consider the mechanisms by which atmospheric circulation can drive FWC changes, with a focus on the redistribution of freshwater via sea ice.

This chapter is structured as follows. Following the introduction to Arctic Ocean circulation and freshwater content given in Section 0.2, we offer here a brief overview of freshwater adjustment processes in the Beaufort Gyre (Section 1.1.1). This is the Arctic's largest freshwater reservoir and its dynamics offer valuable clues to the behaviour of Arctic-wide freshwater changes. We then outline our methodology in Section 1.2. We explore the nature of FWC variability exhibited by the model on different timescales in Section 1.3, before determining the

relationships between FWC and the leading modes of atmospheric circulation in Section 1.4. In Section 1.5.1, we reconstruct FWC changes in the model using sea-level pressure (SLP) variability and the derived relationships. We then exploit these relationship to reconstruct historical changes and attribute them to different modes of SLP variability (Section 1.5.2). We ask how much predictability is afforded by the memory in the system in Section 1.5.3, before discussing the implications of our results in Section 1.6 and offering a concluding summary in Section 1.7.

1.1.1 Freshwater adjustment in the Arctic's largest freshwater reservoir: the Beaufort Gyre

It is now well established from observations and numerical models that the liquid freshwater content of the Arctic Ocean's largest freshwater reservoir, the Beaufort Gyre, varies on seasonal to decadal timescales (e.g. Proshutinsky & Johnson, 1997; Regan, Lique, Talandier, et al., 2019). On interannual timescales, this variability is thought to be primarily related to changes in the surface stress acting on the ocean, which depends on atmospheric circulation but can be significantly modified by sea ice conditions (e.g. Giles et al., 2012; Proshutinsky et al., 2009) and secondarily, on the availability of freshwater sources in the region (Proshutinsky et al., 2009; Proshutinsky et al., 2019).

The relatively fresh state of the Beaufort Gyre is sustained by predominant anticyclonic surface stress, which drives Ekman convergence. Because the Arctic is stratified by salinity, this convergence affects the freshest part of the water column, concentrating freshwater in the Beaufort Gyre and deepening the halocline beneath (Proshutinsky et al., 2009). Intensification of the anticyclonic forcing leads to further freshening (J. Marshall et al., 2017; Proshutinsky et al., 2009). Recent observational studies suggest that for at least some of the year, despite an anticyclonic atmospheric circulation, surface ocean velocities match or exceed those of the sea-ice, which hence acts as a drag on the circulation (S. Dewey et al., 2018; Meneghello, Marshall, Timmermans, et al., 2018); a phenomenon referred to as the *ice-ocean governor* (Meneghello,

Marshall, Campin, et al., 2018). Nonetheless, the gyre is in a long-term state of annual-mean Ekman convergence; there must be one or more processes opposing freshwater accumulation in order that a quasi-steady state is reached (Manucharyan et al., 2016).

In idealized models and theory, this freshwater accumulation is arrested by baroclinic eddies; isopycnal slopes increase until eddies (resolved or parameterized) are able to bring the system into equilibrium, such that the FWC of the Beaufort Gyre is sustained by a balance between Ekman convergence and an eddy-induced volume transport towards the boundary (Davis et al., 2014; Lique et al., 2015; Manucharyan et al., 2016; Manucharyan & Spall, 2016). After a change in surface stress, the FWC in these models comes into equilibrium on decadal timescales, determined by the eddy diffusivity. Visible from satellite imagery, eddies are ubiquitous in the ice-free surface ocean during summer (Kozlov et al., 2019). In the winter, frictional dissipation leads to a quiescent eddy field immediately below the ice, however eddies can persist all-year round in the halocline and below, enabled by baroclinic instability in the Arctic interior (Meneghello et al., 2021).

1.2 Model details and methodology

We analyze monthly mean output from a 150-year control integration performed with the High-Resolution Global Environmental Model (HiGEM). HiGEM is a fully coupled climate model based on the Hadley Centre Global Environmental Model version 1 (HadGEM1; Johns et al., 2006) with a relatively high resolution ocean and a reasonable representation of the Arctic (Lique & Johnson, 2015; Lique et al., 2018). The model is described and evaluated in Shaffrey et al. (2009). It uses a spherical latitude-longitude grid with an atmospheric horizontal resolution of 0.83° latitude by 1.25° longitude (N144) and 38 vertical levels, and an oceanic resolution of 1/3° by 1/3° with 40 unevenly spaced vertical levels. In the ocean, the lateral mixing of tracers is parameterized using the isopycnal formulation of Griffies et al. (1998) with constant isopycnal diffusivity; there is also a scale-selective biharmonic scheme for momentum dissipation, and a biharmonic scheme to represent enhanced mixing of temperature and salinity in the upper

20 m. Eddies are permitted at mid- to low latitudes but parameterized at high latitudes by a biharmonic version (Roberts & Marshall, 1998) of the Gent and McWilliams (1990) adiabatic mixing scheme with a latitudinally varying thickness diffusion coefficient. The sea-ice model is based on the Community Ice Code (CICE; Hunke & Dukowicz, 1997) and uses an elastic-viscous-plastic rheology with a five-category ice thickness distribution.

The atmosphere and ocean are initialized from rest using data from the European Centre for Medium-Range Weather Forecasting analysis and the World Ocean Atlas 2001 (Boyer et al., 2005), respectively. In this control integration greenhouse gases are held constant at late 20th-century concentrations (345 ppm CO_2) and there is no source of external forcing, such that all climate anomalies can be attributed to internal variability. We disregard the first 20 years, during which there is a significant spin-up in FWC.

We utilise linear response theory (Hasselmann et al., 1993) following Kostov et al. (2017) and Kostov et al. (2018) to determine the response of Arctic FWC in the HiGEM control run to a step change in atmospheric forcing. We first define our timeseries of interest. In general terms, the method hinges on relating three variables: a *forcing* timeseries, in our case SLP variability; a *target* timeseries, FWC; and an impulse response function. With knowledge of the *forcing* and the *target*, one can estimate the impulse response function using multiple lagged regression. With knowledge of the impulse response and the *forcing*, one can reconstruct/predict the *target* using convolution. This is illustrated schematically in Figure 1.1

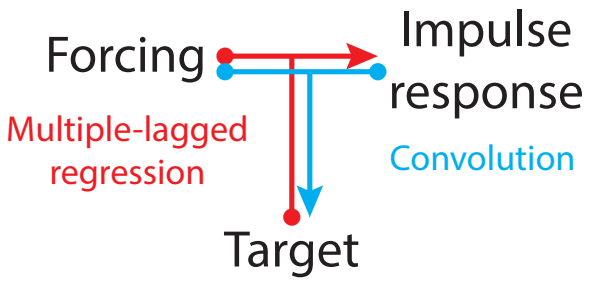


Figure 1.1: Conceptual summary of linear response methodology. Terms explained in the text.

Our *target* timeseries is Arctic FWC, relative to a reference salinity of S_{ref} = 34.8 (Aagaard &

Carmack, 1989) and integrated down to the 34.8 isohaline over the entire Arctic domain shown in Figure 1.2. FWC is calculated as

$$\mathrm{FWC}(t) = \iiint_{z(S=S_{ref})}^{0} \frac{S_{ref} - S(t)}{S_{ref}} dV \tag{1.1}$$

We characterize the variability in atmospheric circulation over the Arctic using the first three empirical orthogonal functions (EOFs) of the SLP field (with mean seasonal cycle removed) north of 70 °N and their principal component time series. These are then our *forcing* terms. By writing the FWC timeseries (*target*) as the convolution of an impulse response function G (a Green's function) with the history of the *forcing*, we can see how G can be estimated through multiple linear lagged regression.

$$\mathrm{FWC}(t) = \int_{0}^{\tau_{max}} G(\tau)\mathrm{PC}(t-\tau)d\tau \; + \epsilon(t) \tag{1.2}$$

Here $\mathrm{PC}(t)$ is one of the principal components of SLP, normalised by its standard deviation; τ is the time lag, τ_{max} is an imposed maximum cutoff lag beyond which we assume the ocean has no memory of SLP, $\epsilon(t)$ is residual noise, and $G(\tau)$ represents the time-dependent response to an impulse perturbation of magnitude one standard deviation in PC.

We discretise in steps of 1 month (the data is archived as monthly means) and express Equation 1.2 as the system of equations

$$\mathbf{M}G = \mathrm{FWC} \tag{1.3}$$

Here, $\mathbf{M}$ is a matrix containing the PC forcing, while G and FWC are column vectors. In $\mathbf{M}$, each row contains a timeseries of PC forcing, from τ_{max} months prior to the time t at which FWC is being predicted, up to the zero-lag time. We can then solve for $G(\tau)$ using multiple linear least-squares regression.

We obtain an ensemble of estimates for G by varying the cutoff lag, τ_{max}, incrementally be-

tween 30 and 35 years, and by considering subsets of the full FWC and PC timeseries. We then limit all estimates of G to a maximum lag of 30 years for consistency. At each lag, we calculate the standard deviation across the spread of estimates. For each estimate of G we can also calculate the residual term $\epsilon(t)$, from the difference of the *target* FWC timeseries and the reconstruction based on G. This residual gives us another error estimate for each fit. We combine this residual error estimate with the standard deviation of the spread of estimates for G in quadrature in order to gain an estimate of the true uncertainty.

The step response function is then simply the integral of $G(\tau)$ through the 30 years. The step response function is equivalent to a 'climate response function' (CRF; J. Marshall et al., 2017).

To reconstruct historical FWC variability, we convolve the impulse response function G with SLP variability from an atmospheric reanalysis; we utilise ERA-Interim (Berrisford et al., 2001) and ERA-20C (Poli et al., 2016). We use the ERA-20C up to 1979 and the ERA-interim record thereafter. ERA-20C has been used in several Arctic studies (e.g. Belleflamme et al., 2015; Close et al., 2017) and is thought to successfully reproduce the North Atlantic Oscillation, for example (Poli et al., 2016; Weisheimer et al., 2017). ERA-Interim has been assessed in the Arctic by Simmons and Poli (2015) and Lindsay et al. (2014). It is one of the leading atmospheric reanalyses in terms of correspondence to independent Arctic observations (Lindsay et al., 2014). We compare our historical FWC reconstruction with estimates of Arctic FWC from Rabe et al. (2014) and Polyakov et al. (2013).

1.3 FWC variability in HiGEM

Patterns of seasonal and interannual FWC variability

The model's time-mean integrated Arctic FWC is 109,000 km^3 (Figure 1.2a), which is close to that estimated from recent observations (101,000 km^3; Haine et al., 2015). The amplitude of the seasonal cycle (Figure 1.2b) is about 10% of this total, in accordance with observations (Serreze et al., 2006) and Coupled Model Intercomparison Project Phase 5 (CMIP5) models (Ding et al.,

2016). There is a FWC minimum in March and a maximum in September, in antiphase with the freshwater stored as sea ice, reflecting the exchange between the two phases over the seasonal cycle. Precipitation minus evaporation, together with river run-off, also contribute to the seasonal cycle. Both peak during the summer (Figure 1.2b), and principally affect regions on the shelves (Figure 1.2d). The same factors are found to determine the seasonal cycle in Arctic FWC in CMIP5 models (Ding et al., 2016).

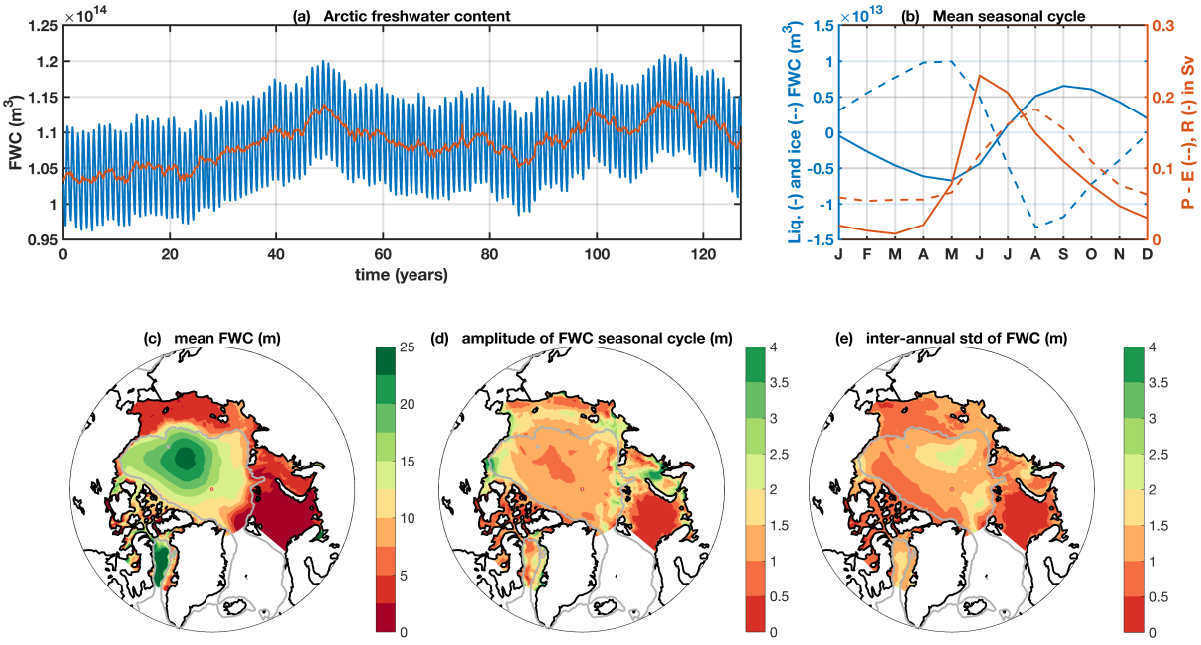


Figure 1.2: (a) Time series of Arctic FWC. Monthly mean values are plotted in blue, and the time series with mean seasonal cycle removed is shown in red. (b) Mean seasonal cycle in Arctic liquid FWC (solid blue line) and sea-ice (dashed blue line); freshwater fluxes from snowfall plus precipitation minus evaporation (red dashed line) and river runoff (solid red line). Spatial distribution of the (c) mean FWC, (d) amplitude of the mean seasonal cycle, and (e) standard deviation after mean seasonal cycle removed.

Although the Beaufort Gyre is the largest freshwater reservoir (Figure 1.2c), it exhibits a modest seasonal cycle (Figure 1.2d). The shelves and perimeter of the basin show the most intense seasonality, in keeping with the large seasonal cycles of sea ice growth/melt, river runoff and Bering Strait inflow. The spatial pattern likely also reflects some redistribution between the interior and shelves, which dominates the variability in steric height on seasonal timescales (Armitage et al., 2016).

Interannual variability in FWC, however, is largest in the basin interior (Figure 1.2e), suggesting that on these timescales, the dynamics of the Beaufort Gyre and the strength of the Transpolar Drift play a key role (Niederdrenk et al., 2016). Although the Canada and Makarov Basins, which contain the Beaufort Gyre, represent only 23% of the area considered, the magnitude of the interannual standard deviation of FWC in these basins is 68% of the magnitude of the equivalent for the entire Arctic. On these timescales FWC variability in the Beaufort Gyre region is also well-correlated with that for the whole Arctic. Interannual FWC variability is also large north of Svalbard, possibly reflecting variability in the Atlantic inflow, and, consequently, the sea-ice edge.

Since we seek to understand interannual and longer-term variability, we remove seasonality by subtracting monthly means. This seasonal cycle is largely associated with freshwater exchange between sea ice and the ocean. On these longer timescales, Arctic FWC variability is dominated by interior regions of the Arctic where we expect wind-driven ocean dynamics to dominate.

Contributions of different fluxes to FWC variability

In Figure 1.3, we show the freshwater fluxes in the liquid and solid phases (upper and lower panel, respectively) through the straits that define the gateways to our Arctic domain. Heavy lines show the timeseries in question after removal of the mean seasonal cycle, whereas the seasonal cycle is retained in the respective transparent lines. Solid fluxes are dominated by the contribution through Fram Strait, with smaller outflow contributions from Davis Strait and a minor contribution from Bering Strait inflow. In the liquid fluxes, Bering Strait inflow is out-weighed by the sum of Fram Strait and Davis Strait outflows. These fluxes are similar to those estimated from observations (Haine et al., 2015; Serreze et al., 2006); however, in observations Davis Strait liquid outflow is the largest of all the freshwater fluxes through the straits, whereas in HiGEM its magnitude is smaller than Bering and Fram Strait fluxes.

The cumulative sum of freshwater fluxes that feed or drain the FWC reservoir should, in prin-

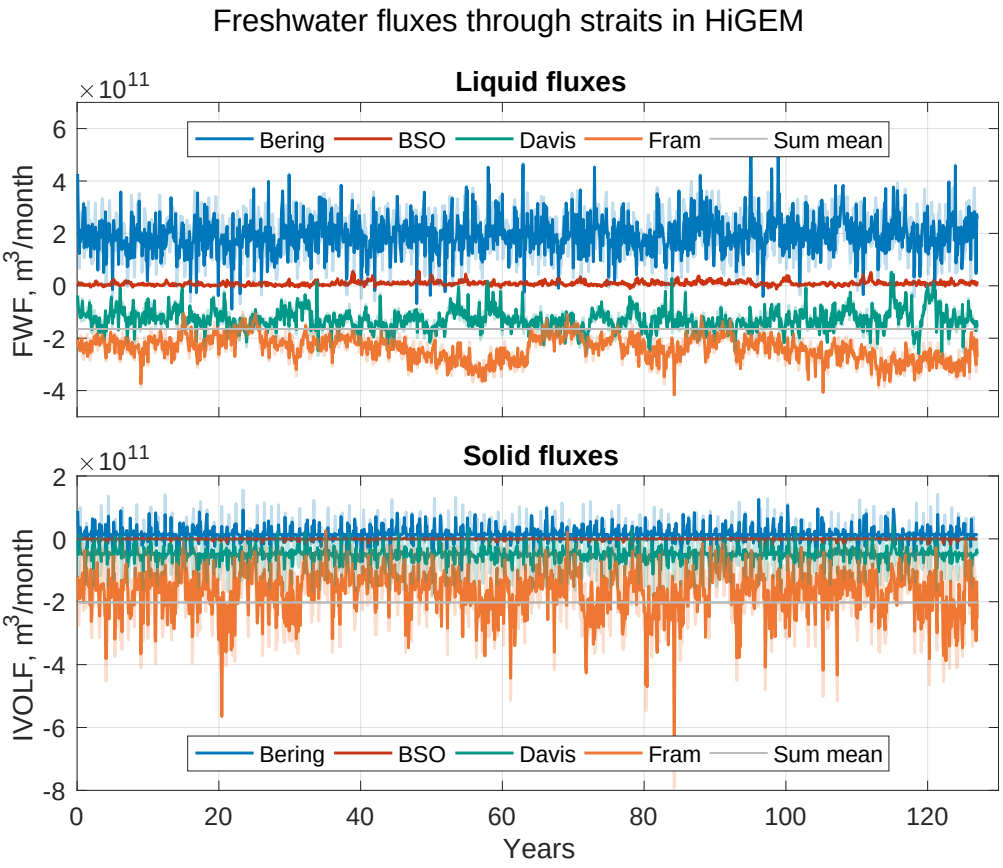


Figure 1.3: Freshwater fluxes through the straits that define the gateways to our Arctic domain. Upper panel shows liquid freshwater fluxes (FWF), lower panel shows freshwater fluxes as sea ice (IVOLF stands for ice volume fluxes). Straight grey line indicates the time mean of the sum of all straits in both cases. Transparent lines are the complete timeseries, heavier lines show the same data after removal of a seasonal cycle.

ciple, explain the variability of the reservoir. In Figure 1.4, we show the accumulated fluxes in comparison to the FWC variability. It is clear that, when accumulated, freshwater fluxes from sea ice export, liquid export and ice-to-ocean fluxes show similar characteristics of variability to the FWC timeseries, in terms of timescales and magnitudes. By contrast, precipitation plus runoff minus evaporation shows comparatively muted interannual variability, though it is important on an annual mean basis. Individually, cumulative liquid and ice-to-ocean fluxes explain 64% and 53% of the FWC variance, respectively. Sea ice volume fluxes can influence FWC via ice-to-ocean fluxes, an issue we will explore in more detail in chapters 3, 4 and 5. In-

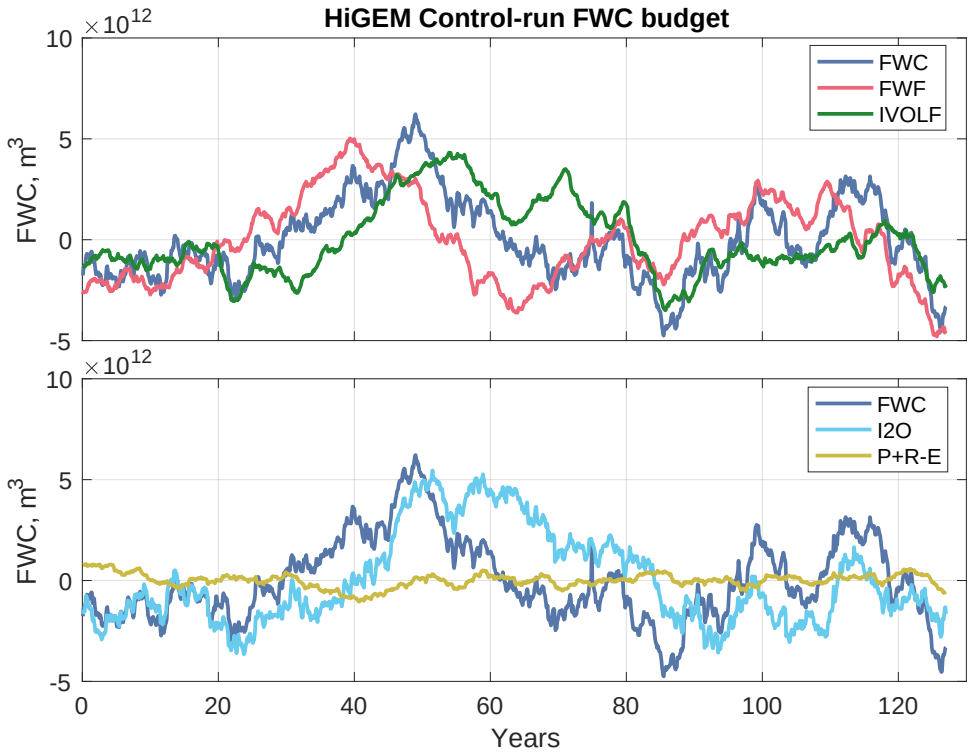


Figure 1.4: HiGEM pre-industrial control run FWC timeseries after removal of time-mean (109,000 km^3), compared with: upper panel—accumulated liquid freshwater fluxes (FWF) and sea ice volume fluxes (IVOLF); lower panel—accumulated ice-to-ocean freshwater fluxes due to freezing and melting (I2O) and accumulated precipitation plus runoff minus evaporation (P+R-E).

deed, the accumulated ice-to-ocean and sea ice volume fluxes are highly correlated (R = 0.91). Together, accumulated liquid and ice-to-ocean fluxes explain 87% of the variance in FWC. In this model then, liquid FWC changes are driven primarily by changes in the solid and liquid fluxes through the straits that connect the Arctic domain to the wider ocean.

1.4 Relationship between sea-level pressure and FWC

The ocean surface stress driving Ekman convergence in the Beaufort Gyre arises due to wind forcing, modulated by the sea-ice conditions (e.g. T. Martin et al., 2014), though the details of momentum transfer through sea ice are not fully accounted for in state-of-the-art climate

models (T. Martin et al., 2016; Tsamados et al., 2014). Here, we take the simplest approach, as in previous studies (e.g. Morison et al., 2012; Proshutinsky et al., 2009), and consider the relationship between Arctic FWC and SLP—a good proxy for surface winds.

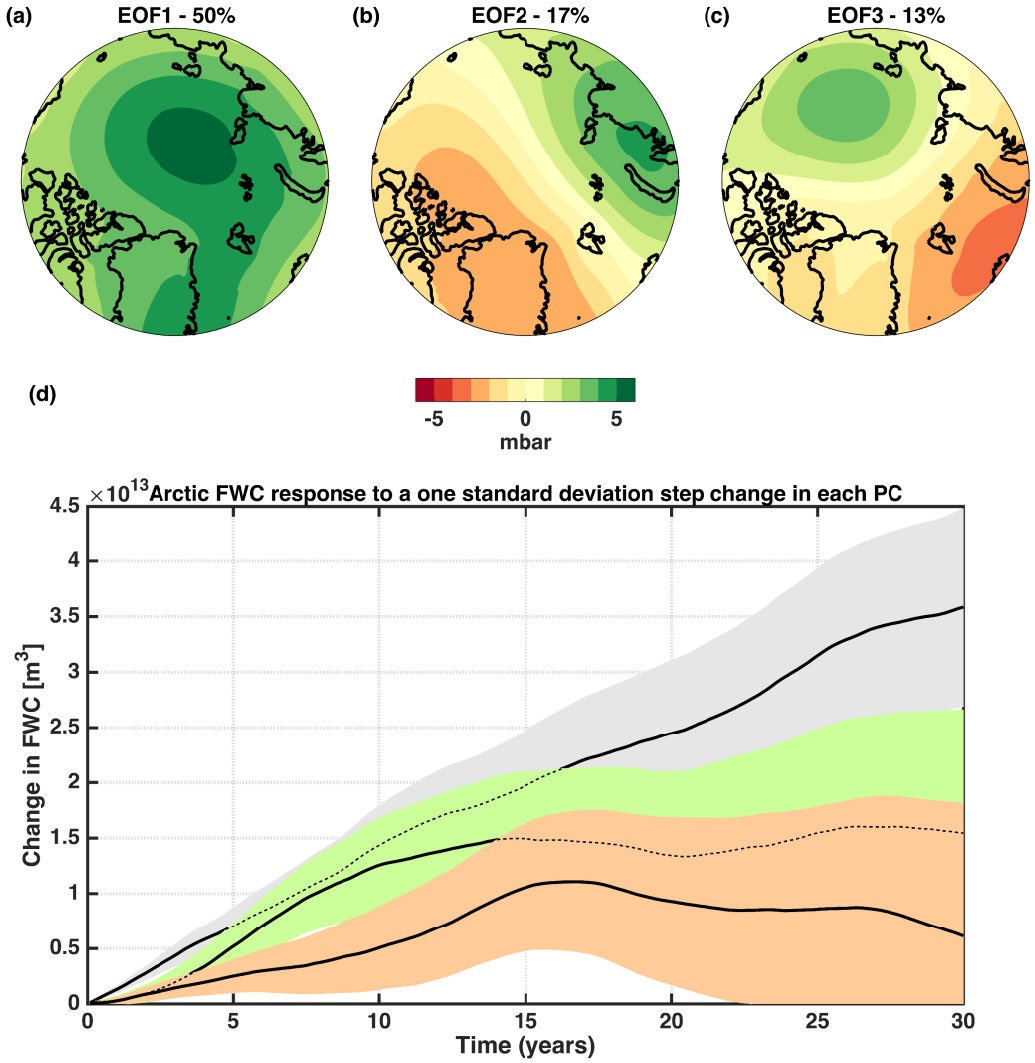


Figure 1.5: (a–c) First three empirical orthogonal functions (EOFs) of the sea-level pressure north of 70 °N. (d) Change in Arctic freshwater content (FWC) in response to a step change of one standard deviation in each of the three principal components of sea-level pressure: PC1 (orange), PC2 (green), and PC3 (grey). Black lines show the mean estimate and shaded envelopes the uncertainty. A step change in sea-level pressure of the magnitude and sign shown in (a)–(c) would result in the change in FWC shown in (d).

Figure 1.5 shows the first three EOFs of sea-level pressure north of 70 °N in the model control

run (after removal of seasonal cycle). These three modes explain the vast majority of SLP variance: 50%, 17%, and 13%, respectively. For comparison, EOF 4 explains $< 5\%$. These leading EOFs are very similar to those calculated from reanalysis data (e.g. Wu et al., 2006).

The first mode is the pattern associated with the Arctic Oscillation (AO; Thompson & Wallace, 1998), which is thought to play a variety of roles in relation to FWC variability. Armitage et al. (2018) show from sea-surface height satellite retrievals that AO-driven wind anomalies lead to shelf-basin freshwater redistribution via Ekman transport, as well as triggering opposing inflow anomalies through the Barents Sea opening and the Bering Strait. The cyclonic (positive) mode of the AO may increase freshwater availability in the Beaufort Sea via rerouting Eurasian river pathways into the Western Arctic (Morison et al., 2012; Morison et al., 2021), though it is the anticyclonic mode that is associated with a strengthened and broadened Beaufort Gyre circulation (Armitage et al., 2018; Kwok et al., 2013; Proshutinsky & Johnson, 1997; Rigor et al., 2002). Gradients in the second mode project onto the Transpolar Drift, and therefore might be expected to influence ice and freshwater export through Fram Strait. Indeed, this pattern closely resembles the Arctic Dipole (Wu et al., 2006), which plays a strong role in sea ice export (Tsukernik et al., 2010; E. Watanabe et al., 2006). The third EOF in this model shows a centre of action over the Canada and Makarov Basins; associated winds are therefore likely to influence the strength of the Beaufort Gyre.

In Figure 1.5d we show the response of Arctic FWC to a step change of one standard deviation in each of the three PCs of SLP. The magnitude of the forcing change in each case is given by the amplitude of the EOF patterns in Figure 1.5a-c. After a step change in PC1 or PC2, the FWC adjusts to a new equilibrium over 10–20 years. The response to a step change in PC3, on the other hand, does not appear to level off over 30 years. These responses are consistent with our expectation that the adjustment timescale of the Beaufort Gyre is decadal, and with the results of Beaufort Gyre-focused step change experiments in ocean-sea-ice models (Chapter 5; J. Marshall et al., 2017).

In terms of its adjustment processes, the interior Arctic Ocean is somewhat unique. Since

it is centred on the pole, gradients in the Coriolis parameter are small—it approximates an f-plane (J. Yang et al., 2016)—such that Rossby waves are slow and travel around the basin, rendering them ineffective at communicating change into the interior. Vertical diffusion is small (Guthrie et al., 2013; Lincoln et al., 2016; Shaw & Stanton, 2014) due to the strength of the stratification, sea ice cover and small tidal amplitude. Additionally, there can be no zonally integrated meridional geostrophic flow above the level of bathymetry (where zonal pressure gradients cannot be supported). In the absence of faster adjustment mechanisms, we might expect intensification of Ekman convergence to steepen isopycnals until eddy generation via baroclinic instability arrests this steepening and allows the system to reach a new equilibrium state. This is indeed what happens in a range of idealised models of the Beaufort Gyre (Davis et al., 2014; Lique & Johnson, 2015; Manucharyan & Spall, 2016). Simple scaling analysis applied to the volume budget of water above the halocline suggests that the adjustment timescale is decadal and that it is set by the properties of the eddy field (Davis et al., 2014). The step response functions shown in Figure 1.5 indicate that total Arctic FWC in the HiGEM control run adjusts to a change in forcing on a similar, decadal timescale.

Our focus is broader than just the Beaufort Gyre, however, and a range of mechanisms can be expected to be at play in the Arctic-wide adjustment. The large response to a step change in PC2 suggests that the advection of freshwater through Fram and/or Davis straits via the Transpolar Drift may be important (as shown on shorter timescales by Niederdrenk et al., 2016). A positive Arctic FWC anomaly results from strong southerly winds along the gradients in EOF2, while in the opposite polarity, northerly winds lead to freshwater flushing (the responses are linear, and therefore symmetrical). It is the anticyclonic mode of the AO (PC1) that leads to freshwater accumulation. This is consistent with modeling and observational results that show a weakened Fram Strait freshwater export, increased Bering Strait inflow (a key freshwater source) and an intensified Beaufort Gyre under the anticyclonic (negative) mode of the AO (Armitage et al., 2018; Lique et al., 2010). The largest FWC accumulation is in response to EOF3; likely due to a projection onto Beaufort Gyre variability.

The amplitude of the (linear) FWC response to a one standard deviation step increase in any of the first three PCs (Figure 1.5d) is large (10,000–40,000 km^3), one to four times the amplitude of the seasonal cycle in FWC and an order of magnitude larger than the deseasonalised standard deviation of FWC (2,050 km^3). The control FWC timeseries is in constant adjustment to the present, and—in accordance with the response functions—past, atmospheric forcing, which varies on subdecadal timescales (as well as longer timescales; it is approximately white noise). As such, it makes sense that the FWC response to a sustained one standard deviation step change in forcing exceeds the standard deviation of the FWC timeseries. We note that the linearity assumption underpinning these estimates is supported by the strong correlations exhibited between the FWC reconstructions and original FWC timeseries (Section 1.5.1).

Based on the understanding that the FWC variability in this model is primarily driven by fluxes of freshwater through the Arctic gateways (Figure 1.4), it seems most likely that sea-level pressure is able to exact the FWC responses shown in Figure 1.5 by modifying these gateway fluxes. In other words, this is the mechanism we suggest underlies the observed response functions.

1.5 Reconstructing freshwater variability

1.5.1 Model FWC variability

By convolving the model's time history of sea-level pressure with the impulse response function G (Equation 1.2) for each PC, then summing the contributions from the three PCs together, we are able to reconstruct a time series of interannual Arctic FWC variability in the control run (Figure 1.6). The resulting reconstructions are well correlated with the model FWC timeseries (the original *target*); the R values for the reconstructions using PC1, PC2 and PC3 are 0.77, 0.82 and 0.67, respectively. The combination of the PC1 and PC2 reconstructions correlates with the original timeseries at R = 0.90, while adding the third PC marginally improves the fit to R = 0.93.

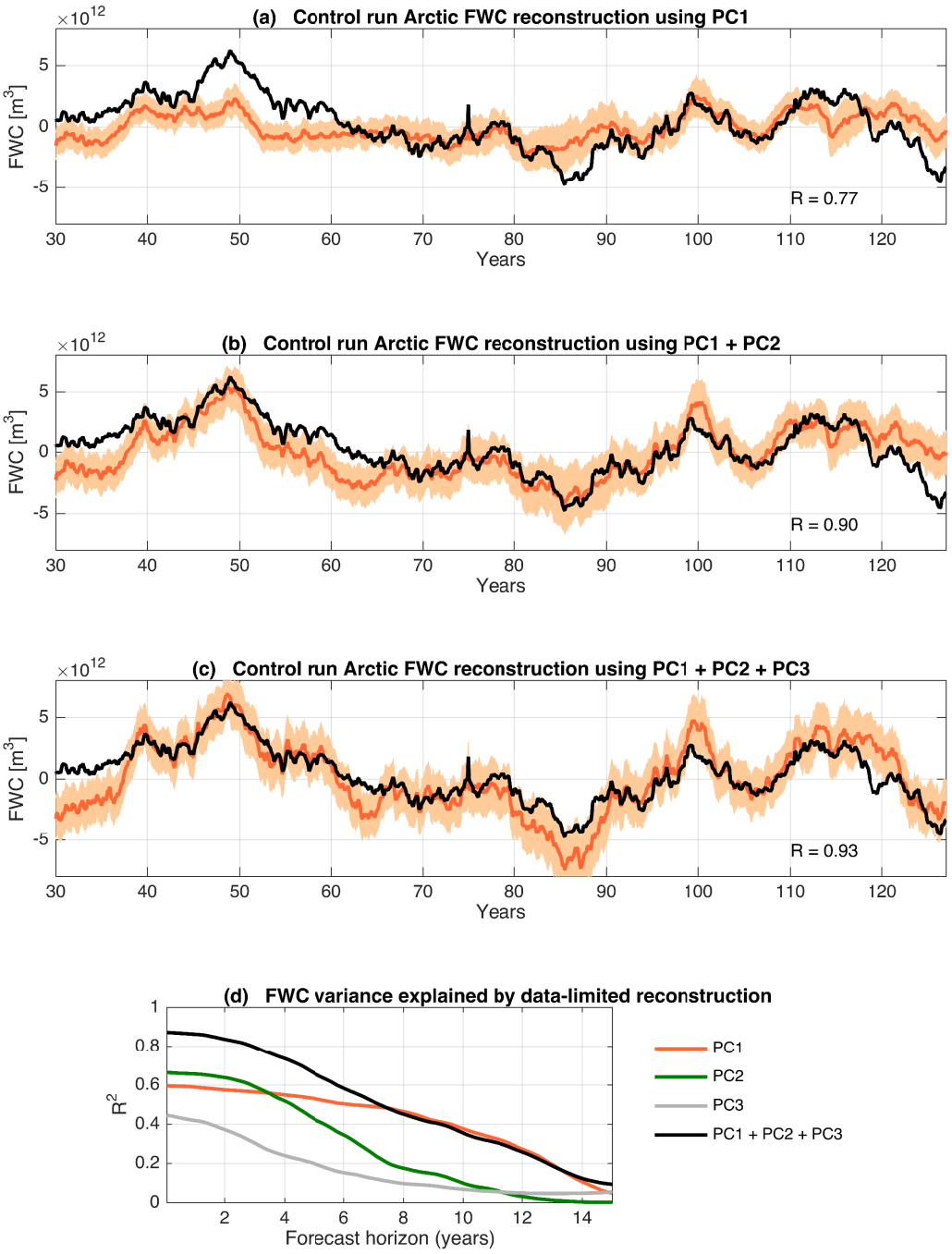


Figure 1.6: Reconstructed time series of Arctic freshwater content (orange line) in the control run, based on a convolution of the impulse response function with the model SLP field using (a) PC1 only; (b) PC1 and PC2; and (c) PC1, PC2, and PC3. The model's (detrended) Arctic FWC is shown in black. Plotted in (d) is the fraction of FWC variance explained (R^2) when the convolution excludes SLP data from the most recent time period (the forecast horizon).

While the EOFs of SLP are independent, they may overlap in their impact on FWC. It is clear, for instance, that the decadal variability is overestimated in the reconstructions (Figure 1.6).

The good agreement in the reconstructions in Figure 1.6b&c indicate that we can be confident that SLP variability plays an overwhelmingly dominant role in controlling FWC variability in the HiGEM control run, and that we can fairly characterise the memory of SLP as decadal (though we cannot resolve timescales longer than 30 years), given the timescale of the derived step response functions (Figure 1.5). Moreover, it suggests that the assumptions underlying our methodology are fair: namely that the response of FWC to SLP forcing can be approximated as linear, and that our statistically derived response functions are good approximations of the 'true' underlying response functions.

Our method explicitly treats a red noise timeseries as the convolution of a white noise forcing and a filter (or response function). In other words, the FWC timeseries is explicitly treated as the result of SLP changes. Because it is the history of SLP that is used to predict FWC, our results do not permit the interpretation that changes in FWC are driving the changes in SLP. We cannot rule out that changes in SLP and FWC are being independently driven by a common, external forcing, and that there is in fact no causal link between SLP and FWC. However, in absence of any clear physical mechanism to that extent we consider it an unlikely scenario. Given the strong experimental and theoretical precedent for a causal connection between wind forcing and FWC, we conclude that the result of our statistical inquiry reflects a physical connection.

1.5.2 Historical freshwater changes

We now turn our attention to historical changes in Arctic FWC inferred from observations. We use the impulse response functions derived from our HiGEM analysis. The *forcing* timeseries (c.f. Figure 1.1) is now taken from atmospheric reanalysis: ERA-20C for the period 1900–1978 and ERA-Interim from 1979–2018. To obtain the necessary PC timeseries, we regress the reanalysis SLP variability onto the EOF patterns from HiGEM. We then convolve the resulting

PC timeseries with the corresponding impulse response function G, yielding the three contributions (orange lines in Figure 1.7b-d) that we sum to obtain the FWC timeseries shown in Figure 1.7a. The grey windows in Figure 1.7a indicate where there is incomplete information to provide a reconstruction using the full 30 years of the impulse response functions.

The reconstructed FWC timeseries exhibits pronounced decadal and multidecadal variability of amplitude 10,000 km^3. SLP variations projecting onto EOF3 contribute to the longer term variability (Figure 1.7d) and variations projecting onto EOF1 and EOF2 lead to decadal changes (Figure 1.7b&c).

There is a striking correspondence between the reconstructed FWC and inferred Arctic FWC changes from observations between 1992 and 2012 (black stars, Figure 1.7a; Rabe et al., 2014). A longer history of Arctic FWC changes comes from the observational data presented by Polyakov et al. (2013). We take the best-fit line through this data as presented by Polyakov et al. (2013), however we note that the underlying data shows substantial scatter about this smoothed line. There is also a notable agreement in the general trends exhibited by the FWC reconstruction and this observation-based timeseries (blue line; Figure 1.7a). It appears that the decadal-scale changes in our reconstruction somewhat overestimate the changes in the Polyakov et al. (2013) observational record. This may be consistent with the slight overestimation exhibited by the FWC reconstruction in the HiGEM model itself (Figure 1.6c). We also note that the uncertainty in both the reconstruction and the observational record is large. The shaded uncertainty envelope shown in our reconstructions in Figure 1.7 only reflects that associated with the impulse response functions, and not the reanalysis SLP data.

The marked decrease in Arctic FWC during the late 1960s and early 1970s coincides with the time during which the early 1970s Great Salinity Anomaly (GSA) propagated into the subpolar North Atlantic (Belkin et al., 1998; Dickson et al., 1988), suggesting a role for upstream Arctic SLP changes in this event. R. Curry and Mauritzen (2005) estimate that a freshwater flux of about 10,000 km^3 over 5 years would have been required to produce the observed salinity anomalies; this is indicated as an equivalent loss of freshwater in Figure 1.7a (dashed cyan

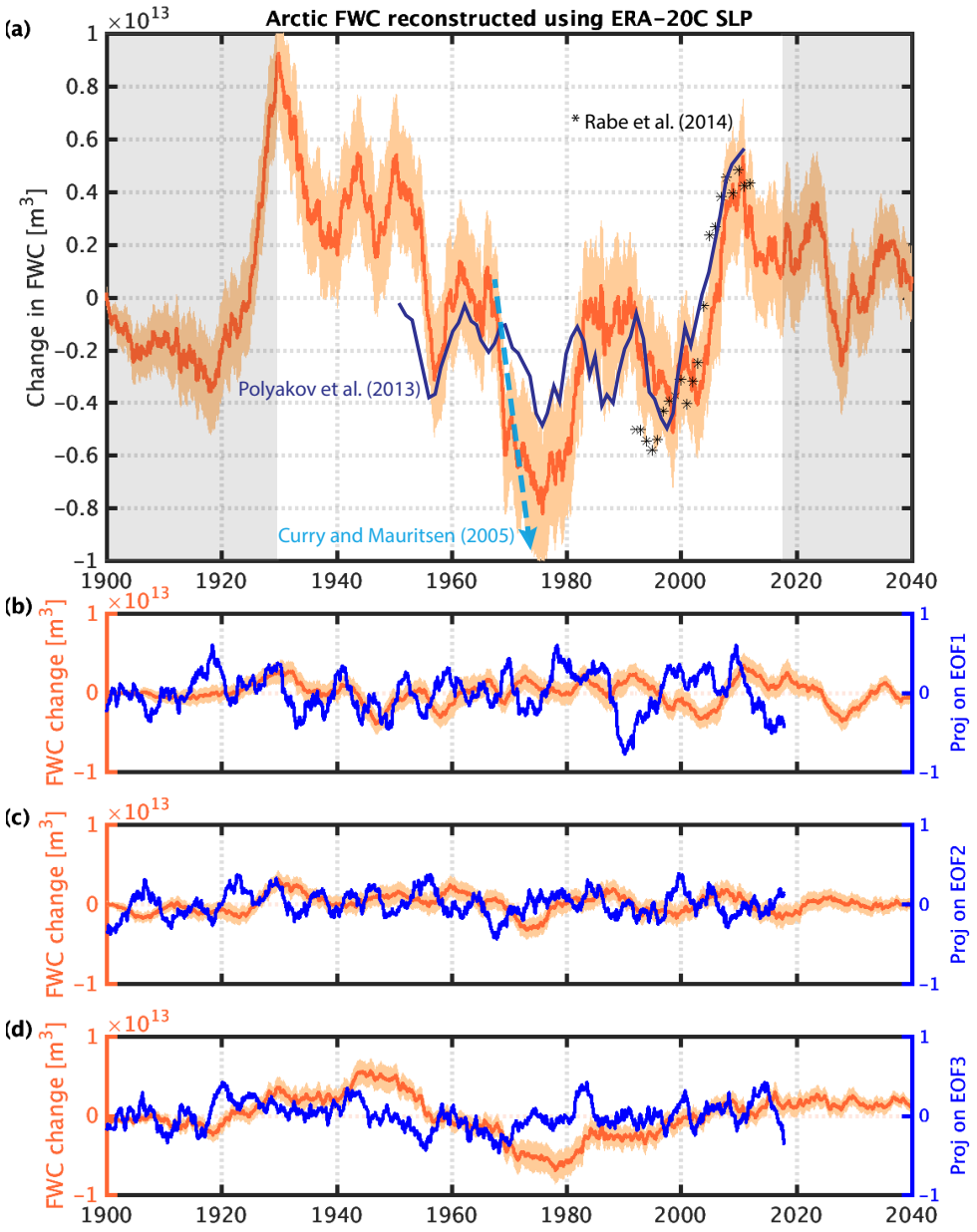


Figure 1.7: Reconstructed time series of Arctic FWC (orange line) using reanalysis (ERA-20C and ERA-Interim) and impulse response functions derived from HiGEM. Black stars: observational data from Rabe et al. (2014). Blue line: best fit line through Polyakov et al. (2013) observational data. Cyan arrow: flux of freshwater proposed by R. Curry and Mauritzen (2005). Blue line in (b), (c), and (d): projections of the ERA-20C sea-level pressure variability onto EOF1, EOF2, and EOF3, respectively (36-month running means); contribution to the FWC shown in orange. Time series in (a) sums the orange lines in (b), (c), and (d). Shaded windows (a): periods in which the convolution uses less than full 30-year response functions.

arrow). Part of this freshwater export may have been in the form of sea ice, however. Another GSA, in the 1980s, is thought to have involved a 'local' mechanism of generation rather than Arctic freshwater export at that time (Belkin et al., 1998).

Based on the correspondence between our reconstruction and the available observational data, we suggest that changes in Arctic FWC can be dominantly explained by SLP variability—including the recent freshening from 1992–2012.

1.5.3 Predictability of freshwater changes

The long memory of SLP variability exhibited by Arctic FWC raises the potential for predictability. In Figure 1.6d, we present a test of the predictability, in which we exclude SLP data from the most recent months of the convolution. We compute the control run Arctic FWC variance explained by the reconstruction for each choice of the number of months excluded. The 'forecast horizon' thus corresponds to the number of years excluded from the convolution in each test. When all three principal components of SLP are included in the convolution, the FWC reconstruction can capture half of the interannual variability in FWC in this model when predicting 7 years ahead. If the memory of SLP in the Arctic is indeed decadal, as we suggest it is, we might expect similar predictability to be available in nature. The forecast horizon to the sharp decline predicted in Arctic FWC in Figure 1.7a in the mid-late 2020s is in the range 5–10 years. Based on the HiGEM predictability, we might expect between 65–35% of variance to be explained over this range, respectively.

1.6 Discussion

Through linear response theory, we find that Arctic Ocean FWC in a fully coupled climate model has a memory of atmospheric circulation that extends over a decade. This long response timescale is in accordance with our expectations from theory and idealised numerical models of the Beaufort Gyre (Davis et al., 2014; Manucharyan & Spall, 2016). Our results suggest that a similar decadal adjustment timescale applies to FWC integrated over the entire Arctic basin

in a more realistic system, with additional complexity introduced by bathymetry, sea-ice, and atmosphere-ocean coupled processes. We suggest that the decadal timescale reflects a combination of the Beaufort Gyre's equilibration timescale and the influence of wind-driven sources and sinks of freshwater through the Arctic's gateways, which—in the case of liquid fluxes—adjust to SLP in a manner that reflects changes in barotropic and baroclinic flow. The latter, related to the tilts of isopycnal surfaces, should adjust slowly in the Arctic, whether related to wave-related processes (e.g. Luneva et al., 2012; J. Yang et al., 2016; B. Zhao & Timmermans, 2018) or eddy activity (e.g. Manucharyan & Spall, 2016).

As a result of the long memory of atmospheric forcing, attribution of changes in Arctic FWC is challenging; while FWC starts to react immediately to a change in SLP, a new equilibrium is not often reached because the forcing generally exhibits higher frequency variability. It follows that persistent atmospheric forcing has the biggest effect.

The slow decay of the influence of variations in atmospheric forcing can be likened to a piano and its sustain pedal. In this analogy, the fingers striking the keys represent atmospheric variability. The ocean integrates a long memory of atmospheric forcing; much as when the sustain pedal is held on, the sound integrates a long memory of different notes that have been played. If the pianist continually depresses the sustain pedal and proceeds to play, it can be hard to disentangle the original melody (the atmospheric forcing). In the same way, the ocean's long memory of SLP variability means that it can be challenging to attribute FWC changes to SLP variations in nature (e.g Rabe et al., 2014) or in coupled climate models. It is only by considering the FWC changes as a convolution of the atmospheric circulation and corresponding impulse response functions that we are able to cleanly attribute the causes of past FWC variability. Similarly, with knowledge of the decay curve of a note played on the piano (its impulse response function), it would—in theory—be possible to unravel even the most complex of melodies heard with the sustain pedal depressed.

Between 1992 and 2012, the Arctic accumulated c. 10,000 km^3 of fresh water (Giles et al., 2012; Rabe et al., 2014). Our reconstruction suggests that all three leading EOFs contributed to this

change. PC3 provided a steady, long-term increase over this window. Positive changes from PC2 in FWC kicked in from 2000, while PC1 dominated the increase over the second half of the observational period (the anticyclonic mode leading to freshwater accumulation). The sharp decline predicted in the mid-late 2020s is primarily driven by the dominance of the cyclonic mode of PC1 in the late 2010s.

Our results do not implicate decreases in Arctic sea ice cover in these historical FWC changes—they are based on unforced control run relationships and SLP changes only. They do, however, capture forced changes due to anthropogenic emissions to the extent that the SLP variability in the atmospheric reanalysis we use displays a forced signal. Jahn and Laiho (2020) demonstrate that in the large ensemble of the Community Earth System Model, forced changes in Arctic FWC should already be detectable outside the range of pre-industrial internal variability (agnostic of the mechanism by which these changes occurred). We save more detailed discussion of the likely roles of a forced signal and natural internal variability in the recent FWC accumulation during the 2000s for the Concluding Discussion, Section 6.2.

In the ice-ocean model FESOM, Q. Wang et al. (2019) show, using two parallel ice-ocean model simulations—one forced by reanalysis and one held at climatological values of surface air temperatures, longwave and shortwave radiation—that the recent total Arctic FWC increase was not driven by sea ice decline. In their simulations, however, sea ice decline is implicated in diverging freshwater trends across the Arctic Basin: enhanced freshening of the Beaufort Gyre (see also Q. Wang et al., 2018), and a relative salinification of the Eurasian Basin. The role of sea ice decline in these internal Arctic FWC changes is primarily via its influence on surface stresses and circulation patterns (Q. Wang et al., 2019), rather than the direct freshwater contribution of melting. In the simulations accompanying the observational analysis of Proshutinsky et al. (2019), the liberation of freshwater by sea ice melt is a relatively minor contribution to the Beaufort Gyre freshening; sources of freshwater from the Mackenzie river and Bering Strait dominate, and atmospheric circulation helps to determine the pathways of freshwater supply.

While the details of the response functions illustrated in Figure 1.5 may well be model-dependent, we expect the decadal memory of sea-level pressure to be robust. Neither the adjustment timescale of the PC1 and PC2 responses, nor the success of the FWC reconstructions in figures 1.6 and 1.7 are sensitive to the details of our analysis method (e.g., area over which the EOFs are calculated, maximum cutoff lag τ_{max}, reference salinity choice for FWC calculation). Ocean-only models forced with a step change in anticyclonic winds over the Beaufort Gyre exhibit a similar response (e.g. J. Marshall et al., 2017, see also Chapter 5).

Our results suggest that changes in Arctic FWC may well be predictable several years ahead, potentially providing valuable early warning of any significant change in freshwater export to the North Atlantic. However, we note that the links between freshwater changes in the Beaufort Gyre and export from the basin are not well understood (Rabe et al., 2013; Q. Wang et al., 2016), and local forcing in the Arctic gateways is also important for freshwater export (e.g. B. Curry et al., 2011; Houssais & Herbaut, 2011).

One might question how robust the derived relationships between SLP patterns and Arctic FWC are likely to be in the future. Since sea-ice influences the transfer of momentum from the atmosphere to the ocean (e.g. T. Martin et al., 2014), as sea-ice conditions continue to change we would expect the relationships between atmospheric patterns and FWC also to evolve. This is something we delve more deeply into in Section 6.2. In addition, changes in source terms such as runoff, freshwater from ice melt, and precipitation minus evaporation may play a larger role in a warmer climate. As such, although the FWC changes observed to date appear to have been driven by SLP variability, other influences may emerge in the future. Additionally, given the possibility that our historical FWC reconstruction overestimates FWC changes due to SLP alone (c.f. Figure 1.6 and 1.7), we cannot entirely rule out a role for other drivers of freshwater change that are largely unrelated to SLP variability in the recent FWC increase (for instance, net sea ice melt and an enhanced hydrological cycle).

1.7 Concluding summary

We summarise our primary conclusions below:

- Arctic FWC in a coupled climate model has a decadal memory of SLP
- Arctic FWC in this model can be reconstructed with a high degree of skill through convolution of the first three PCs of SLP and corresponding impulse response functions (R = 0.93)
- There is a striking correspondence between reconstructed Arctic FWC (using the model-derived response functions and SLP from reanalysis) and Arctic FWC from observational data. As such, historical changes in FWC appear to be primarily driven by SLP variability, including the recent freshening from 1992–2012 and the GSA of the early 1970s
- The decadal memory in the system affords some predictability of FWC changes several years ahead

Chapter 2

Response of Arctic Freshwater to the Arctic Oscillation in Coupled Climate Models

Abstract

We explore the relationship between atmospheric circulation and Arctic FWC in 12 pre-industrial control run simulations from phase 5 of the Coupled Model Intercomparison Project. Using multiple lagged regression, we seek the time-evolving response function of Arctic FWC to an impulse in the strength of the Arctic Oscillation (AO) as well as the second and third orthogonal modes of SLP variability. Integrating this impulse response function through time yields a step response function. There is broad agreement among models that a step change to a more anticyclonic AO leads to an increase in Arctic FWC, with an e-folding timescale of 5–10 yr. However, models differ in the degree to which a linear response to SLP variability can explain FWC changes, suggesting inconsistency in the physical origins of FWC variability. We perform statistical tests to establish levels of confidence in these results, and explore sources of error. When convolved with SLP reanalysis, four selected sets of impulse response functions successfully reproduce part of the observed FWC increase of the late 1990s and 2000s, consistent with the idea that this change was largely wind-driven.

Based on work published in *Journal of Climate* (https://doi.org/10.1175/JCLI-D-19-0685.1)

2.1 Introduction

The physical dynamics of the Arctic encompass atmospheric, oceanic and cryospheric processes; all of which are interlinked at the surface of the ocean. Above the Atlantic Water layer, the Arctic Ocean is stratified by salinity—it is a so-called β-ocean (Carmack, 2007)—and therefore freshwater in the Arctic represents an important control on these linkages, because its abundance modulates the connections between the surface of the ocean and the relatively warm Atlantic Water below. Changes to the freshwater reservoir, and therefore the stratification, have implications for sea ice stability and growth, vertical heat fluxes, mixing of nutrients, the carbon cycle, and broad indirect implications for climate and biology (Carmack et al., 2016). We provide further introduction to Arctic freshwater and its significance in Section 0.2.

Any attempt to understand the future evolution of the Arctic climate system would benefit from an improved representation of the processes governing freshwater variability (Lique et al., 2016). Furthermore, changes to Arctic freshwater content (FWC) should be closely related to changes in the supply and export of freshwater (e.g. Haine et al., 2015). Enhanced freshwater export to the North Atlantic has the potential to affect the Atlantic Meridional Overturning Circulation (AMOC) by modifying the salinity and stratification in regions of deep water formation (Jahn & Holland, 2013; H. Wang et al., 2018), and/or altering the densities along boundary currents in the subpolar gyre (Pickart & Spall, 2007).

A prerequisite for improving simulated FWC variability is the ability to assess and evaluate existing simulations. Indeed, we must go beyond comparing the mean state and variability of the Arctic FWC reservoir in coupled climate models, and evaluate the physical relationships between drivers and responses. Here, we isolate what is considered to be an important mechanism in the natural variability of Arctic FWC across 12 different Coupled Model Intercomparison Project Phase 5 (CMIP5) model simulations: the response of Arctic FWC to changes in the dominant patterns of large-scale atmospheric circulation over the Arctic region. These atmospheric circulation patterns are described by the leading modes of sea-level pressure (SLP) variability. In order to appropriately capture a relationship where memory is

important, we use linear response theory. Our method, following the approach of Kostov et al. (2017), Kostov et al. (2018) and Chapter 1 (H. L. Johnson et al., 2018), yields impulse response functions and their time-integrals: step response functions. We derive these relationships in the relatively long, unforced, pre-industrial control runs.

The chapter is structured as follows. We first provide an introduction to wind-driven Arctic FWC variability and possible connections with the Arctic Oscillation (AO), the leading mode of SLP variability (Section 2.1.1). In Section 2.2.1 we introduce the models we use and provide background to the relevant climatology in each model in sections 2.2.2 and 2.2.3. We describe our method for deriving linear response functions and reconstructing FWC variability in Section 2.2.4. In Section 2.2.5 we document Monte Carlo approaches that we employ to determine: a) response function uncertainty, and b) levels of statistical significance for our response functions.

In Section 2.3.1, we present the linear response of Arctic FWC to a one-standard deviation change in the strength of the AO, and the second and third orthogonal modes of SLP variability. Through convolution of the derived linear response functions with the original SLP, we attempt to reconstruct the FWC timeseries of each model. To the extent that the derived relationships are representative, we are then able to evaluate both the nature of the FWC-SLP relationship and its importance in determining overall FWC variability in each model. This intercomparison of SLP-FWC relationships across models, with an emphasis on the AO, is a central objective of the chapter. In Section 2.3.2, we investigate sources of uncertainty in the derivation of the response functions. We then exploit the fact that spectral properties affect the response function uncertainty in Section 2.3.3, and employ filtered timeseries to reduce this uncertainty and perform a secondary test of statistical significance.

In Section 2.4, we employ the historical runs of each model in order to select a subset of response functions with which we attempt to reconstruct historical FWC changes. The rationale is that the response functions that offer good reconstruction skill in both the control and the historical runs are perhaps the most robust. The response functions are derived from the con-

trol runs, so the historical run serves as an external test.

In section 2.5.1 we describe the selected response functions that show skill across both pre-industrial and historical runs. We then seek to evaluate whether the selected model-derived relationships are at all an accurate reflection of the relationship between Arctic liquid FWC and SLP in nature. In section 2.5.2, we convolve the model-derived impulse response functions with reanalysis SLP data from ERA-20C (Poli et al., 2016) and ERA-Interim (Berrisford et al., 2001). This yields a comparable FWC accumulation in the late 1990s–2000s to that reported by Rabe et al. (2014) and Polyakov et al. (2013). In this manner, our method is a novel means for reconstructing and assessing changes driven by SLP variability in coupled models. Because coupled climate models have freely evolving atmospheric components, this information cannot be obtained from historical simulations alone.

In Section 2.6 we offer discussion of the strengths and weaknesses of the linear response function methodology, explore the potential physical mechanisms behind the connection between the AO and FWC, and consider what our results suggest about the Arctic FWC changes in the context of climate change. Continued discussion is provided in Section 6.2. Finally, we offer a summary of our conclusions in Section 2.7.

2.1.1 Arctic FWC and the Arctic Oscillation

The Arctic Ocean maintains a relatively fresh state thanks to its position at the northerly node of the global hydrological cycle (e.g. Carmack et al., 2016; Haine, 2020). Fluxes of freshwater from Eurasian and North American rivers, flow of relatively fresh Pacific Water through the shallow Bering Strait, and an imbalance of precipitation and evaporation supply freshwater to the Arctic Ocean at a net rate of c. 10,000 km^3/yr (Haine et al., 2015). The freshwater reservoir of the Arctic Ocean and Canadian Arctic Archipelago (CAA) comprises both liquid (c. 100,000 km^3) and solid (with an annual mean of c. 14,000 km^3) components (Haine et al., 2015), unevenly distributed across the Arctic basins, shelf regions and the CAA. Both the solid and liquid components show a pronounced seasonal cycle, and both the regional distribution of

liquid freshwater and the total liquid Arctic FWC vary significantly on interannual to decadal timescales (e.g. Polyakov et al., 2008).

It has been understood for some time that winds can drive the redistribution and export of liquid freshwater, which resides at the surface of the Arctic Ocean (e.g. Proshutinsky & Johnson, 1997; X. Zhang et al., 2003). Atmospheric circulation affects the pathways and fluxes of inflowing Pacific waters (Alkire et al., 2007; Steele et al., 2004) and low-salinity waters from the Siberian shelves (Morison et al., 2012; Newton et al., 2008; Timmermans et al., 2011), as well as more saline Atlantic waters (Morison et al., 2006; Muilwijk et al., 2019). These connections are mediated by the sea ice cover, and its decline over recent decades may have contributed to the increased salinity contrast between the fresher Amerasian basin and the more saline Eurasian Basin (Q. Wang et al., 2019). Redistribution of liquid freshwater within the Arctic is itself important for establishing geostrophic circulation via the tilting of the halocline; these dynamics are perhaps most clear in the Beaufort Gyre, the largest reservoir of FWC in the Arctic Ocean (e.g. Manucharyan & Spall, 2016).

As the leading mode of extra-tropical sea-level pressure variability in the northern hemisphere, the Arctic Oscillation (AO; Thompson & Wallace, 1998) captures the dominant variability in the large-scale wind forcing and therefore represents a natural starting point in identifying causal relationships between atmospheric and oceanic/cryospheric variability. Indeed, several studies have focussed on determining the influence of the AO on patterns of sea ice drift (Armitage et al., 2018; Kwok et al., 2013; Kwok, 2009; Rigor et al., 2002) and surface geostrophic circulation (Armitage et al., 2018; Morison et al., 2012; Morison et al., 2021). There has, however, been substantial difficulty in linking observed Arctic FWC changes to atmospheric variability in coupled climate models and observations (Rabe et al., 2014). Much of this difficulty arises from the fact that the ocean responds slowly to an atmospheric perturbation. Theory and idealised modelling suggest that FWC in the Arctic Ocean, or at least in its largest reservoir the Beaufort Gyre, bears a multi-year to decadal memory of past atmospheric forcing (Davis et al., 2014; Doddridge et al., 2019; Manucharyan & Spall, 2016; Manucharyan & Isachsen, 2019). Our

Table 2.1: Models used and their characteristics. Grid resolutions are displayed as longitude × latitude, followed by the number of vertical depth levels *(lev)*. Sea-ice grids match the ocean component, except for the sea ice grid of CanESM2, which matches the atmosphere component. Full definitions of model names can be found online (https://www.ametsoc.org/PubsAcronymList)

Model	Atmosphere grid	Ocean grid	Sea ice model	Reference
ACCESS 1-0	1.88 ° × 1.25 °	Tripolar, 1 ° × 1 °, 50 lev	CICE, v4.1	Dix et al. (2013)
ACCESS 1-3	1.88 ° × 1.25 °	Tripolar, 1 ° × 1 °, 50 lev	CICE, v4.1	Dix et al. (2013)
CanESM2	2.81 ° × 2.79 °	1.41 ° × 0.94 °, 40 lev	CanSIM1	Chylek et al. (2011)
CCSM4	1.25 ° × 0.94 °	Dipolar, 1.11 °× (0.27–0.54) °, N Pole in Greenland, 60 lev	CICE, v4.0	Gent et al. (2011)
CNRM-CM5	1.4 ° × 1.4 °	ORCA-1 ° tripolar, 42 lev	GELATO (v5)	Voldoire et al. (2013)
GFDL CM3	2.5 ° × 2 °	Tripolar, c. 1 ° × 1 °, 50 lev, tripolar	SISp2	Griffies et al. (2011)
GFDL-ESM2M	2.50 ° × 2.02 °	Tripolar, c. 1 ° × 1 °, 50 lev	SISp2	Dunne et al. (2012)
IPSLA-CM5A-LR	3.75 ° × 1.89 °	ORCA-2 °, tripolar, 31 lev	LIM2	Dufresne et al. (2013)
IPSLA-CM5A-MR	2.5 ° × 1.27 °	ORCA-2 °, tripolar, 31 lev	NEOM-LIM2	Dufresne et al. (2013)
MIROC5	1.41 ° × 1.4 °	Shifted poles, c. 1.4 °×(0.5–1.4) °, 50 lev	COCO4.5	M. Watanabe et al. (2010)
MPI-ESM-LR	1.88 ° × 1.87 °	Shifted poles, c. 1.5 ° × 1.5 °, 40 lev	MPIOM	Giorgetta et al. (2013)
MPI-ESM-MR	1.88 ° × 1.87 °	Shifted poles, c. 0.4 ° × 0.4 °, 40 lev	MPIOM	Giorgetta et al. (2013)

approach is designed to to overcome this difficulty, by describing the relationships between variables in a manner that accounts for the memory of the system.

2.2 Materials and methods

2.2.1 Models used

We use monthly mean data from 12 different model contributions to the CMIP5 ensemble (Table 2.1). For the principal analysis, we use the pre-industrial control runs of each model, because these are long, unforced runs in which the internal variability is most likely to be characterised by stationary processes. Following the definitions below, we compute one-dimensional timeseries for our analysis: de-seasonalised Arctic liquid freshwater content and principal component timeseries of SLP variability north of 70 °N.

Table 2.2: Pre-industrial control run Arctic liquid FWC characteristics. Standard deviation is taken after de-seasonalising and linearly de-trending the FWC timeseries. De-correlation timescale is the e-folding timescale of the autocorrelation function, given to the nearest year.

Model simulation	S_{ref} (mean Arctic)	Mean FWC (km^3)	Std dev (km^3)	Decorrelation timescale (yr)
ACCESS 1-0	34.64	78,000	4,100	14
ACCESS 1-3	34.71	77,000	3,500	21
CanESM2	34.71	109,000	3,700	7
CCSM4	34.77	75,000	2,500	6
CNRM-CM5	34.40	107,000	2,800	19
GFDL CM3	34.65	90,000	2,600	6
GFDL-ESM2M	34.73	76,000	2,600	9
IPSLA-CM5A-LR	34.63	128,000	3,000	9
IPSLA-CM5A-MR	34.68	136,000	3,100	12
MIROC5	34.79	64,000	2,800	7
MPI-ESM-LR	34.69	80,000	2,300	13
MPI-ESM-MR	34.61	82,000	2,400	8

2.2.2 Representation of Arctic freshwater

FWC in the Arctic Ocean is commonly defined relative to a reference salinity, S_{ref}, usually chosen as the mean salinity of the Arctic: 34.8 (Aagaard & Carmack, 1989).

$$\mathrm{FWC}(t) = \iiint_{z(S=S_{ref})}^{0} \frac{S_{ref} - S}{S_{ref}} dV \tag{2.1}$$

This definition of S_{ref} also physically corresponds to the salinity at a depth near the base of the Arctic halocline, meaning that it has real utility in quantifying the expansion and freshening of this upper fresh layer. Because the integration extends only as far down as the halocline, changes below the halocline—for instance, from changing Atlantic Water inflow—are not considered. In this analysis, we take the reference salinity as the mean Arctic Ocean salinity for each model in question (Table 2.2), in order to avoid the effects of salinity biases in the models relative to the real Arctic. In each model simulation, these reference salinities all lie near the base of the halocline (not shown).

In constructing our freshwater budget for each model, we exclude the Canadian Arctic Archipelago, which is represented very differently between models. As such, we use the same Arctic Ocean domain as chosen by Serreze et al. (2006) in their observational synthesis (Figure 2.2). Note that the archipelago is often included in other Arctic freshwater budgets (e.g. Haine et al., 2015).

We report key statistics pertaining to the characteristics of Arctic FWC in Table 2.2, and show the deseasonalised Arctic FWC timeseries in Figure 2.1. The model simulations show a range of FWC mean states, with a factor of two difference between the ensemble members with the greatest and smallest FWC mean states (Figure 2.1, Table 2.2). For reference, Serreze et al. (2006) estimate the pre-2000 climatological mean liquid FWC to be 74,000 $\pm$ 7,400 km^3, based on hydrographic observations. We note that inter-model comparisons of absolute values of freshwater can be ambiguous (Schauer & Losch, 2019); to provide as much parity as possible, we report our linear response functions in terms of the fractional change in each model's Arctic FWC reservoir.

As seen in Figure 2.1, some of the pre-industrial control simulations exhibit a clear trend in FWC through the run (CanESM2, CNRM-CM5, and MIROC5). In all cases, we linearly detrend the FWC timeseries before performing the analysis. We group model runs into lengths of 3,600, 6,000 and 9,600 months, in order to standardise our regression procedure (Section 2.2.4). Where we truncate model runs to fit this grouping scheme, we begin from the first month in all cases except MIROC5 and MPI-ESM-MR, which display trends in the early part of the runs that are inconsistent with the rest of the timeseries. In these two simulations we omit the first 1,008 months.

The mean freshwater distributions (Figure 2.2) and vertical profiles of salinity (not shown) within the Arctic also vary between model simulations. Broadly, however, the models capture the greater depth-integrated freshwater storage in the deep basins compared with the shelves, a greater FWC and deeper halocline in the Amerasian Basin than the Eurasian Basin, and a saline and weakly stratified Barents Sea. The models show some common biases with respect

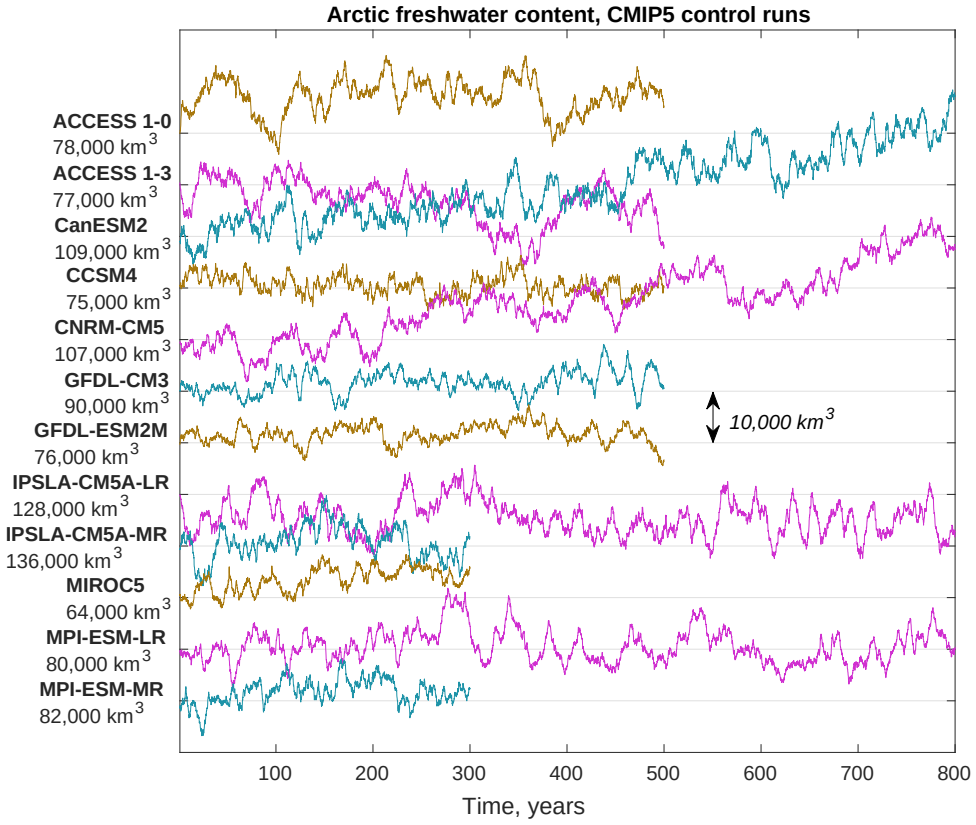


Figure 2.1: De-seasonalised Arctic FWC timeseries in 12 CMIP5 pre-industrial control runs. Model simulations are categorised into lengths of 3,600, 6,000 and 9,600 months (see text). Mean FWC is given beneath the name of each simulation. Magnitude of variability can be seen by comparison with y-axis spacing of 10,000 km^3. The timeseries are positioned on the y-axis such that the first value is anchored to this spacing.

to observations (e.g., the Polar Science Center Hydrographic Climatology, Steele et al., 2001): the Beaufort gyre is more spatially diffuse, situated further from Canada and Alaska, and the central Arctic is overly fresh. These biases are also clear in the CMIP5 multi-model mean freshwater distribution (Shu et al., 2018). Additionally, the IPSL models show an overly fresh Barents Sea (Figure 2.2).

Coupled climate models from two other modelling generations have been investigated in terms of their Arctic Ocean hydrography: Holland et al. (2007) compare ten models from CMIP3 (an earlier generation), and Zanowski et al. (2021) compare seven CMIP6 models, which succeeds

the generation we investigate here. With regard to the CMIP5 models, Ding et al. (2016) examine the seasonal heat and freshwater cycle across models, and Shu et al. (2018) assess freshwater characteristics and projected changes in the multi-model mean. There is clear improvement in the CMIP5 generation relative to the CMIP3 models in terms of freshwater distribution, surface salinities and gateway fluxes relative to observations (c.f. Holland et al., 2007; Shu et al., 2018), though the spread across models is large. An important improvement in CMIP6 over CMIP5 is that all models have an open gateway west of Greenland (Zanowski et al., 2021). However, the CMIP6 freshwater distributions appear to show similar levels of bias relative to the Steele et al. (2001) climatology as the CMIP5 models do, and relatively few CMIP6 models consistently show agreement with observations in terms of freshwater storage and gateway fluxes (Zanowski et al., 2021).

2.2.3 Representation of atmospheric variability

The Arctic Oscillation (AO) is a winter-intensified, annular mode of sea-level pressure variability that is linked to the polar vortex (Thompson & Wallace, 1998). The AO correlates strongly with the North Atlantic Oscillation (NAO), especially during winter (Deser, 2000), but affects climate beyond the Arctic and indeed beyond the Atlantic sector (Thompson & Wallace, 2001). The positive (negative) mode of the AO corresponds to the cyclonic (anticyclonic) sense of this pattern.

In this analysis, we restrict our attention to sea-level pressure variability north of 70 °N, and define the AO as its leading empirical orthogonal function (EOF). Figure 2.3 shows the AO as defined above, using ERA-Interim reanalysis data provided by the European Centre for Medium-Range Weather Forecasting (Berrisford et al., 2001). As plotted, the positive phase of this EOF corresponds to the anticyclonic, negative mode of the Arctic Oscillation. The first EOF (EOF1) of each model simulation considered here shows a high degree of spatial correlation with this definition of the AO (Table 2.3), and also with EOF1 from the other models. The PC1 timeseries for each model also show similar spectral densities to one another and to the PC1

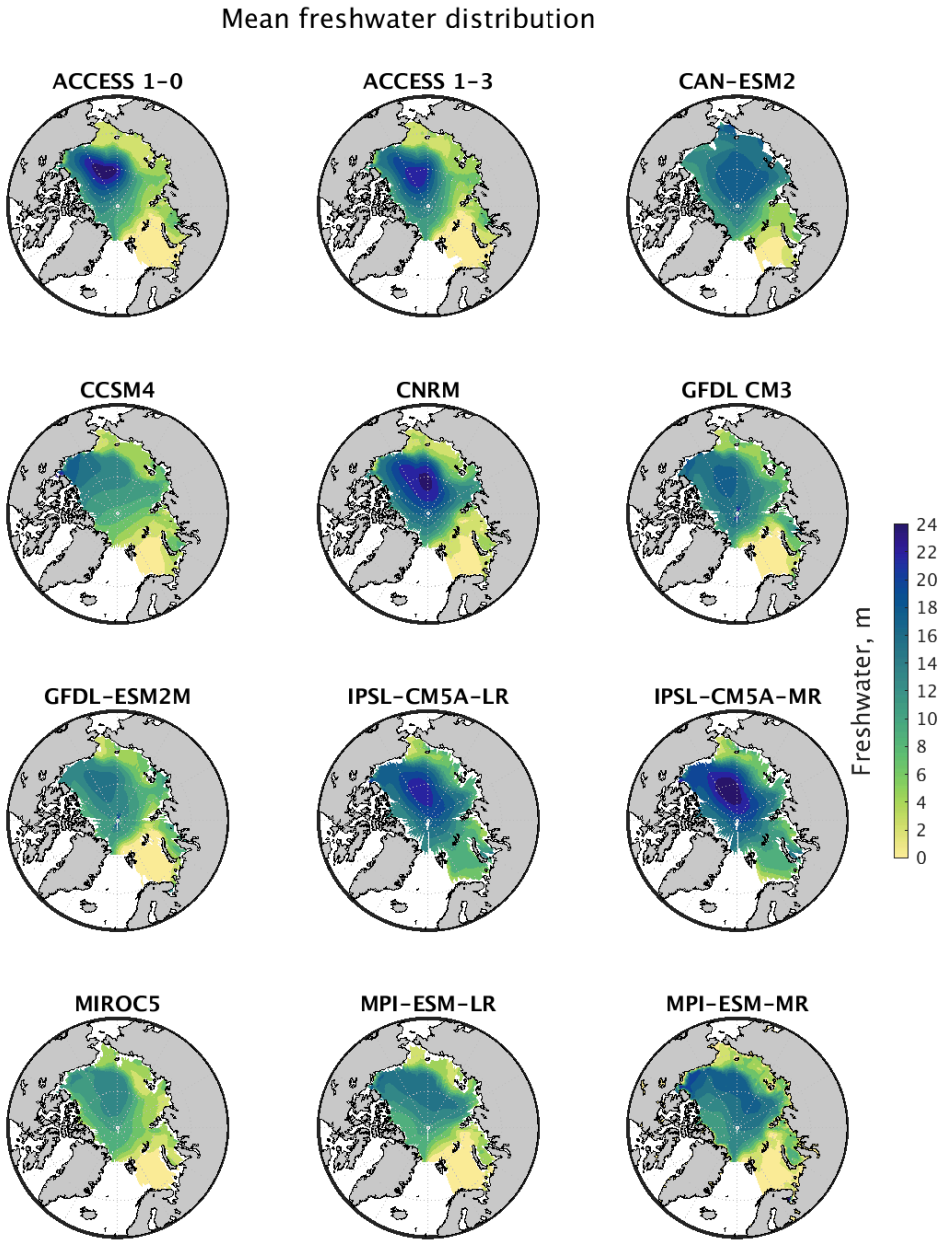


Figure 2.2: Mean freshwater distribution, in metres, over the Arctic Ocean domain considered here. Mean taken over a 50 year period selected randomly from within the pre-industrial control runs.

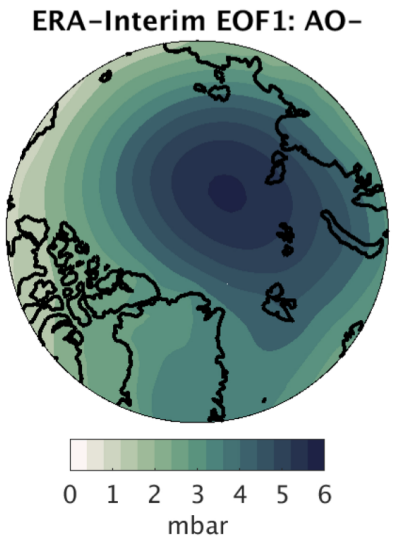


Figure 2.3: The negative AO as represented by ERA-Interim (Berrisford et al., 2001). Calculated as the first EOF of SLP variability north of 70 °N, this mode explains 53% of the variance in ERA-Interim SLP data spanning 1979–2018.

timeseries from ERA-Interim and ERA-20C data (not shown).

The spatial patterns of the second and third EOFs, by contrast, vary considerably amongst models (see also Cai et al., 2018). Furthermore, as the variance explained by PC1 is substantially higher than that explained by PC2 and PC3 in all cases (Table 2.3), EOF1 must be close to the true underlying leading mode. In contrast, the variances explained by PC2 and PC3 are closer together (not shown), raising the possibility that our estimated EOF2 and EOF3 might be linear combinations of the true underlying second and third modes (North et al., 1982). As such, we only compare the response functions for PC1 in this chapter, though we also calculate the response functions for PC2 and PC3 as part of the analysis. (Section 2.2.4).

2.2.4 Linear response function method

We employ linear response theory (e.g. Hasselmann et al., 1993) as per Kostov et al. (2017), Kostov et al. (2018) and Chapter 1 (H. L. Johnson et al., 2018) to determine the response of the Arctic FWC reservoir to a one-standard deviation step change in the strength of the neg-

Table 2.3: Pre-industrial control run AO characteristics.

Model simulation	SLP % variance explained by EOF1	SLP % variance explained by first three EOFs	EOF1 spatial correlation (R^2) with ERA-Interim EOF1
ACCESS 1-0	63	86	0.96
ACCESS 1-3	65	87	0.96
CanESM2	67	87	0.93
CCSM4	73	90	0.87
CNRM-CM5	68	87	0.95
GFDL CM3	70	87	0.90
GFDL-ESM2M	68	89	0.93
IPSLA-CM5A-LR	73	90	0.97
IPSLA-CM5A-MR	70	89	0.96
MIROC5	68	87	0.94
MPI-ESM-LR	69	88	0.96
MPI-ESM-MR	71	89	0.97

ative (anticyclonic) AO. We also determine the responses of FWC to one-standard deviation step changes in the second and third EOFs of SLP and employ these response functions in our reconstructions, however we do not directly compare them for reasons given above (Section 2.2.3). Our approach is a statistical alternative to active model perturbation experiments (see J. Marshall et al., 2017; Muilwijk et al., 2019), and permits the investigation and comparison of fully coupled models.

Firstly, we define our timeseries of interest. Our findings in Chapter 1 (H. L. Johnson et al., 2018) indicate that all of the first three PCs of SLP are significant in explaining freshwater variability—in both a coupled model context and most likely the real Arctic. As a result, we choose to consider the first three PCs of SLP. As shown in Equation 2.2, for each model simulation we treat the timeseries of Arctic FWC as the sum of convolutions of the first three PCs of atmospheric forcing, PC_i, with their respective unknown impulse response functions, G_i, integrated over time lags τ, from any given time, t, to τ_{max} years prior (with dτ = 1 month), plus a residual $\epsilon(t)$ which varies in time.

We choose τ_{max} as 20 years. This is long enough to resolve the decadal timescale found in Chapter 1. The fact that it is shorter than the the value used in Chapter 1 reflects a change in

our method. The simultaneous approach to finding the impulse responses used in this chapter means that each regression must solve for three times as many values of G as compared with the approach in which the responses for each PC are solved independently (used in Chapter 1). Although we are helped by the target timeseries being longer here than in Chapter 1, we adopt a shorter timescale here to reduce the likelihood of overfitting.

The first three principal components of SLP are considered, hence $n = 3$. We thus express FWC as:

$$\mathrm{FWC}(t) = \sum_{i=1}^{n} \int_{\tau=0}^{\tau_{max}} G_i(\tau)\mathrm{PC}_i(t-\tau)d\tau + \epsilon(t) \tag{2.2}$$

We solve for the three impulse response functions, G_i, simultaneously using multiple linear lagged regression. In practice, this means that the matrix $\mathbf{M}$ and vector G (as per Equation 1.3) are expanded three-fold to accommodate the three forcing modes and responses simultaneously to provide a solution for the timeseries of FWC. This allows the combination of these three orthogonal modes to maximise the variance explained in Arctic FWC. We can then attempt to reconstruct the original FWC timeseries by convolving the impulse response functions with the forcing as $\mathrm{FWC}(t)^{recon} = \sum_{i=1}^{3} \int_{\tau=0}^{\tau_{max}} G_i(\tau)\mathrm{PC}_i(t-\tau)d\tau$. See Figure 2.4 for an example of this reconstruction in the CCSM4 control run. The fit between the reconstruction and the original timeseries indicates how much FWC variability in the model can be explained as a linear response to the first three modes of SLP, over lags of up to 20 years. The misfit, on the other hand, gives us the residual term, i.e. $\epsilon(t) = \mathrm{FWC}(t) - \mathrm{FWC}(t)^{recon}$. This residual noise is employed in the uncertainty estimation procedure (Section 2.2.5).

For each model simulation, we attempt to minimise overfitting by assembling over 1000 different estimates for the impulse response functions and taking their mean. We compute this ensemble of estimates by varying: a) the cutoff lag applied to our impulse response functions, between 20 and 30 years; b) the part of the run that we select for the regression; and c) the length of this part. We group the models by length and adopt a consistent approach to sub-

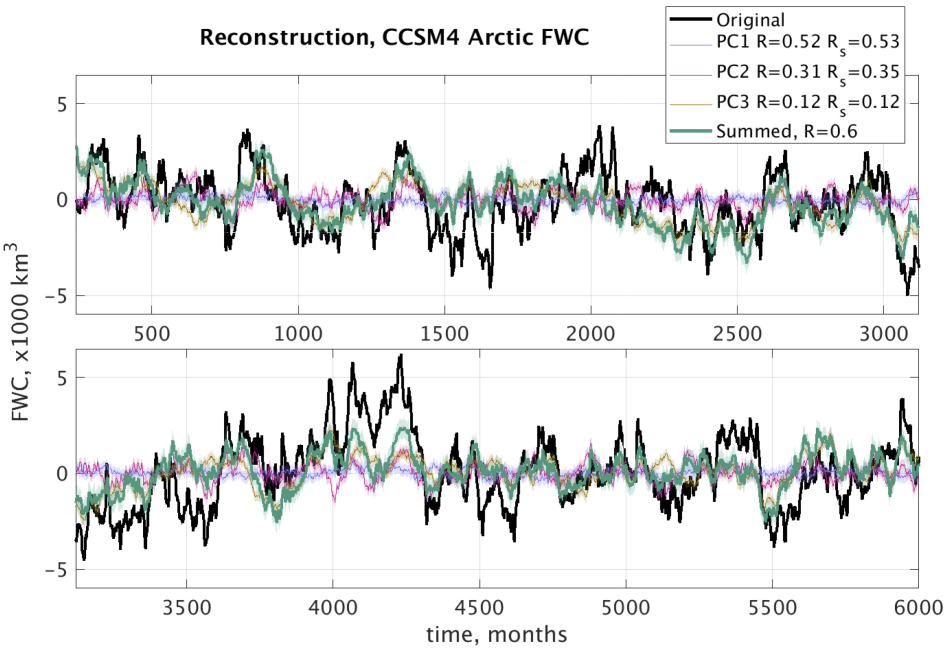


Figure 2.4: Pre-industrial control run reconstruction of Arctic FWC in CCSM4 using SLP and estimated response functions. R denotes the correlation of the reconstructed timeseries with the original FWC timeseries. R_S denotes the correlation after removal of the FWC contributions from the other components.

sampling the runs for all models (see Table A1 in Cornish et al., 2020).

The final impulse response function is a mean of all estimates over time lags up to 20 years (we terminate impulses with greater cutoff lags at a lag of 20 years in order that all response functions used are the same length). We then integrate the impulse response function through time lags to obtain the step response function, also known as a Climate Response Function (CRF; e.g. J. Marshall et al., 2017; Muilwijk et al., 2018, see also Chapter 5). We next evaluate the statistical robustness of these response functions using a Monte Carlo procedure (Section 2.2.5).

This linear response function methodology follows that of Kostov et al. (2017), Kostov et al. (2018), Chapter 1 (H. L. Johnson et al., 2018) and the Oxford-HiGEM contribution to the multi-model CRF study by Muilwijk et al. (2019). What is new here is the addition of a) a simultaneous approach to finding the impulse responses to each PC, b) Monte Carlo evaluations of response

function uncertainty and significance, c) high-pass filtering to reduce uncertainty and test confidence, and d) testing the reconstruction skill of the response functions in another run from the same model (the historical run) as an independent test of robustness.

2.2.5 Monte Carlo methods

Statistical significance

Regression techniques may produce relationships that do not reflect a causal mechanism, but are simply a statistical artefact of the attempt to best-fit the target data. This is an issue because it is unknown a priori how much of the variance the forcing should be able to explain; the impulse response functions will inevitably fit variability that is unrelated to the forcing, a problem which becomes exacerbated as forcings explain progressively less variance in the target data.

Monte Carlo methods have become a standard tool for the statistical testing of regression-derived relationships in the climate sciences (e.g. Lund, 1970) and beyond. Here, we use a Monte Carlo approach to help establish the statistical significance of the relationships derived by our linear response function approach.

We repeat our method for finding the response functions and computing reconstructions, but exchange the models' PC1 for a randomised forcing timeseries. The randomised, or surrogate, timeseries are generated by phase randomisation of the original PC1 timeseries as described in Schreiber and Schmitz (2000), and are designed to have the same spectral properties as the original timeseries. Periodicity artefacts are minimised by first making each timeseries periodic by appending its reflection in time, then using only half the length of the resulting surrogate timeseries. We use the same procedure on every occasion that we generate randomised or surrogate timeseries. We perform 1,000 such trials, and also repeat the procedure for the case where we have three simultaneous random forcing timeseries (emulating our three PCs).

We can then ask, for both the case of PC1 alone and all three PCs combined: does the FWC

reconstruction for each model explain more variance than that which could be explained using random forcing, at the 95% certainty level?

If a response function derived from the original model SLP forcing explains more FWC variance than the 95th percentile value from the trials with random forcing, it is most likely not an artefact of the regression method. It is worth noting that the true relationship between a given mode of atmospheric forcing and the FWC response in any given model may explain a low degree of FWC variance (lower than the significance level) and still be physical. If a low-variance explaining relationship exists, however, its representation in the impulse response function may be distorted by the attempt to best fit the residual noise.

Response function uncertainty

To establish uncertainty estimates for our linear response functions, we again employ a Monte Carlo approach. We start with the expectation that a given response function *is* physical. We find the fraction of the model simulation's FWC variance (R^2 in Equation 2.3) that is explained by this response function and determine the spectral density of the residual noise. We then create an ensemble of 1,000 synthetic FWC timeseries. Each synthetic timeseries contains a mixture of the FWC timeseries derived from: a) the convolution of our original response function G_1 with randomised SLP forcing PC_1^{rand}, (note for Equation 2.3 that the resulting timeseries of this convolution has a standard deviation $\sigma_{G\times PC}$); and b) a random timeseries, $\mathrm{FWC}(t)^{RandRes}$, that has the same spectral density as the residual noise, $\epsilon(t)$, and has a standard deviation $\sigma_{RandRes}$. Note that the abbreviation *RandRes* stands for randomised residual. We scale the two timeseries in accordance with the appropriate division of variance explained, and sum them to create the synthetic FWC timeseries, $\mathrm{FWC}(t)^{syn}$:

$$\mathrm{FWC}(t)^{syn} = \int_{\tau=0}^{\tau_{max}} G_1(\tau)\mathrm{PC}_1^{rand}(t-\tau)d\tau + \sqrt{\frac{1-R^2}{R^2}} \times \left(\frac{\mathrm{FWC}(t)^{RandRes}}{\sigma_{RandRes}/\sigma_{G\times PC}} \right) \tag{2.3}$$

Taking this ensemble of 1,000 synthetic FWC timeseries, $\mathrm{FWC}(t)^{syn}$, and 1,000 corresponding randomised forcing timeseries, PC_1^{rand}, we use multiple lagged regression to estimate an

impulse response function, G_1^{est}, which best relates the two timeseries, as per: $\mathrm{FWC}(t)^{syn} = \int_{\tau=0}^{\tau_{max}} G_1^{est}(\tau)\mathrm{PC}_1^{rand}(t-\tau)d\tau$. The full procedure is illustrated in Figure 2.5.

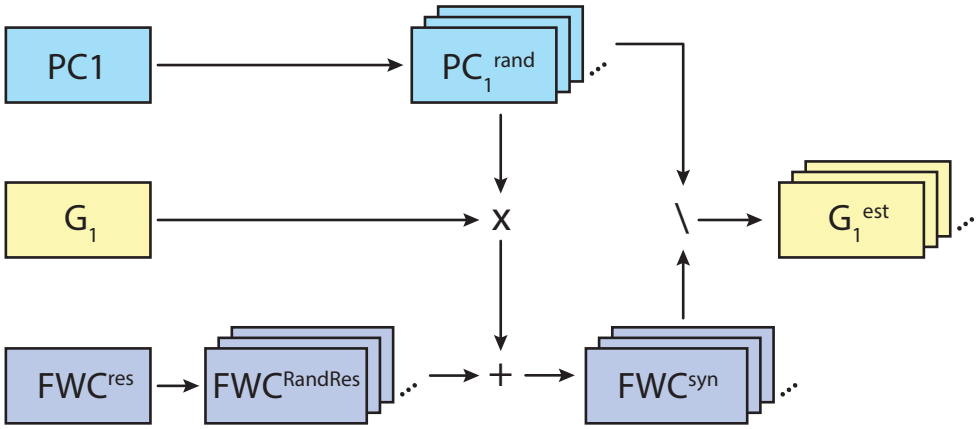


Figure 2.5: Flow chart illustrating our Monte Carlo method for calculating the uncertainty on the response functions. Repeated boxes and ellipses indicate the presence of 1,000 versions of the given timeseries. $\mathrm{PC1}^{rand}$ and $\mathrm{FWC}^{RandRes}$ are generated through randomisation of PC1 and FWC^{res}, respectively. The randomisation process is described in Section 2.2.5. The $\times$ symbol indicates convolution (first term on the RHS of Equation 2.3); + refers to the addition and rescaling process that completes the RHS of Equation 2.3; $\backslash$ is shorthand for the multiple lagged regression used to estimate impulse responses.

The resulting ensemble of 1,000 response functions, G_1^{est}, answers the motivating question: how reliably can we 'back out' a physical response function, $G_1(\tau)$, when it only explains a certain degree of variance, R^2, and the residual noise, $\mathrm{FWC}(t)^{RandRes}$, has a given spectral density? In each case, the mean of the 1,000 estimates faithfully reproduces the original impulse response function, $G_1(\tau)$. However, the spread may be large. We use the standard deviation of this spread of 1,000 estimates to construct the uncertainty envelopes on our response functions.

The magnitude of the one standard deviation uncertainty on each response function is related to both the variance explained and the spectral properties of the residual noise with which we dilute the target timeseries. This is something we explore further in Section 2.3.2.

2.3 FWC step response functions in pre-industrial control runs

2.3.1 Results

In Figure 2.6 we show the estimated responses of Arctic FWC in each model simulation to a step change in the strength of the AO. Though confidence in the results varies across the ensemble, we note the following. While the simulations exhibit a range of responses, there is broad agreement that the freshwater reservoir grows in size following a step change to a more negative (anticyclonic) AO. All models show a positive response after 10 years. Only GFDL-ESM2M and IPSL-CM5A-LR show negative mean responses by the end of the 20 year cutoff lag, however these results show large uncertainty windows which encompass positive responses. The ensemble mean shows a c. 7.5% inflation of the freshwater reservoir after 20 years.

The timescales of response are also broadly similar across the 12 model simulations. On the whole, the step response functions approach a new equilibrium after ten years. Similarly, in Chapter 1, we show that in the coupled climate model, HiGEM (Shaffrey et al., 2009), Arctic FWC increases by c. 8% of the reservoir size, reaching a new state that approximates equilibrium 15 years after a hypothetical step change to a more anticyclonic AO (H. L. Johnson et al., 2018). We save more detailed analysis of the forms of the response functions for Section 2.5.1, in which we describe a selection of response functions that also show reconstruction skill in their respective CMIP5 historical runs (Section 2.4).

It is important to note that, in the frequency domain, the impulse response function is a transfer function relating the spectral densities of the forcing and target timeseries. A transfer function that acts as a filter mapping approximately white noise (SLP) onto red noise (FWC) will have a slow adjustment timescale in the time domain. Even in the absence of a genuine physical connection between the forcing and response timeseries, the spectral densities of the forcing and target will dictate the spectral density of the transfer function, because the regression

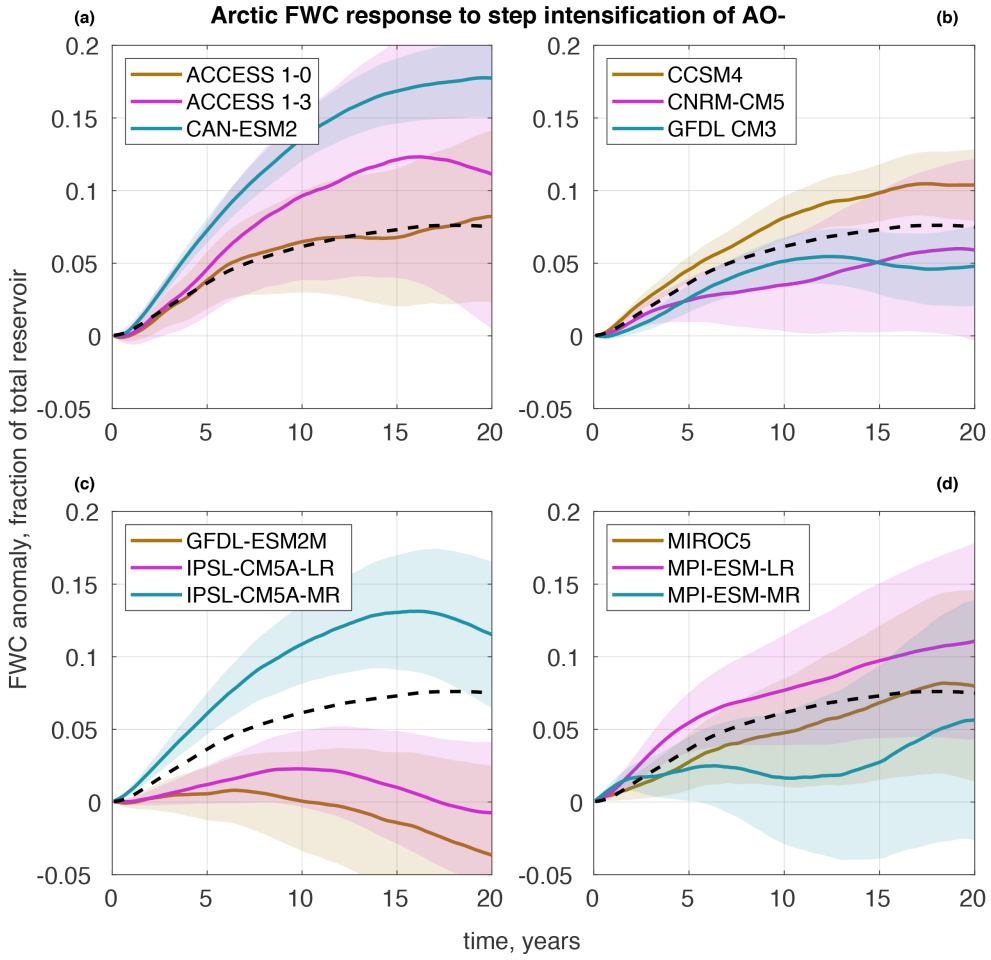


Figure 2.6: Response of Arctic FWC to a step change to a more anticyclonic (more negative) AO in 12 CMIP5 pre-industrial control runs. Shaded areas show the one standard deviation uncertainty, calculated using Monte Carlo method in Section 2.2.5. Black dotted line in all panels is the ensemble mean step response across all 12 models. Response functions are divided into four panels for legibility.

method seeks the best fit.

As such, the spectral density/adjustment timescale of the transfer/impulse response function alone is not decisive evidence that the ocean has a decadal memory of a particular mode of atmospheric variability. A more convincing case would incorporate: a) strong theoretical grounds, or b) statistical approaches that robustly reproduce such a relationship. We note the

existence of the former for certain atmospheric modes (e.g. Davis et al., 2014; Manucharyan & Spall, 2016), and test the second condition in these models here using Monte Carlo analyses.

In Figure 2.7 we show the FWC reconstruction skill across models using the linear response functions (crosses), alongside the significance levels (bars; see Section 2.2.5 for method). There are major differences across models in the extent to which these linear response functions can explain the FWC variability, with the lowest PC1 reconstruction R values around 0.2 and the highest around 0.6. We find that only four model simulations show AO-FWC relationships that are sufficiently strong to exceed the significance levels: CanESM2, CCSM4, GFDL CM3, IPSL-CM5A-MR (see blue bars and crosses in Figure 2.7). Note that the addition of the second and third EOFs must, by construction, increase the variance explained (Equation 2.2; see pink bars and crosses in Figure 2.7). For some simulations (CNRM, IPSL-CM5A-LR, MIROC5) the combination of the first three PCs explains a statistically significant degree of variance, whereas the first PC alone does not. In other words, we cannot be confident at the 95% level that the PC1 response is not an artefact of regression between two unrelated timeseries, whereas in the combination of the first three PCs, we can. The opposite occurs when the second and third modes are included for GFDL CM3; the combined response functions are not significant at the 95% confidence level. In Section 2.3.3, we exploit the fact that the uncertainty is related to the spectral properties of the FWC timeseries and apply filtering to gain further insight into how confident we can be that the response functions we derive are robust.

Assuming that there is a causal relationship between SLP and FWC, there are a number of possible physical reasons why the models might show apparently weak relationships between FWC and SLP. These reasons include: non-linearity of the relationship; non-stationarity (for instance, the relationship might be modulated by a changing ice regime); a dominance of other forcing mechanisms, whether far-field or local; and compensation from competing mechanisms of FWC change. The alternative, of course, is that a relationship between SLP and FWC is absent.

Different sea ice representations across the models (the sea ice model used in each case is

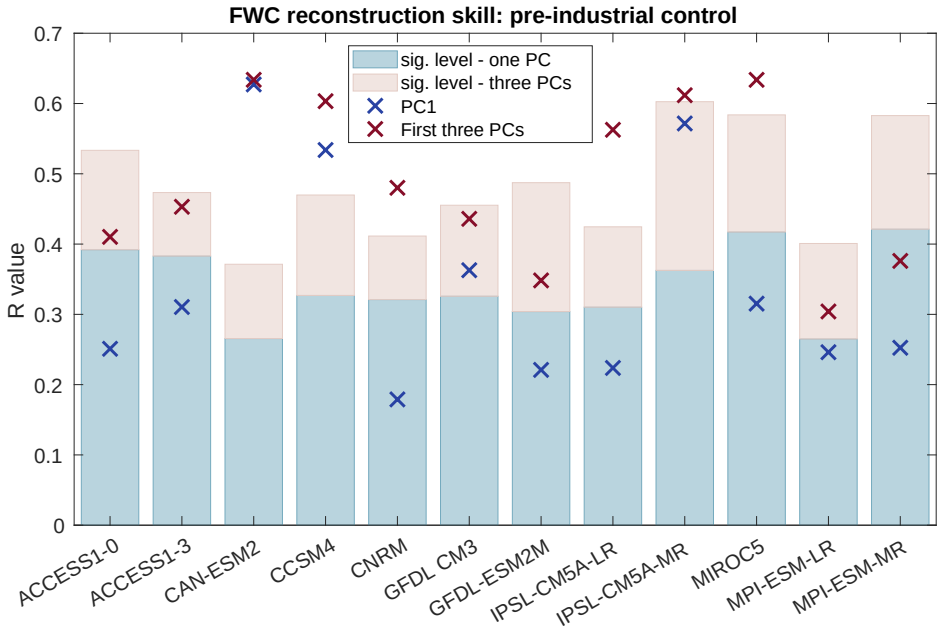


Figure 2.7: Reconstruction skill of response functions, pre-industrial control run. Bars indicate what reconstruction skill would be significant at the 95% confidence level; blue and red shading mark the significance thresholds for PC1 and all three PCs, respectively. Significance levels are derived using the Monte Carlo technique. Blue crosses indicate the R value from the correlation of reconstructed FWC using PC1 and the actual FWC timeseries, after removal of the reconstructions using PC2 and PC3. Red crosses give the R value for the timeseries correlation of FWC and the reconstruction using all three PCs.

listed in Table 2.1) have the potential to modulate the nature and strength of the SLP-FWC relationship. In Figure 2.8 we show that there is significant variability in sea ice representations across the pre-industrial control runs, especially in sea ice volume—less so in sea ice extent. Indeed, models are commonly tuned to reduce biases in the hemispheric sea ice extent, but this can result in biases in other aspects of sea ice representation (Ivanova et al., 2016). While the variability in sea ice representation is a possible explanation for differences in the SLP-FWC relationships, we do not find a consistent link of this nature across models (Appendix B, Cornish et al., 2020).

The FWC variance explained in each model is not evenly shared between the modes of forcing. For example, in MIROC5, the response to PC2 dominates the FWC variance explained by SLP

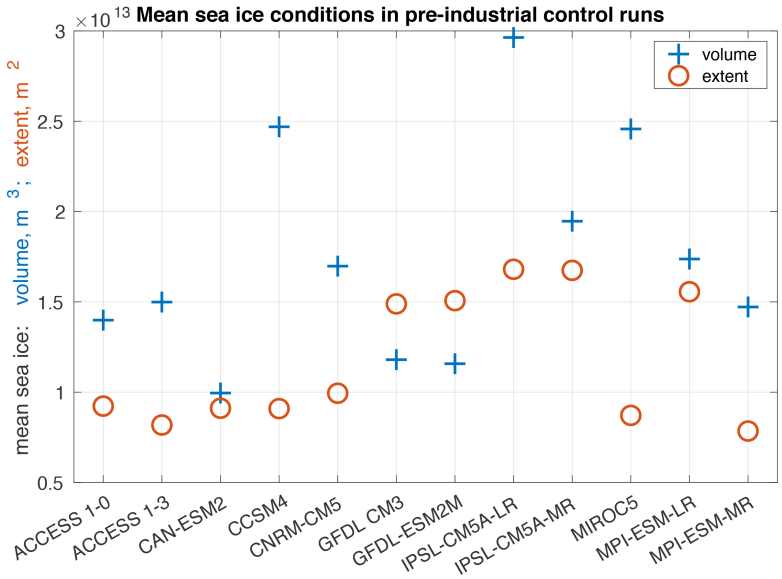


Figure 2.8: Mean sea ice volume and extent in pre-industrial control runs of 12 CMIP5 model simulations.

in this model. By contrast, in CanESM2, the AO is dominant in explaining FWC variability. These differences may be related to the different FWC distributions between models, onto which the EOFs of SLP project differently, hence producing a range of responses.

The accumulation of FWC under the AO- that is exhibited in all models (up to 10 years) is consistent with evidence from satellite retrievals of sea surface height. These data show a zero-lag monthly-mean connection between an intensified Beaufort gyre, weakened Fram strait freshwater export, and increased Bering Strait inflow under the AO- (Armitage et al., 2018). Our results are also consistent with the analysis of annual mean transports through the Arctic straits during AO+ and AO- years in the model study of Lique et al. (2010). We discuss the potential mechanisms at play in more detail in Section 2.6.

2.3.2 Spectral properties and sources of uncertainty

In this section, we explore the sources of uncertainty in deriving the response functions. We then exploit what we learn in this section in Section 2.3.3 to attempt to reduce the uncertainty

on our response functions, and learn more about how confident we can be in results that do not appear to be statistically significant (Figure 2.13). It is worth noting that in our synthetic tests we are able to quantify *error* from a true value explicitly, and so we can discuss the results in terms of *error*. In the context of the derivation of response functions from the CMIP5 control runs, we do not know the true underlying response function, and therefore we discuss the *uncertainty*. We calculate the one standard deviation *uncertainty* using the *error* found in synthetic tests; as described in Section 2.2.5.

In Table 2.4 we explore the sources of PC1 response function uncertainty through regressing likely sources of this uncertainty (the regressors) against values of the response function uncertainty (the regressand) across the 12 models. The size of the dataset is small—12 models—so the numerical values for variance explained should be treated as a guide rather than as definitive. The decorrelation timescale of the FWC timeseries (shown in Table 2.2) plays a part in determining the uncertainty on the response function that we calculate. We define the decorrelation timescale as the time taken for the autocorrelation function to reach a value of $1/e$ (it is an e-folding timescale). In general, across the 12 models, the 'redder' or longer the decorrelation timescale of the FWC timeseries, the greater the response function uncertainty. If the decorrelation timescale is normalised by the total length of the FWC timeseries, this improves linear fit with the uncertainty (R^2 = 0.51). The idea is that the more 'decorrelation cycles' that fit within the length of the timeseries, the smaller the uncertainty. The correlation improves yet further if, instead of choosing the raw FWC timeseries, we take the decorrelation timescale of the residual—what is left after computing the FWC reconstruction using the response functions. Including the inverse of the variance explained by the response function reconstruction (ie., $1/R^2$) as a second regressor improves the fit further: the weaker the strength of the relationship (and larger $1/R^2$), the greater the uncertainty.

We next perform synthetic experiments to investigate the roles of the decorrelation timescale and the $1/R^2$ value on response function uncertainty in an idealised setting. We construct predictable FWC timeseries using a known impulse response function and known (white noise)

Table 2.4: Table exploring different sources of uncertainty in the PC1 response functions. Table shows the variance explained in the response function uncertainty across models by linear regression with one or two regressors, and thus indicates the main sources of uncertainty. *FWC decorr. timescale* is the decorrelation timescale of the FWC timeseries (see Table 2.2 and Figure 2.10). *Rescaled* refers to rescaling this timescale by the total length of the FWC timeseries. The *FWC residual* is what is left after subtracting the reconstructed timeseries from the original FWC timeseries. The regressor $1/R^2$ is the inverse of the R^2 value for FWC variance explained by the reconstruction using the response function and the forcing timeseries (see Section 2.3.1).

Regressor(s)	% Variance explained in response function uncertainty (n=12)
FWC decorr. timescale	42
Rescaled FWC decorr. timescale	51
Rescaled FWC decorr. timescale + $1/R^2$	76
Rescaled FWC residual decorr. timescale + $1/R^2$	77

forcing timeseries. We can then 'mix' these predictable signals with 'residual noise' timeseries that we calculate as AR(1) processes using convolution with an exponential impulse response function, $G(\tau) = \mathrm{e}^{-\tau/T}$. This yields AR(1) timeseries with an autocorrelation function, $r(\tau) = a^\tau$ that has an e-folding decorrelation timescale, $T = -1/\ln a$. We next mix these AR(1) timeseries with the predictable FWC timeseries. We control the manner in which we mix these signals in order that the predictable FWC signal explains a certain degree of the variance of the overall signal. We then have a FWC timeseries that, in principle, is predictable to the degree of variance specified. We construct FWC timeseries for a range of choices of both the decorrelation timescale and the variance explained by the predictable part. For each choice of parameters, we compute 500 unique FWC timeseries.

We then undertake multiple linear lagged regression to attempt to find the original, known, response function. This yields 500 response function estimates for each choice of parameters. We find the standard deviation of the spread of estimates at each time lag, and integrate this standard error through all time lags to gain a single value of the error. In Figure 2.9, we plot this integrated error against the decorrelation timescale for different values of the variance that

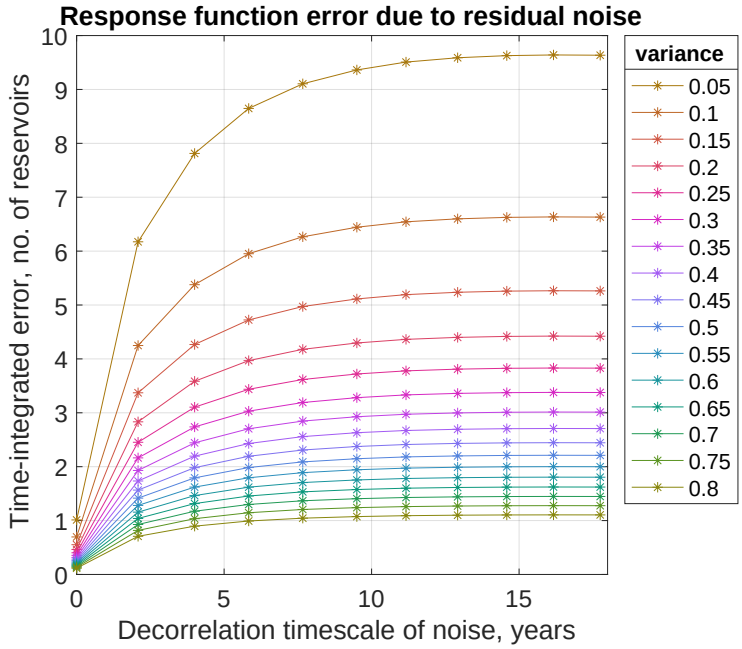


Figure 2.9: Mean synthetic response function error (n = 500) associated with the synthetic test outlined in the text. Legend heading *variance* refers to the variance explained by the predictable part of the signal. The other part of the 'target' FWC timeseries is comprised of 'residual noise' with the decorrelation timescale specified. As the variance explained decreases, the residual noise becomes increasingly dominant. Error is integrated through time and given relative to the size of the FWC reservoir. The PC1 response function for ACCESS 1-0 is used as the initial response function for these synthetic tests.

can be explained by the predictable part of the FWC signal. Error—and therefore uncertainty in the derivation of response functions more generally—increases with both the residual noise decorrelation timescale and the inverse of variance explained. This analysis provides insight into the fundamental caveat of the regression technique: it cannot be known a priori what proportion of the FWC variability should be explainable by a given forcing, so if the selected mode of forcing does not dominate the variability (i.e. small variance explained; large inverse variance), the response function will inevitably be trained to best fit residual noise. And the 'redder' that residual noise is (i.e. longer decorrelation timescale), the greater the error.

An additional source of uncertainty arises from the use of a relatively short response function cutoff lag. As the decorrelation timescale of the FWC timeseries approaches and exceeds the

cutoff lag timescale, uncertainty grows. Using another synthetic test, we find that, for a 20-year cutoff lag, increasing the decorrelation timescales yields an additional error to that shown in Figure 2.9, from close to zero additional error at a decorrelation timescale of 5 years, to 0.7 reservoir fractions at 20 years (not shown).

Regarding the spectral properties of the FWC timeseries, we find that: a) red residual noise increases the uncertainty in the determination of impulse response functions, b) additional uncertainty grows as the decorrelation timescale of FWC approaches and exceeds the response function cutoff lag. We also know that c) the residual noise generally has similar spectral properties to the original FWC timeseries (not shown). Given these pieces of information, it is apparent that filtering the data with a high-pass filter might be an effective way to reduce uncertainty. It is conceivable that other sources of variability possibly unrelated to Arctic SLP (e.g., changes in Atlantic inflow) add noise on longer timescales and contribute to uncertainty. Other sources of uncertainty (i.e., the lack of variance explained by the response functions) cannot be altered, however we can modify the FWC decorrelation timescale. We argue here that filtering can help to confirm (or otherwise) whether the more uncertain response functions that come from the full, unfiltered data, are indeed statistically significant.

2.3.3 Reducing error with high-pass filtered FWC timeseries

In order to exploit what we have learned regarding response function uncertainty and decorrelation timescales, we next filter our timeseries and repeat the analysis. We apply a fourth-order high-pass Butterworth filter with a cut-off at a 40 year period. In Figure 2.10a we show the effect of this on the Arctic FWC power spectra across models. In Figure 2.10b&c we show how the autocorrelation functions change before and after filtering, respectively. There is considerable spread in the decorrelation timescales of the original FWC timeseries (as shown in Table 2.2), which we define as the e-folding time of the autocorrelation function (time taken to reach the horizontal black line in Figure 2.10b&c). After filtering, the decorrelation timescales are much shorter and more similar, and there is a new periodic behaviour with a period of

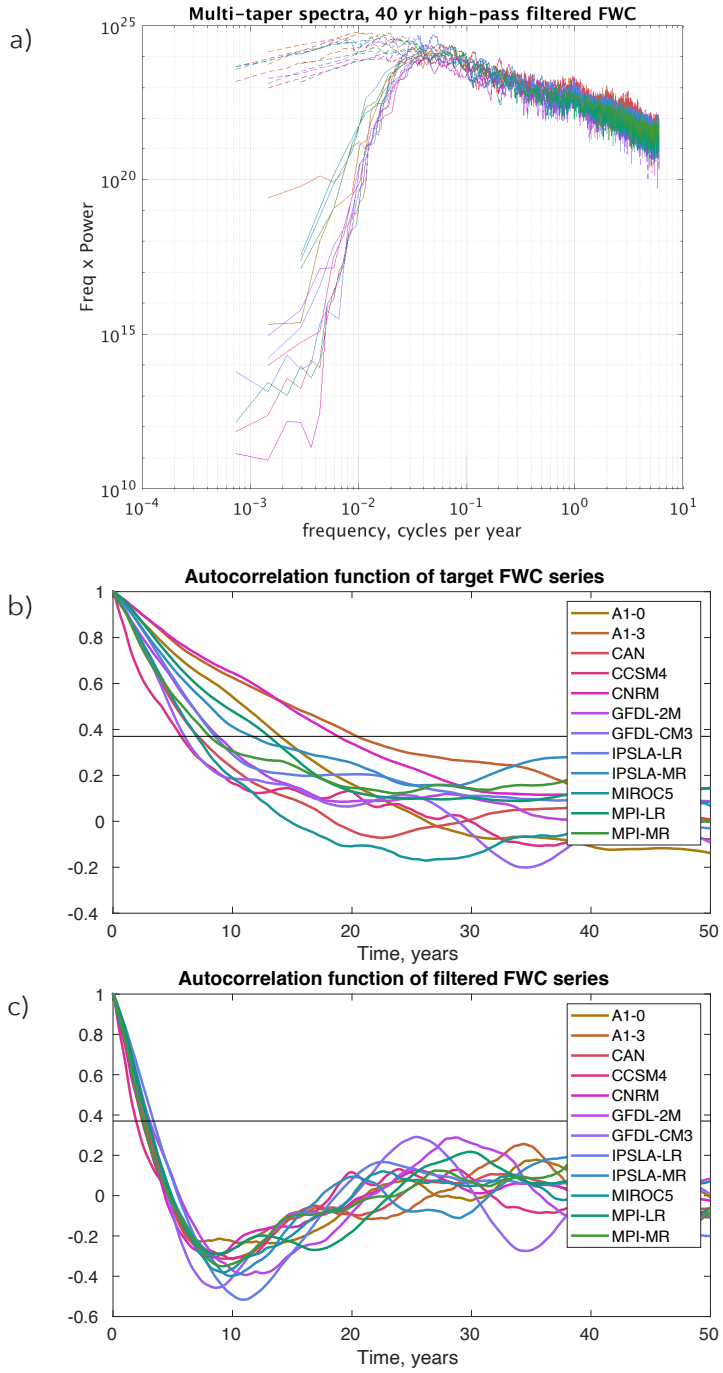


Figure 2.10: a) Power spectra of Arctic FWC in all models, before (dashed line), and after (solid line) filtering with a 40 year high-pass filter. b) Autocorrelation functions for original FWC timeseries. c) Autocorrelation functions for filtered FWC timeseries. Horizontal black line indicates the $1/e$ value. Curves intersect this value at the e-folding decorrelation timescale.

25–35 years. This periodicity is a natural consequence of high-pass filtering a red timeseries, for which power increases with decreasing frequency, because a new peak is created in the power spectrum at frequencies immediately above the high-pass threshold, effectively forcing the timeseries to become periodic on these timescales. This new peak is clearly visible in the solid lines in Figure 2.10.

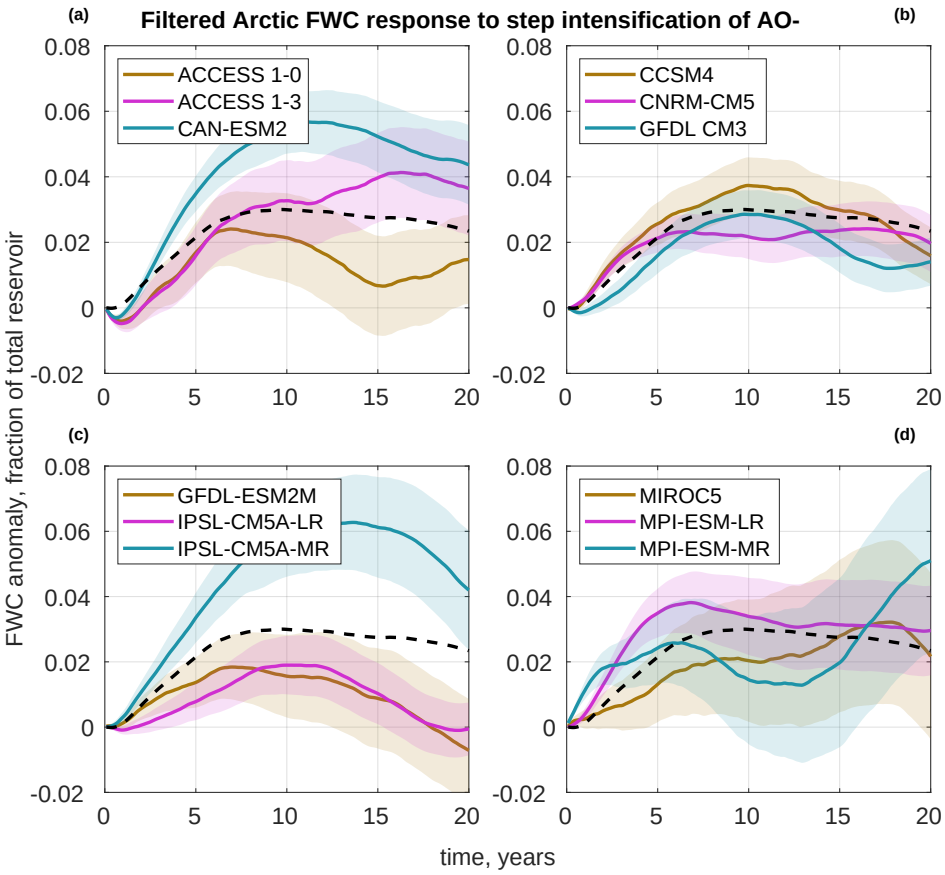


Figure 2.11: Step responses of Arctic FWC to a step increase in the strength of the anticyclonic AO-, using high-pass filtered FWC timeseries. Dashed line shows the ensemble mean response of all 12 models. Shaded envelopes show the one standard deviation uncertainty.

It is evident that the nature of the FWC timeseries has been severely altered and the results from this exercise should only inform the confidence we have in our earlier results with the full timeseries, not replace them. We repeat the analysis described in sections 2.2.4 and 2.2.5 with these filtered timeseries and plot the new response functions in Figure 2.11. The response func-

tion uncertainty—calculated using the Monte Carlo method as before—is markedly reduced versus Figure 2.6. All response functions from the filtered data show qualitatively similar shapes to the original response functions, but now have a pronounced oscillatory component; this is expected due to the periodicity that has been introduced. The magnitude of responses is also much reduced, as the variability of the underlying FWC timeseries has been reduced by the filtering.

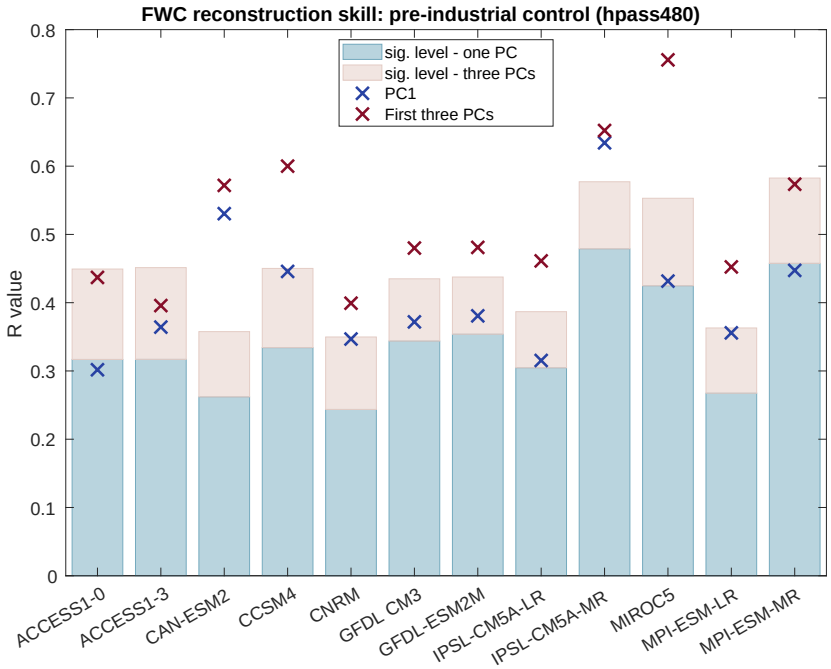


Figure 2.12: Reconstruction skill of response functions computed using filtered pre-industrial control run FWC timeseries. Bars indicate what reconstruction skill would be significant at the 95% confidence level; blue and red shading mark the significance thresholds for PC1 and all three PCs, respectively. Significance levels are derived using the Monte Carlo technique. Blue crosses indicate the R value from the correlation of reconstructed FWC using PC1 and the actual FWC timeseries, after removal of the reconstructions using PC2 and PC3. Red crosses give the R value for the correlation of the actual FWC timeseries and the reconstruction using all three PCs.

In Figure 2.12, we show the skill that these response functions afford in reconstructing the 'target' filtered FWC timeseries. The blue and red bars indicate the 95% confidence limits, derived

using an ensemble of randomised timeseries, as described in Section 2.2.5. This time, 10 out of 12 models have response functions for both PC1 and the first three PCs that meet this criteria. Additionally, the reconstruction skill is generally higher across models. This, combined with the similarities in response function shapes between figures 2.6 and 2.11 suggests that we can indeed be confident that 10 out of 12 of models exhibit response functions that are robust in the pre-industrial control run and not simply artefacts of regression between two unrelated variables. The models with response functions that do not meet this significance level, for both PC1 and all three PCs, are ACCESS 1-0 and MPI-ESM-MR. These response functions also do not meet the 95% confidence level in the analysis of the full timeseries (Figure 2.7).

2.4 Investigating CMIP5 historical runs

We attempt to reconstruct Arctic FWC in each model's historical run (spanning 1850–2005) using the linear response functions described in Section 2.3.1, with several objectives in mind. Firstly, we seek to select a subsample of response functions that we consider most robust, and most appropriate for the purpose of reconstructing historical changes (Section 2.5). The performance of the response functions in reconstructing FWC variability in their respective historical runs provides a good test to select such a subsample for this purpose. Our hypothesis is that, providing the nature of the SLP-FWC relationship is largely unchanged between the pre-industrial control run and the historical run of a given model, response functions trained on the control run should be capable of reproducing some of the FWC variability in the historical run. However, these historical runs are short, and given the low degree of FWC variance some of these response functions explain, it is very possible that what are robust—but weak—relationships in the pre-industrial control run appear meaningless in the historical run. Additionally, changes forced by climate change in the historical runs may affect the skill of the reconstructions.

Our second objective is to search for the strongest possible SLP-FWC relationship in the historical runs using a host of synthetic response functions. We derive these synthetic response

functions using a Monte Carlo approach, and they enable us to estimate the upper bounds on reconstruction skill in the historical runs (as described in Section 2.4.1).

2.4.1 Methods

Timeseries and reconstruction skill

Firstly, we again define our timeseries of FWC and PCs of SLP in the same way as in section 2.2, but based on the historical run data. We detrend the FWC timeseries as before, but do not attempt to decipher or remove any influence of radiative forcing. We regress the SLP variability of the historical run onto the first three EOFs of SLP from the control run, then attempt to reconstruct the historical FWC timeseries by convolving the impulse response functions derived from the control run, G_i^{PIC}, with the SLP forcing from the historical run, PC_i^{HIST} (Equation 2.4).

$$\mathrm{FWC}^{HIST}(t) = \sum_{i=1}^{n} \int_{\tau=0}^{\tau_{max}} G_i^{PIC}(\tau)\mathrm{PC}_i^{HIST}(t-\tau)d\tau \tag{2.4}$$

We then calculate the correlation coefficient between this estimate of the historical FWC and the original historical FWC timeseries, which gives us the reconstruction skill.

Monte Carlo estimate of upper bound on reconstruction skill in historical runs

The Monte Carlo procedure in section 2.2.5 yields an ensemble of 1,000 synthetic impulse response functions for each model, symmetrically distributed about zero. We use this ensemble here to estimate bounds on the potential reconstruction skill in the historical runs by convolving the synthetic response functions and historical run SLP to yield 1,000 reconstructions. The 1,000 reconstructions in turn yield a range of correlation coefficients (R) with the original historical FWC timeseries. The 1,000 R values comprise a distribution that is symmetrical about R = 0. Because the ensemble of 1,000 response functions spans the plausible space of possible impulse responses, some should offer reconstructive skill by chance. We take the 95th

percentile value of the R value as the estimated upper bound on reconstruction skill; this also enables an equivalent comparison against the significance level.

Ranking procedure using historical run as an independent test

We seek to rank the performance of our pre-industrial response functions against the performance of the response functions derived from random forcing, which are used to determine the significance levels (Section 2.2.5). In other words, we seek to know in what percentile of reconstruction skill do our response functions lie, relative to a random ensemble? Because we use the exact same 1,000 synthetic impulse response functions in both the pre-industrial control run setting and for the purposes of estimating the upper bound on reconstruction skill in the historical run (above; Section 2.4.1), we are able to include the historical run reconstructions in the ranking procedure, and find out how our response functions compare to a random ensemble in the independent setting of the historical run.

The procedure is as follows, and as outlined in Appendix A of Cornish et al. (2020). For each unique synthetic response function, we sum the FWC reconstruction R value from the control and historical run. Summing the reconstruction R value from our reconstructions of historical and control FWC variability—derived using our control run response functions—we again rank our response functions relative to the ensemble of synthetic response functions in terms of reconstruction skill. In Table 2.5, we show side by side the control run rank ($>$95% corresponds to statistical significance), and the change in rank when results for the control run and historical runs are combined. The combined rank is a qualitative metric; it is the change in rank (whether up or down) that is more informative than the absolute value.

2.4.2 Results

In Figure 2.13, we show that convolution of historical run forcing with impulse responses estimated from the pre-industrial control run yields a wide range of FWC reconstruction skill across the 12 models. In some cases, all reconstruction skill disappears, and/or the correlation

with the actual FWC timeseries becomes negative. In these cases, we may assume: a) the original response functions were not representative of a physical relationship, b) the relationship between SLP and FWC may differ between the control and historical runs, or c) the historical runs are too short for the statistical relationships apparent in the pre-industrial control run to manifest.

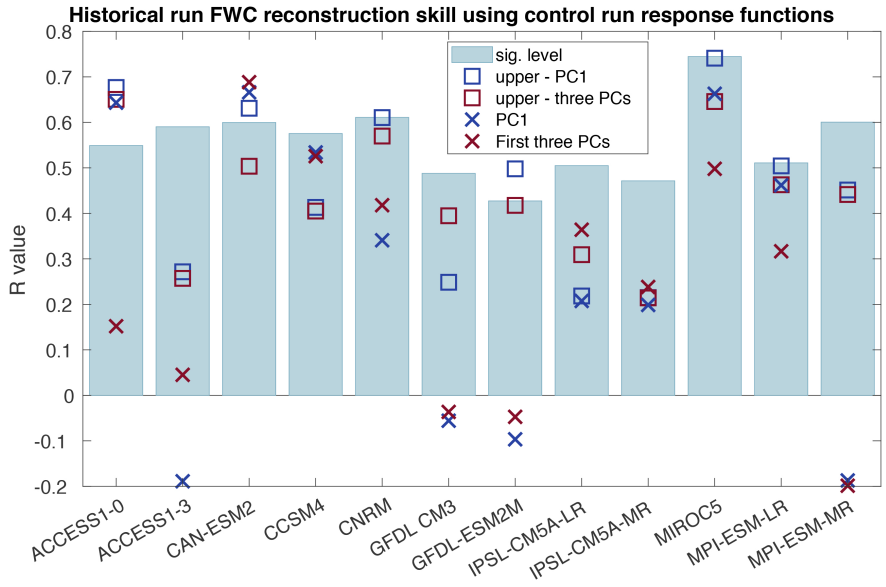


Figure 2.13: Monte Carlo evaluation of historical runs. Blue bars indicate the significance levels for a single forcing component. Crosses show the reconstruction skill using linear response functions derived from the pre-industrial control run, calculated after removal of the FWC contributions from PC2 and PC3. Squares represent the 95th percentile reconstruction skill using a Monte Carlo ensemble of synthetic response functions—an *upper* estimate of possible reconstruction skill with linear responses.

Comparison of the R value from our reconstructions (crosses in Figure 2.13) with the upper bounds on reconstruction skill derived using random response functions (squares in Figure 2.13; see Section 2.4.1 for method), indicates whether the impulse response functions derived in the control are also the most skilful possible linear description of the SLP-FWC relationship in the historical simulations. If the reconstruction skill is similar to, or higher than, the Monte Carlo estimate of the upper bound, then the response functions estimated from the control run are also appropriate at relating SLP and FWC variability in the historical run. Both

of these metrics link the model's actual SLP to its actual FWC variability. By contrast, the blue bars in Figure 2.13 indicate the 95th percentile level of R values that can be achieved with random forcing and new impulse response functions trained on the historical run with this random forcing (the method is the same as in section 2.2.5, but with the historical run data). Note that because the historical runs are short, these new response functions can be easily overfitted and will therefore produce a high bar for the significance levels. We suggest that they should be seen as a guide rather than absolute markers for significance. Comparison of these significance levels (blue bars) with the previous two metrics (squares and crosses) helps to establish how likely it is that the historical run SLP forcing timeseries itself can robustly explain FWC variability in the historical run.

To aid with the interpretation of this combination of metrics, we provide two examples. The linear response functions for GFDL-ESM2M lose all reconstructive skill when convolved with the historical SLP variability; the R values are low or even negative (crosses in Figure 2.13). Clearly, if a relationship between SLP and FWC exists in this run, it is not well described by these linear response functions. To test whether or not a statistical relationship between SLP and FWC does exist, we next look to the Monte Carlo estimate of the upper bound on reconstruction skill (square), and compare this against the significance level (bar). The fact that the estimated upper bound on reconstruction skill for PC1 is greater than the significance level indicates that there may be a significant statistical relationship between PC1 and FWC in the historical run, which explains a notable portion of the FWC variance (R = 0.5), but that relationship is different to the one obtained in the pre-industrial control run.

The reconstruction skill in the CanESM2 historical run is high when using the response functions derived from the pre-industrial control run (crosses, Figure 2.13). Indeed, comparison with the R values from the Monte Carlo ensemble (squares) shows that these relationships are highly skilful in relating SLP and FWC variability, even though they were trained on a different run. This consistency with the significant result in the pre-industrial control run convinces us that this is a robust relationship, and will be appropriate for reconstructing his-

Table 2.5: Response function evaluation in historical run context by model. The R value rank, given as a percentile, is explained in Section 2.4.1. These metrics, in combination with the filtering test (Section 2.3.3) guide to select the following model results for reconstructing historical FWC changes: CanESM2, CCSM4, IPSL-CM5A-MR and MPI-ESM-LR.

Model simulation		R value rank as %	
		PIC	Change: PIC+HIST
ACCESS 1-0	PC1	55.1	+32.9
	All PCs	64.2	-1.6
ACCESS 1-3	PC1	84.1	-49.4
	All PCs	92.0	-7.6
CanESM2	PC1	100	0
	All PCs	100	0
CCSM4	PC1	100	0
	All PCs	99.9	+0.1
CNRM-CM5	PC1	64.8	+4.6
	All PCs	99.1	-3.4
GFDL CM3	PC1	96.0	-25.6
	All PCs	91.3	-29.9
GFDL-ESM2M	PC1	67.8	-18.6
	All PCs	51.2	-2.6
IPSL-CM5A-LR	PC1	73.0	+18.3
	All PCs	100	0
IPSL-CM5A-MR	PC1	99.6	+0.3
	All PCs	95.4	+4
MIROC5	PC1	68.0	+19.8
	All PCs	98.7	-3.3
MPI-ESM-LR	PC1	90.1	+4.6
	All PCs	67.7	+18.5
MPI-ESM-MR	PC1	38.5	-4.5
	All PCs	21.6	+1.7

torical FWC changes in Section 2.5.

In Table 2.5, we evaluate the response functions and their reconstruction skill relative to a synthetic ensemble (as described in Section 2.4.1). Again, to aid with interpretation, we provide two examples. The reconstruction skill for GFDL CM3 in the control run is statistically significant for PC1 and almost so for the combination of three PCs. Both are significant when the analysis is repeated with high-pass filtering of FWC. Application of the pre-industrial control run response function to the historical run, however, yields effectively zero reconstruction skill. Indeed, the rank of the response functions for this model—relative to the synthetic

ensemble—drops markedly when including the historical run (Table 2.5). As a result we would not select these response functions to reconstruct historical FWC changes. By contrast, the rank of the response functions for model MPI-ESM-LR improves when including the historical run. The historical run results provide more confidence in the MPI-ESM-LR control run responses functions and their suitability for reconstructing historical changes, and so we include them in Section 2.5. The four models that provide the response functions we select for the purpose of reconstructing historical FWC changes are: CanESM2, CCSM4, IPSL-CM5A-MR and MPI-ESM-LR.

2.5 Reconstructing historical FWC changes

In this section, we compare historical changes in FWC (Rabe et al., 2014) to reconstructed changes in FWC using our model-derived response functions and SLP data from reanalysis. We select a subset of response functions for this purpose and briefly analyse them in Section 2.5.1. We then employ these response functions to reconstruct historical FWC changes in Section 2.5.2.

2.5.1 Selected response functions

Based on the statistical tests described in Section 2.4, we select the pre-industrial AO-FWC response functions that are successful in reconstructing variability in their respective historical runs as well as being robust in the pre-industrial context (Table 2.5). The selected response functions come from the following models: CanESM2, CCSM4, IPSL-CM5A-MR and MPI-ESM-LR, and we show their responses to a step change to a more negative AO in Figure 2.14.

These step response functions bear certain similarities. They are all positive, with adjustment magnitudes greater than the previous ensemble mean (grey curve), and they show a broadly similar, quasi-exponential form. After a relatively slow first-year adjustment, the FWC reservoir grows rapidly within the first ten years, approaching a new equilibrium between 15 and 20 years. Over-interpretation of the precise shapes of these response functions should be

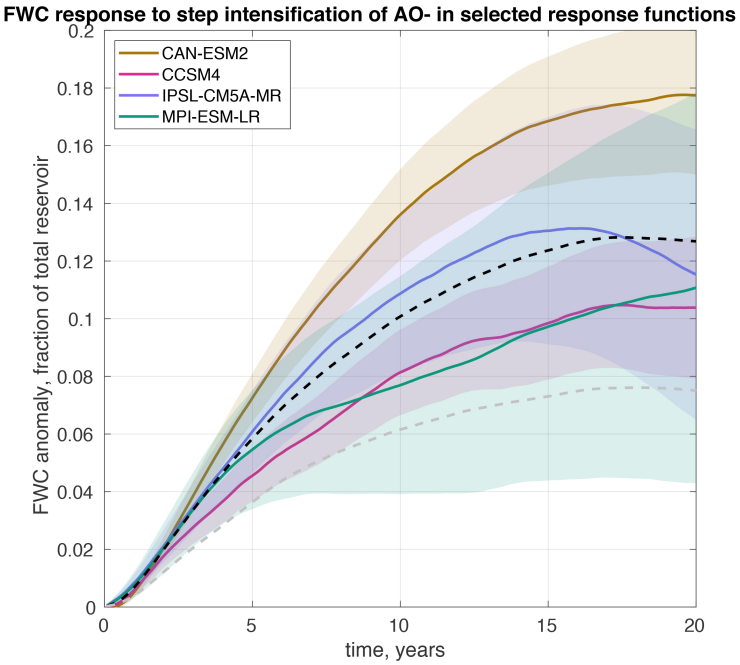


Figure 2.14: Selected response functions: response of Arctic FWC to a step change to a more negative AO in pre-industrial control runs. Selected based on performance in both pre-industrial and historical runs. Black dashed line shows mean of selected response functions, grey dashed line shows mean of all 12 response functions presented in this chapter.

avoided—note that the error bars would accommodate a range of shapes. The ensemble mean of these four functions (black curve) has an e-folding timescale of 7.4 years, and a maximum freshwater change of 12.8% of the total Arctic FWC reservoir.

2.5.2 Reconstructions with selected response functions

Having extracted SLP-FWC relationships in each model, we seek to determine what, according to these model relationships, the SLP-driven changes in FWC would hypothetically have been over the past decades. We convolve reanalysis SLP data with our selected (impulse) response functions, as per Chapter 1 (H. L. Johnson et al., 2018). We use ERA-Interim (Berrisford et al., 2001) and ERA-20C (Poli et al., 2016) reanalysis data as the forcing. ERA-Interim data is available from 1979 onwards, so we use the ERA-20C record only up to 1979.

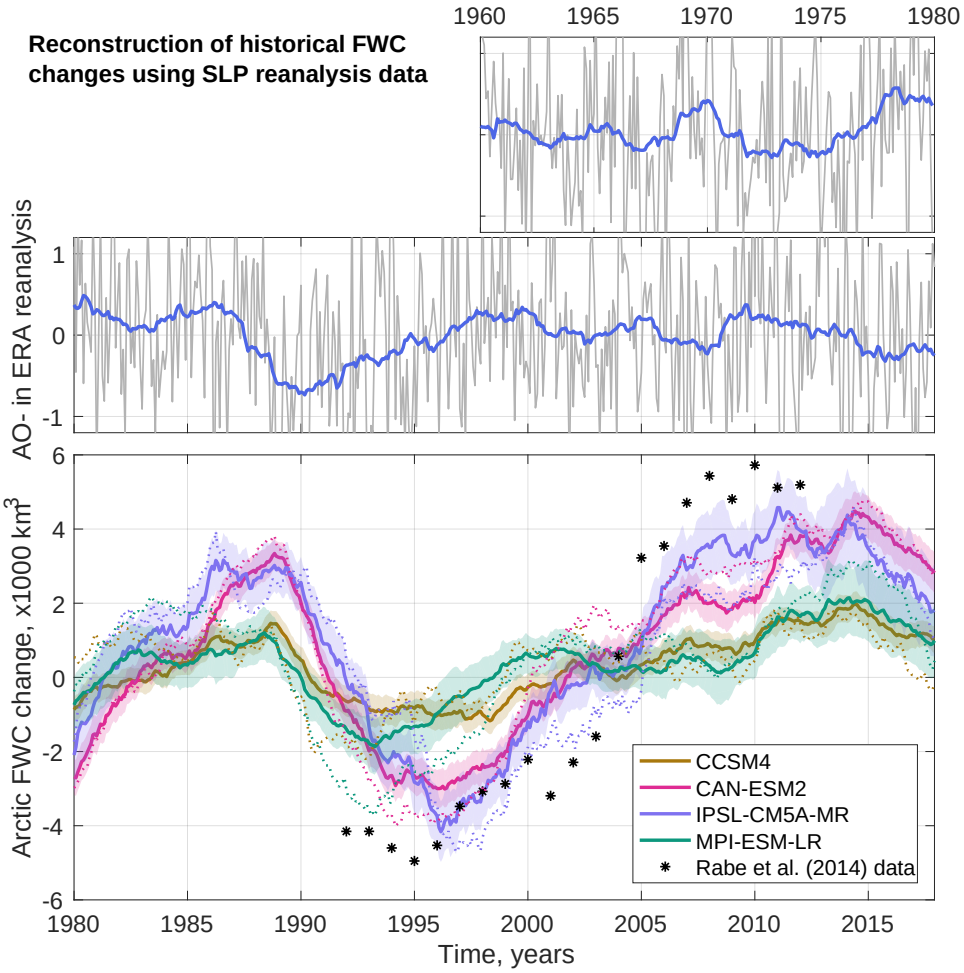


Figure 2.15: Reconstruction of historical FWC changes from 1980. Calculated using SLP from reanalysis and response functions estimated from pre-industrial control runs of each model, and compared against FWC data from Rabe et al. (2014). The upper panels show the negative AO in ERA-20C (1960–1978) and ERA-Interim (1979–2018) reanalysis SLP data, normalised to one standard deviation in the monthly data. Note that positive values indicate a more negative AO. Grey line: monthly timeseries; blue line: three-year moving mean. Solid line in lower panel denotes reconstruction using PC1 alone while dotted line is for all three PCs.

In this analysis, we focus on the AO (EOF1), because it is consistently represented across the ensemble of models and the reanalysis SLP data (Table 2.3). We regress the reanalysis SLP data onto the first three EOFs of SLP for each selected model, then convolve the resulting PC timeseries with their respective response functions. This yields SLP-driven timeseries of FWC

through the historical period, based on linear model-derived relationships. In Figure 2.15, we plot reconstructions using PC1 alone in bold, and reconstructions using the first three PCs as dotted lines. We show the period 1980–2017, and compare with observations of Arctic FWC from Rabe et al. (2014). Note that we require a full 20 years of forcing before the results reflect the full memory in the response functions, and as such we require reanalysis forcing from 1960 onwards to build these reconstructions. To calculate the uncertainty envelope around each AO (PC1) reconstruction, we use the ensemble of 1,000 impulse response functions described in section 2.2.5. Convolving these 1,000 response functions with the atmospheric forcing yields 1,000 different reconstructions. We plot the standard deviation of these reconstructions as the shaded uncertainty envelopes.

Changes in the AO dominate the FWC variability; including the second and third modes does not significantly change the reconstruction. A sharp downward trend in FWC during c. 1988–1995 is evident in all reconstructions, and is the result of a strong and sustained shift towards a positive phase of the AO at the start of that period. All four model-based reconstructions show an increase in Arctic FWC coincident in time with that reported by Rabe et al. (2014) during 1995–2012, due to a sustained shift towards a negative phase of the AO at the start of that period. The magnitude of change is somewhat smaller (c. 30–80%) in the reconstructions than the observations, with CanESM2 and IPSL-CM5A-MR coming the closest to reproducing the observed increase. Note that differences in the magnitudes of variability also reflect the different mean states of Arctic FWC in each model (Figure 2.1, Table 2.2). For each model, the variability in reconstructed FWC changes is considerably larger than the associated uncertainty.

For comparison, Shu et al. (2018) show that the CMIP5 historical run multi-model mean captures c. 50% of the observed freshening during the 1992–2012 observational period. This multi-model mean can be assumed to average across a range of variations in SLP forcing, suggesting a significant role for an enhanced hydrological cycle and sea ice melt in this signal, amongst other possible changes (which could include changes to SLP variability).

2.6 Discussion

Here, using linear response theory, we isolate the time-evolving response of Arctic FWC to a step change in the Arctic Oscillation (AO) across the pre-industrial control runs of 12 CMIP5 models. In all models, the response functions reveal that the anticyclonic phase of the AO drives FWC accumulation over the first 10 years of the response, and 10 out of 12 models still show a positive response after 20 years. The reconstruction skill afforded by the response functions, however, varies widely amongst models. In Chapter 1, using a higher resolution coupled climate model—HiGEM—we found that linear responses to the first three modes of SLP forcing could explain FWC variability with a reconstruction skill of $R = 0.93$ (H. L. Johnson et al., 2018). None of the CMIP5 models studied here exhibit SLP-FWC relationships that are as strong as that found in HiGEM. The relationship varies considerably in strength from model to model, indicating inconsistency in the underlying causes of FWC variability.

A major caveat of the regression technique is that it cannot be known a priori what portion of the FWC variability should be explainable by a given forcing, so if the selected mode of forcing does not dominate the variability, the response functions will inevitably be trained to best fit residual noise. Error increases as the decorrelation timescale of this residual increases (Section 2.3.2). As such, our technique is most effective when there are strong relationships between the variables of interest, and when the decorrelation timescale of the 'target' is shorter than the cut-off lag used in the response function. Even with random forcing timeseries, the regression technique will yield response functions that will find some level of reconstruction skill, which may vary widely on a random basis. We outline here a Monte Carlo approach to fairly assess the level of confidence we can have that the derived relationships are not simply artefacts of regression derived using a random forcing timeseries. In many cases, with the raw FWC timeseries, the variance explained is insufficiently high for us to be confident that the derived relationships are robust. However, we can also exploit the relationship between decorrelation timescale and error, and high-pass filter the FWC data in order to reduce the uncertainty. After filtering, we find that 10 out of 12 of the response functions meet the 95%

confidence level (Section 2.3.3). Moreover, these response functions show clear correspondence in form to the original response functions, which lends support to the robustness of the original response functions, despite the larger uncertainties.

We select a subset of response functions from four models that not only show robust relationships in the pre-industrial control run but also show reconstruction skill in the historical run. All four indicate that a one-standard deviation enhancement of the anticyclonic AO- leads to significant freshwater accumulation. The mean of these four responses has a magnitude of c. 13% of the total Arctic FWC reservoir, and an e-folding time of c. 7 years.

The utility of our technique, despite its caveats, is evident in several aspects. The technique allows us to cleanly isolate relationships between variables with very different spectral characteristics in a computationally efficient manner. These relationships can then easily be compared and evaluated in terms of their nature and strength across a range of coupled climate models. Here, we establish a baseline for the Arctic SLP-FWC relationship in CMIP5 models, against which the effects of future model development in coupled climate models can be assessed. Further, the technique provides a novel means for model evaluation against observations, through the convolution of estimated response functions with forcing timeseries from observations or reanalysis data.

While it is beyond the scope of this chapter to determine the physical mechanisms by which freshwater adjustments in response to the AO occur, we note that dedicated modelling and observational studies provide insight as to how the AO- SLP pattern might lead to Arctic FWC accumulation, and we expect similar mechanisms to be at play in the CMIP5 models. Lique et al. (2010) show, using a Lagrangian analysis applied to a high-resolution ocean-ice model, that the Beaufort gyre expands and intensifies under AO- forcing relative to AO+, while the export of liquid and solid freshwater through the Fram Strait decreases. Similarly, X. Zhang et al. (2003) find in an ocean-ice model forced by atmospheric reanalysis that solid and liquid freshwater transports through Fram Strait increase when the AO changes phase from negative to positive. Studies employing satellite observations also report expansion of the Beaufort

gyre under AO- forcing, and a more Eurasian position of the Transpolar Drift (Kwok et al., 2013; Rigor et al., 2002; Steele et al., 2004). These changes are largely connected to the impact of AO-related winds on Ekman pumping within the Arctic (e.g. Ma et al., 2017), which influences the surface geostrophic circulation. Armitage et al. (2018) show with sea-surface height data that the AO forcing drives cross-shelf Ekman transport, which excites along-shelf flow. Furthermore, Armitage et al. (2018) find that the AO- is associated with enhanced Bering Strait inflow (of relatively fresh waters) and decreased Atlantic inflow through the Barents Sea Opening; another change that favours accumulation of FWC in the Arctic Ocean. These studies do not capture the time-evolving response of the variables in question to the AO, however, as we do here.

Different physical mechanisms have different timescales of adjustment that may be detectable in the form of the response functions. Thermodynamic sea ice changes should adjust rapidly to a change in the atmospheric circulation (e.g. Wernli & Papritz, 2018). Sea ice growth perturbations can remain important on longer timescales, however, if changes to the sea ice export result in sustained anomalies in upstream dynamic thickness or ice-free area, leading to sustained sea ice growth anomalies; we investigate this idea in more detail in Chapter 3. Mixing across the halocline is low (e.g. J. Zhang & Steele, 2007), in the main due to strong stratification rather than sea ice cover (Guthrie et al., 2013; Lincoln et al., 2016). However, vertical mixing might be altered with SLP-driven changes to the stratification, especially in shelf regions, and with changes in eddy activity. Liquid freshwater fluxes through the Arctic gateways adjust to SLP anomalies via both barotropic and baroclinic flow. Sea-surface height gradients should respond quickly to SLP anomalies by Ekman pumping. In the interior of the Arctic Ocean, the tilts of isopycnal surfaces are expected to adjust more slowly, whether by processes related to topographic and planetary Rossby waves (Luneva et al., 2012; J. Yang et al., 2016; B. Zhao & Timmermans, 2018) or by eddy activity (e.g. Manucharyan & Spall, 2016). In the Beaufort gyre, the timescale of adjustment is affected by a combination of eddy diffusivity and seasonally-occurring drag on the geostrophic circulation by overlying sea ice, yielding a multi-year timescale that is shorter than that due to eddy diffusivity alone (Doddridge et al.,

2019).

In section 2.5.2, we compare FWC changes from observational data (Rabe et al., 2014) with reconstructions using a subset of model-derived response functions, chosen based on their performance in both the pre-industrial control and historical runs of the respective models. The convolution of reanalysis SLP data with the response functions recovers between 30 and 80% of the observed freshwater accumulation 1992–2012, and exhibits similar timing of changes. This provides some confidence that the model-derived response functions are useful representations of climate dynamics in nature, and is consistent with the idea that these changes were largely wind-driven (as per Chapter 1). While coupled climate models may be able to reproduce the amplitude and frequency of internal atmospheric variability (e.g. the AO) we do not expect model SLP to vary with the same phase as in the real atmosphere—either in the historical runs or the future—meaning we should exercise caution in interpreting FWC changes exhibited in these runs. As such, our approach provides one solution to the problem of determining the origins of historical changes, and although we cannot predict SLP variability years in advance, memory in the system may afford a few years of potential predictability for Arctic FWC (as shown in Chapter 1).

As CMIP6 data becomes available, we suggest that this approach of deriving response functions and convolving with reanalysis has broad utility in evaluating coupled climate models—where the atmosphere is a freely evolving component—against observations. Because SLP changes may be driven by climate change, it should be noted that such an approach does not entirely distinguish changes arising from forced versus internal variability. Jahn and Laiho (2020) have recently shown that in the Large Ensemble of the Community Earth System Model, significant increases in Arctic FWC occur across all ensemble members in the 21st century, and that these changes depart from the typical range of interannual FWC variability in the model's pre-industrial control run in the early 21st century. In other words, their model results suggest that forced changes in FWC should already be detectable.

However, our observational record is short and sparse; we simply do not know what the 'nor-

mal' range of Arctic FWC variability should be, nor what the relative contributions of forced changes and internal variability are to the recently observed FWC accumulation. As mentioned in Chapter 1, and by Jahn and Laiho (2020), the historical FWC changes we attribute in Chapter 1 and in this chapter to SLP changes may indeed contain a forced climate change signal if those SLP changes themselves are partially driven by climate change. Indeed, forced SLP changes may be part of the equation in the CESM-LE FWC changes. However, as we consider in the Concluding Discussion (Section 6.2), the AO is projected to become more cyclonic with climate change (e.g. Choi et al., 2010)—whereas the recent accumulation was in large part associated with the anticyclonic AO (as well as contributions from other modes of SLP variability). For this reason we suspect that the SLP contribution to the recent FWC accumulation is one that is better characterised by internal variability than by forced change.

Additional contributions—largely unrelated to Arctic SLP—to the recent accumulation of FWC are increases in freshwater inflows from an enhanced hydrological cycle and river runoff: changes predicted in many climate models (Haine et al., 2015; Jahn & Laiho, 2020; Zanowski et al., 2021) and observed in nature (e.g. Holmes et al., 2018; Peterson et al., 2002). A further element to consider is the reduction in sea ice concentration and thickness, which provides a direct liquid FWC contribution through the reduction in net thermodynamic growth rate in the Arctic Ocean, but also modulates the way wind stress is imparted on the ocean (T. Martin et al., 2014; T. Martin et al., 2016). As such, the decline in sea ice cover may affect ocean currents, freshwater distribution and freshwater storage (Q. Wang et al., 2018; Q. Wang et al., 2019), and may ultimately modify the FWC-SLP relationships. Our results here and in Chapter 1 suggest that these influences are likely secondary to SLP-driven changes in the recent FWC accumulation observed by Rabe et al. (2014). However, time will reveal more clearly the relative roles of these influences on FWC changes, as we discuss in more detail in the Concluding Discussion (Section 6.2).

Finally, we note that our finding that CMIP5 models exhibit markedly different strengths of SLP-FWC relationships indicates that the physical origins of interannual FWC variability are

quite inconsistent between models. This serves as a cautionary point as scientists seek to understand the sources of future Arctic FWC variability in the climate change runs of coupled climate models.

2.7 Concluding summary

We offer a summary of our main conclusions below.

- Relationships between the AO and FWC vary in strength markedly across CMIP5 models, but on the whole we find that the anticyclonic mode of the AO leads to freshwater accumulation
- We investigate the caveats of using linear response theory to infer response functions in coupled climate models, and establish a Monte Carlo test of significance
- High-pass filtering reduces uncertainty but distorts the SLP-FWC relationship; it can be used to check the confidence of results but not to generate realistic response functions
- In the models where the relationship is robust in both the pre-industrial and historical runs, a one-standard deviation step change to a more negative AO results in a freshwater accumulation of c. 13% of the Arctic FWC reservoir, with an e-folding timescale of c. 7 years
- When convolved with SLP data from atmospheric reanalysis, selected response functions explain 30–80% of the observed freshwater accumulation over 1992–2012 (Figure 2.15)
- Given that the atmospheric component in coupled climate models evolves freely, convolution of model-derived response functions with atmospheric reanalysis is a useful way to evaluate coupled models against observations

Chapter 3

Wind-Driven Export: a 'Sea Ice Conveyor' of Arctic Freshwater?

Abstract

This chapter explores the effect of sea ice export on the liquid freshwater content (FWC) of the Arctic Ocean. Based on analysis from the coupled model HiGEM, we develop a hypothesis, in which wind-driven changes in Arctic liquid freshwater content (FWC) manifest in large part through changes to the export of ice through the Arctic gateways. The hypothesis contends that the upstream divergence associated with sea ice export promotes thermodynamic growth of sea ice within the Arctic, allowing winds to drive not only a lateral flux of solid freshwater from the Arctic but also a flux from the liquid to the solid reservoir. This hypothesis is termed the 'sea ice conveyor'. We test this hypothesis by analysing observationally-derived data, and by performing model perturbation experiments with two models: the MITgcm and CREG025. We find that the association between ice export and liquid FWC changes is affected by the pattern of imposed winds and the dynamic response of sea ice to that pattern.

3.1 Introduction

In chapters 1 and 2 we provide evidence that interannual Arctic liquid freshwater content (FWC) variability is largely driven by variations in atmospheric circulation. We now turn our attention to considering the mechanisms by which such wind-driven changes can occur. Changes to the total liquid FWC must clearly arise from changes to the fluxes that supply or drain the freshwater reservoir. Analysis of the HiGEM model (Figure 1.4) suggests that liquid and solid fluxes of freshwater through the straits are the leading candidates for driving interannual variability in Arctic FWC (see the Concluding Discussion, Section 6.2 for further consideration of this subject). In this chapter, we investigate the solid pathway in detail, using follow-up experiments from the analysis presented in Chapter 1 as motivation. We outline a mechanism by which sea ice export variability might drive liquid freshwater content changes, which we dub the 'sea ice conveyor'.

There are two core elements to this investigation. Namely, a) to question how much FWC signal the mechanism could, in principle, explain amidst the noise of other sources of variability, and b) to test the proposed cause-and-effect links in the mechanism.

The chapter is structured as follows. In Section 3.1.1, we review observational and model-derived estimates of Arctic freshwater fluxes; context for the forthcoming investigation that also informs point (a) above. In Section 3.2.1, we explore the likely physical origin of two of the FWC response functions presented in Chapter 1. Our hypothesis is that a mechanism resembling a sea ice conveyor of freshwater can explain these results. In Section 3.2.2, we formally describe the chain of cause and effect that the 'sea ice conveyor' hypothesis would depend on. We then seek to test the connections in that chain. In Section 3.3, we focus on the link between sea ice area export and divergence—the creation of open water—within the Arctic Ocean during winter time. We compare this to other processes that create open water in winter time. (This line of enquiry leads on to the investigation into the controls on winter ice production in the Kara and Laptev seas in Chapter 4.) In Section 3.4, we directly test the hypothesis in a model setting with two forced climate model experiments. We perturb the

surface winds in two ice-ocean models in order to generate anomalously high sea ice export through Fram Strait. We use two different wind patterns; one represents a local wind forcing over Fram Strait, whereas the other emulates the Arctic Dipole, a pan-Arctic pattern. We describe the models used in Section 3.4.1, the experimental design in Section 3.4.2 and the results in Section 3.4.3. We discuss the implications of our results and consider the potential role of the 'sea ice conveyor' hypothesis in Section 3.5, before offering a concluding summary in Section 3.6.

3.1.1 Fram Strait sea ice export

In the Haine et al. (2015) synthesis of observational records, Arctic solid and liquid freshwater inflows total 8,800±530 km^3/yr during 1980–2000, and 9,400±490 km^3/yr during 2000–2010. Solid and liquid outflows, meanwhile, total 8,700±700 km^3/yr and 8,250±550 km^3/yr, during 1980–2000 and 2000–2010, respectively. The depletion of freshwater by mixing with saltier waters below the Arctic halocline is considered negligible in this budget, on account of the strong stratification and low rates of mixing (Haine et al., 2015). Changes in the total FWC reservoir result from an imbalance between inflows and outflows. In this chapter, we focus on the potential role of Fram Strait sea ice export in causing that imbalance, and on how sustained such an imbalance could be.

Over the last few decades, ice export through the Fram Strait has been roughly an order of magnitude greater than that through the Davis and Bering straits (Haine et al., 2015; Serreze et al., 2006). As such, Fram Strait sea ice export is the only candidate for the mechanism we investigate in this chapter. Fram Strait sea ice export represents approximately 25% of the Arctic solid and liquid freshwater export from the Arctic Ocean to the North Atlantic (Haine et al., 2015; Lique et al., 2009; Serreze et al., 2006), the rest predominantly coming from liquid fluxes through Davis Strait and Fram Strait. The annual sea ice area export through Fram Strait represents c. 10% of the mean Arctic sea ice area (Smedsrud et al., 2017). Because the sea ice fluxed through Fram Strait is thicker than the Arctic average, this equates to c. 14% of the

mean Arctic sea ice volume (Spreen et al., 2020).

The longest observational record permitting some kind of reconstruction of Fram Strait sea ice export comes from ship logbooks and ice charts from the waters off southwest Greenland. Based on this proxy data, Schmith and Hansen (2003) formulate a statistical model to estimate Fram Strait export from 1820–2000. The record appears to reveal decadal and multidecadal variability that the authors suggest is linked to variability in North Atlantic sea surface temperatures. The most obvious long-term features of their record are a decline in ice export between 1900–1940 from a multi-year mean of c. 3,700 km^3/yr to c. 2,500 km^3/yr; coincident in time with the early twentieth century Arctic warming (e.g. Schweiger et al., 2019). This is followed by an increase during 1950–1980 to a multi-year mean of c. 3,200 km^3/yr. In their reconstruction, both the early 1970s Great Salinity Anomaly (GSA) and early 1980s GSA (Belkin et al., 1998; Dickson et al., 1988) can be linked to periods of high ice export. Indeed, with a model forced by atmospheric reanalysis, Ionita et al. (2016) find similarly high ice export immediately preceding the 1970s GSA, which they attribute to atmospheric blocking stalling the export of ice during 1962–1966, ending in a 'flushing' event in the late 1960s. Their model shows similar large-scale multi-year variability in ice export to the Schmith and Hansen (2003) reconstruction (though the mean values of export are quite different).

With the advent of the satellite-based era of Earth observation in 1978, estimates of sea ice concentration and drift have become available on a near continuous basis, at least in the winter season. (Summertime measurements are more error-prone due to difficulty of distinguishing melt ponds from open water.) Since 1990, a maximum of four upwards-looking sonars (ULSs) deployed in Fram Strait have measured the thickness of ice below the sea surface—the sea ice draft (e.g. Melling et al., 1995). Before this, submarine cruises occasionally provided ULS data that was used to estimate export (e.g. Wadhams, 1983). The draft measurements can be converted to sea ice thickness assuming hydrostatic balance and by making assumptions about the relative densities of water and sea ice, and the weight of snow cover.

Spreen et al. (2020) rely on the Fram Strait ULS record to reconstruct sea ice export between

1992 and 2014. Their record, which is within error of previous estimates (Kwok et al., 2004; Spreen et al., 2009; Vinje et al., 1998), shows a gradual decline by 27%/decade over 1992–2014. The average export over this record is 2,400 km^3/yr $\pm$ 640 km^3. During 1990–1996, Vinje et al. (1998) estimate the mean as c. 2,850 km^3/yr, with a maximum of c. 4700 km^3/yr during 1994-1995 and a minimum c. 2,050 km^3/yr 1990–1991. The authors attribute these differences dominantly to atmospheric forcing and to a lesser extent ice thickness. Estimates from Kwok et al. (2004) suggest lower export magnitudes during the 1990s, with a mean of 2,218 km^3/yr. Spreen et al. (2020) show that the decline in the volumetric export of ice roughly mirrors the decline in Arctic sea ice volume; as a share of Arctic sea ice volume, export shows no discernible long-term trend over 1990–2014, at c. 14%/yr.

More recently, wintertime estimates of sea ice volume export have also become available from satellite observations, relying on satellite retrievals of freeboard height, drift speed and concentration. The freeboard is the height of the reflection surface—commonly assumed to be the ice-snow interface (e.g. Laxon et al., 2013; Willatt et al., 2011)—above the sea surface. Ricker et al. (2018) present a timeseries of Fram Strait sea ice volume export during the winter months of Oct–Apr from winter 2010–2011 to 2016–2017, based on CryoSAT-2 thickness estimates and several different drift products from satellite retrievals. Their record has a mean winter outflow of 1,700 km^3, with variations between years of up to 500 km^3. There is a 25% difference between estimates based on different drift products (Ricker et al., 2018).

Indeed, while it is widely accepted that Arctic sea ice drift speeds within the basin have increased over recent decades (Kwok et al., 2013; Olason & Notz, 2014; Rampal et al., 2009; Spreen et al., 2011; J. Zhang et al., 2012), there is not unanimous agreement on the current trend in estimates of sea ice area export through Fram Strait; Smedsrud et al. (2017) show an increase of 6% per decade from 1979 onwards, while Kwok et al. (2013) find no trend. In addition, Spreen et al. (2020) find no trend in ice drift velocities through Fram Strait. Another source of error in comparisons between estimates comes from the range of choices of latitude for flux gates chosen (this matters because significant melting can occur in the eastern part of the Fram Strait;

Ricker et al., 2018; Spreen et al., 2020).

It is widely understood that cross-strait sea-level pressure differences drive sea ice export through Fram Strait (Kwok et al., 2004; Smedsrud et al., 2017; Vinje, 2001). In terms of links to wider scale patterns of atmospheric circulation, evidence for correlations with the Arctic Oscillation or North Atlantic Oscillation appears in some periods (particularly positive phases of the two modes), but not in others (e.g. Hilmer & Jung, 2000; Kwok & Rothrock, 1999; Kwok, 2009; Schmith & Hansen, 2003; Vinje, 2001); other studies suggest stronger links to dipolar patterns of sea-level pressure (SLP) across the Arctic (Fučkar et al., 2016; Smedsrud et al., 2017; Tsukernik et al., 2010; E. Watanabe et al., 2006; Wu et al., 2006).

Climate models generally predict a significant decline in Fram Strait ice export with climate change, in tandem with decreases in ice volume within the Arctic Ocean (e.g. Haine et al., 2015; Jahn & Laiho, 2020; Zanowski et al., 2021). For instance, in the ensemble mean of the seven CMIP6 models studied in the synthesis of Zanowski et al. (2021), the 1980–2000 Fram Strait export average is 1,739 km^3/yr, decreasing to a mean of 625 km^3/yr and 96 km^3/yr during 2080–2100 in the low emissions SSP1-2.6 and high emissions SSP5-8.5 scenarios (O'Neill et al., 2016), respectively. Meanwhile, liquid freshwater fluxes are predicted to exhibit marked increases (Haine et al., 2015; Jahn & Laiho, 2020; Zanowski et al., 2021).

The co-decline of Fram Strait sea ice export and Arctic Ocean sea ice volume suggests that long-term volume decreases are not driven by ice export but by reduced net thermodynamic growth within the basin (e.g. Spreen et al., 2020). However, several studies have found that interannual variations in export explain a sizeable portion of multi-year ice variability (Kwok et al., 1999; Ricker et al., 2018); with the decline in Arctic ice age from the mid-1980s to mid-1990s being attributed to strong cyclonic atmospheric circulation (the positive AO) and export of thick, old sea ice through Fram Strait (Maslanik et al., 2007).

This review of observational and model-based data already makes it clear that the potential for Fram Strait export to influence the Arctic FWC budget was likely greater in the past when

absolute fluxes and variability were higher, and will likely decline further with climate change.

3.2 The ‘sea ice conveyor’ hypothesis

3.2.1 Motivation: HiGEM experiments

In Chapter 1, we use the pre-industrial control run of the coupled climate model HiGEM as a platform for exploring Arctic FWC variability. We see that the liquid FWC variance can be dominantly explained by a combination of liquid freshwater fluxes and (via ice-to-ocean fluxes) sea ice fluxes through the Arctic straits, in roughly equal measure (Figure 1.4). One might ask, then, how these fluxes are implicated in the FWC response functions we present in Section 1.4. Here, we explore the contribution of sea ice fluxes in the FWC responses to the second and third principal components of sea-level pressure variability (SLP); in these modes we see a consistent mechanism at play, whereas the response to the first mode of SLP variability does not appear to activate the same mechanism.

In Figure 3.1 we show the mean step responses—from many estimates (see Section 1.2)—for the different components of the HiGEM liquid freshwater budget to the second and third principal components (PCs) of SLP. These were computed by performing the same multiple lagged regression procedure as described in Section 1.2, but this time with new ‘target’ timeseries (as per Figure 1.1). Instead of just liquid FWC, we include as target timeseries: a) accumulated ice-to-ocean fluxes, and b) accumulated liquid freshwater fluxes. Here, however, we exploit the fact that the response functions are—by definition—linear, and flip the signs of the forcing patterns and responses relative to Section 1.4. We do this in order that we may investigate the response to anomalously high ice export, which is easier to visualise than anomalously low export. We see that, for PC2, the liquid FWC changes (solid line) are explained at first by an increase in the liquid export (dashed line), which causes a commensurate decrease in liquid FWC. However, after about 5 years, a clear trend emerges in the ice-to-ocean (I2O) fluxes (dotted line); one that drains the liquid freshwater reservoir. By around 10 years, this I2O flux

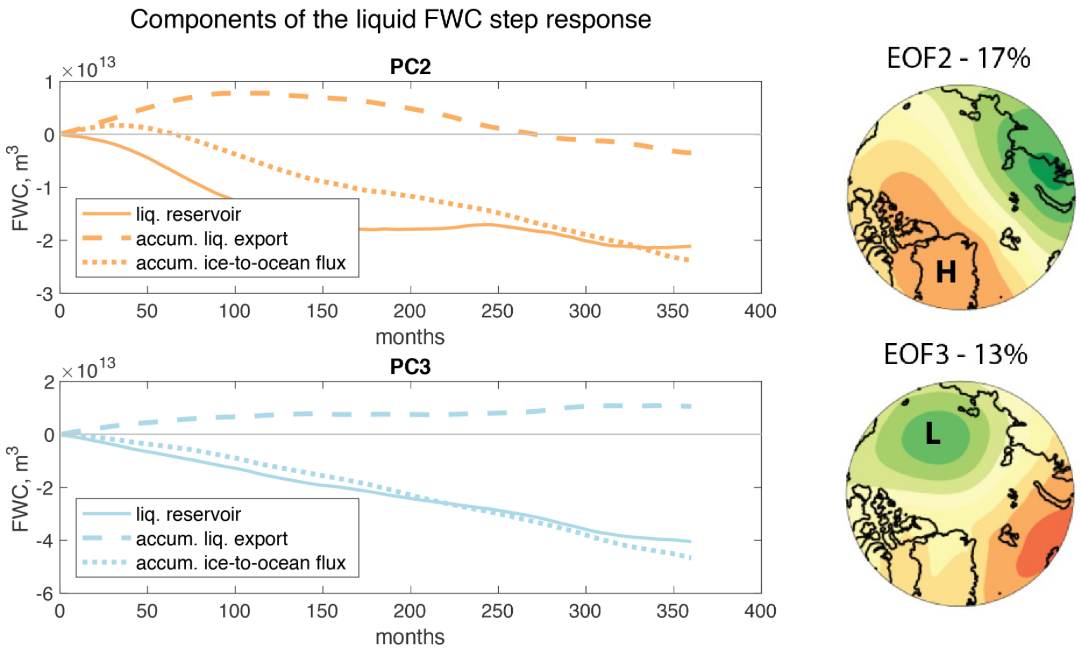


Figure 3.1: Components of the liquid Arctic FWC responses to PC2 (upper panel) and PC3 (lower panel) in coupled climate model HiGEM. Corresponding empirical orthogonal functions (EOFs) of SLP are shown on the right, flipped in sign from those presented in Chapter 1, such that the responses (left) describe freshwater export. 'H' indicates high pressure, while 'L' indicates low pressure. Note that a positive export is a loss of FWC from the Arctic Ocean, while negative ice-to-ocean fluxes are a loss of FWC from ocean to sea ice.

begins to dominate the response of liquid FWC, and continues on a relatively linear trajectory until the end of the response functions. By comparison, the liquid FWF returns to zero or just below after 20 years. A similar response is seen in PC3 (Figure 3.1, lower panel), with an even smaller role for liquid FWF relative to I2O fluxes. The linear trend in accumulated I2O fluxes appears to be what causes the responses to PC3 to continue increasing until the end of the response function (and not level off). The residual in both responses is small to negligible (the FWC changes are well explained by the combination of I2O fluxes and liquid export).

Given that both response functions show a clear role for ice-to-ocean fluxes draining the freshwater reservoir in response to the SLP forcing patterns shown, we must next turn our attention to the sea ice reservoir in order to understand how these fluxes can be sustained: do these fluxes simply build the sea ice volume reservoir over time, or are they balanced by volumetric

export of sea ice?

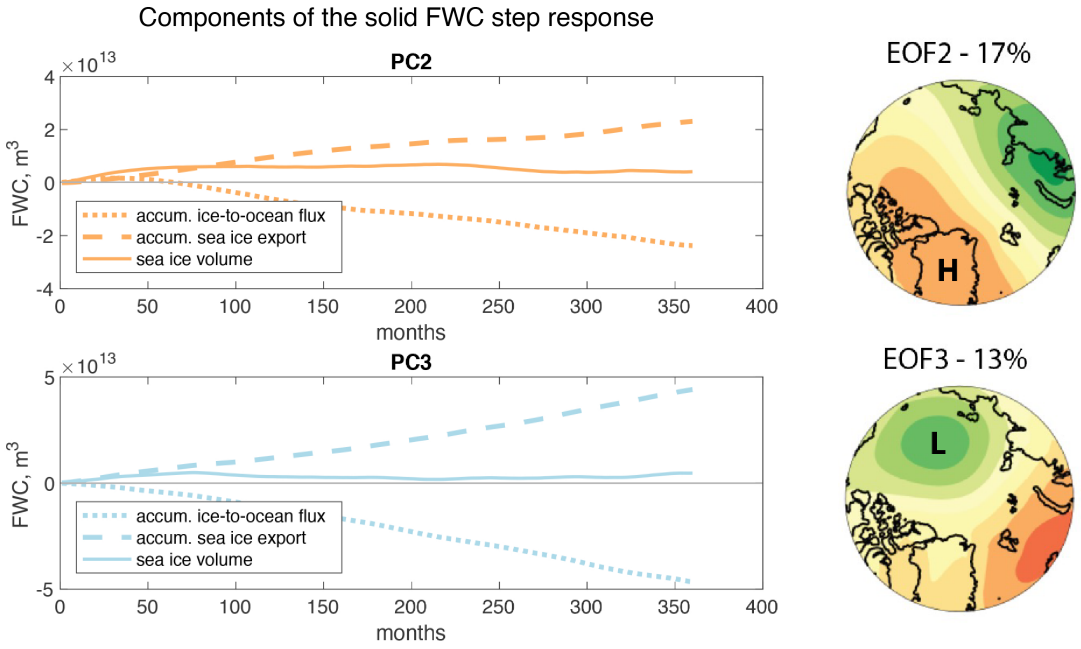


Figure 3.2: Components of the Arctic solid freshwater responses to PC2 (upper panel) and PC3 (lower panel) in coupled climate model HiGEM. Corresponding EOFs of SLP are shown on the right, flipped in sign from those presented in Chapter 1. 'H' indicates high pressure, while 'L' indicates low pressure. Note that a positive export is a loss of sea ice from the Arctic Ocean, while negative ice-to-ocean fluxes drain the liquid freshwater reservoir and add to the solid reservoir.

In Figure 3.2, we show again the responses of ice-to-ocean (I2O) fluxes (dotted line; negative means adding to sea ice volume). This time, however, we plot them in comparison to sea ice volume (solid line) and sea ice export (dashed line; positive means draining sea ice volume). In the responses to both PC2 and PC3, sea ice volume increases gently over the first 5 years of the response, but equilibrates thereafter. The long-term trend in the ice-to-ocean fluxes is balanced by ice export; the balance between the two is responsible for the relative stability of sea ice volume after about 5 years.

The HiGEM results presented abve suggest that wind-driven sea ice fluxes can explain the long-term response of ice-to-ocean fluxes to PC2 and PC3 of SLP (Figure 3.2). This ice-to-ocean flux in turn largely explains the liquid FWC responses for PC2 and PC3 (Figure 3.1). A

credible mechanism for these connections is that sea ice export drives upstream sea ice growth (manifesting as I2O fluxes) due to dynamic thinning, which drains the liquid FWC reservoir. (We describe this in greater detail in Section 3.2.2.) In absence of a credible mechanism by which decreased liquid FWC could drive increased sea ice export (if anything, we would expect the reverse, via the stabilising influence of FWC on sea ice volume), we assume that the causality at play here is that sea ice export drives liquid FWC.

We now briefly consider the shapes of the response functions. The linear trend of the accumulated sea ice fluxes is notable; it is the result of the time accumulation of a relatively constant anomalous flux of sea ice through the Arctic straits. Intuitively it makes sense that a sea ice flux, under constant winds and resupplied by ice growth upstream, should be constant with time. On the other hand, we might expect liquid freshwater fluxes to be dependent on FWC, that is, not time-independent in a forcing scenario. This is because the ocean undergoes decadal adjustment processes (as described in chapters 1 and 2), and the upstream freshwater availability would change over the timescale of the response as FWC is modified.

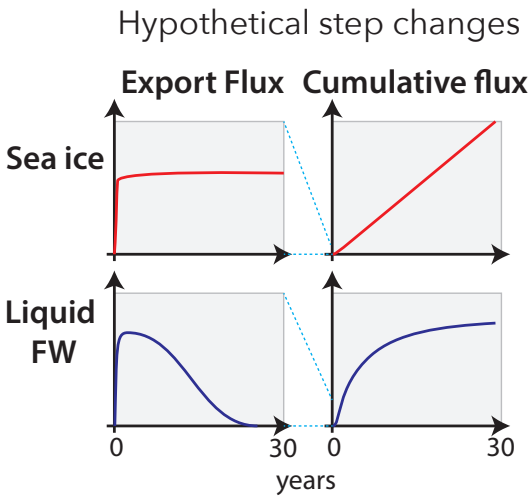


Figure 3.3: Illustration of hypothetical responses of sea ice export (upper row) and liquid freshwater fluxes (bottom row) to a step change in atmospheric forcing. The panels on the left show the time-instantaneous fluxes, whereas the panels on the right show the accumulated fluxes. The difference in scales is schematically indicated by cyan dashed lines.

In general terms then, we might summarise the shapes of the response functions due to these

different fluxes as shown schematically in Figure 3.3. Sea ice export fluxes are assumed in this idealised context to be time-independent in response to winds. Liquid freshwater fluxes, on the other hand are assumed to adjust over time; the cumulative flux (Figure 3.3, bottom right) reaches equilibrium once the anomalous time-instantaneous flux (bottom left) returns to zero. These contributions are clearly relevant in the HiGEM FWC responses and might offer assistance in interpreting the form of liquid FWC step responses in other models—if, that is—the assumptions described above hold.

3.2.2 Proposed mechanism

In the HiGEM response functions shown in figures 3.1 and 3.2, it appears that sea ice export fluxes are driving the long-term wind-driven changes in Arctic FWC. Here, we outline a mechanism that can explain this relationship, which we term the ‘sea ice conveyor’. We illustrate the steps in this mechanism below:

$$\text{Winds} \uparrow \text{Ice export} \uparrow \text{Divergence} \uparrow \text{Ice growth} \downarrow \text{FWC}$$

Winds drive enhanced ice export (which represents a ‘permanent’ removal of freshwater from the Arctic Ocean). Ice export, in turn, causes upstream divergence in the ice pack. By divergence theorem, the area of ice that is exported through Fram Strait must be balanced by an equivalent expansion—or creation—of open water area upstream within the Arctic basin (unless it is balanced by advection of ice through other Arctic straits). This is because ice cracks under tension, rather than thinning in a ductile manner. Thus, area divergence equals open water creation. Thinner ice grows faster than thicker ice (e.g. Bitz & Roe, 2004; Thorndike et al., 1975), and therefore the loss of ice through export might be compensated by faster growth within the basin, restoring the sea ice volume reservoir and depleting liquid FWC. If the flushing winds are sustained, the newly grown ice may be exported, continuing the depletion of FWC. In this manner, the export of wind-blown ice can be considered as part of a wind-driven conveyor-belt system. This is schematically illustrated in Figure 3.4. The same

relationships can be hypothesised to hold in the opposing direction; decreased export should cause less divergence within the Arctic pack ice, and therefore drain the liquid FWC reservoir to a lesser extent, allowing inflows of freshwater to exceed outflows and therefore increasing Arctic FWC. It is important to note that even in this idealised scenario, ice growth is unlikely to perfectly compensate sea ice export at a 1:1 ratio; exported ice often has a high multi-year fraction (Ricker et al., 2018), and is thicker on average than the thickness first year ice can reach in once winter. The thinner the exported ice, the closer the compensation is likely to be. We expand on this point in Section 3.3.

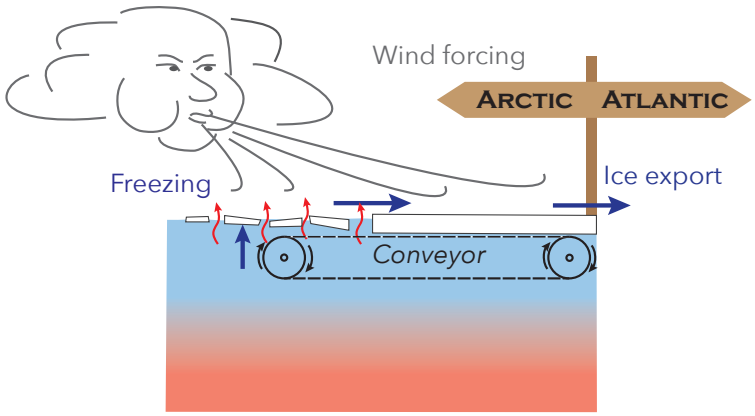


Figure 3.4: Schematic illustrating the 'sea ice conveyor' mechanism: depletion of liquid FWC by freezing and wind-driven ice export to the North Atlantic. Note that there is no 'return flow' included in the conveyor mechanism (i.e. no lower branch).

The potential importance of this mechanism clearly rests on the relative magnitude and variability of sea ice volume fluxes relative to the other freshwater fluxes (as explored in Section 3.1.1). But it also depends on the assumptions underpinning the mechanism. Namely, that thermodynamic ice growth responds to changes in export in order to directly tie sea ice fluxes to freshwater losses, and that this process can be sustained. On long timescales, in absence of forced changes, we expect ice production to balance export. Indeed, this long-term setting is the one in which the mechanism appears to dominate in the HiGEM results. However, the hypothesised mechanism implies predictability not just on these decadal timescales, but also on interannual timescales. Furthermore, winds show variability on long (decadal)

and shorter (interannual) timescales; we also need to understand this mechanism on a shorter timescale such that we can predict its role, if any, under realistic atmospheric forcing. In the remaining sections of this chapter we investigate whether we should expect such predictability from the connections between the steps in the chain of reasoning outlined above, with a focus on annual to interannual timescales. We begin in Section 3.3 with an analysis of the contribution of sea ice export to area divergence within the Arctic.

3.3 Contribution of sea ice export to open water in the Arctic Ocean

In this section, we explore the contribution that Fram Strait sea ice export makes to the expansion of open water within the Arctic Ocean, and compare it to other contributions to open water. These are: a) the open water left available for freezing by the September sea ice area minimum, and b) the accumulated area of wintertime sea ice divergence within the basin that is not compensated by export. Because the proposed link between sea ice export and ice growth is via divergence, we seek to assess here the relative importance of sea ice export in controlling the open water available for freezing. This can help us to assess whether we can expect export to yield predictable interannual variability in sea ice growth—and consequently FWC—via its impact on upstream divergence.

The purpose of this section is to gain a first-order assessment, rather than to undertake an exhaustive analysis. As such, we simplify and use readily available data products where possible.

3.3.1 Materials and methods

We use the Smedsrud et al. (2017) record of monthly Fram Strait area export from 1979–2014, which is available online at https://doi.pangaea.de/10.1594/PANGAEA.868944. This record relies on manually tracked sea ice drift speeds using ASAR WideSwath and Radarsat-2 ScanSAR images captured 3 days apart between 2004–2014. Prior to this, the record uses cross-strait

mean sea-level pressure from observing stations as a proxy for export, corrected for seasonality and biases. The proxy-based record agrees well with the manually tracked timeseries during 2004–2014 (see Smedsrud et al., 2017, for discussion and evaluation of assumptions). We assume, by divergence theorem and the knowledge that—rather than thinning in a ductile manner—ice cracks under tension, that the Fram Strait area export creates an equal area of open water within the Arctic basin.

Summertime melting creates open water that is then available for freezing. We quantify this area by considering the change in sea ice area from September to April. We compute this over two different regions. Firstly, we utilise monthly northern hempisphere sea ice area from the US National Snow and Ice Data Center's Sea Ice Index (Fetterer et al., 2017), available online at https://doi.org/10.7265/N5K072F8. Secondly, we focus solely on the Arctic basin, and utilise gridded sea ice concentration from the NASA Goddard Space Flight Centre (Comiso et al., 1997), accessible at: https://nsidc.org/data/G02202/versions/3. In the Northern Hemisphere case, we compute the area difference between sea ice area in September and April. In the Arctic basin case, we compute the September sea ice area within the Arctic basin (using the same masked region as used in Figure 3.11) and simply use the total area enclosed by the mask as the April value (8.76 million km^2), because this area is always close to 100% ice covered in April. In this way, the Arctic basin winter sea ice area change is entirely driven by the September sea ice area minimum. The reason behind using a Northern Hemisphere record is to have an equivalent comparison with an accessible record of sea ice volume data (described below).

A third source of open water is divergence within the ice pack that is unrelated to export. We calculate sea ice divergence from the NSIDC Polar Pathfinder v4.1 dataset of sea ice motion vectors, gridded at 25×25 km resolution and in weekly means (Tschudi et al., 2019). The data are accessible at https://nsidc.org/data/NSIDC-0116/versions/4. We compute the divergence within the Arctic basin, excluding the Barents Sea and Canadian Arctic Archipelago. We seek the divergence that creates open water within the ice pack, but that does not lead to export or

total area expansion of the sea ice area (after refreezing of open water). To compute this, we first sum the total contributions from the divergent part of the divergence field (i.e. the positive part, which leads to open water creation), and then we subtract the net divergence (which is the export and/or total area expansion). In other words, we can calculate the divergence (div) over elements i, where i includes spatial and temporal axes (x, y, t). The dummy variable i captures all grid cells over which divergence is calculable, throughout the winter. Upon evaluating the divergence, we can define a set, S, of values of i, over which $\mathrm{div}_i > 0$. The compensated divergence is then

$$\text{compensated div} = \sum_{i \in S} \mathrm{div}_i - \sum_{i=1}^{n} \mathrm{div}_i \tag{3.1}$$

The reason we subtract the net divergence is to avoid double-counting; it is already included in the other metrics (overall area change and Fram Strait export, respectively). The part of the divergence we are left with is called the 'compensated' divergence because it is balanced by convergence elsewhere. It is worth noting that this compensated divergence metric is likely to be overestimated to the extent that the sea ice motion data is subject to noise; unlike in mean motion metrics, noise is not smoothed out but counted.

Finally, we utilise Northern Hemisphere sea ice volume from the Pan-Arctic Ice Ocean Modeling and Assimilation System (PIOMAS; Schweiger et al., 2011). PIOMAS is an ice-ocean model that is forced by atmospheric reanalysis, and is constrained through the assimilation of observed information such as sea ice concentration and sea surface temperature. We compute the difference between October and April sea ice volume as the total winter net growth of ice. The data are available at: http://psc.apl.uw.edu/research/projects/arctic-sea-ice-volume-anomaly/data/.

We seek to roughly estimate the contribution of each source of open water makes to the ice volume budget. In order to translate area changes to volume changes in Section 3.3.2, we make some simple assumptions about ice growth through the course of a winter. In the case of the sea ice area change from September to April, we know that the open water in question

is available from the very start of the winter. We assume that an average of 1.5 m of ice grows over the winter season within this area. For export and divergence, on the other hand, we make the simplest possible assumption that the total area made available to open water is accumulated at a steady rate through the winter. We assume that ice grows with the square root of time; a result of integrating the growth rate equation, which goes with inverse thickness of ice (e.g. Petrich & Eicken, 2010). If we assume that the area diverged accumulates linearly with time, we can derive an equation for the volume of sea ice created by integrating through each increment of area in which sea ice grows (to a thickness $H = k\sqrt{t}$), where the time t is limited to the time between the creation of the area increment and until the end of the growth season. The total volume of sea ice created in diverged waters by the end of the season is then equal to

$$\mathrm{vol} = \frac{2}{3} H_{\mathrm{wint}} A \tag{3.2}$$

where A is the total area diverged in one winter and H_{wint} is the thickness it is assumed ice can grow over an entire winter season: 1.5 m in this case. Given this choice of H_{wint} the total volume is simply equal to 1 m $\times$ the total area diverged. For simplicity, we assume that the contribution to sea ice growth from compensated divergence is not offset by the damping effect on growth of convergence elsewhere (we look into this matter in more detail in Chapter 4).

3.3.2 Results and discussion

In Figure 3.5, we compare the Northern Hemisphere sea ice area change (blue line) from September to April, the Arctic Basin sea ice area change (green line), the cumulative area created by divergence within the ice pack in the Arctic basin (magenta line) and the Fram Strait area export (cyan line). The metrics are comparable because they all contribute open water area available for freezing during the winter. In the case of divergence and export, this area is accumulated throughout the winter, whereas in the sea ice area change records it is available from the very beginning of winter and measured relative to the sea ice area at the end of winter. In the Arctic basin case (magenta line), the winter sea ice area change is dictated by the September sea ice area minimum.

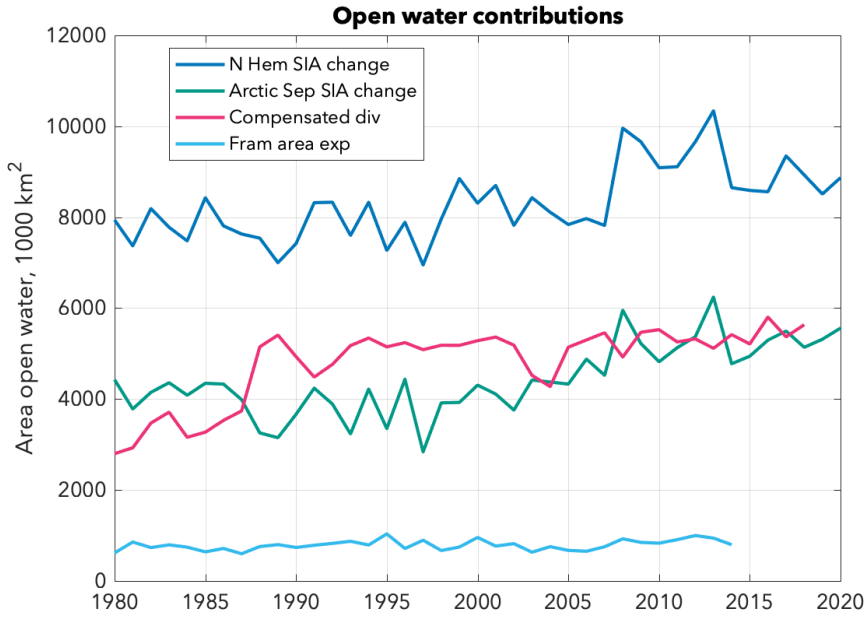


Figure 3.5: Contributions to open water area available for freezing during winter. Winters are labelled such that the winter of 2010/2011 lies at 2011 on the x-axis. Sources of data are described in Section 3.3.1.

The open water area contributed by Fram Strait export (c. 10% of the annual mean sea ice area; Smedsrud et al., 2017) is much smaller than both the winter sea ice area change (whether in the Arctic basin or over the whole hemisphere) and the compensated divergence within the pack ice. Moreover, the interannual variability in the other sources, particularly the winter sea ice area change, is significantly greater than that in the Fram Strait area export record (c. 8 times greater in the case of September ice area). We might expect then, these other sources to exact a stronger influence on sea ice growth during the winter. To assess this, we compare sea ice growth estimates from each contribution with the PIOMAS Northern Hemisphere Oct–April volume change in Figure 3.6. The PIOMAS winter sea ice volume change record shows a strong correspondence with the assumed contribution to sea ice growth from the Northern Hemisphere winter sea ice area change. The two timeseries are highly correlated (R = 0.86), and match closely in the magnitude of interannual variability. By contrast, variability in assumed ice production due to export is small.

Adding the compensated divergence contribution to the contribution from Northern Hemisphere sea ice area change does not improve the fit with PIOMAS data. As such, if the PIOMAS timeseries is a good reflection of Arctic sea ice production, we may fairly assume that we overestimate the contribution to ice growth from compensated divergence here (likely due to noise in the sea ice motion data, Section 3.3.1). However, the PIOMAS record equally may not accurately represent the variability in ice production due to ice divergence.

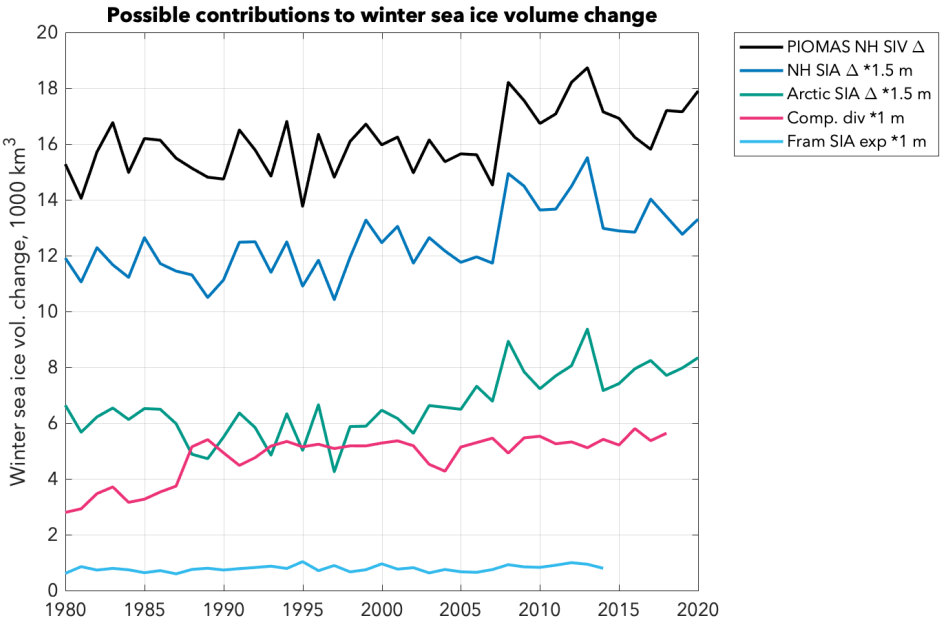


Figure 3.6: Possible contributions to winter sea ice growth from each of the sources of open water in Figure 3.5, compared to the volume change from PIOMAS. Different thickness contributions are assumed based on the reasoning given in Section 3.3.1.

Despite the fact that sea ice export is a relatively small contributor to wintertime open water that is available for freezing, it nonetheless represents—through its volume export—a 'permanent sink' of FWC. The other mechanisms, particularly the September sea ice area minimum, may control winter volume growth to a greater degree, but these volume changes may ultimately only be seasonal. On the other hand, their far larger magnitudes of interannual variability may obfuscate any link between Fram Strait anomalies and anomalous ice growth, suggesting that it is unlikely that the proposed 'sea ice conveyor' mechanism offers predictability

on annual-interannual timescales.

A final detail that must be considered is a possible connection between Fram Strait sea ice export one winter and the following September sea ice minimum. Because it is the September sea ice area minimum that chiefly determines the winter sea ice area change, if wintertime Fram Strait export helps to determine the following September sea ice area, then it would play a role in dictating the following winter sea ice area change. This possible connection might therefore afford some predictability to the proposed mechanism. Williams et al. (2016) identify a correlation of $R = -0.72$ between Fram Strait area export (positive, outwards) and September sea ice area during 1993–2014, similarly Smedsrud et al. (2017) find a correlation of $R = -0.74$ over 2004–2014. Williams et al. (2016) explain the changes in September sea ice area in terms of a 'dynamic preconditioning area' (DPA), which is an area bounded by the position of September sea ice edge and the equivalent contour backtracked to early in the preceding winter (see Fig. 1, Williams et al., 2016). This area is highly correlated with (R =0.79), and similar in magnitude to, the Fram Strait export area (also calculated through backtracking). Williams et al. (2016) link this area to advection of thin sea ice produced on the Eurasian shelves which is easily melted in the summer (e.g. Holland & Stroeve, 2011). Clearly though, the interannual variability of the Fram Strait area export (or the dynamic preconditioning of Williams et al., 2016) alone cannot explain the magnitude of interannual variability in Sep sea ice area in the Arctic basin (as captured by the green line, Figure 3.5). We will return to this puzzle in the discussion at the end of the chapter (Section 3.5).

3.4 Forced Fram Strait export model experiments

We next seek to test the 'sea ice conveyor' hypothesis on an annual-interannual timescale by running model perturbation experiments in which the aim is to trigger additional export via a step change in the imposed winds.

3.4.1 Models used

We use two ice-ocean models. Firstly, we use the Estimating the Climate and Circulation of the Oceans (ECCO) version 4 state estimate configuration (ECCO Consortium et al., 2021; Forget et al., 2015) of the MITgcm (J. Marshall et al., 1997). The ECCO v4 solution is a dynamically consistent ocean state estimate that provides a reasonable fit to oceanographic data, and has no unidentified sources of heat and buoyancy (Forget et al., 2015). The model resolution is nominally 1° on a lat-lon-cap grid and there are 50 vertical levels in the ocean domain. The lat-lon grid makes a conformable transition to an 'Arctic cap' grid north of 57 °N, which is topologically equivalent to a cubed sphere. The vertices of the 'Arctic cap' are placed over land. This improvement from earlier ECCO versions means no decreasing time step is required at higher latitudes. The MITgcm sea ice model is tightly coupled to the ocean model, and is based on a variant of the viscous-plastic (VP) dynamic-thermodynamic sea ice model (J. Zhang & Hibler, 1997) first introduced in Hibler (1979). The sea ice model is described and evaluated in (Losch et al., 2010). Atmospheric forcings are taken from ERA-Interim reanalysis (Dee et al., 2011). The state estimate has no salinity relaxation term, so fluxes of salt across the surface of the ocean only occur upon melting or freezing of sea ice (which has a salinity set to 4 g/kg).

Secondly, we use a regional Arctic-North Atlantic 1/4° model configuration named CREG025 (Dupont et al., 2015). CREG025 is a seamless regional extraction (the "north-fold" discontinuity of the global grid is removed) of the ORCA025 configuration developed jointly by the Drakkar consortium and Mercator-Océan (Barnier et al., 2006; Treguier et al., 2014). It is primarily based on the NEMO 3.6 (Bourdallé-Badie et al., 2019) and LIM 3.5 (Rousset et al., 2015) numerical models for the ocean and sea ice components, respectively. The configuration has a high vertical (75 levels) and horizontal (c. 3–4 km) resolution in the Arctic Ocean. Initial conditions are from the World Ocean Atlas 2009 climatology for temperature and salinity. Initial sea ice thickness and concentration are taken from a long ORCA025 simulation performed by the Drakkar Group, which also provides the conditions (comprising 3-D velocities, temperature and salinity) along the lateral boundaries. The atmospheric forcing comes from the Drakkar

Forcing Set (DFS 5.2, which is an updated version of the dataset from Brodeau et al., 2010). New additions to the model include a tidally-induced mixing parameterisation developed by de Lavergne et al. (2019) and updated Greenland runoff from Gillard et al. (2016). CREG025 has been used in a recent Arctic study (Muilwijk et al., 2019), and its higher resolution counterpart was used by Regan, Lique, Talandier, et al. (2019) to investigate the spin-up of the Beaufort Gyre.

We use two models in order to gain a sense of how model-dependent our results might be. The MITgcm is a widely recognised and user-friendly tool in climate sciences, while the higher resolution CREG025 is well regarded in its representation of the Arctic Ocean.

3.4.2 Experimental design and rationale

We seek to investigate the response of divergence and sea ice growth to anomalous winter sea ice export. Of particular interest are the following questions: does the pattern of divergence due to wind forcing matter for ice production? How is the summer season affected by changes during the winter? The underlying question is: does the 'sea ice conveyor' mechanism afford any predictability in liquid FWC changes due to sea ice export?

In order to trigger this anomalous winter sea ice export, we perturb the wind forcing for a finite period of time. We use two distinct wind perturbation patterns. Firstly, we apply a local Fram Strait pattern, which we define through pointwise regression of monthly-mean 10 m winds from ERA5 reanalysis (Hersbach et al., 2020) onto the Smedsrud et al. (2017) monthly Fram Strait area export estimate from 1979–2014. We utilise the spatial R^2 values to taper the applied wind anomaly, such that the map of regression coefficients determining wind vectors is linearly scaled by the R^2 pattern. Regions where the local winds have a greater explanatory power are thus weighted more heavily than regions where the statistical relationship is weaker. We then normalise the perturbation such that the maximum R^2 value corresponds to a one standard deviation anomaly in export. Given that our pattern is based on statistical relationships from relatively long timeseries from independent datasets (ERA5 reanalysis and

Smedsrud et al. (2017) export), we do not necessarily expect the perturbation to cause an exactly one standard deviation export anomaly when applied in a given year (with a particular climatology) to the two models in question.

This first anomaly pattern, shown in Figure 3.7a, is essentially designed to capture local winds over Fram Strait, and cause upstream divergence on a length scale that reflects the atmospheric scales of correlation between winds and export. At any given time this results in an unrealistic wind pattern with strong upstream divergence and downstream convergence (geostrophic winds are non-divergent; surface winds may show some divergence but not as pronounced as this). However, it can be considered a representation of the cumulative effect of different large-/synoptic scale wind patterns that all have in common strong northerly winds over Fram Strait.

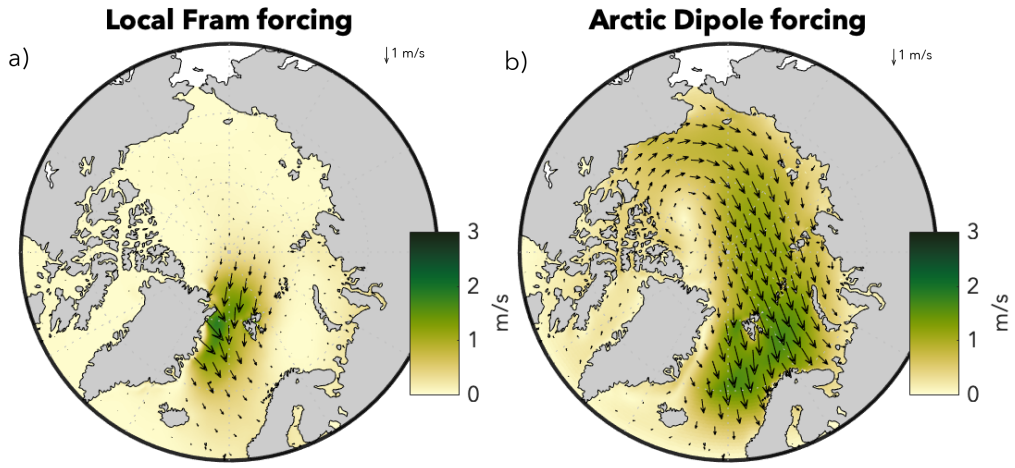


Figure 3.7: Wind perturbations applied. a) Local Fram Strait wind forcing; b) Arctic Dipole pattern. Shown here on the CREG025 grid.

The second anomaly pattern (Figure 3.7b) is designed to represent the Arctic Dipole (Wu et al., 2006). This pattern has been suggested to explain the majority of export variability (e.g. Smedsrud et al., 2017; Tsukernik et al., 2010; E. Watanabe et al., 2006), and may also be enhanced in activity by Arctic sea ice loss (Overland & Wang, 2010). Firstly, we verify that this pattern is suitable. As shown in Figure 3.8, we perform multiple linear regression of the first ten

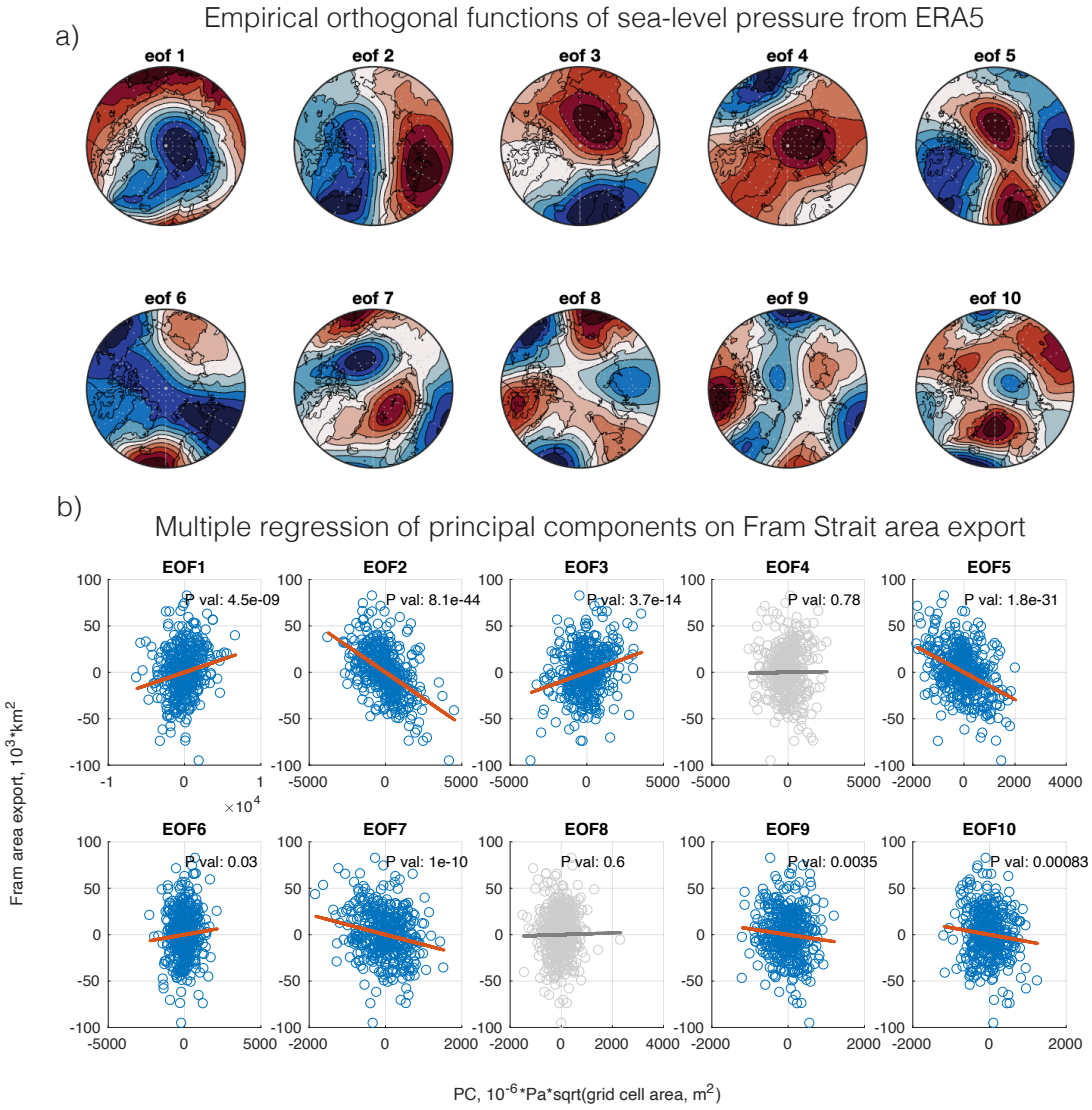


Figure 3.8: a) Empirical orthogonal functions (EOFs) of SLP from ERA5 calculated north of 60N. Red indicates higher pressure, blue indicates lower pressure. b) Regression of principal components (PCs) of SLP on to Fram Strait sea ice area export record of Smedsrud et al. (2017). Polarity of PCs matches that shown in (a). Regressions with a P value of more than 0.05 are greyed out and deemed insignificant at the 95% confidence level. P values for each PC are shown in each subplot. Steepness of regression line (orange) represents the magnitude of the regression coefficient.

principal components (PCs) of mean sea-level pressure from ERA5 against the Smedsrud et al. (2017) area export record. The corresponding empirical orthogonal function (EOF) to each PC is plotted in Figure 3.8a. The second EOF corresponds most closely to the Arctic Dipole (e.g. Cai et al., 2018; Wu et al., 2006). Regression reveals that PC2 does indeed exhibit the strongest relationship to area export. Single linear regression of PC2 against Fram Strait area export yields R^2 = 0.24, higher than any other individual PC. As a whole, the first 25 PCs capture 70% of the variance of Fram Strait area export, and the first ten (as shown here) capture 56%. In Figure 3.8b, we can see that that the PC2 regression has the steepest regression line and the lowest P-value. (Note that the regression lines were fitted based on multiple regression of all PCs simultaneously).

We construct the wind pattern associated with EOF2 of SLP using a composite method. We start by finding the wind field for timesteps with $\pm 1\sigma$ deviations in PC2 from the mean. We subtract the composited values beneath -1σ from those above $+1\sigma$, and rescale such that the overall forcing field has magnitude that corresponds to a $+1\sigma$ pattern of EOF2. We apply a linear smoothing to zero over all longitudes from 70 °N to 60 °N.

We limit our attention to a timescale of around a year, as we seek to investigate the predictability in the proposed 'sea ice conveyor' mechanism on these timescales. A shorter timeframe—compared to the HiGEM response functions—gives us the opportunity to examine mechanisms and regional changes more closely, and is less computationally intensive (given that these are forced model experiments). The timescale is arguably more reflective of atmospheric variability in nature, which is never truly sustained for 30 years, but can show important mean differences in pattern from winter to winter—as well as longer timescales shifts in frequency of a given pattern. As sea ice export is primarily a winter phenomenon, we apply our wind perturbations on 1st December and release them at the end of April. We sustain the simulations until the end of the following winter. We apply the perturbations during the winter of 2009/2010, a low sea ice export year, characterised by a strongly negative AO. The rationale for choosing a low export year is that the additional export should not push the total export

in the perturbed simulation outside of the normal range of export, and thus the results should be representative of anomalies within the normal range of variability.

Our analysis involves comparing a run of the model in which the forcing is abruptly applied, with a control run simulation that covers the same period and is otherwise identical in forcing. We can then find the difference between the two runs; this is the anomaly induced by the perturbation.

In Figure 3.9, we show the mean sea ice thickness in the two models' respective control simulations during March and September of 2010. While there are obvious differences in the small-scale variability of sea ice thickness, likely due to the greater resolution in CREG025 versus the ECCO configuration of the MITgcm, both models show broadly similar patterns of sea ice thickness distribution in both March and September 2010.

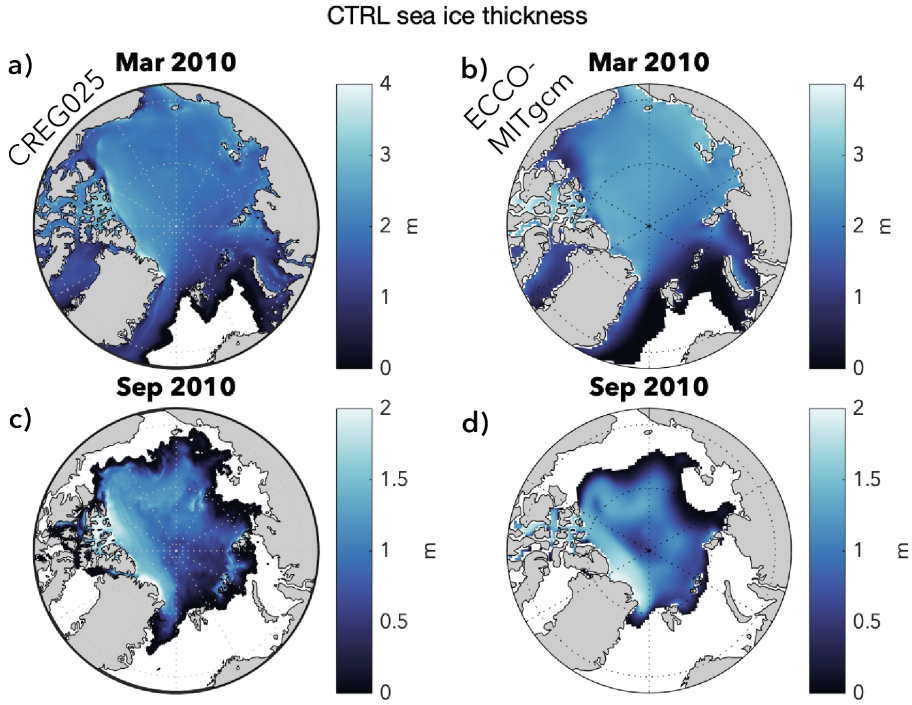


Figure 3.9: Mean sea ice thickness in March and September in the control runs of CREG025 (left) and the ECCO configuration of the MITgcm (right), during the year the experiments are performed.

3.4.3 Results

In this section we explore the results of the perturbation experiments. The main objective is to explore the processes at play in each model, rather than to compare the models.

Local Fram Strait wind forcing

In Figure 3.10 we show the response to the local Fram Strait wind forcing (Figure 3.7a) in the MITgcm and CREG025. Both models show a constant anomalous flux of ice through Fram Strait during the first winter that manifests as a linear response of cumulative export (green line). In Figure 3.10b&d, we compare the sea ice volume export in the perturbed simulation to the control run export in the same winter. Relative to CREG025, the MITgcm shows a greater sea ice export in the winter in question (2009/2010) and a greater anomalous export (though it is within the variability of other winters in the model; not shown). In both models, during the first winter, the exported ice through Fram Strait (green line) is not efficiently compensated by extra upstream sea ice growth—the cumulative freezing anomaly is small in both models (cyan line)—and as a result the total Arctic ice volume (grey line) declines largely in line with the change in the Fram Strait sea ice volume export. The net upstream divergence (purple line, units 1,000 km^2) does not appear to promote net sea ice growth in a spatially-integrated sense over the masked Arctic region.

The measures shown in Figure 3.10 are spatially integrated across the Arctic region. We are, however, also interested in the regional heterogeneity, which can be informative for understanding the dynamics at play. As such, we plot the anomaly patterns in Figure 3.11, still considering only the first winter.

The MITgcm response shows intense convergence in Fram Strait and north of Greenland, reflected in a thick ice anomaly in those regions by April 2010 (Figure 3.11a,c). Upstream, there is broad divergence across the Arctic. Divergence is most intense in the Eurasian Basin north of the Kara Sea. This pattern of divergence leads to 'dynamic thinning'; a widespread thin sea ice thickness (SIT) anomaly reaches over 0.3 m by April in parts of the Eurasian Basin (Fig-

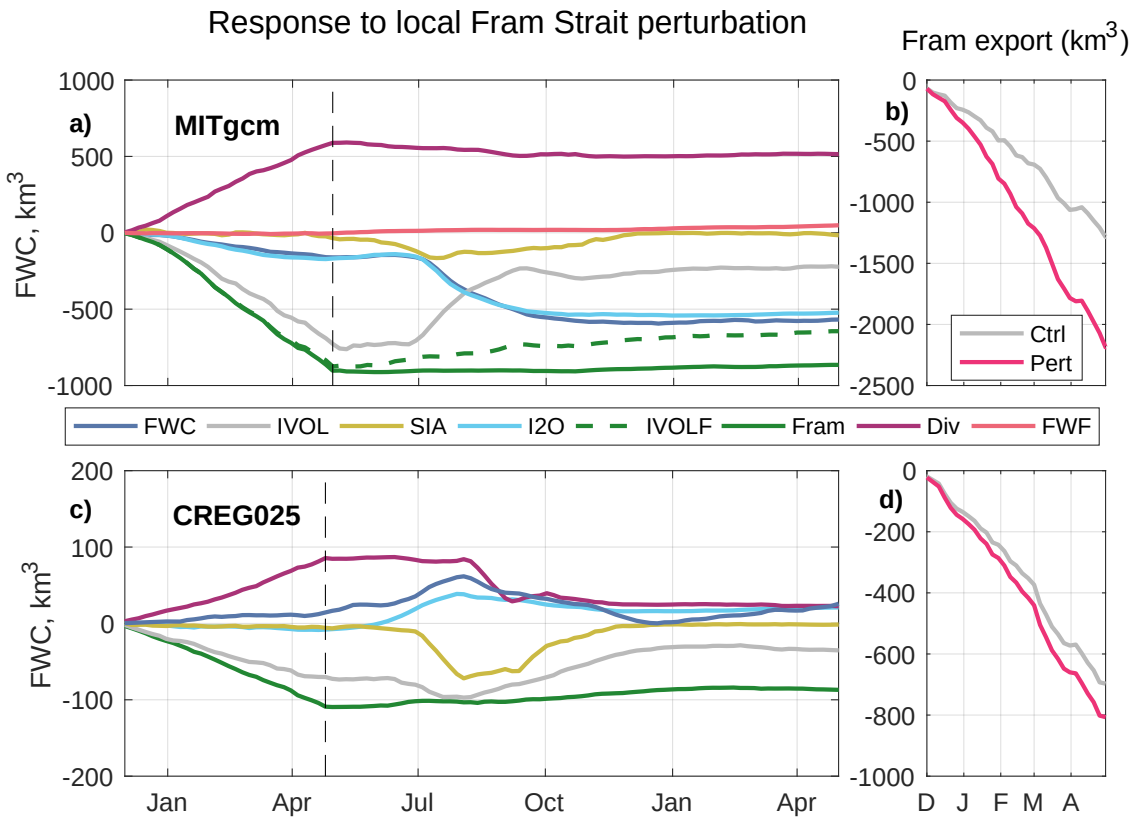


Figure 3.10: Response to local Fram Strait wind forcing in the ECCO configuration of the MITgcm (a,b) and CREG025 (c,d), over the Arctic region shown in Figure 3.11. (Liquid) FWC is relative to a reference salinity of 34.8, IVOL is sea ice volume, SIA is sea ice area in units 1,000 km^2, I2O is cumulative ice-to-ocean freshwater flux due to melting (positive) or freezing (negative), IVOLF is cumulative ice volume flux across all edges of region, Fram is IVOLF only through Fram Strait, Div is cumulative net divergence in units 1,000 km^2, FWF is cumulative freshwater flux across all edges of region. FWF was not available from CREG025. Export from the region is negative. Vertical dashed line in (a) and (c) shows when wind perturbation is switched off. Ice volume fluxes through Fram Strait are compared to control run fluxes in (b) and (d).

ure 3.11c). The thermodynamic response to this pattern of divergence and thinning is a general increase in freezing rates across much of the divergent area, with the notable exceptions of the Kara Sea, away from the coast; the Barents Sea shelf-break; Fram Strait and the Yermak Plateau area north of Svalbard (Figure 3.11e). These are regions potentially more susceptible to heat from Atlantic Waters (e.g. Årthun et al., 2019; Athanase et al., 2020; Polyakov et al., 2020), and it is possible that—in this anomaly—extra-wind driven mixing, or early enhanced

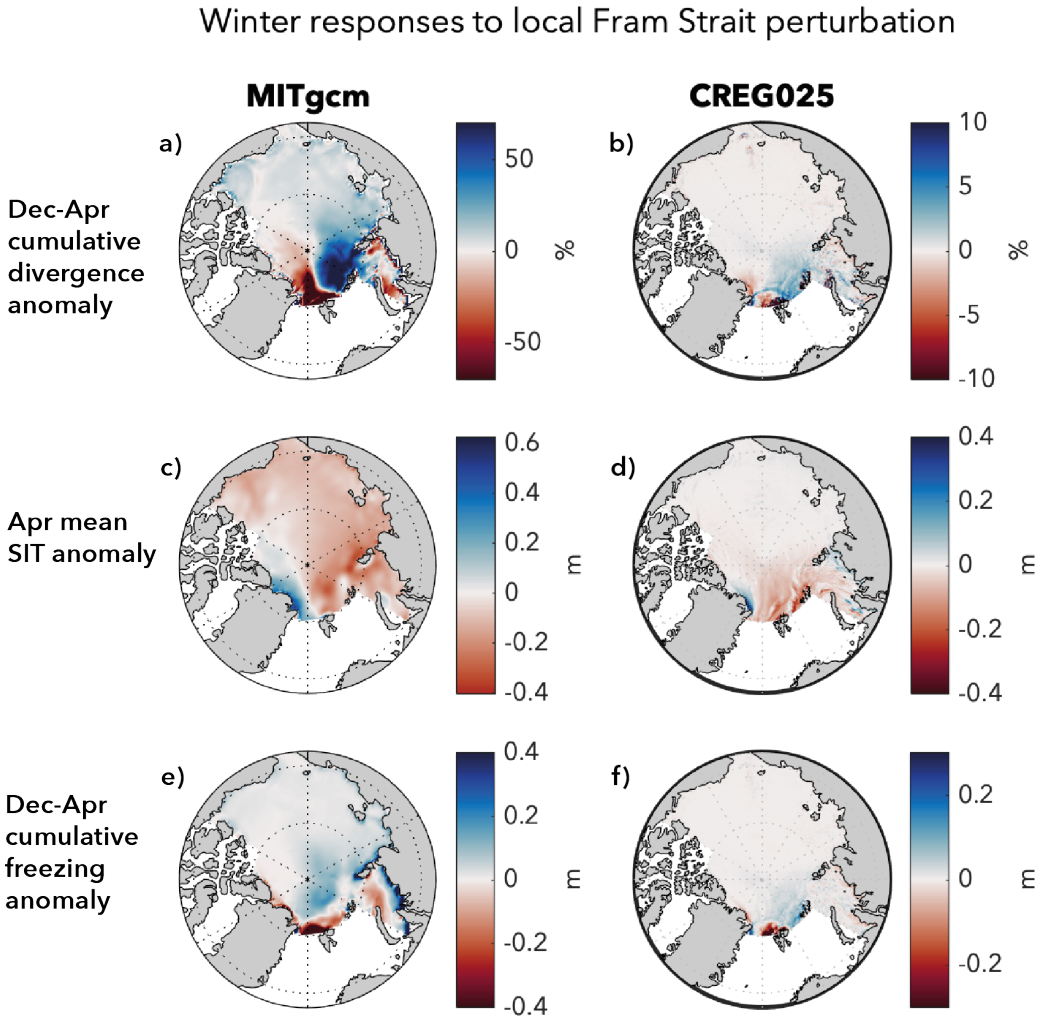


Figure 3.11: Wintertime anomaly maps in the MITgcm and CREG025 to the local Fram Strait perturbation pattern. Variables are integrated over the masked region in order to construct timeseries in Figure 3.10. SIT stands for sea ice thickness.

freezing, promotes higher fluxes of heat in these regions that suppresses ice formation. While freezing is broadly enhanced across the Arctic, particularly in the shallow shelf seas and the central Arctic, there is little change to the net freezing rate across the region. As such, relative to the anomalous ice volume flux, the increase in freezing is small, resulting in a relatively minor FWC decrease during the first winter (Figure 3.10a, blue line). The more significant spatially-integrated impact on FWC occurs during the summer months, when there is anomalously low melting (also evident in the reduction of the negative sea ice volume anomaly). We plot the summertime anomaly maps for ice thickness and ice-to-ocean fluxes (displayed as a

melting anomaly), as well as September sea ice concentration in Figure 3.12. The summertime decrease in FWC is attributable to a reduction in melting in regions where sea ice normally melts (the shelf seas; Figure 3.12c) due to lower than normal sea ice thickness in these regions (Figure 3.12a). In the more central parts of the basin, the thin anomaly appears to drive a slight increase in melting; likely attributable to earlier solar penetration into the upper ocean and the ice-albedo feedback (Perovich et al., 2011; Steele & Dickinson, 2016). The September sea ice concentration shows widespread losses across the basin interior and edges of the marginal seas where the thinning has promoted the retreat of the sea ice edge (Figure 3.12e). In this manner, it is possible to have a September of relatively diminished sea ice area following a summer of relatively low melting, due to preconditioning by widespread dynamic thinning during the winter.

CREG025 shows a more muted and localised response to the perturbation pattern than the MITgcm (Figure 3.11b,d,f). It also shows generally slower sea ice drift and lower sea ice export than the ECCO v4 configuration of the MITgcm in its control state. There is modest convergence north of Greenland, and in parts of Fram Strait. There is fairly widespread divergence in the Nansen Basin, and some subtle divergence in the Kara Sea. The perturbation pattern does not appear to have mobilised the entire Arctic ice pack as it seems to have done in the MITgcm. The sea ice thickness response in April is anti-correlated with the divergence pattern, as expected, with 10–20 cm of thinning widespread in the Nansen Basin and up to 10 cm in the Kara Sea. There is a freezing anomaly in these regions, but it is almost entirely balanced out by the extreme melting anomaly that occurs over the Yermak Plateau, which is within the region we integrate across. Removing this region from the calculations results in a freezing anomaly of 25 km^3 of FWC-equivalent by the end of April. Which choice (of area to integrate over) is the more instructive view for Arctic FWC rests on the nature of the surface currents in the region, and whether the melt-water is advected back into the Arctic Ocean or removed. Regardless, a 25 km^3 anomaly in cumulative freezing is only c. 25% of the anomalous winter Fram Strait export, and a small quantity in the context of freshwater flux variability (Section 3.1.1).

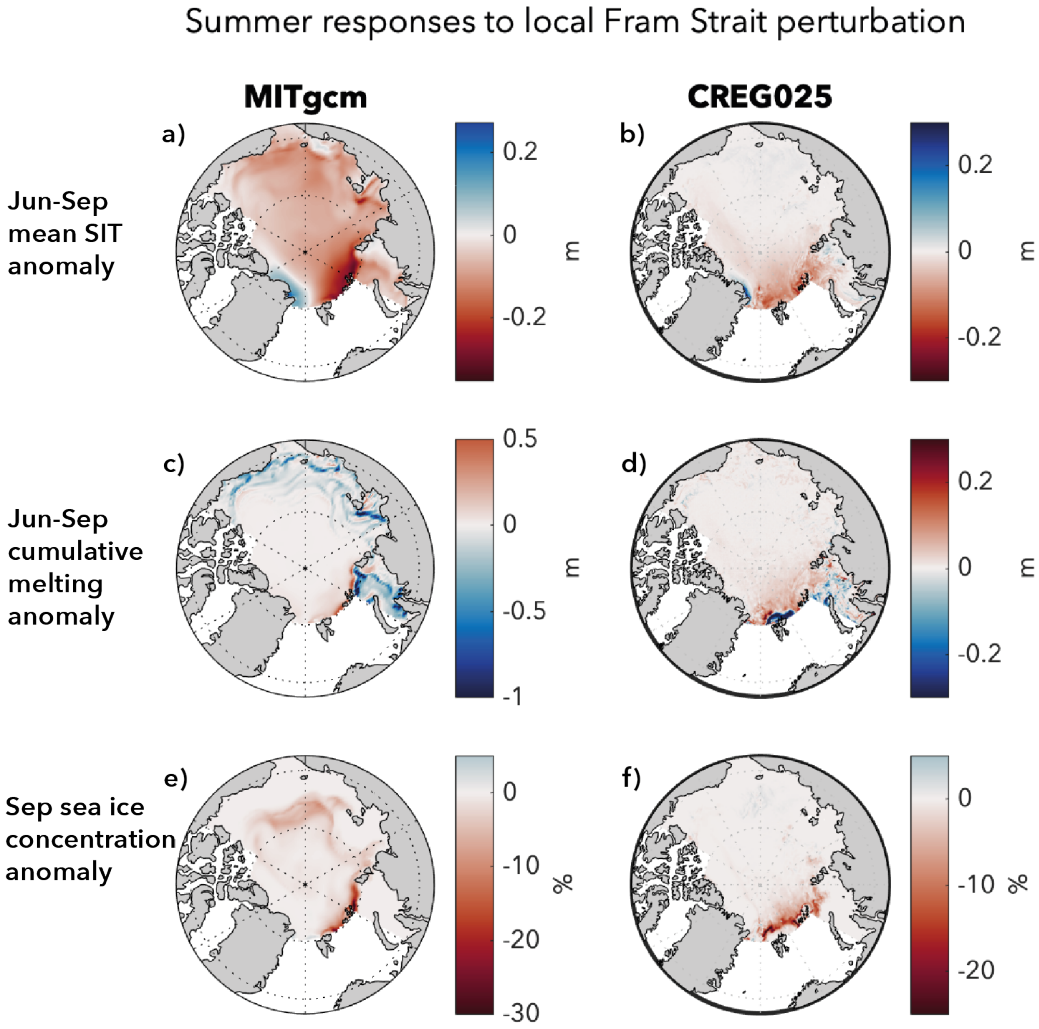


Figure 3.12: Summertime maps of the MITgcm and CREG025 responses to the local Fram Strait perturbation pattern. Ice-to-ocean fluxes are given here in terms of a melting anomaly. For maps (c) and (d), the accumulation of the melting anomaly begins at the start of June (there is no explicit imprint of the prior winter in these maps).

In CREG025, during the months of June and July (after the wind perturbation has been switched off) there is a decrease in sea ice volume that is balanced by a flux of freshwater into the ocean (Figure 3.10c; grey and cyan lines) and acts to increase liquid FWC (blue curve). In Figure 3.12d we can see that this is driven by a widespread melting anomaly of no more than about 10 cm in the Eurasian Basin near the margins of the Barents and Kara seas. This appears to be driven by anomalously thin sea ice in the same region (Figure 3.12b), which may allow earlier solar penetration into the ocean. The sea ice area also declines relative to

the control during July (Figure 3.10c; mustard line), and the September sea ice concentration shows a reduction of order 10% across the aforementioned margin of the Eurasian Basin (Figure 3.12f). On the other hand, there is a reduction in melting immediately north of Svalbard, due to the reduction in sea ice thickness; this is a zone of normally high melting rates due to warm Atlantic inflow. During the late summer and early winter, there is a relative recovery in sea ice volume versus the control run, which appears to be approximately balanced by a reduction in liquid FWC (Figure 3.10c; grey and blue lines).

The two models show rather different responses to the same pattern; the perturbation causes more spatially widespread changes to the sea ice pack and close to an order of magnitude greater sea ice volume export in the MITgcm versus CREG025. This is consistent with the fact that the MITgcm exhibits a more dynamic, faster moving ice pack in its ECCO v4 configuration control run than CREG025 does in its control run. The commonality between the simulations, however, is in the fact that neither the MITgcm nor CREG025 exhibits an efficient compensation of Fram Strait ice export by additional winter freezing—clearly violating the proposed mechanism in the 'conveyor' hypothesis. We next investigate whether this is also the case for a pan-Arctic wind forcing pattern: the Arctic Dipole.

Arctic Dipole wind forcing

In Figure 3.13 we show the net Arctic-wide responses to the Arctic Dipole perturbation (Figure 3.7b) in the MITgcm and CREG025. Both models, again, show a reasonably constant anomalous flux of ice through Fram Strait. The Fram Strait ice export anomaly in CREG025 is almost identical to that in the local Fram Strait experiment, while the anomalous export through Fram Strait is weaker in the MITgcm in this experiment—though this is partially due to a reconfiguration of ice export such that more is exported east of Svalbard into the Barents Sea. The overall ice export is similar to that in the Fram Strait experiment (dashed green line, Figure 3.13a).

In response to this anomalous sea ice export, both models show an increase in winter freezing,

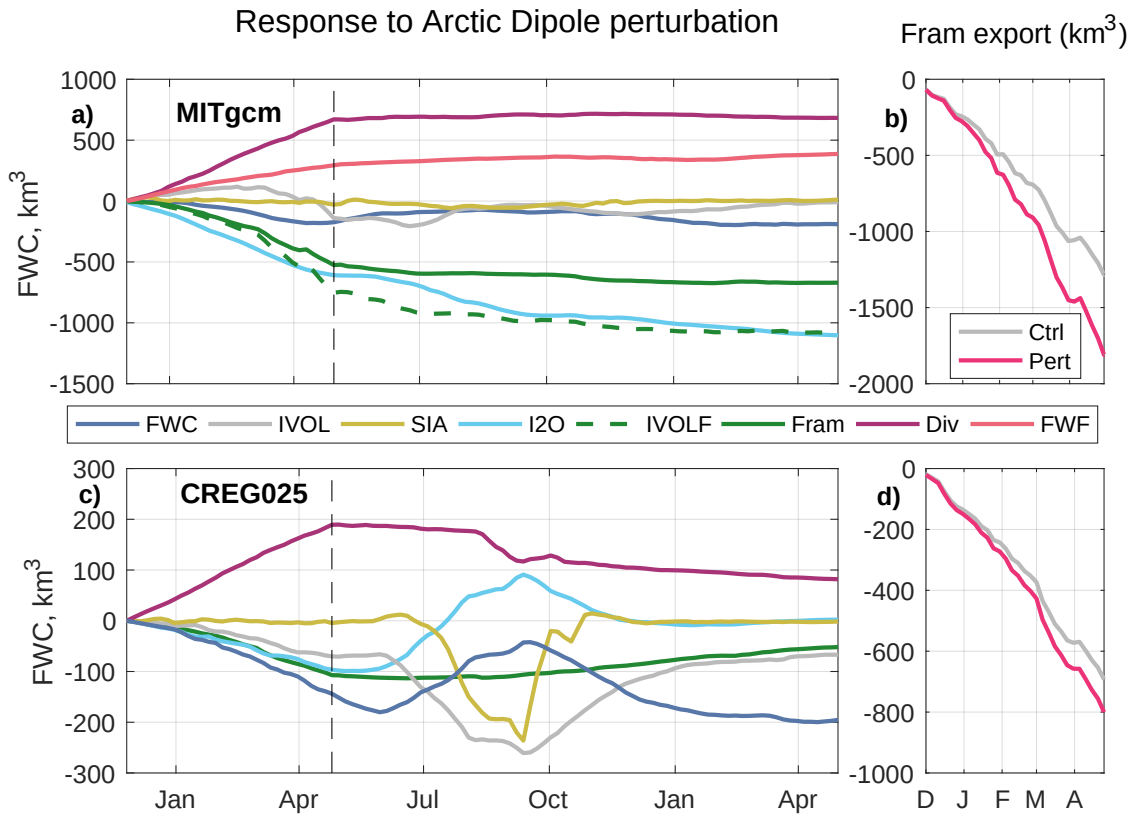


Figure 3.13: Response to Arctic Dipole wind forcing in the ECCO configuration of the MITgcm (a,b) and CREG025 (c,d), over Arctic region shown in Figure 3.11. (Liquid) FWC is relative to a reference salinity of 34.8, IVOL is sea ice volume, SIA is sea ice area in units 1,000 km^2, I2O is cumulative ice-to-ocean freshwater flux due to melting (positive) or freezing (negative), IVOLF is cumulative ice volume fluxes across all edges of region, Fram is IVOLF only through Fram Strait, Div is cumulative net divergence in units 1,000 km^2, FWF is cumulative liquid freshwater flux across all edges of region. FWF was not available from CREG025. Export from the region is negative. Vertical dashed line in (a) and (c) shows when wind perturbation is switched off. Ice volume fluxes through Fram Strait are compared to control run fluxes in (b) and (d).

such that the cumulative ice-to-ocean fluxes (cyan line) closely tracks the Fram Strait export curve (green line). In the MITgcm the tight compensation between export and freezing means that ice volumes remain relatively constant until the onset of the melting season (Figure 3.13a, grey line). The FWC (blue line) in the MITgcm, however, only shows a small downwards trend in response to the extra freezing during the winter, because it is resupplied by anomalous import of freshwater (FWF; pink line). Additional freshwater import through the Bering Strait

is almost entirely responsible for this freshwater import anomaly (not shown). In CREG025, however, the liquid FWC (blue line) does dip downwards, even exceeding the negative ice-to-ocean trend (cyan line). While FWF was not available for this model, we surmise that the difference between the blue and cyan lines must be driven by FWF. Given that the Bering Strait inflow is constrained by imposed boundary conditions in this model, we might infer a role for additional liquid freshwater outflows—likely through Fram Strait—in driving the difference between the blue and cyan curves.

In CREG025, the additional flux of ice through Fram Strait is also compensated by extra sea ice growth, as shown by the tight match between the green and cyan lines in Figure 3.13c. The fact that the sea ice volume does not remain constant, however, indicates that further ice is lost from the Arctic region by transport through Svalbard and Franz Josef Land into the Barents Sea. This is also indicated by the net upstream divergence (purple line), which is twice what it was under the local Fram Strait forcing.

In Figure 3.14, we display the winter anomaly patterns in both models to the Arctic Dipole perturbation. The MITgcm divergence anomaly is mainly divergent around the Arctic Ocean coastal margin from Banks Island in the CAA westwards across to the Kara Sea, with patches of convergence in the East Siberian, Chukchi and Beaufort sea (Figure 3.14a). Sea ice convergence also occurs in the central polar basin, and against the northern coasts of Greenland, Ellesmere Island, Svalbard, and east-facing shores of the Taymyr Peninsula and Severnaya Zemlya. By the end of the winter, in April, the sea ice thickness anomaly field shows clear signs of dynamic alteration, corresponding to this distribution of divergence (Figure 3.14c), and showing a clear dipole between thinning in the shelf seas and thickening in the central Arctic. Winter freezing (Figure 3.14e) is elevated in the dynamically thinned regions, especially along coastlines (Figure 3.14a). Heightened coastal freezing is present along the entire Siberian-Alaskan-Canadian coastal stretch, with the exception of the Taymyr Peninsula, Severnaya Zemlya and Ellesmere Island, which are regions of dynamic thickening. The net Arctic response to the Arctic Dipole forcing shows a clear freezing signal that approximately balances the ice volume lost from the

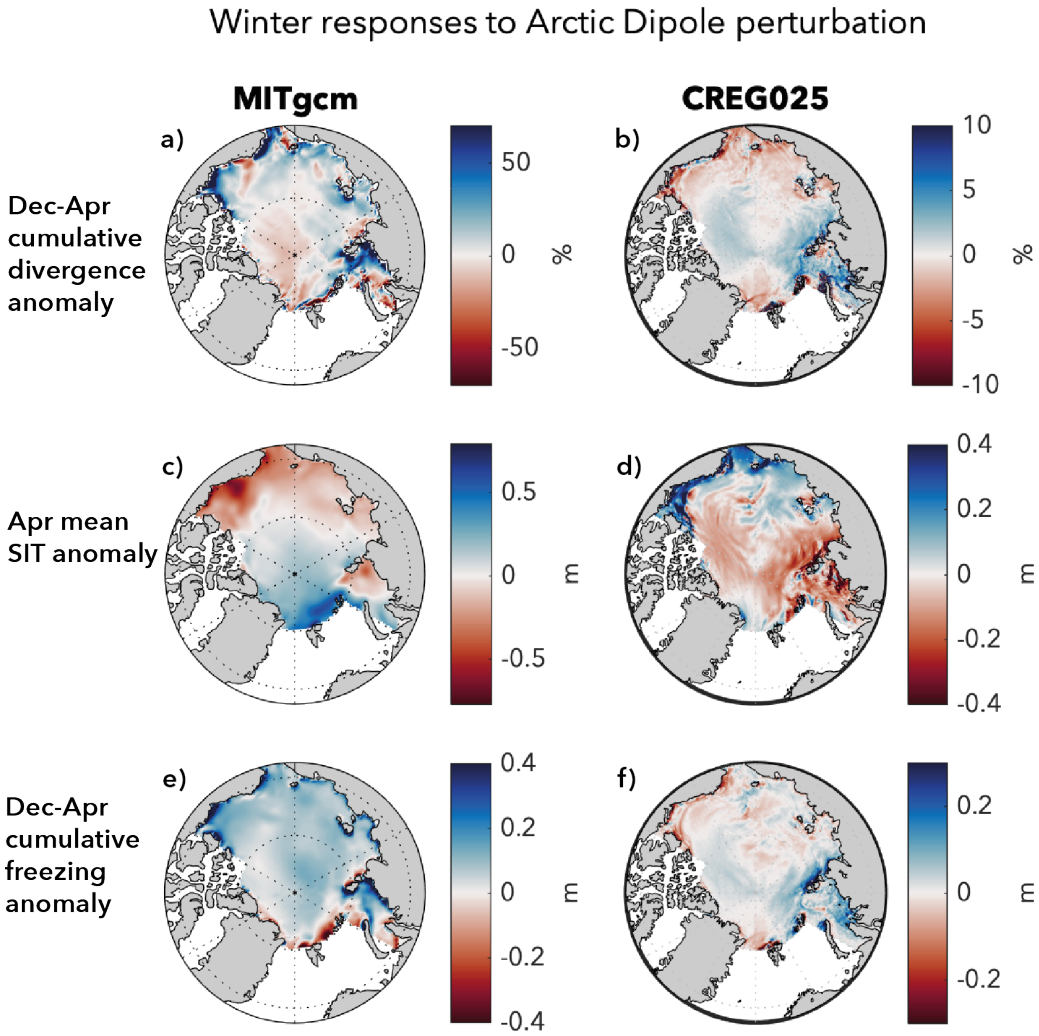


Figure 3.14: Wintertime anomaly maps in the MITgcm and CREG025 to the Arctic Dipole wind perturbation pattern.

Arctic region during the winter months. This stands in contrast to the response to the Fram Strait anomaly perturbation.

As before, the response of sea ice divergence is weaker in CREG025 than the MITgcm (Figure 3.14a,b). CREG025 displays two 'wings' of divergence during the first winter (Figure 3.14b); one in the Amerasian Basin and directly north of the CAA, and one throughout the Kara and Laptev seas and north of Severnaya Zemlya. Unlike in the MITgcm, the Beaufort, Chukchi and East Siberian seas are characterised by sea ice convergence. However, both models show

anomalous sea ice convergence within Fram Strait and directly upstream. CREG025 also shows a clear imprint of dynamic thickness changes on the April-mean SIT anomaly (Figure 3.14d). Thermodynamic sea ice growth (Figure 3.14f) is enhanced in regions of dynamic thinning, and decreased in most regions of convergence and thickening. The strongest freezing anomalies are produced offshore of the north-east facing coasts of Severnaya Zemlya and the Taymyr Peninsula, in the Kara Sea with its coastal polynyas and within the Nansen Basin. The overall dominance of freezing in Figure 3.14f manifests as the Arctic-wide negative response of the cyan I2O line in Figure 3.13c. There is approximately twice as much net divergence in CREG025 under the Arctic Dipole pattern during the first winter than under the local Fram Strait pattern; however the I2O response is more than an order of magnitude greater (compare Figure 3.10c and Figure 3.13c.

Both models are perturbed by the same wind forcing anomaly (Figure 3.7b). Their differing patterns of divergence may be explainable by consideration of a) the distribution of sea ice thickness, strength and mobility at the start of the anomaly, and the manner in which that distribution evolves through the perturbation experiment; b) different angular responses of ice motion to the same winds; c) complex interaction with both the background sea ice circulation and coastal geometry. We do not delve further here into these differences since the main objective is not model intercomparison; however we examine these themes in more detail in Chapter 5.

Next, we examine the evolution of the various anomalies during the first summer. We plot the sea ice thickness and sea ice melting anomaly patterns during the first summer in Figure 3.15.

In the MITgcm, there is markedly reduced melting across the shelf seas. This is a consequence of anomalously thin ice and therefore low freshwater availability (Figure 3.15a&c) in these regions where ice commonly does not survive the summer. The thin anomaly leads to enhanced sea ice retreat in the Amerasian Basin north of the Chukchi and East Siberian seas and a low sea ice area anomaly in this region in September. The total sea ice area (Figure 3.13a, mustard line) is roughly unchanged, however, due to the increased sea ice coverage around Svalbard

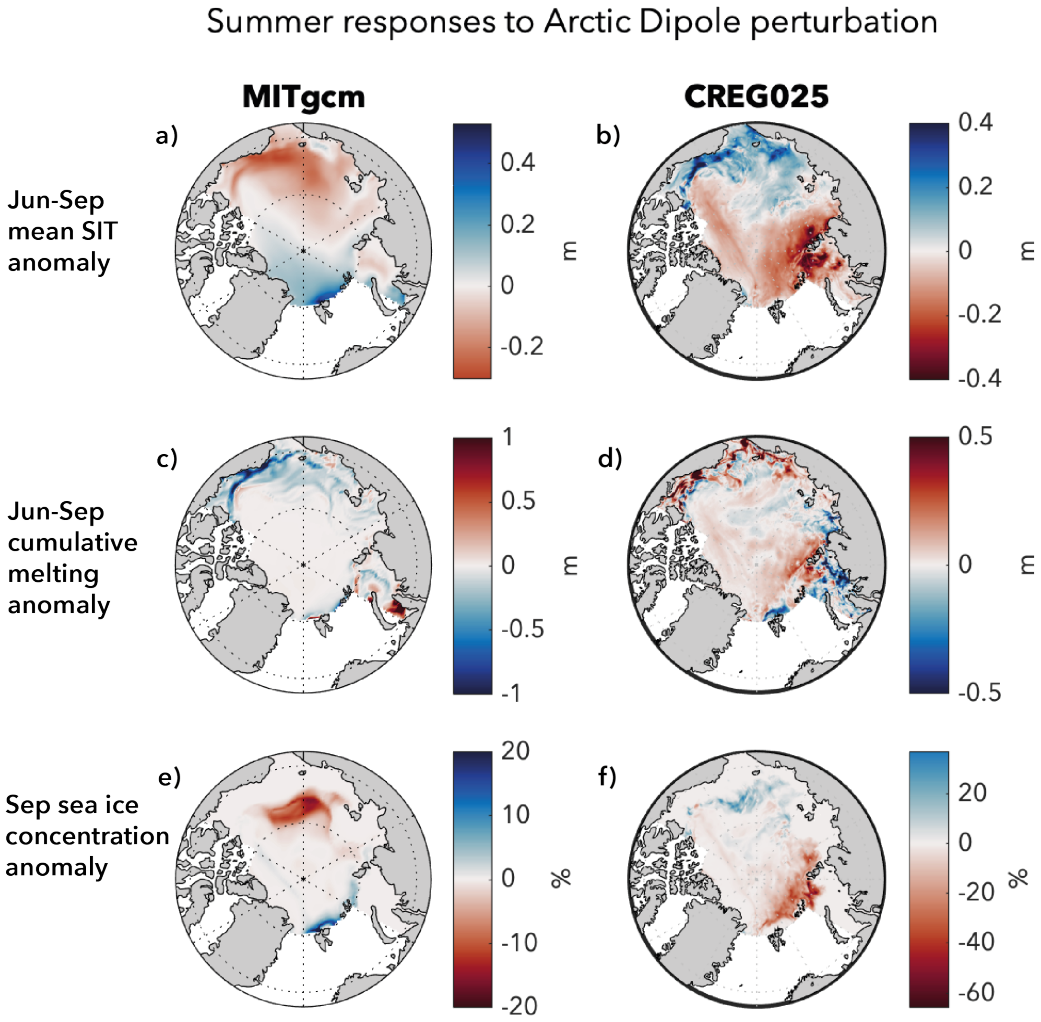


Figure 3.15: Summertime maps of the MITgcm and CREG025 responses to the Arctic Dipole wind forcing perturbation. Ice-to-ocean fluxes are given here in terms of a melting anomaly. For maps (c) and (d), the accumulation of the melting anomaly begins at the start of June (there is no explicit imprint of the prior winter in these maps).

and Franz Josef Land—a consequence of thickening during winter. The downwards curvature of the I2O timeseries (cyan line) over the summer in Figure 3.13a indicates diminishing melting as the summer progresses; consistent with the idea that the anomalously thin ice in the shelf regions is completely melted anomalously early.

The summertime anomaly patterns in CREG025 show similar processes at play (Figure 3.15b,d,f). Where the sea ice in the shelf regions has been dynamically thinned during

the winter, there is reduced overall melting (Kara and Laptev seas), whereas thinning within the basin interior elicits a clear melting anomaly, and indeed a low September sea ice concentration. Similarly, thickening in the Beaufort and Chukchi shelves, and the eastern part of the East Siberian Sea, results in increased melting; more ice is available to melt in this zone that is vulnerable to warm Pacific inflow and relatively high solar insolation (Perovich et al., 2011; Serreze et al., 2016; Timmermans et al., 2017; Woodgate et al., 2010).

The net Arctic-wide effect of this summertime pattern of melting in CREG025 is a significant overall melting anomaly (Figure 3.13c); trends in ice volume and cumulative I2O are tightly balanced (grey and cyan lines), such that by mid-September, freshwater fluxes due to freezing/melting actually represent a net input of freshwater into the ocean since the start of the perturbation. There is also a sharp decrease in sea ice area (mustard line). At the onset of freezing in the second winter, there is a recovery of sea ice area and volume, presumably due to the larger than usual area of open water available for freezing (as found in Section 3.3.2). By December, the net change in I2O over the annual cycle is approximately zero. The overall decrease in ice volume seems to lessen the Fram Strait export in the second winter relative to the control run: the export anomaly slopes back towards zero. The FWC curve (blue line) in Figure 3.13c shows a clear influence of the ice-to-ocean freshwater fluxes (cyan line), but is gradually offset from the cyan line as the anomaly proceeds. As mentioned earlier, we must assume that this is due to the effect of liquid freshwater fluxes through the gateways. In particular, we suggest that a response of increased FWF through the outflow gateways can explain the difference. Bering Strait freshwater fluxes are constrained by the boundary conditions in this model, so we cannot test whether the Bering Strait inflow observed in the MITgcm response is consistent with CREG025.

In summary, in response to the Arctic Dipole perturbation, the MITgcm shows spatially integrated changes in I2O that are consistent with the 'conveyor' hypothesis: ice volume export in the first winter is efficiently compensated by upstream freezing. The reduction in melting during summer acts to further deplete the liquid freshwater reservoir. The effect on FWC is

counteracted, however, by an increase in the liquid freshwater import through Bering Strait (Figure 3.13a, pink line).

CREG025 also shows enhanced freezing during the first winter, which balances Fram Strait ice volume export, but apparently not the total ice export (the overall sea ice volume still declines). The significant summertime melting anomaly, though partially offset by enhanced early second-winter freezing, leads to an I2O anomaly that is essentially zero after a complete annual cycle. This clearly is not in agreement with the 'conveyor' hypothesis, which proposes that enhanced winter export is compensated by enhanced freezing, without confounding summertime effects. An overall response of decreased FWC in CREG025 must be driven by enhanced liquid freshwater outflows. The overall balance of (unresolved) FWF cannot, however, be fully realistic in CREG025 because Bering Strait freshwater fluxes are constrained by boundary conditions. Therefore, for the sake of evaluating the 'conveyor' hypothesis, it is more informative to focus on the ice-to-ocean flux curve.

The difference between the net I2O curves in CREG025 and the MITgcm during summer appears to be driven by the differing response of sea ice divergence and therefore dynamic sea ice thickness. The MITgcm shows significant thinning across the shelf regions, and some dynamic thickening in the Eurasian Basin; whereas CREG025 shows thickening in the Beaufort, Chukchi and East Siberian seas, and thinning across the interior basins. Both models display a generally positive correlation between sea ice thickness at the start of summer and melting on the shelves (with the exception of the East Siberian Sea in the MITgcm), and a generally negative correlation between sea ice thickness and melting in the interior basins. Therefore, while the summertime thermodynamic responses to sea ice thickness between the models are consistent spatially, it is the different dynamic sea ice responses due to the wind forcing that precipitates the stark difference in the overall response of thermodynamic ice-to-ocean fluxes during summer. The September sea ice area is accordingly affected by the patterns of sea ice thinning during winter. Where thinning occurs in the basins, low September sea ice anomalies can be expected. This is only the case in the local Fram Strait experiment for MITgcm,

but occurs in both CREG025 experiments. In the CREG025 experiments, there is a close correspondence between the net divergence (or total sea ice area export) accumulated by the end of the winter and the anomalous sea ice area loss in September (Figure 3.13; compare purple and mustard lines).

3.5 Discussion

In this chapter we explore one possible mechanism for wind-driven Arctic-wide changes in FWC. Based on results from the HiGEM model, the so-called 'sea ice conveyor' hypothesis causally connects anomalous wind-driven sea ice export to the draining of Arctic FWC. The HiGEM results suggest that there is a long-term balance between sea ice export and sea ice growth within the Arctic Ocean, in a pre-industrial climate. By using observational-based evidence and model perturbation experiments, we have investigated the proposed mechanism on shorter timescales, and in the contemporary Arctic—which of course differs in climatology to a pre-industrial scenario. The questions we consider are: how does the potential effect of the proposed mechanism compare to other influences on FWC? How robust—and predictable—are the proposed steps in the mechanism? Are there other, confounding effects that might erode the signal?

We begin this discussion by assuming that the mechanism predictably connects Fram Strait sea ice export to Arctic FWC changes. In this context, how much FWC signal could be generated from interannual Fram Strait sea ice export variability, in the presence of other freshwater fluxes? In the pre-industrial control runs of CMIP5 models, Arctic FWC has a mean standard deviation of 2,950 km^3 (Chapter 2). In order to drive significant interannual variation, Fram Strait ice fluxes should be capable of causing an imbalance between inflows and outflows of that order of magnitude, integrated over a year to a decade (the mean liquid FWC decorrelation timescale in CMIP5 models is just over a decade).

During the 1990s, Fram Strait sea ice export was higher and its variability greater than in

recent years. According to Vinje et al. (1998), the mean volume export during the years 1990–1991 to 19995–1996 was 2,850 km^3/yr, with a standard deviation of 878 km^3/yr and interannual changes as large as 2,000 km^3/yr. The Kwok et al. (2004) record suggests lower fluxes; for the period 1991–1992 to 1998–1999 these authors find a mean of 2,218 km^3 and a standard deviation of 497 km^3/yr. Whichever record is closer to the truth, this is variability that is certainly significant in the FWC budget, especially considering that anomalies may be integrated over several years. Further back in time, the proxy record suggests similarly high, or at times higher, mean ice export fluxes and variability (Ionita et al., 2016; Schmith & Hansen, 2003). In the HiGEM pre-industrial control run, accumulated sea ice export fluxes clearly vary with the same magnitude as FWC, and are correlated with it (R = 0.58); the same may be true for other pre-industrial or historical model runs.

Turning to recent years, the Spreen et al. (2020) 2009–2013 annual mean sea ice export using ULSs is c. 1,700 km^3; the same as the highest of the three winter mean estimates provided by Ricker et al. (2018) over 2010–2017 using satellite-based estimates of thickness and three different drift products. The standard deviation of this Ricker et al. winter export dataset is 236 km^3. There has been, therefore, a marked decline in the mean and variability of sea ice export since the 1990s. Sea ice export anomalies of this magnitude have weaker potential to drive a clear FWC signal. In the future, climate models predict that Fram Strait ice outflow will shrink further, while other freshwater fluxes increase (Haine et al., 2015; Jahn & Laiho, 2020; Zanowski et al., 2021). Fram Strait export will not offer any significant control over Arctic-wide FWC variability in these scenarios.

We next turn to examining the links in the proposed mechanistic chain, to see if a) they are robust, and predictable; and b) whether other mechanisms might dominate the proposed links—through either unrelated or correlated variability. The first link we isolate is the connection between sea ice area export and upstream divergence. As shown in Section 3.3, the magnitude and variability of area diverged due to sea ice export through Fram Strait is on the order 10 $\times$ smaller than the area made available for winter freezing by summertime melting (the

September sea ice minimum). The 'compensated' divergence within the basin also appears to offer a greater area of open water over the course of a winter, though we note our estimate in Figure 3.5 is likely an overestimate.

The notion that the September sea ice area (which dominantly controls the winter sea ice area change) is a more important control on winter ice growth than sea ice export is supported by the high correlation between PIOMAS northern hemisphere ice volume changes and northern hemisphere sea ice area change over the winter (R = 0.86). This PIOMAS ice volume change record is also well-correlated with the sea ice area change within the Arctic basin (R = 0.80). Furthermore, when the sea ice area change timeseries are multiplied by a uniform ice thickness of 1.5 m, they exhibit similar magnitudes of variability to the PIOMAS winter volume changes.

It seems likely, then, that the influence Fram Strait sea ice export has over Arctic-wide winter ice production, a key component in the proposed 'conveyor' mechanism, is an order of magnitude weaker than the influence of variability in September sea ice area. This suggests that the year-to-year predictability in ice production changes from Fram Strait sea ice export should be limited, because the signal is likely swamped by other sources of variability.

An interesting caveat to this is that winter Fram Strait sea ice area export correlates with the following September sea ice extent at around R = -0.73 (Smedsrud et al., 2017; Williams et al., 2016). In observations, Fram Strait area export does not directly provide enough upstream divergence and thin ice within the basin to explain the magnitude of September sea ice area changes (Figure 3.5). However, according to the nature of the wind patterns, Fram Strait ice export may be correlated with additional dynamic thinning upstream, that is not balanced by export, or causes export through gateways other than Fram Strait. We discuss this in more detail in the Concluding Discussion, Section 6.3. In addition, the effect of the dynamic thinning within the basin that is related to Fram Strait ice export may be amplified by enhanced melting associated with the greater prevalence of melt ponds on thin ice (Landy et al., 2015) and earlier penetration of solar radiation into the mixed layer (Perovich et al., 2011; Steele & Dickinson, 2016).

The next link we consider is the connection between sea ice divergence, due to export, and sea ice growth. In an idealised scenario described in Section 3.3.1, we would expect ice production during the winter to be equal to $\frac{2}{3}H_{\text{wint}}A$, where H_{wint} is the sea ice thickness achieved by thermodynamic growth over a whole winter, and A is the total ice export area. For the sake of the discussion, we assume H_{wint} = 1.5 m. As the exported ice through Fram Strait is likely thicker than 1 m, the relationship implies a partial, but incomplete compensation of the anomalous exported volume by sea ice growth.

In Section 3.4, we investigate this proposed compensation in two forced ice-ocean model experiments. Our results suggest that the pattern and magnitude of upstream ice divergence is important for the degree to which ice growth compensates export. In both models, this compensation is very limited under the local Fram Strait wind forcing (Figure 3.10), where upstream sea ice divergence is predominantly accommodated in the Nansen Basin (Figure 3.11). Under the Arctic Dipole forcing the compensation is much more pronounced (Figure 3.13), with significant freezing occurring in both models in the Kara and Laptev seas—though the patterns of divergence and freezing are otherwise quite different.

Next, we ask whether other effects can systematically 'cancel out' the influence wind-driven sea ice export has on ice growth and therefore FWC. In the MITgcm, we see that the Arctic Dipole wind forcing activates a significant liquid freshwater flux (FWF) anomaly through Bering Strait (Figure 3.13a). This is of a similar magnitude to the ice-ocean freshwater exchange anomaly, but is of the opposite sign and therefore effectively nullifies the net impact on FWC. The response of FWF is not caused by the Fram Strait ice export but covaries with it; both are driven by the wind pattern.

In CREG025, the Bering Strait is close to the edge of the regional model domain, and thus Bering Strait FWF is constrained by boundary conditions. It appears, however, that there are increased liquid freshwater outflows in response to the Arctic Dipole wind forcing that serve to drain the FWC reservoir, and therefore act in the same direction as the proposed conveyor mechanism.

The dominant effect that opposes the sea ice conveyor mechanism in the CREG025 simulations is enhanced summertime melting, which returns freshwater to the ocean, and is driven by wintertime dynamic thinning of sea ice in the basin interior, which promotes enhanced melting. Thinner ice may melt more rapidly than thicker ice for several reasons. While neither CREG025 nor the MITgcm in ECCO v4 configuration parameterise melt ponds, we note that thin, first-year ice can accommodate larger fractions of melt ponds during summer (Landy et al., 2015), decreasing the albedo of the ice. Thin ice also gives way to open water sooner, allowing earlier solar heating of the mixed layer, which increases SSTs (Steele & Dickinson, 2016) and drives basal melting of ice (Perovich et al., 2008; Perovich et al., 2011); effects that we expect to be captured in both models. When ice is dynamically thinned in the shelf seas, the result in both models appears to be a reduction in melting, because these are regions where little ice survives the summer, and thus reduced ice thickness equates to reduced freshwater availability.

In the MITgcm, unlike in CREG025, the pattern of dynamic thinning is concentrated in the shelf seas. The result is that over a complete annual cycle, the effect on net sea ice thermodynamic growth is to drain the FWC reservoir. In CREG025, divergence is accommodated within the basin interior, leading to an increased seasonal exchange of freshwater transfer between ice and ocean within the Arctic basin, rather than a net draining of liquid FWC.

In all model experiments presented in Section 3.4, when dynamic thinning occurs in the interior basins, there is anomalously low sea ice area in the summer. In the CREG025 experiments, these September sea ice area anomalies are close in magnitude to the accumulated net divergence (or overall sea ice area export from the Arctic) at the end of winter. This is consistent with the idea that September sea ice area anomalies are related to dynamic preconditioning by divergence the previous winter Williams et al. (2016), however our simulations suggest that this thinning must occur within the basins in order to lead to this correspondence.

In a hypothetical Arctic in which sea ice can survive the summer in the shelf seas, we might expect that wintertime dynamic thinning, independent of where it occurred, should precon-

dition enhanced summer melting and anomalously low September sea ice area. Our results indicate that in the present Arctic, the connection between wintertime dynamic thinning and summertime melting is dependent on the spatial pattern of that wintertime thinning. Given that sea ice export may be associated with a variety of patterns of upstream divergence, there is, therefore, no instantly predictable link between Fram Strait sea ice export and September sea ice extent, or summertime melting, or net annual liquid FWC changes. A corollary of this is that such links in climate model simulations are highly sensitive to the way in which sea velocities are simulated in response to winds. In particular, the turning angle of sea ice under the imposed winds may be important for controlling the resulting divergence patterns.

3.6 Concluding summary

We summarise our main conclusions below:

- In the pre-industrial control run of the coupled climate model HiGEM, variability in sea ice volume export is a significant contributor to liquid FWC changes. Sea ice volume export is also implicated in explaining the response of FWC to the second and third modes of SLP variability in a manner that can be explained by the operation of a so-called 'sea ice conveyor' of freshwater.

- Based on these HiGEM results, we propose a hypothetical 'sea ice conveyor' mechanism. The hypothesis contends that wind-driven sea ice export variability can drive FWC changes via the compensation of exported sea ice by upstream ice growth. The thinner the exported ice, the more complete the compensation, and the more sustained the winds, the more sustained the effect on FWC.

- In observations, sea ice area export correlates with the following September sea ice area minimum, but the actual sea ice area diverged due to export is an order of magnitude smaller than the winter sea ice area change within the Arctic basin. If there is a causal connection in this correlation, it must be through the amplification (by the ice-albedo

positive feedback) of the relatively small anomaly introduced by Fram Strait export, or due to additional upstream dynamic thinning that is not balanced by Fram Strait sea ice area export (or both).

- In our simulations, the patterns of sea ice divergence in response to the imposed winds vary considerably between models. This appears to be the source of the overall differences in the net annual response of thermodynamic sea ice growth, which is affected not only by changes in wintertime freezing but also by changes in summer melting.
- When dynamic thinning occurs in the interior basins of the Arctic, there is elevated summer melting and anomalously low September sea ice area. When thinning occurs in the shelves, there is low summer melting. Both models appear to behave consistently in this thermodynamic response to dynamically driven anomalies in sea ice thickness distribution (while the dynamic responses are very different).
- It is, therefore, not the total sea ice export that determines the net changes in freshwater exchanges between ice and ocean, but the distribution of upstream sea ice divergence. Similarly, links between sea ice export and September sea ice area depend on where the upstream divergence occurs.

Chapter 4

Rise and Fall of Sea Ice Production in Arctic 'Ice Factories'

Abstract

Arctic sea ice extent and thickness is in a well-documented decline, yet winter sea ice production appears to have been increasing. The Kara and Laptev seas are sometimes referred to as the 'ice factories' of the Arctic Ocean, for their outsized role in supplying the Arctic Ocean with first-year sea ice. We analyse winter ice production in this region in the 20th Century and RCP8.5 runs of the Community Earth System Model's Large Ensemble (CESM-LE). An idealised linear model based on internal variability in September sea ice area, sea ice divergence, snow depth, surface ocean temperatures and surface atmospheric temperatures successfully captures forced changes—both the recent increase in ice production and the predicted future decline—and enables attribution of these trends to the different mechanisms at play. We compare the trends of all key metrics in CESM-LE with available reanalyses and satellite products, before using the relationships derived from CESM-LE to reconstruct historical changes in ice production in the Kara and Laptev seas. Our results indicate that ice production has likely already passed a peak. A key factor in this projection is the approach of September sea ice area in the region to zero, meaning there can be no further year-on-year increases in the open water area available for re-freezing.

4.1 Introduction

As Arctic sea ice diminishes, its volume and area budget are increasingly dominated by the seasonal cycle. Winter ice growth becomes critical in restoring the ice pack before the onset of polar day, when sea ice and its snow cover play a crucial role in the radiative balance of the region—and the Earth, more broadly. The presence or otherwise of sea ice is also important during the winter; it limits heat fluxes from the ocean to atmosphere and plays a complex part in the surface momentum balance. Sea ice growth also plays an important hydrographic role via brine rejection during freezing, which densifies surrounding water, and through the redistribution of freshwater that occurs by virtue of sea ice motion acting as a vector between locations of growth and melt (Aagaard & Carmack, 1989; Steele & Flato, 2000).

For these reasons, amongst others, we seek to understand in more detail the physical controls on sea ice production, and understand how it is likely to change in the future. The Kara and Laptev seas, as the principal 'ice factories' of the Arctic (Reimnitz et al., 1994), are a fitting region to focus attention. In this chapter, we analyse sea ice production in the Kara and Laptev seas in a coupled climate model, CESM-LE. Previous work has shown that sea ice production in these regions has been increasing due to negative feedbacks (described in Section 4.1.1), but that this trend is likely to change as atmospheric and oceanic warming overwhelm these negative feedbacks (Petty et al., 2018; Stroeve et al., 2018). However, consistent physical mechanisms that could explain both the increase and proposed decrease in production have not been identified. With reference to the growth rate equation of sea ice, we develop a linear model that can explain both the rise and fall of ice production in the Kara and Laptev seas, as simulated under climate change forcing in the 20th Century and 'high-emissions' RCP8.5 runs of CESM-LE. Further, we investigate the shifting spatial patterns of Arctic sea ice production under anthropogenic climate forcing, which is of key relevance for freshwater distribution and halocline stability.

In Chapter 3, we saw that the Kara and Laptev seas are regions of highly efficient sea ice growth, and that sea ice production in these regions can correlate with Fram Strait export,

at least under wind forcing that resembles the Arctic Dipole. As such, it represents a key region in the potential link between sea ice export and Arctic-wide liquid freshwater changes. Moreover, ice production in the region has great relevance for its role in redistributing liquid freshwater within the Arctic Ocean via the processes of freezing, drift and melt. As such, this chapter develops on chapters 1 and 2, wherein we consider freshwater changes on a pan-Arctic scale.

The chapter is structured as follows. In Section 4.1.1, we introduce the motivating questions behind our analysis of sea ice production in a climate change setting. In Section 4.1.2, we outline the oceanographic setting of the Kara and Laptev (KL) seas, and review the oceanic relevance of ice production in the context of the changing Arctic. In Section 4.2, we introduce the materials used in our study and the manner in which we extract parameters of interest. We explain methodological details that are closely related to our science questions alongside results in Section 4.3, in which we seek to understand changes in the Kara and Laptev ice factories, using insights from a large ensemble of a coupled climate model, CESM-LE, and a variety of satellite and reanalysis data, which we group under the collective term *observation-based estimates* (OEs). In Section 4.4, we discuss the implications of our results, before offering conclusions in Section 4.5.

4.1.1 Arctic sea ice in decline, winter growth in ascendance?

Situated at the interface between ocean and atmosphere, sea ice in the Arctic not only plays a critical role in modulating the connections between these domains, but also strongly influences the Arctic's radiative budget by virtue of its high albedo (particularly of overlying snow). The loss of sea ice is perhaps the starkest indicator of climate change in the Arctic. Because sea ice is an integral part of the Arctic climate system, it participates in these changes in a dynamic manner that varies between the seasons (e.g. Serreze et al., 2009, and as reviewed in the Introduction, Section 0.1).

Sea ice volume is the integral of its thickness over its area. Of these two geometric aspects, our

knowledge of changes in sea ice area are far more complete; total sea ice extent (SIE) has been monitored and reported from passive microwave satellite retrievals since October 1978 (e.g. Cavalieri & Parkinson, 2012; Stroeve et al., 2012). The recent synthesis of Stroeve and Notz (2018) documents a 45.2% loss of September sea ice extent from 1979 to 2018, relative to the 1979–1989 mean, and a 10.6% loss of March sea ice extent. In absolute area, the total ice loss in September is approximately twice as great as that in March; summer losses are compensated to some extent by increases in winter re-freezing. However, this first-year ice is relatively thin and has a low survival rate during the following summer; sea ice thickness/thinness remains the best predictor of summer sea ice extent (Holland & Stroeve, 2011).

Sea ice thickness is determined by both thermodynamics (growth/melt) and dynamics (ridging, rafting and divergence; Hibler, 1979; Thorndike et al., 1975). In-situ records of sea ice thickness are sparse (Lindsay & Schweiger, 2015), but have been augmented by retrievals from NASA's IceSAT between 2003–2008 (e.g Kwok & Rothrock, 2009) and the European Space Agency's CryoSat-2 from 2011 onwards (Wingham et al., 2006). These satellites use radar altimetry to measure freeboard: the height of the sea backscatter horizon (commonly assumed to be the sea ice-snow interface) above sea level. Assumptions about the properties of overlying snow and the ice itself are required to convert these retrievals to sea ice thickness. Several sea ice thickness products derived from CryoSat-2 exist (e.g. Kurtz & Harbeck, 2017; Ricker, Hendricks, Kaleschke, et al., 2017; Tilling et al., 2018), though significant uncertainties remain in some of the underlying assumptions (e.g. Landy et al., 2020; R. D. Mallett et al., 2020; R. D. Mallett et al., 2021, see also the Concluding Discussion, Section 6.7.1). Using these satellite retrievals, Kwok (2018) shows that the rate of volumetric sea ice loss from the Arctic Ocean is greater between consecutive summers than winters (Figure 4.1). This is a result also seen in estimates of sea ice volume from PIOMAS, the Pan-Arctic Ice Ocean Modeling and Assimilation System (Schweiger et al., 2019). PIOMAS is a model-based sea ice reconstruction that is forced by atmospheric reanalysis and assimilates sea ice observations (Schweiger et al., 2011; J. Zhang et al., 2000), and offers sea ice thickness and volume estimates and uncertainties that are of similar magnitude to those currently available from satellite (e.g. Labe et al., 2018; Schweiger

et al., 2011).

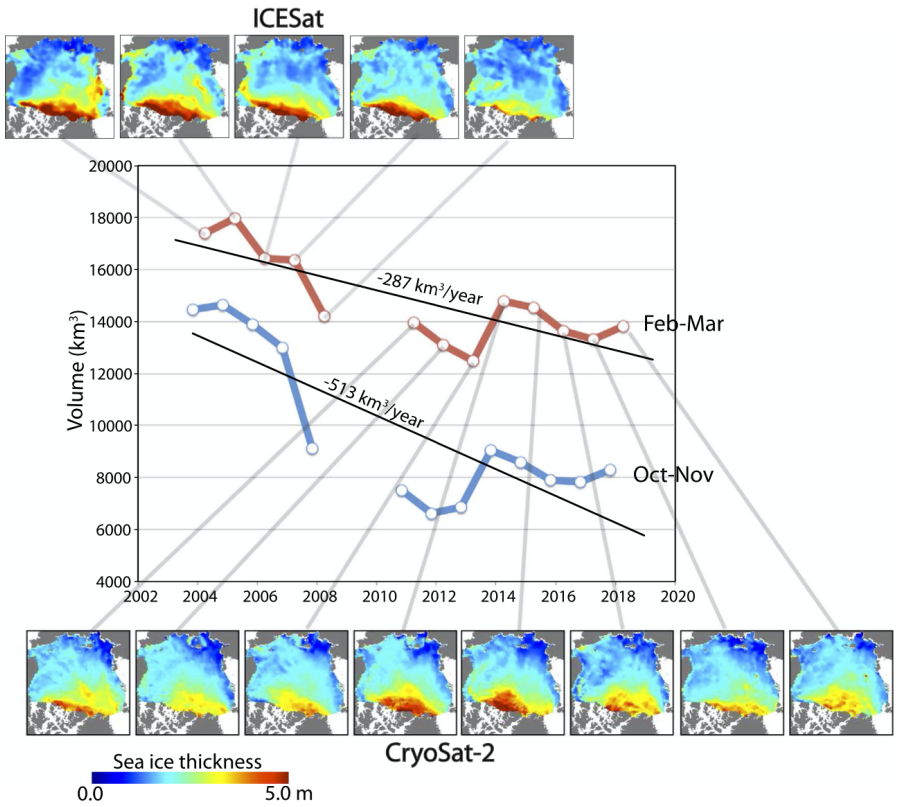


Figure 4.1: Arctic sea ice volume trends from satellite retrievals. Figure from Kwok (2018)

There is an apparent contradiction in the occurrence of rising winter sea ice growth in concert with Arctic Amplification, which is intensified in the autumn and winter seasons (e.g. Screen & Simmonds, 2010, see the Introduction, Section 0.1 for a review of Arctic Amplification). However, the two phenomena can be understood to be integrally linked. During the autumn and winter, heat sequestered in the Arctic Ocean during the summer is released into the atmosphere through cooling prior to and during sea ice growth. Sea ice thinner than 0.4 m thick permits heat fluxes one to two orders of magnitude larger than that from perennial ice (Maykut, 1978); winter thinning is an essential part of Arctic Amplification, to which Lang et al. (2017) attribute 1 °C of surface air temperature warming per decade. This surface warming may be partially offset by increased long-wave emission, and reduced atmospheric heat transport from lower latitudes (Tietsche et al., 2011). However, the atmospheric structure of winter

Arctic warming is bottom-intensified due to the predominantly stable atmospheric stratification. As a consequence, long-wave emission is far less efficient than at lower latitudes where convective mixing communicates surface warming to the top of the atmosphere—this is the *lapse-rate feedback* (e.g. Bintanja et al., 2011; Payne et al., 2015; Pithan & Mauritsen, 2014).

Sea ice growth is inextricably linked to these heat fluxes from the ocean to the atmosphere in the Arctic; growth rate is determined by the energy balance at the lower boundary of the ice. Thin ice also grows much faster than its thicker counterparts (e.g. Thorndike et al., 1975). This thickness-growth relationship constitutes a well-known negative feedback in Arctic sea ice loss (Bitz & Roe, 2004; Stroeve et al., 2018). There are other effects, however, that act to promote sea ice growth in a warming Arctic. For one thing, ice that is formed later in the season is more likely to avoid the damping effects of snow—an effective insulator—on growth rate (Merkouriadi et al., 2017; Notz, 2009). Moreover, snow melt during summer preconditions more rapid growth at the beginning of the freezing season due to the loss of this insulating snow cover (Bigdeli et al., 2020). Additionally, thinner sea ice is weaker and more mobile, leading to an increase in wind-driven sea ice divergence (Kwok et al., 2013; Rampal et al., 2009; Spreen et al., 2011) which has long been recognised to promote winter freezing (Hibler, 1979).

These negative feedbacks provide stability to the Arctic sea ice system, such that rapid 'tipping-point' losses for summer sea ice area are unlikely (Eisenman & Wettlaufer, 2009; Notz, 2009; Tietsche et al., 2011).

Recent warm winters such as 2015/2016 and 2016/2017, in which growth suppression and even winter melting were observed (Boisvert et al., 2016; Graham et al., 2017; Ricker, Hendricks, Girard-Ardhuin, et al., 2017; Stroeve et al., 2018), have raised questions over whether these negative feedbacks may be weakening or becoming overwhelmed by warming. Based on simulations with the sea ice model CICE, Stroeve et al. (2018) suggest that the thermodynamic growth during the winter 2016/2017 was 11–13 cm down on the 2011–2017 mean, with the overall positive trend in winter ice growth from 1985 ending in 2012; ice growth then weak-

ens until the end of the model run in 2018. Using the same coupled climate model we use here (CESM-LE), Petty et al. (2018) identify that the positive correlation between temperature and winter growth weakens through the mid-century under the RCP8.5 emissions scenario, eventually becoming a negative relationship—indicative of warming overwhelming the negative feedbacks on sea ice loss.

Attention on the decline of winter sea ice production is also motivated by the question of whether—in a steadily warming world—after the Arctic Ocean has become seasonally free of ice, the transition to an annually ice-free ocean would be gradual or sudden. Unlike for summer sea ice loss, coupled Earth system models generally predict a rapid loss of winter sea ice (Bathiany et al., 2016).

Observational evidence of increasing winter sea ice production, and model-based suggestions of an imminent or recently-begun decline, motivate the questions: when will this transition between rising and falling ice production begin? What physical indicators may help us to predict when we are at this turning point? Building on the recent work of Petty et al. (2018) and Stroeve et al. (2018), can we understand the changes in ice production in terms of underlying physical characteristics and processes? We seek here to answer these questions with a regional focus on the Kara and Laptev seas, a region long recognised as the 'ice factory' of the Arctic Ocean (e.g. Reimnitz et al., 1994).

4.1.2 The Kara and Laptev seas

Oceanic setting

The Kara and Laptev seas receive 50% of the freshwater runoff to the Arctic Ocean (Gordeev et al., 1996). The Arctic Ocean itself, though only 1% of the global ocean volume, receives 10% of global river discharge (Aagaard & Carmack, 1989; McClelland et al., 2006). Topologically, the Kara and Laptev seas are classified as interior shelves of the Arctic (Carmack & Wassmann, 2006), yet they nonetheless represent hydrographically complex zones, featuring narrow straits and troughs, extreme seasonal modification, and strong gradients in surface wa-

ter properties from the interaction of several water masses: Siberian river water, saline waters formed in polynyas and Atlantic waters along the shelfbreak (Janout et al., 2017; Osadchiev et al., 2020; Tarasenko et al., 2021).

Riverine inputs into the Eurasian shelf seas increased by 7% from 1936 to 1999 (Peterson et al., 2002), a trend that has continued; in the last 15 years, Eurasian river discharge exceeded the 1980–1989 mean in all but two years (Holmes et al., 2018). Climate models suggest that river runoff to the Arctic will continue to increase in a warming world (e.g. Jahn & Laiho, 2020; Zanowski et al., 2021), with mixed effects expected for sea ice. On the one hand, riverine input stabilises stratification, thus favouring ice growth (Nummelin et al., 2016). On the other, riverine heat delivery during summer months—with inflow temperatures of c. 15 °C (Whitefield et al., 2015)—can have a significant impact in shelf regions by delaying the onset of freezing (Carmack et al., 2015).

'Ice factories' of the Arctic

Climatological wind patterns propel sea ice away from the Siberian coast of the Kara and Laptev seas, creating perennial flaw leads or flaw polynyas (the terms are often used interchangeably), where open water separates land-fast ice from mobile pack ice (e.g. Morales Maqueda et al., 2004). The Laptev Sea flaw lead, hundreds of kilometres long, provides a good habitat for walrus and supports one of the richest benthic communities in the Arctic Ocean (Reimnitz et al., 1994). Mean sea ice motion vectors in the Arctic Ocean from satellite retrievals—as shown in Figure 4.2—reveal that the Kara and Laptev seas are regions of persistent sea ice divergence.

Sea ice forms rapidly in the open water created in polynyas and leads, where heat fluxes to the atmosphere are two orders of magnitude greater than over sea ice more than 0.4 m thick (Alam & Curry, 1997; Maykut, 1978). Estimates of sea ice production in the Kara and Laptev from models and observations vary. Areal estimates of mean production from the Laptev Sea are 373,000 km^2/yr (Rigor & Colony, 1997, during 1979—1993), and 483,000 km^2/yr (Alexandrov et

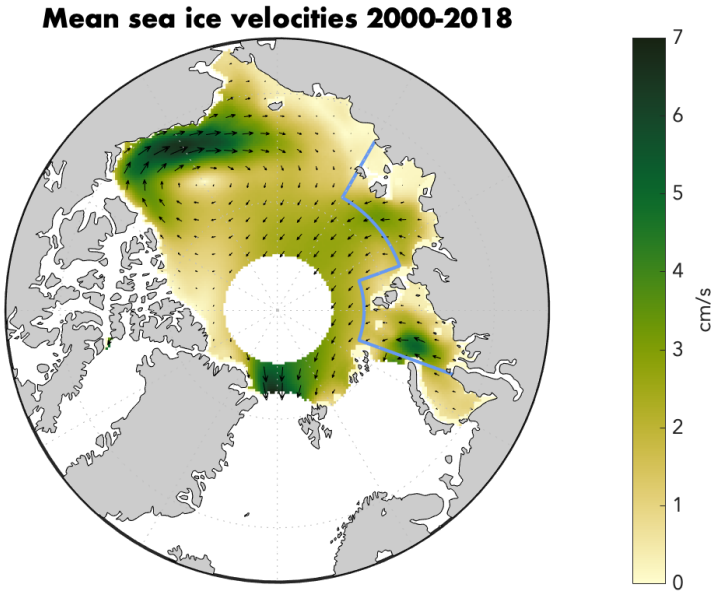


Figure 4.2: Mean Arctic sea ice velocities 2000–2018 from the Polar Pathfinder sea ice drift product (Tschudi et al., 2019), which is based on satellite retrievals. Kara-Laptev study region outlined by blue box.

al., 2000, during 1979–1995). Rigor and Colony (1997) estimate that a mean of 256,000 km^2/yr survived the summer melt during 1979—1993, ultimately comprising 20% of the ice area exported through Fram Strait. In terms of sea ice volume produced per unit area, mean winter growth estimates are 5–8 m/yr in the Kara and Laptev shelves (Pemberton et al., 2014, using an ice-ocean model forced by reanalysis), up to 5 m/yr (Tamura & Ohshima, 2011, using thin ice thickness estimates from SSM/I satellite retrievals), 3–4 m (Dmitrenko et al., 2005, based on hydrographic data), and up to 21 m in the polynyas offshore of Severnaya Zemlya, which lies between the two seas (S. Martin & Cavalieri, 1989, from observational heat flux estimates).

Sea ice production in the Kara and Laptev seas is affected by patterns of atmospheric circulation and resulting patterns of sea ice drift. The cyclonic mode of the Arctic Oscillation, AO+, increases the advection of ice away from the Siberian coasts, filling more of the Arctic basin with thin sea ice (Armitage et al., 2018; Rigor et al., 2002). Most CMIP5 models show an increasing positive AO+ trend during the 21st century under RCP8.5 (Cai et al., 2018). Historically, the

winter AO+ has been correlated with the following September sea ice extent (Rigor et al., 2002; Williams et al., 2016). This observation has been attributed to the larger expanse of first year ice created under the AO+ versus the AO-, which can melt away to open ocean more rapidly in the summer than thicker ice, generally resulting in a lower September sea ice extent (Rigor et al., 2002). However, and as we discuss in more detail in the Concluding Discussion (Section 6.3), this correlation between the AO and September sea ice extent may now be breaking down (e.g. Stroeve et al., 2011), primarily because multi-year ice moved anticyclonically under the AO- now often does not survive the summertime melt in the Beaufort/Chukchi region.

Sea ice from the Kara and Laptev seas carries sediment, pollutants, trace elements and gases (Krumpen et al., 2019; Peeken et al., 2018; Rigor & Colony, 1997) into the central Arctic Ocean, a result of turbulent entrainment in frazil ice during autumn storms (the fetch can be 1000 km at the end of summer), and the scraping action of anchor ice on the sediment (Reimnitz et al., 1994). Any change in the long-range transport of sea ice from these regions therefore affects the redistribution of biogeochemical matter, with implications for primary production and biodiversity (Krumpen et al., 2019).

Oceanic role

High rates of freezing and brine-rejection in Arctic flaw leads/polynyas has long been recognised to be important for the replenishment of the cold Arctic halocline (Aagaard et al., 1981; Cavalieri & Martin, 1994). The cold halocline separates relatively fresh waters in the surface mixed layer from the relatively warm and salty Atlantic waters below, a transition that occurs at c. 100–300 m depth, generally trending deeper from eastern to western Arctic (e.g. Aagaard et al., 1981; Polyakov et al., 2020, Figure 0.3b). The halocline limits vertical heat fluxes from Atlantic Waters and restricts the depth of water that must be convectively cooled in order for sea ice to form (Bulgakov, 1962). The original Aagaard et al. (1981) model of halocline renewal argues from hydrographic principles that cold shelf waters, salinified during winter by brine-rejection, advect and interleave into the deep basins; this is an 'advective mode' of halocline renewal. Mixing with fresh river inputs to the Eurasian shelf seas is implicated in preventing

these waters densifying further and sinking to the abyss. In the analysis of Aagaard et al. (1981), however, shelf seas east of the Kara Sea could not contribute to the halocline because their waters are too fresh, even in winter, due to year-round river runoff.

An alternative perspective (Rudels et al., 1994) is that winter convection down to the halocline is followed by surface injection of cold and fresh waters from the shelf seas or from sea ice melt (Rudels et al., 2004), thus renewing the cold halocline via a 'convective mode'. Steele and Boyd (1998) pointed out that these modes may operate in different seasonal and spatial contexts. This is a suggestion borne out by hydrographic evidence that the advective mode dominates where the Barents and Kara seas meet the Nansen Basin, while the convective mode is likely more important in the Amundsen Basin (Woodgate et al., 2001). Support for multiple sources of halocline renewal comes from modelling (Pemberton et al., 2014) and suggestions that the Arctic polynyas alone could not supply enough water to maintain the cold halocline layer (S. Martin & Cavalieri, 1989; Winsor & Björk, 2000). Chemical signatures characteristic of the Eurasian shelves found in the halocline over the Alpha ridge suggest that advection plays at least some role in the renewal of the central Arctic halocline (Jones & Anderson, 1986).

Freezing and brine rejection is also implicated in transforming Atlantic waters that then feed into the abyss via the St Anna Trough, and on the shelf break north of Severnaya Zemlya (Rudels, 2015).

Of concern, especially in a climate change context, is the stability of the cold halocline in the Eurasian Basin (Polyakov et al., 2018) and the northern Barents Sea (Lind et al., 2018). In the Eurasian Basin, winter mixing associated with winter storms and brine rejection may reach down to the Atlantic Water, and has been associated with shoaling of Atlantic waters and increased heat fluxes in the 1990s (Martinson & Steele, 2001) and during recent winters (Polyakov et al., 2017; Polyakov et al., 2020). However, Rudels (2015) argues that entrainment generated by saline convection is a self-regulating process: less freezing leads to reduced mixing. By contrast, mechanical mixing along the shelfbreak can maintain a larger upward heat transport (R. Dewey et al., 1999).

Theoretically, degradation of the cold halocline would change the Eurasian Basin from an Arctic regime, with heat fluxes of order 1 Wm^{-2} to an Antarctic-type regime—which is vertically less stable and where polynya activity results in deepwater formation (Gill, 1973)—with attendant increases in heat fluxes 15–20 Wm^{-2} (Martinson & Steele, 2001). Episodic collapses of the cold halocline have been observed in recent years (Polyakov et al., 2017), with increases in heat fluxes from 3–4 Wm^{-2} in 2007/2008 to $>$10 Wm^{-2} in 2016/2017, levels at which sea ice growth may be halved (Polyakov et al., 2020). Indeed the long-term Arctic boundary between vertically stable and unstable waters—the polar front—now defines the limit of winter sea ice extent (Barton et al., 2018). The extent to which halocline degradation is driven by increased saline convection, decreased freshwater input, increased wind-driven mixing due to a more mobile sea ice cover, or increased Atlantic inflows remains debated (Årthun et al., 2012; Asbjørnsen et al., 2020; Davis et al., 2016; Lind et al., 2018; Polyakov et al., 2020).

Sea ice formation in the Kara and Laptev seas appears to be in favour of strengthening the stratification of the Eurasian Basin. This is because sea ice formation on the shelves can help to renew the cold halocline via both the 'advective' and 'convective' modes: brine rejection densifies cold fresh waters that can advect into the halocline, and sea ice produced on the shelves can later melt in the basin. Further, winter saline convection on the shelf cannot cause shoaling of Atlantic Waters, because Atlantic Waters rarely upwell on to the shallow shelves (Janout et al., 2017). Instead, winter convection can only propagate to the seafloor—it may do so along flaw leads (Dmitrenko et al., 2005; Reimnitz et al., 1994). However, enhanced ice formation may be correlated with other processes that weaken the stratification, such as the diversion of fresh shelf waters eastwards along the Siberian coast—implicated in the halocline weakening of the 1990s under the cyclonic AO+, a pattern that can also increase ice production by driving coastal divergence (M. A. Johnson & Polyakov, 2001; Steele & Boyd, 1998).

4.2 Materials and Methods

4.2.1 Climate model

To analyse the forced response of sea ice production in the KL seas to climate change, we make use of data from the Community Earth System Model Large Ensemble (CESM-LE, Kay et al., 2015). CESM-LE is comprised of 40 ensemble members, and as such is well-suited to discerning forced responses to climate change in the context of internal climate variability (Kay et al., 2015). It is based on the fully coupled model CESM1.1, and comprises the Community Atmosphere Model, version 5 (CAM5); the Parallel Ocean Program, version 2 (POP2); the Community Land Model, version 4; and the Los Alamos Sea Ice Model CICE, version 4 as its sea ice component. The version of CICE used features some notable improvements to shortwave radiation interactions, including the effects of melt ponds and aerosol deposition on ice (Holland et al., 2012). The spatial resolution of the CESM1.1 ocean and sea ice models is nominally $1° \times 1°$ longitude by latitude, while the atmospheric model is $0.9° \times 1.25°$.

All 40 CESM-LE members are forced by the same external forcing data, separated into two runs. Firstly, a run from 1920–2005 forced by historical external forcing data (Lamarque et al., 2010) that we refer to as 20C; secondly, from 2006–2100, a high-emissions RCP8.5 run (Meinshausen et al., 2011), leading to over 4 °C warming by 2100. The RCP8.5 scenario at present slightly underestimates observed emissions; although it is a 'high-emissions' scenario, it presently represents a realistic or even conservative one (Peters et al., 2013; Schwalm et al., 2020). The ensemble spread is entirely generated by simulated internal climate variability originating from very small, random differences in the initial air temperature fields.

Here we rely on monthly data between 1920–2080—sufficient time to assess major forced changes in ice production in the Kara and Laptev seas—from 35 ensemble members. Jahn et al. (2016) assess the statistical implications of using different numbers of ensemble members in predicting the timing of a summer ice-free Arctic; there is minimal difference between 35 and 40. Further, in their study detecting forced changes in Arctic freshwater variability,

Jahn and Laiho (2020) found minimal difference between using 11 ensemble members versus 40. However, the number of ensembles required for statistical significance varies depending on the climate parameter in question. Barnhart et al. (2016) deemed 30+ ensemble members necessary for such precise metrics such as the 'last day of ice coverage' or the 'last year with ice coverage for 182 days'.

CESM1.1 and CESM-LE have been used in a broad swathe of Arctic climate studies and generally perform well (e.g. Årthun et al., 2019; Barnhart et al., 2016; DeRepentigny et al., 2016; England et al., 2019; Jahn, 2018; Jahn et al., 2016; Morrison et al., 2019; Petty et al., 2018; Swart et al., 2015). Arctic sea ice thickness in CESM-LE broadly corresponds in spatial mean pattern and trend during 1980–2015 with PIOMAS, though exhibits slightly thicker (order several 10 cm) sea ice than PIOMAS (e.g. Labe et al., 2018; Petty et al., 2018). Although the satellite record of sea ice thickness is short, CESM-LE compares well with estimates of inter-seasonal thickness changes and interannual variability (Petty et al., 2018). Declining Arctic sea ice concentration and extent in CESM-LE has been more comprehensively compared to observations, which fit within its ensemble spread and compare well across all seasons (Barnhart et al., 2016; Jahn et al., 2016; Swart et al., 2015). The changing open water season also shows correspondence with satellite observations, including in the Laptev Sea (Barnhart et al., 2016).

Climate variables computed

To capture winter thermodynamic sea ice production, we use monthly data from October to April, inclusive, as per Petty et al. (2018). We analyse freshwater exchanges with the ocean, rather than changes in ice thickness (c.f. Petty et al., 2018) in order to explicitly isolate thermodynamic changes. Sea ice production is calculated as the sum of only the ocean-to-ice part of thermodynamic ice-ocean freshwater fluxes.

The other parameters we consider here are: snow depth on sea ice (note that this is different to snow volume per unit grid cell area), sea ice concentration, sea ice divergence, surface air temperatures, and ocean temperatures in the top (10 m thick) grid cell. We investigate two

types of sea ice divergence. Firstly, the *net* divergence, which—by the divergence theorem—is equivalent to the area expansion of the sea ice area, or, when that area encompasses the whole KL region, it is the area export of sea ice from the region. We are also interested, however, in divergence within the region that is compensated by convergence somewhere else in the region; this divergence can open or expand leads but still not lead to export. To capture this compensated divergence, we record the *positive* divergence, which is counted only over cells where the divergence is positive. The compensated divergence is then found as $compensated\ div = positive\ div - net\ div$ (see also Equation 3.1).

All parameters (except when plotted as spatial maps) are computed over the study region shown in Figure 4.2 and appropriately area-weighted. Further nuances related to the treatment of parameters is provided where relevant in the rest of the chapter. When plotting data, we identify the winter spanning years n and $n + 1$ with year $n + 1$; the winter 2015/2016 is labelled 2016. The variables extracted from the observation-derived estimates are computed in a consistent manner to their equivalents from CESM-LE.

4.2.2 Observation-based estimates

Atmospheric reanalysis

We utilise monthly mean 2 m temperatures from the ERA5 global reanalysis (Hersbach et al., 2020), gridded at 0.25° × 0.25° resolution. ERA5 is the fifth generation of atmospheric reanalyses from the ECMWF, and is widely used in climate research and for forcing ice-ocean models. We use the terms surface air temperatures and 2 m temperatures interchangeably here. Surface air temperatures from ERA5 generally perform well in the Arctic relative to in situ observations, however consistently show warm biases of order several degrees over sea ice in winter months (C. Wang et al., 2019).

We gather ERA5 data spanning the winters 1979/1980 to 2019/2020. The data are accessible via the Copernicus Climate Change Service portal (https://cds.climate.copernicus.eu/).

Sea ice motion vectors

To plot mean sea ice velocities (Figure 4.2) and calculate sea ice divergence, we make use of the National Snow and Ice Data Center Polar Pathfinder v4.1 product, gridded at 25×25 km resolution and in weekly means (Tschudi et al., 2019).

We present data from Polar Pathfinder encompassing the winters 1979/1980 to 2017/2018. The data are accessible at the NSIDC website (https://nsidc.org/data/NSIDC-0116/versions/4).

Sea ice concentration

To document changes in sea ice area, we utilise sea ice concentration data from passive microwave satellite retrievals, prepared by the NASA Goddard Space Flight Centre (NASA GSFC). We used the 'merged' data, which combines data derived from the Bootstrap and Nasa Team algorithms (Comiso et al., 1997), and compares well with other estimates (Meier et al., 2017; Peng et al., 2013).

We use data spanning the winters 1978/1979 to 2018/2019. The data are accessible at the NSIDC website (https://nsidc.org/data/G02202/versions/3).

Snow on sea ice

We use data from a Lagrangian snow evolution model, SnowModel-LG, which provides daily data on a 25 km × 25 km grid and is forced by ERA5 and MERRA-2 reanalyses (Liston et al., 2020). We use the mean of the two versions, and our dataset spans winters 1981/1982 to 2016/2017. SnowModel-LG compares well to observational datasets in spatial and seasonal variability of snow depth and density (Stroeve et al., 2020).

Pending publication, SnowModel-LG data will be available on the NSIDC website (Liston, G. E., J. Stroeve, and P. Itkin; Lagrangian Snow Distributions for Sea-Ice Applications; http://dx.doi.org/10.5067/27A0P5M6LZBI).

Consistent with our snow depth acquisitions from CESM-LE, we present snow thickness on

sea ice where present, rather than snow volume per unit area.

Sea surface temperature

We make use of monthly-mean sea surface temperature data at a $1° \times 1°$ resolution from the NOAA Optimum Interpolation Sea Surface Temperature v2 (NOAA OI SST v2) dataset (Reynolds et al., 2002). This SST product is used in the Arctic Report Card assessments of Arctic changes (Timmermans & Labe, 2020).

Sources of bias in the satellite retrievals include partial contamination by clouds and atmospheric aerosols. Comparisons with other SST products show relatively large root-mean square differences of 0.5 °C in the Arctic Ocean (Reynolds et al., 2002); in-situ for testing these data are sparse in the Arctic Ocean.

The SST corresponds to the temperature at a depth of approximately 0.5 m. As such, there is a disparity in depth with the top 10 m mean temperature that we compare this record to from CESM-LE. However, as our work mostly concerns trends, we suspect this distinction will be relatively unimportant.

We utilise data from the winters 1981/1982 to 2019/2020. The NOAA OI SST v2 dataset is provided by the NOAA/OAR/ESRL PSL, Boulder, Colorado, USA, and accessible at their website (https://psl.noaa.gov/data/gridded/data.noaa.oisst.v2.html).

4.3 Understanding changes in the Kara and Laptev 'ice factories' using CESM-LE

4.3.1 Shrinking growth season, rising growth rate

Through the summer melt season, the sea ice edge retreats towards the pole. The refreeze, however, begins along the Siberian coastline. Figure 4.3 shows how the ensemble mean sea ice extent moves through the months of October to December. By 2030, much of the Kara

sea is ice-free in October, and the connection with pack ice in the Laptev sea retreats towards Severnaya Zemlya—one of the most northerly islands of the Arctic Ocean. First year sea ice reconnects with the polar ice in an hourglass shape that becomes progressively pinched, and occurs later, through the 21st century.

A key factor behind this hourglass shape—which also appears in observations (e.g. Stroeve et al., 2012)—is that in summer and during the onset of freezing, the waters northeast of Severnaya Zemlya are relatively cold compared to the surrounding shelves (Tarasenko et al., 2021). According to the nature of the atmospheric circulation, the warm Yenisey and Ob river plume to the southwest generally either flows south of Severnaya Zemlya through Vilkitsky Strait in a baroclinic flow along the coast, or spreads northwards into the Transpolar Drift (Janout et al., 2017; Osadchiev et al., 2020; Steele & Ermold, 2004). Similarly, the Lena river plume in the Laptev Sea generally spreads northwards and eastwards (Osadchiev et al., 2020; Tarasenko et al., 2021). If waters from Eurasian rivers reaches the ocean northeast of Severnaya Zemlya, they are likely to have cooled on their transit through interaction with the ambient ocean and sea ice melt-waters (e.g. Tarasenko et al., 2021). In addition, the surface waters north of Severnaya Zemlya are not directly influenced by either warm Pacific summertime inflow (which affects the western Arctic e.g. Proshutinsky et al., 2019; Timmermans et al., 2014) or Atlantic Waters (which reside below the cold halocline, with low mixing across it).

Changes in monthly sea ice production are shown in Figure 4.4. The characteristic shape is one of a sharp increase in ice production near the start of the season, reaching a peak in usually the second month of meaningful ice production. The ice production curve then gradually curtails through the winter season before dropping off more steeply with the coming of the summer melt in April.

Several factors contribute to this characteristic shape: the slowing of ice growth as the ice thickens through the season (growth rate is proportional to the inverse of thickness, e.g. Thorndike et al., 1975); the accumulation of snow throughout the season (Ledley, 1991; Maykut, 1978; Merkouriadi et al., 2017); the reduction in sea ice mobility and polynya activity that oc-

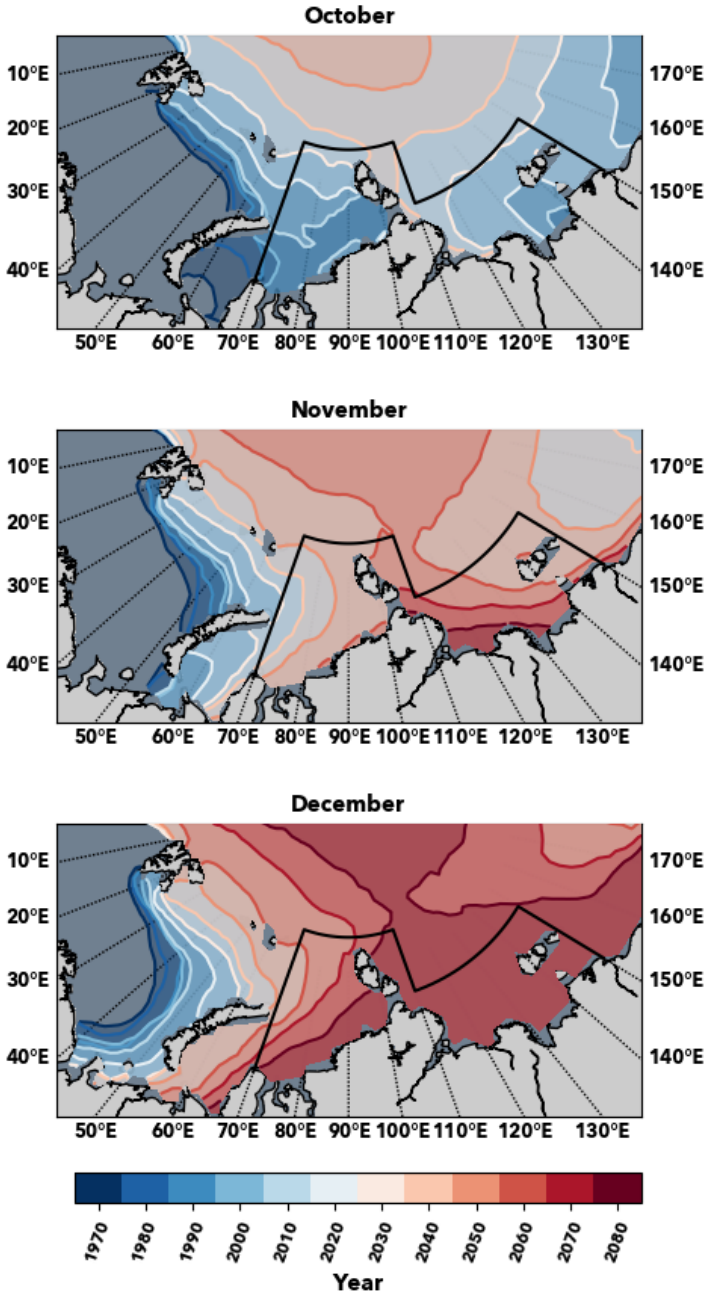


Figure 4.3: Decadal ensemble mean changes in early winter sea ice extent edges in CESM-LE from 1970–2080. Figure prepared by co-author of manuscript in preparation, J. Dörr. Study region indicated by black box.

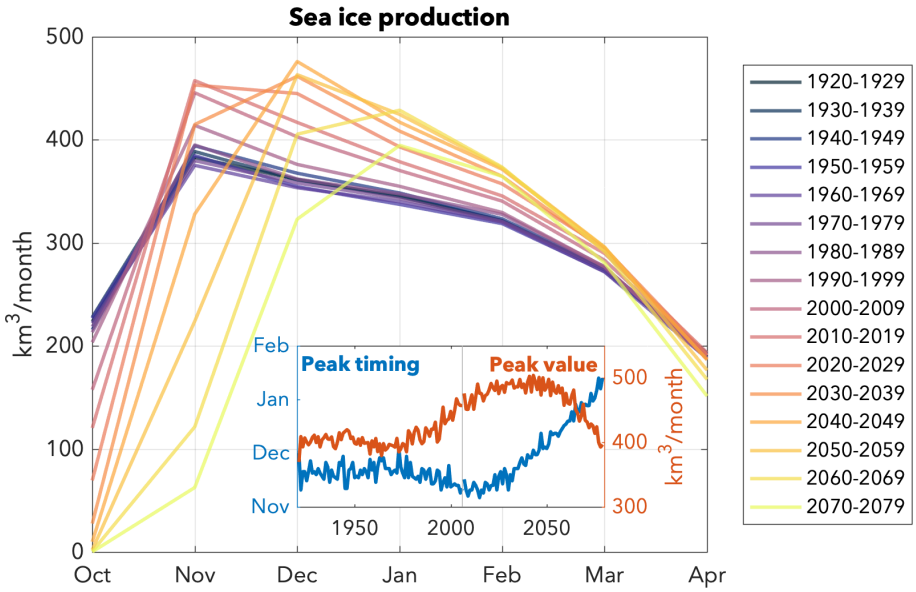


Figure 4.4: Decadal mean changes in sea ice production across winter months in CESM-LE. Inset panel shows changes in the timing of peak sea ice production and changes in the amplitude of the peak value.

curs as the season progresses, both a result of thickening ice and seasonality in mean sea-level pressure patterns.

As the climate begins to exhibit marked warming from c. 1980, the October sea ice production falls, approaching zero by 2030–2039 (Figure 4.4). Initially this trend is compensated by a rapid recovery and a higher sea ice production peak in November, connected to the freeze-back of a larger open water area (compare with Figure 4.3). The sea ice production peak itself shifts later after 2010–2019, and continues to increase in magnitude until 2040–2049, before falling rapidly to 20C levels by 2080. The magnitude and timing of the ice production peak are shown inset in Figure 4.4. Because we combine 35 ensemble members, we are able to interpolate the ensemble mean peak timing to a daily resolution, even though the original data describes monthly means. This interpolation may not accurately resolve the underlying maximum of the daily-scale probability density function of each winter peak if those functions are not evenly distributed.

The overall trend is one of progressively delayed onset, followed by freezing that is, throughout

the RCP8.5 run, more intense during mid-winter (Jan, Feb, Mar) than in the 20C run. The link between the delaying onset and monthly atmospheric temperatures is shown in Figure 4.5. The fastest warming in a given month from one year to the next occurs during the month in which freeze-up—which migrates progressively later—falls. This illustrates the role that oceanic heat loss (preceding or in the early stages of freezing) plays in warming the atmosphere. As the freezing onset migrates later into the winter, so to does accentuated atmospheric warming.

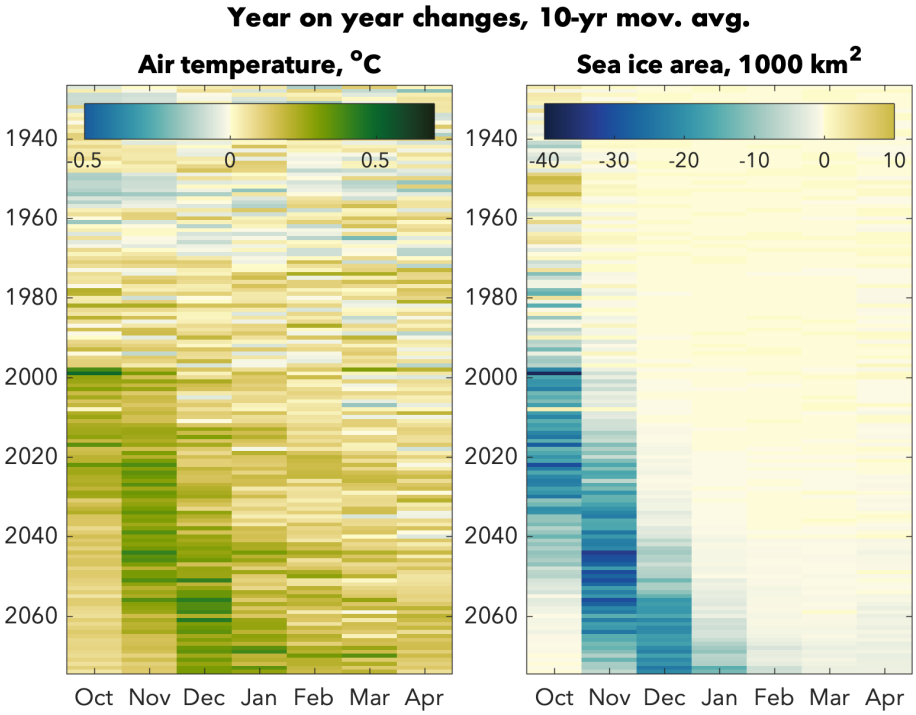


Figure 4.5: Ensemble mean of changes from one year to the next in monthly surface air temperature and sea ice area in CESM-LE. The plots indicate the change in air temperature (left) and sea ice area (right) in a given month and year from that same month the prior year. The yearly trends for each month are smoothed using a 10-year moving average.

The graph-area under each monthly ice production curve in Figure 4.4 is the total winter ice production—our main quantity of interest in this chapter. As we can see from Figure 4.4, ice production is not uniform process throughout the winter, but exhibits a significant monthly pattern, that becomes further enhanced in RCP8.5 relative to 20C. In order to understand total winter ice production, it is important to consider further the processes at play during the winter months that yield these characteristic monthly patterns in ice production.

In order for freezing to begin, the surface ocean must cool to the freezing temperature, which in the Arctic is -1.8 °C. The amount of heat stored in the upper ocean, largely determined by solar heating during summer months (e.g. Maykut & McPhee, 1995; Perovich et al., 2008; Shaw et al., 2009; Steele et al., 2010), and factors controlling the fluxes of heat to the atmosphere (such as atmospheric temperature and winds, the presence or otherwise of pre-existing sea ice), will determine the length of time taken for freezing to begin. The process of heat loss from the upper ocean occurs in tandem with the expansion of the mixed layer down towards the halocline, driven by elevated wind-mixing and convection due to brine-rejection and cooling. As the mixed layer deepens, it entrains heat from solar radiation sequestered below the summer mixed layer, which can then be released to the atmosphere (e.g. Maykut & McPhee, 1995). As discussed in Section 4.1.2, the strong vertical stability of the Arctic halocline generally limits the depth of the reservoir that must be cooled, and also limits the heat fluxed upwards from deeper waters.

During the winter season, when incoming shortwave radiation is negligible, the growth of ice thickness, H, depends on a greater conductive heat loss to the atmosphere through the ice, F_c than heat flux from the ocean at its base, F_w, as shown in Equation 4.1, where ρ_i is the density of ice, L_i is the latent heat release/uptake on freezing/melting, and fluxes are positive upwards. Assuming no thermal inertia and no internal heat source, we may write:

$$\rho_i L_i \frac{dH}{dt} = F_c - F_w \tag{4.1}$$

The winter equilibrium thickness of ice, therefore, is reached when there is a balance of heat fluxes at through the top and bottom surfaces of ice: $F_c = F_w$. As the ice thickens, the conductive heat fluxes F_c through the ice diminish, bringing the growth rate down towards zero, according to the size of the oceanic heat flux, F_w. Other factors also control F_c, including the air temperature and snow cover. In the marginal seas around Antarctica, where F_w is on the order several tens of Wm^{-2}, the equilibrium thickness of undeformed sea ice may be as little as 0.5–0.7 m (Petrich & Eicken, 2010; Wadhams et al., 1987). In the Arctic Ocean, on the

other hand, F_w is generally low during the freezing season, of order 1 W/m^2 or less in the basin interiors, but sometimes higher directly over the AW boundary current or over rough topography (see Carmack et al., 2015, for a synthesis of observational estimates). Unlike in Antarctica, these low heat fluxes are generally no impediment to the growth of first year ice (Petrich & Eicken, 2010).

Based on this understanding we can roughly divide the Arctic winter into two regimes: 1) an early period in which the upper ocean is above the freezing temperature, and ice growth is limited by heat fluxes to the surface as mixing removes heat from the mixed layer; and 2) the freezing season proper, in which upwards heat fluxes from the ocean are small, and the growth rate is dictated in the main by the conductive heat flux, F_c, which evolves through the winter. As such, we can divide ice production into two components, considering both spatial and temporal variability. Firstly, we can consider the spatio-temporal duration of freezing, and secondly, the mean growth rate where and when ice is indeed freezing. Because we use a fixed winter time window, the spatio-temporal duration of freezing by definition also tells us the spatio-temporal duration of regime (1) above. The duration of regime (1) is naturally dictated by different physics to that which governs the growth rate during regime (2); decomposing total ice production into these two constituent parts is motivated by a difference in the physics that dominates each regime.

Ice production (in units of volume) is thus explained by the product of freezing area days (in units of area $\times$ time) and the corresponding mean growth rate (in units of vertical length scale/time) over those freezing area days. To extend the metaphor of the 'ice factory', the number of freezing area days can be considered the *usage* of the factory in space and time. The growth rate is then the *efficiency* of the factory—over the space and time it is *in use*. We illustrate this decomposition of ice production in Figure 4.6.

The ensemble mean total winter ice production (Figure 4.6, upper panel) shows a gentle decline after the early twentieth century warming (see e.g. Schweiger et al., 2019, for the expected impact on sea ice during that period), followed by a steady increase up until 2010–2020, where

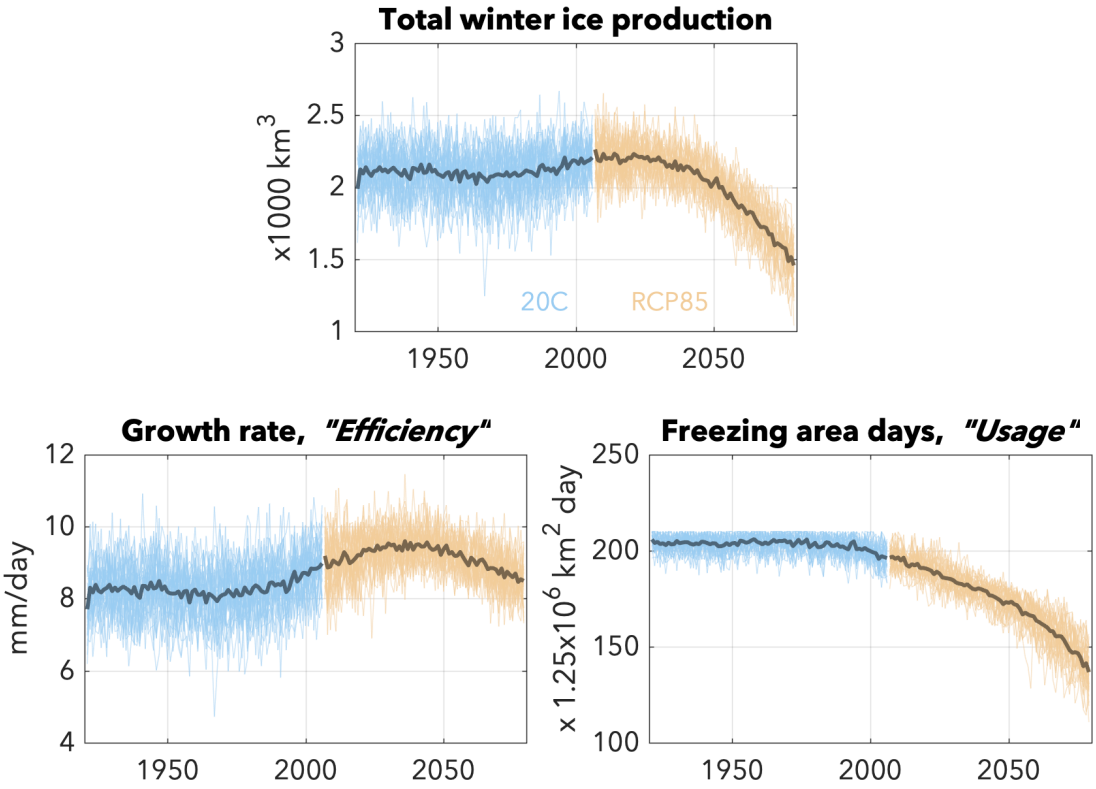


Figure 4.6: Winter ice production (top) and decomposition into growth rate (left) and freezing area days (right). Note that the freezing area days is rescaled in terms of the total KL area, such that the upper limit is 210 on the y scale: the duration of our seven month winter period in days.

it reaches just over 2,200 km^3. Ice production then curves downwards, decreasing rapidly by the mid-century to 1,500 km^3 by 2080. Internal variability around the ensemble mean is considerable and greater than any forced changes during 20C. This relationship changes as the declining ensemble mean reveals clear forced changes to ice production during RCP8.5, while the magnitude of internal variability is reduced on 20C levels. The decline in internal variability is pronounced around the turn of the 21st century, and there is a notable increase in the ensemble minimum ice production values between c. 1990 and 2020.

The number of freezing area days, or *usage* (Figure 4.6, right) is relatively consistent throughout 20C, showing a slight decline around the turn of the 21st century. The *usage* is rescaled in terms of the KL area (c. 1,250,000 km^2) in Figure 4.6, such that the maximum possible value

corresponds to the total number of days we consider in our winter season. From the beginning of RCP8.5, the *usage* decline gradually accelerates, curving down to the equivalent of 140 days of the KL area by 2080. It is worth remembering, however, that the *usage* captures both spatial and temporal variability. Internal variability in the *usage* is relatively small compared to the forced changes exhibited in the ensemble mean trend.

In contrast to the total ice production and *usage*, the mean growth rate during freezing, or *efficiency*, reaches consistently higher values during RCP8.5 than 20C (Figure 4.6, left). The ensemble mean *efficiency* trend shows a similar form to the 'peak value' displayed inset in Figure 4.4, curving upwards towards a broad culmination during 2030–2040, before declining through to 2080. The forced change in the rise in *efficiency* is notably larger relative to internal variability than the forced increase in ice production that occurs c. 1980–2020.

4.3.2 A linear model for ice factory production

We seek a set of parameters that are capable of explaining forced changes in ice production in the long term, through both the rise and the fall discussed in Section 4.3.1. In this manner, we seek to understand the underlying drivers of these changes. In doing so, we aim to advance on previous work describing the changes in ice production in terms of changing correlations between climate variables such as surface air temperature and ice production (Petty et al., 2018).

In order to permit application to observationally-derived estimates (OEs), we limit our attention to variables for which there is an accessible and sufficiently long OE record (approximately spanning the satellite era from 1979 onwards). Further, on the grounds that it is determined in large part by the variable we aim to predict, we avoid using sea ice thickness as an explanatory variable during the winter season (whereas as an initial condition it is permissible).

In our search for such relationships, we consider the physical distinctions between the two components of ice production introduced above (Section 4.3.1): a mean growth rate during

the *usage* of the 'ice factory', and the *usage* itself. Although we ultimately seek to develop a linear model to explain changes in ice production, our approach to doing so is guided by the physics underpinning these two components. In the rest of this subsection, we delve into the physics of these components and build linear models for each, separately. Based on the success of these individual models, we construct a linear model for ice production—the main focus of this chapter.

To confirm whether the dependencies on annual *usage* and *efficiency* hypothesised above do indeed exist in CESM-LE, we construct linear models to explain internal variability in these metrics across the ensemble. To do this, we subtract the ensemble mean from all variables considered so that we deal only with internal variability. We restrict our attention here to winter means, though a more sophisticated model might consider the evolving monthly relationships.

A linear model for *usage*

Following the evidence outlined above in Section 4.3.1, we expect the end-of-summer upper ocean temperature to be key in determining *usage*. We capture this as mean September top 10 m ocean temperatures (Sep 10 m T). The logic is that the total amount of heat in the upper ocean largely determines the time taken for it to cool. Another factor that we can expect may be important is the air temperature at the time of cooling: the colder the temperature, the more rapid the heat loss. We capture this as the Oct-Nov-Dec mean surface air temperature (OND SAT). We can thus write a linear model, including regression coefficients, β_n:

$$\text{Usage} = \beta_1 \text{Sep 10 m T} + \beta_2 \text{OND SAT} \tag{4.2}$$

Because this linear model concerns the internal variability, no β_0 is included because all variables are centred on zero after subtraction of the ensemble mean.

In the 20C run, mean Sep 10 m T alone, as a single regressor, is successful in dominantly capturing internal variability in *usage*, with R^2= 0.74. Adding OND SAT as a second regressor

slightly improves the reconstruction of *usage* (R^2= 0.78). Using the mean September top 50 m ocean temperature instead of the surface 10 m affords no improvement in reconstructing *usage*. During RCP8.5, the linear model weakens in its reconstructive power, and the addition of OND SAT becomes more important; R^2= 0.61 using both Sep 10 m T and OND SAT, and R^2= 0.46 using only Sep 10 m T. In the RCP8.5 run, unlike in the 20C run, inclusion of Sep 50 m T instead of Sep 10 m T marginally improves the reconstruction (by several percentage points in R^2).

A linear model for *efficiency*

Once freezing begins, however, we expect the ocean to play a secondary if not negligible role in determining the growth rate, or *efficiency*. Where F_w is negligible, we can write:

$$\rho_i L_i \frac{dH}{dt} = F_c \tag{4.3}$$

The growth rate is thus determined by parameters that explain the conductive heat flux, F_c. Assuming a layer of snow with thickness, h_s, atop ice with thickness, H, with corresponding thermal conductivities λ_s and λ_i, respectively, and linear temperature profiles through both media, the conductive heat flux is

$$F_c = \frac{\Delta T}{\frac{1}{k} + \frac{H}{\lambda_i} + \frac{h_s}{\lambda_s}} \tag{4.4}$$

where k is an effective heat transfer coefficient between the snow/ice surface and atmosphere, and ΔT = T_w - T_a; in which T_w is the freezing temperature of water and T_a is the surface atmospheric temperature. We set T_w = -1.8 °C.

We can see from Equation 4.4 that the conductive heat flux is linearly dependent on the surface air temperature, and inversely dependent on snow and ice thicknesses. Since snow is much more insulating than ice ($\lambda_s \approx 0.1\lambda_i$), even a thin layer of snow may have a substantial effect

on the conductive heat flux (Petrich & Eicken, 2010). Equation 4.4 also makes it clear that the direct physical effect of increased surface air temperatures, which lessens ΔT, is to decrease the conductive heat flux, and thereby decrease the growth rate (Equation 4.1). The identification of positive correlations between surface air temperatures and growth rate (e.g. Petty et al., 2018) rests on a causality in the opposite direction: increased growth rates and attendant upwards heat fluxes serve to boost surface air temperatures. We must therefore include the effect of air temperature in a way that explicitly captures its causal impact on sea ice growth. We do this—as detailed below—by mimicking the growth rate equation, and including ΔT as a factor in each of our regressors.

The sea ice thickness H features on both sides of the growth rate equation (see equations 4.3 and 4.4). Therefore, to avoid circular logic we must not include its evolution in our model. Instead, we can consider initial conditions from which H evolves according to the growth rate. These 'initial conditions' can be both the thickness at the start of the season, and occasions during the season when H is set to zero (by divergence) as an initial condition for growth. The minimum sea ice area (usually occurring in September) determines the area over which $H = 0$ at the start of the season. We term this area a 'sea ice area deficit': the area available for freeze-back. In addition, open water is created near-continually throughout the freezing season by divergence. Under extensional stress, ice cracks in a brittle manner rather than thinning; divergence introduces a delta function in the sea ice thickness distribution at $H = 0$ (Haas, 2010; Thorndike et al., 1975). The open water area is equal to the area diverged. After divergence occurs, we can assume H evolves from zero according to the growth-rate equation (Equation 4.3) over the area opened.

Divergence of the Arctic ice pack is spatially and temporally complex, and to understand its effect on thermodynamic growth we must also consider the role of convergence, which thickens ice and may partially balance divergence that occurs in a given area. Because the growth rate of ice is an inverse function of its thickness (Equation 4.4), and because ice cracks under tension rather than thinning in a ductile manner—thus setting H = 0 in the diverged area—we

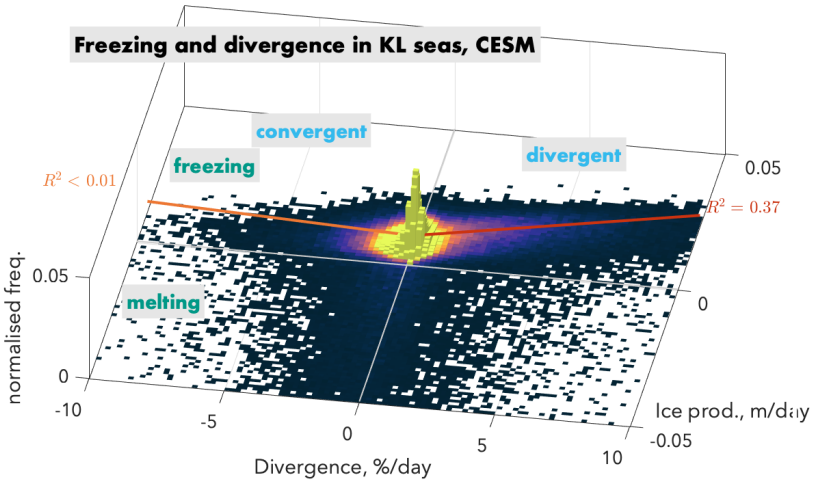


Figure 4.7: 3D histogram showing divergence and ice-to-ocean fluxes in all grid cells within the KL seas during winters 1990–1999 from CESM-LE. First 10 million such grid points shown.

can expect the effect of convergence and divergence on growth rate to be asymmetric.

In Figure 4.7, we plot as a 3D histogram the value of divergence and growth rate in winter in each grid cell during a specified time window (1990–1999); we take the first 10 million such grid cells from multiple models in the ensemble. In the freezing-divergent quadrant, it can be seen that monthly mean divergence in a given grid cell explains a substantial amount of the variance (37%) of thermodynamic ice growth. There is no significant relationship, however, between convergence and ice growth in the convergent-freezing quadrant. Therefore, we must consider not only the net divergence over the region, but also the divergence within the region that is balanced by convergence elsewhere, on account of the fact that the influences of convergence and divergence are asymmetrical. We term this latter type of divergence the *compensated* divergence (Section 4.2.1). There is, by design, no double-counting between the *net* and *compensated* divergence. They are therefore relatively weakly correlated—preferable for the purposes of building a linear model.

We can include the effect of snow as $\Delta\ T/h_s$. We can identify that open water creation will

lead to ice growth that will evolve as a function of Equation 4.4, over the area of water that has been created. The growth in those open water areas will be linearly related to $\Delta\ T$ and the area that has been opened. We classify three settings of open water creation: September SIA deficit (the open water area in September), open water due to net divergence and open water water due to compensated divergence. The three can be expected to impact the growth rate differently (resulting in different values for their regression coefficients), according to the way their occurrence maps onto the changing winter temperature (not captured directly by our winter mean $\Delta\ T$). Additionally, we might expect compensated divergence to have a lesser positive impact on growth rate due to compensating thickening. Because we seek the growth rate here, and not the total ice production, we consider the divergence as strain rate (related by a constant area term to rate of open water production). As such, we consider the influence on growth rate in settings of net divergence as $\Delta\ T(\nabla \cdot \mathbf{u})_{net}$, and in settings of compensated divergence as $\Delta\ T(\nabla \cdot \mathbf{u})_{comp}$, where $\mathbf{u}$ is the ice velocity field, and in both cases the values are appropriately area-weighted. Additionally, we normalise the influence of September open water area by the length of the remaining winter season, t_{rem}, after the onset of freezing (defined as the month in which >50% grid cells are freezing). As such, the impact on growth rate from this metric is weighted according to the time left in the freezing season. (This is not necessary when we consider the total ice production.)

Our linear model, including regression coefficients, β_n, for growth rate (*efficiency*) is then:

$$\text{Growth Rate} = \beta_1 \frac{\Delta\ T}{h_s} + \beta_2 \frac{\Delta\ T \text{SIA}_{deficit}}{t_{\mathrm{rem}}} + \beta_3 \Delta\ T(\nabla \cdot \mathbf{u})_{net} + \beta_4 \Delta\ T(\nabla \cdot \mathbf{u})_{comp} \quad (4.5)$$

In the 20C run, the model reconstructs internal variability in growth rate with R^2 = 0.86, and R^2 = 0.81 in RCP8.5. A small improvement in reconstruction skill is afforded if sea ice volumes are used instead of September sea ice area as the initial condition: R^2 = 0.90 in 20C but this advantage disappears in the RCP8.5 run (R^2 = 0.81) when initial thicknesses play less of a role in determining the growth rate. Nonetheless, we choose to use the September sea ice area rather than volume, because it is a measure available from satellite retrievals back to 1979 (whereas a continuous record of satellite-derived estimates of ice thickness only exists from

2011).

Finally, we note that this treatment of surface air temperatures enables the forced changes in 20C and RCP8.5 to be recovered by this linear model when reconstructing the ensemble mean trends (not shown). If, however, surface air temperatures are stripped out of each regressor and included separately as another regressor, the forced changes cannot be recovered. This is due to the fact that surface air temperatures correlated with growth rate in the 20C run, but this correlation changes sign during the RCP8.5 run (as shown in Petty et al., 2018, and confirmed in our investigations, not shown).

A linear model for ice production

Because the relationship between mean growth rate and total growth is linear, we can start to build our linear model by including explanatory variables that we use in the growth rate model, with small modifications. Namely, we now seek the total area diverged during the freezing season, A, rather than the divergence as a rate of open water production. And we now utilise the September sea ice area deficit in its full form and no longer normalise by t_{rem}. We again the effect of snow as $\Delta\, T/h_s$. Finally, we need to include the role of declining *usage*. We do this simply by including the September top 10 m grid cell temperature, following the arguments above.

Our linear model for ice production, including regression coefficients, β_n is then:

$$\text{Ice Prod} = \beta_1 \Delta\, T/h_s + \beta_2 \Delta\, T\text{SIA}_{deficit} + \beta_3 \Delta\, TA_{net} + \beta_4 \Delta\, TA_{comp} + \beta_5 \text{SST}_{Sep} \quad (4.6)$$

The relevant variables required to build the model are shown in Figure 4.8, and compared with corresponding climate variables from observation-derived estimates in red.

We perform multiple linear regression to find the regression coefficients for our linear model using internal variability during a) 20C, b) RCP8.5 and c) the full timeseries. By comparing the coefficients between these time periods, we can check how physically robust to different

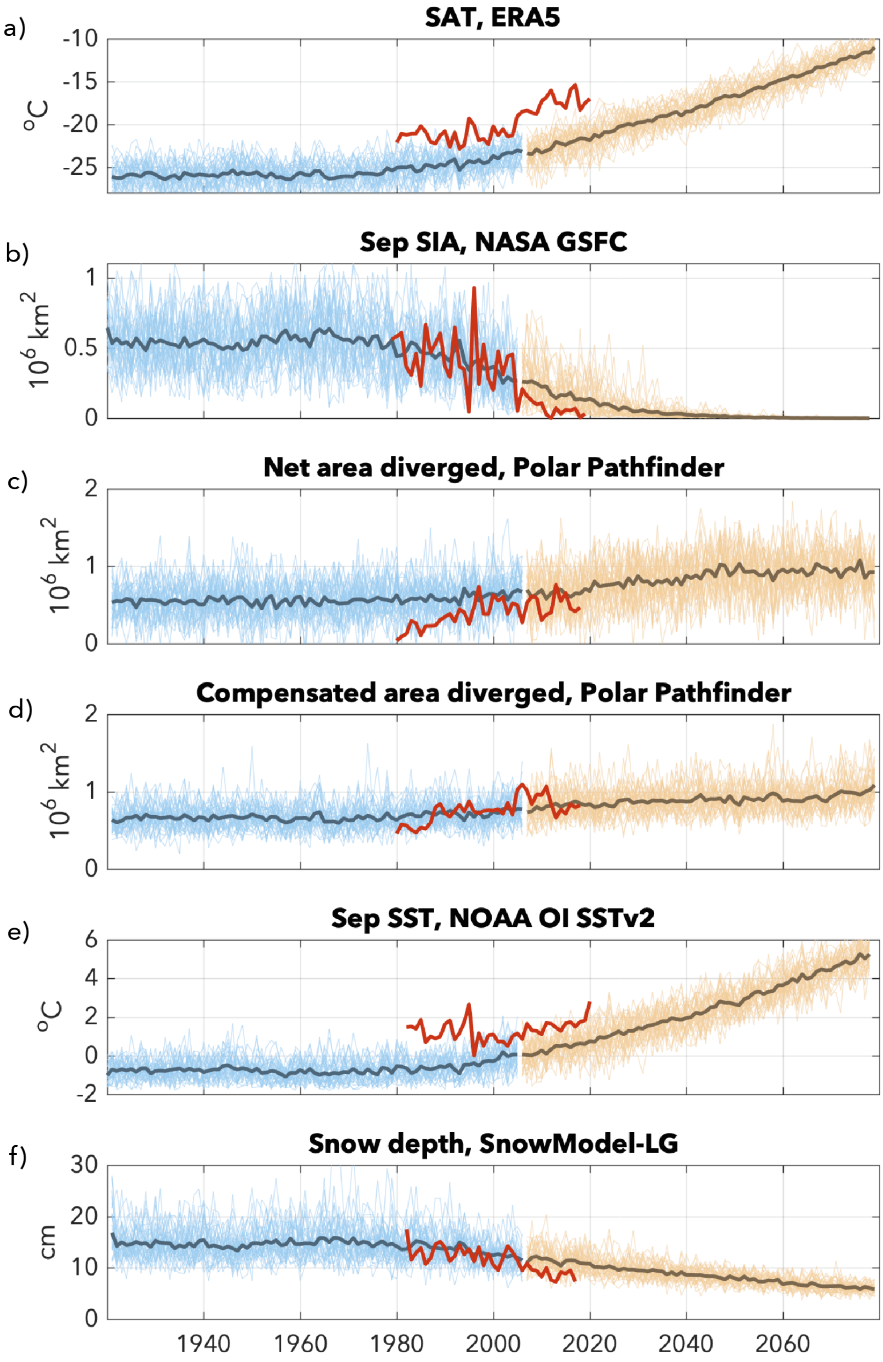


Figure 4.8: Timeseries comparison of key parameters in CESM-LE and real-world estimates (red line): a) surface air temperatures, b) September sea ice area, c) net area diverged, d) compensated area diverged, e) September 10 m T in CESM-LE and SST in NOAA OI SSTv2, f) snow depth on ice. 20C is shown in blue and RCP8.5 in orange; ensemble mean indicated by darker line.

conditions our model is. The coefficients are compared in Figure 4.9. The coefficients are standardised by the standard deviation in 20C. This standardisation indicates which variables have the largest effect on ice production in terms of the natural range of variability in 20C. In order that the metrics are consistent in absolute terms, we stick to this standardisation across the 20C, RCP8.5 and the full timeseries. The variance in the CESM-LE internal variability explained by the linear model is consistently high; 81% during 20C, 76% during RCP8.5 and 78% over the full run.

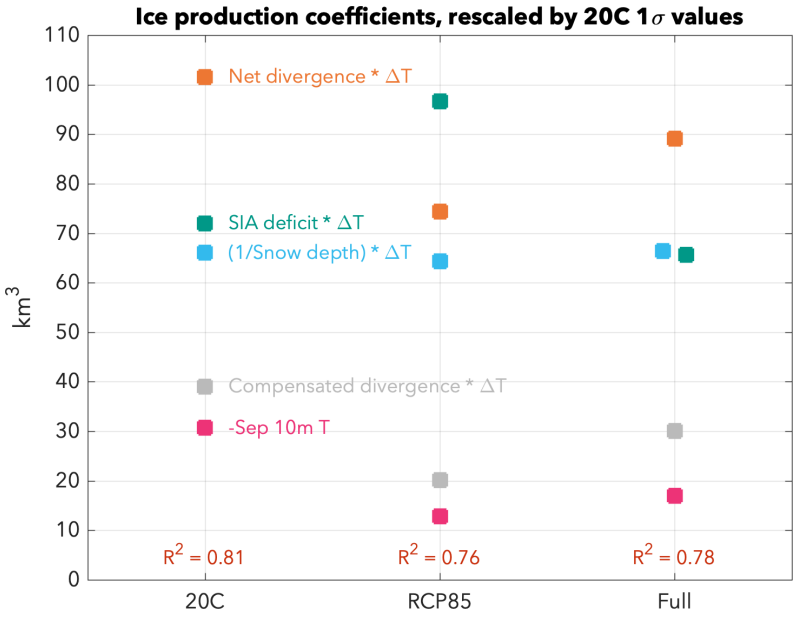


Figure 4.9: Winter ice production regression coefficients for key parameters, standardised by one standard deviation in 20C. Regressions calculated using internal variability, with the ensemble mean removed. Variance explained is shown.

There is relatively good agreement in the amplitude of coefficients between 20C, RCP8.5 and the full timeseries, and unanimous agreement in the sign. The absolute magnitude of the ΔT/snow depth coefficient is remarkably similar between runs. This gives us confidence that our statistical model is sufficiently physically robust, and that our treatment of temperature has solved the problem of temperatures correlating with sea ice growth during 20C but not during RCP8.5 (Petty et al., 2018) and enabled us to derive a model with reconstructive power under a range of conditions.

All explanatory variables show vanishingly small p values. Three regressors are consistently dominant in their contribution to the internal variability: net divergence * ΔT, SIA deficit * ΔT, and inverse snow depth * ΔT. It is worth noting, however, that their role in forced changes in ice production—as given by the ensemble mean—will also depend on the magnitude of respective forced trends exhibited (as shown in Figure 4.8).

4.3.3 Explaining forced changes in ice production

We apply our linear model—based on internal variability—to ensemble mean data in order to attempt to reconstruct forced changes in sea ice production throughout the full 1920–2080 timeseries. Figure 4.10 shows this reconstruction, using the model trained on a) 20C data only; b) RCP8.5 data only and c) the full timeseries. All three estimates successfully capture the overall shape and interannual variability in the ensemble mean over the full period. The timing of the 2010–2020 turning point from rising to falling ice production is also successfully resolved.

The lower panel of Figure 4.10 shows the contributions to the overall change in terms of the explanatory variables used in our linear model. Interpretation of these trends should critically consider that each regressor except for Sep 10 m T contains the product of surface air temperatures (as ΔT) and another climate variable. The trends of the underlying timeseries, as shown in Figure 4.8, are useful aids.

Perhaps the most striking effect is the rise and fall of ice production in the September open water setting, given by the SIA deficit * ΔT regressor. As the SIA deficit increases during c. 1980 to 2020 (seen as decreasing Sep SIA in Figure 4.8b), the contribution of this regressor—despite SAT warming—is to increase the ice production. The SIA deficit naturally approaches a maximum as Sep SIA approaches zero; once the September SIA has reached zero, no additional positive contribution to ice production can be made from this variable—the negative feedback on sea ice loss has reached a limit. The ensemble mean Sep SIA begins to slow in its decline to zero at around 2020. It is at this point that the atmospheric warming takes over in the SIA

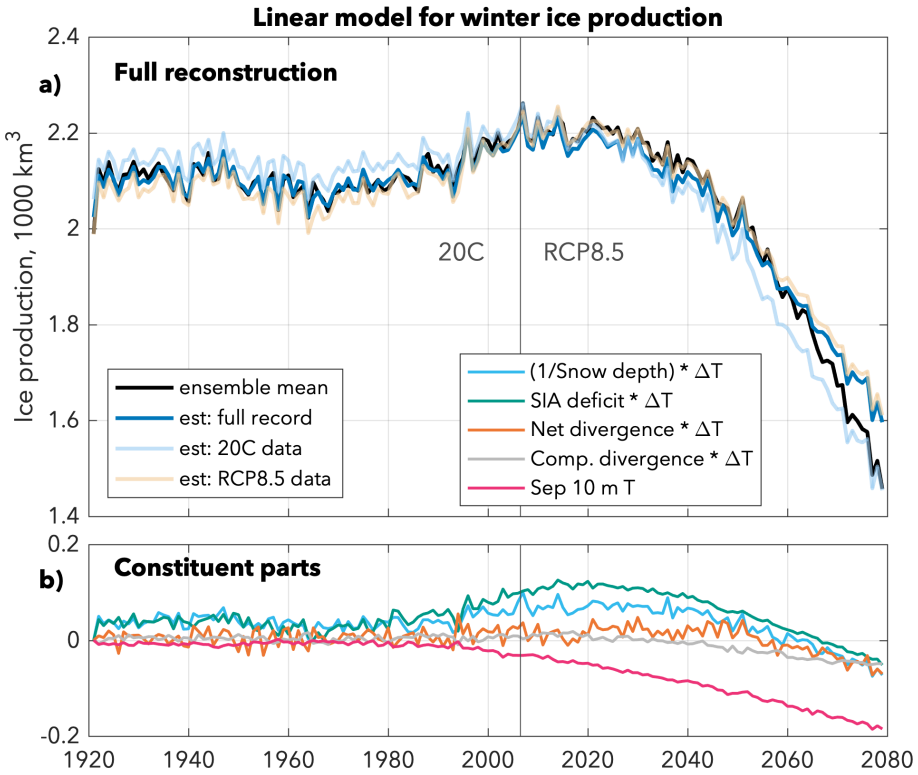


Figure 4.10: a) Ensemble mean winter sea ice production (black line), and reconstruction of ensemble mean using regressions trained on internal variability over the 20C (light blue line), RCP8.5 (light orange line) and full 1920–2080 timeseries (heavy blue line). Lower panel shows the contribution to the summed reconstruction made by different components of the linear model, plotted relative to the first winter (1920/1921).

deficit * ΔT regressor, resulting in a negative trend in the ice production attributable to this open water setting.

Changes in the snow thickness on sea ice are also responsible for a large part of the signal. As described in Section 4.1.1, thinning snow cover with anthropogenic warming (due to later freeze-up and summer melting over second-year ice), is a negative feedback on sea ice loss (Bigdeli et al., 2020; Merkouriadi et al., 2017; Notz, 2009). Indeed, we see that the inverse snow * ΔT regressor contributes to increasing ice production between c. 1980 and 2010, reaching a broad peak between c. 2010–2030. While snow continues to thin to 2080 (Figure 4.8f), after c. 2030 this thinning is out-competed by the effect of warming temperatures, and the regressor contributes to a decline in ice production.

The two divergence * ΔT terms show more muted forced changes, implying a close balance through time between the positive effects of divergence and the negative effects of increasing temperatures. This suggests that divergence will remain a meaningful negative feedback during the warming 21st century. The net area diverged * ΔT term also clearly contributes to ensemble mean interannual variability.

The September 10 m T term, though showing the weakest regression coefficient in the internal variability space, contributes markedly to the forced changes—indeed Figure 4.8e shows that Sep 10 m T exhibits a clear forced signal in RCP8.5 that rapidly departs from the range of 20C internal variability.

There is clearly, therefore, a role for ocean heat derived from summer heating in delaying the freezing season and thus decreasing ice production. But is there a role for ocean heat in changing growth rate or ice production once the freezing season has begun? We plot the mean winter heat fluxes from the ocean to ice, F_w, during the freezing season in Figure 4.11. Heat fluxes are generally low during 20C at c. 0.5 W/m^2, however show an accelerating rise throughout RCP8.5 to nearly 2 W/m^2 by 2080. This, however, does not appear to noticeably impede ice growth in CESM-LE; indeed, F_w is a statistically insignificant term when added to the linear models for both ice production and growth rate, even in RCP8.5. This indicates that our assumption regarding the relative smallness of F_w in comparison to F_c is robust and holds throughout the time under consideration.

4.3.4 Application to the observable Arctic

Having developed a linear model that succeeds in explaining forced changes in a coupled climate model, we now apply this model to observation-based estimates in order to estimate—and seek to explain—historical changes in ice production. Our choice of explanatory variables provides a far wider time window over which we can estimate ice production than direct observational estimation would allow. This is because direct estimation depends on satellite estimates of thickness—only available 2004–2008 and 2011 onward (e.g. Kwok, 2018).

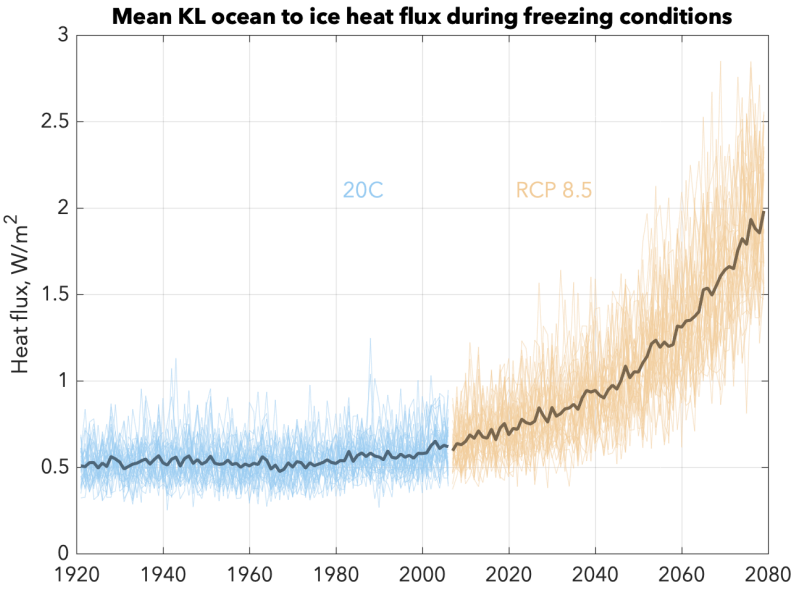


Figure 4.11: Mean ocean-to-ice heat flux in the Kara-Laptev seas during the freezing season (values retrieved from grid cells showing net ice growth). 20C shown in blue, RCP8.5 shown in orange. Ensemble mean shown by darker lines.

All of the observational estimates utilised here have their own associated errors, though these are not always readily available to the user. As such, we stress that our results must be interpreted as a 'best-guess'.

Comparison of changes in key climate variables: observation-based estimates and CESM-LE

In order to contextualise the changes exhibited in the relevant Kara-Laptev climate variables, we plot pan-Arctic spatial changes in the observation-based estimates (OEs) and the CESM-LE ensemble mean side-by-side in Figure 4.12. The figure shows these spatial trends as the difference between the 1980–1999 and 2000–2019 means. Note that in some cases the OE data does not span this entire window (see Section 4.2), but gaps are at most 3 years.

The ensemble mean CESM-LE changes robustly represent forced changes, and as such, internal variability should be largely averaged out. Similarly, we expect somewhat smoother spatial changes in the maps from CESM-LE as there is naturally a strong spatial component to internal

variability (e.g. Mahlstein et al., 2011). The OEs on the other hand, though we use a wide averaging window of c. 20 years, will include some internal variability.

Surface air temperature (SAT) in CESM-LE (Figure 4.12a) exhibits pan-Arctic warming, centred on the central Arctic and Beaufort/Chukchi/East Siberian Sea sectors, where it approaches 3 °C. By comparison, ERA5 (Figure 4.12b) shows strong warming in the northern Barents Sea of as much as 6 °C (this has been widely documented, see e.g. Lind et al., 2018). There is a secondary warm patch over the East Siberian and Chuckchi seas. Both CESM-LE and ERA5 show polar amplification of warming relative to lower latitudes, however the warming trend is significantly greater in ERA5, including in the KL region as can be seen in Figure 4.8a. The ERA5 warm bias over sea ice in winter of several °C (C. Wang et al., 2019) might explain the mean difference in the timeseries (Figure 4.8).

Changes in the September pattern of sea ice retreat are similar between CESM-LE and the NASA GSFC product (Figure 4.12c and d), but overall the observation-based losses are more severe, showing widespread 60% losses in the Chukchi/Beaufort region. Outside of the CAA, the strongest losses of 30% are centred over the East Siberian Sea in CESM-LE. The pattern of loss is similar in the KL region, though again more intense in the OE. This can also be seen in Figure 4.8; September sea ice area falls to near zero in 2007 and remains well below the CESM-LE ensemble mean after that.

The pattern of changing divergence is, as might be expected, far more spatially variable in Polar Pathfinder than in CESM-LE (Figure 4.12e&f). We do not plot contours in Figure 4.12e&f owing to this intense spatial variability (how much of which is instrumental or measurement noise is hard to say). The Polar Pathfinder data also exhibits more intense magnitudes of change, generally showing increases over the Arctic Ocean, with significant increases in the Beaufort sector as well as the Kara and Laptev seas. Increasing divergence in CESM-LE is smoothly distributed across the Arctic basin interior, and is more intense along the Eurasian coastline, though even here the trends are about half the magnitude of the equivalent changes in the Polar Pathfinder estimate. It is worth noting that the Polar Pathfinder data shows a more

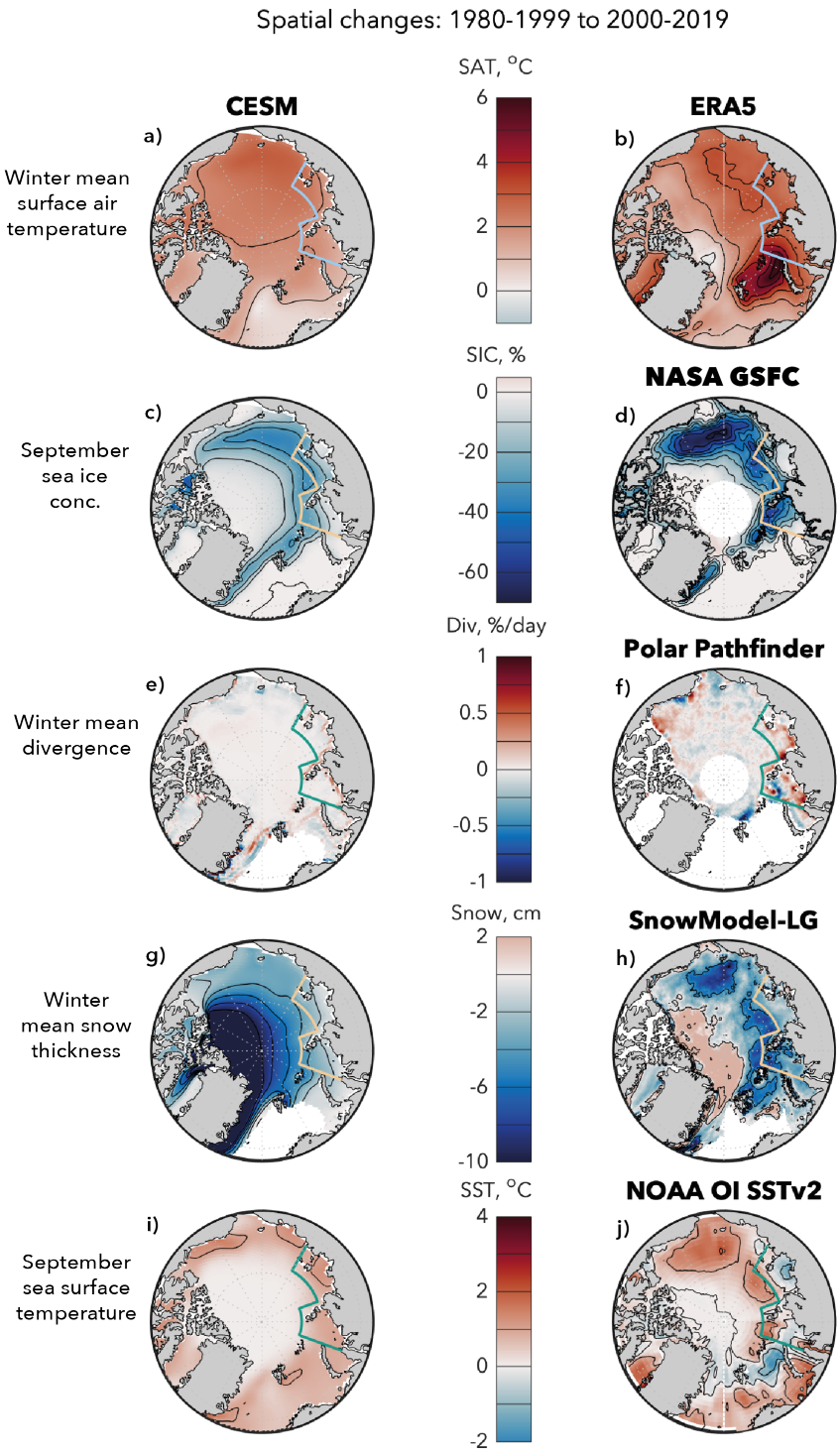


Figure 4.12: Comparison of the spatial pattern of ensemble mean changes in CESM-LE between 1980–1999 and 2000-2019 to changes in observation-based estimates over approximately the same time period. (See Section 4.2 for exact time periods covered.)

distributed increase in ice divergence in the KL region, whereas in CESM-LE the increase is restricted to the grid cells closest to the coast. A similar pattern is seen in the mean state (not shown) and is likely due to CESM-LE not simulating the winter expansion of landfast ice into the shallow sea, which moves the flaw lead well away from the coastline (c.f. Rigor & Colony, 1997). The slight decreases in divergence near the ice edge around Svalbard and in the Chukchi Sea in both datasets likely reflects a later freeze-up in those areas, such that ice is not present during the stormy early winter period. It is not an artefact of a shorter ice presence duration; means are only taken over the times that ice is present.

Snow thickness, of all the variables, exhibits perhaps the most striking difference between the OE and CESM-LE (Figure 4.12g&h). The centre of snow thinning in CESM-LE is in the region characterised by multi-year ice north of Greenland and the CAA. The loss exceeds 10 cm over most of this region, and might be related to summer melting of accumulated deep snow during this time period. This may be because model struggles to limit snow depths, whereas in nature winds tend to redistribute snow and blow snow into leads, thereby preventing excess thickening on Arctic sea ice except in topographic drifts. SnowModel-LG shows a very small increase in thickness in the same region, and instead shows centres of loss in a pattern that corresponds closely to the pattern of September sea ice loss from NASA GSFC (see Stroeve et al., 2020, for more analysis of spatial trends in SnowModel-LG). This is likely due to sea ice growth after the onset of early winter snow storms (a mechanism described by Merkouriadi et al., 2017).

The spatial pattern of changes in september SST is quite simple in CESM-LE (Figure 4.12i), involving warming constrained largely to the shelf regions, which are progressively ice free in the summer, allowing for increased solar heating (e.g. Maykut & McPhee, 1995). There is also warming in the Atlantic inflow regions that were never ice-covered, however. The spatial changes recorded in NOAA OI SST v2 (Figure 4.12j) data show strong warming in the Chukchi/Beaufort sector and around the interior side of the NASA GSFC ice loss pattern (Figure 4.12d). There is a slight cooling trend in parts of the KL seas, however according to

Timmermans and Labe (2020) these cooling areas are not statistically significant. The last two decades have seen a steady warming trend in the KL seas (Figure 4.8e).

Reconstructing historical changes in ice production

We next take the relevant climate variables from the observation-based estimates and apply them to the linear model for winter ice production in the KL seas, as derived from CESM-LE. Figure 4.13, shows the results of this reconstruction, in terms of both the overall change in ice production and the contributions of each constituent term. The changes are all relative to a value of 0 in the first winter of 1982/1983.

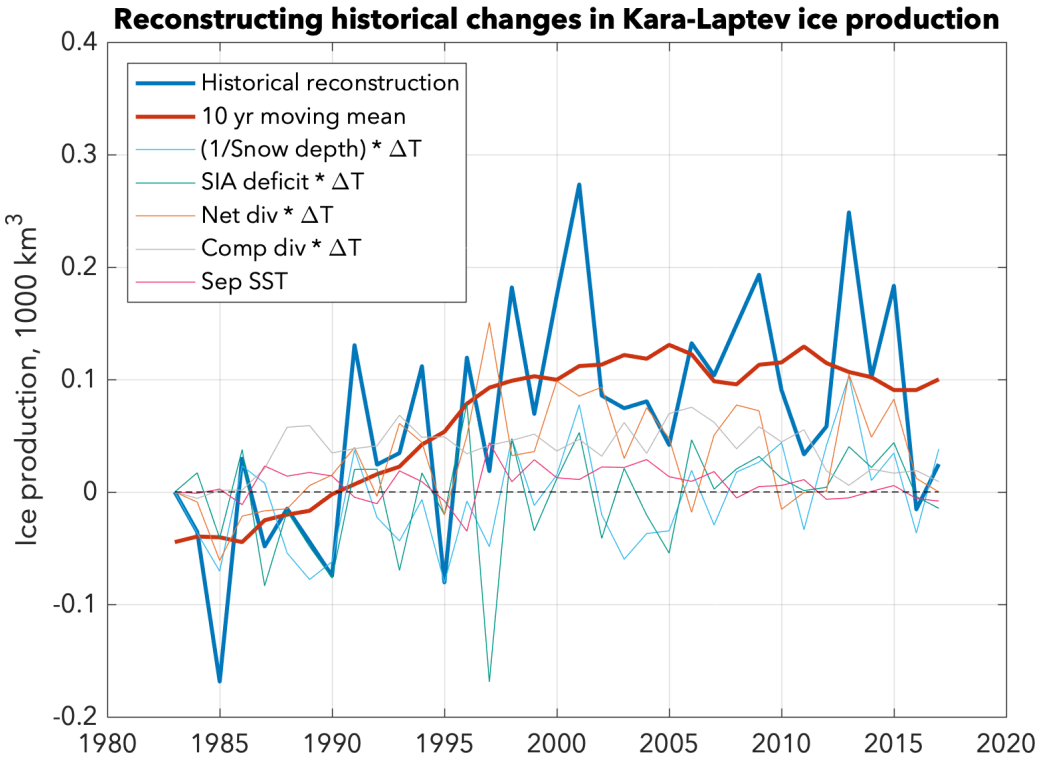


Figure 4.13: Reconstruction of historical changes up to 2016/2017 in the winter ice production in the KL seas relative to the first winter of the reconstruction: 1982/1983. Reconstruction uses climate variables from observation-based estimates and the linear model trained on CESM-LE internal variability.

The reconstructed ice production reconstruction (blue line) shows similar interannual variability to CESM-LE (Figure 4.6), and the 10-yr moving mean (red line) strikingly similar pattern

of change as the CESM-LE: increasing from 1983 to 2000 by order 100 km^3, before plateauing 2000–2010 and apparently beginning a decline after c. 2010. We see that the early decline of September SIA to zero and relatively high SAT in the low SIA years limits the positive contribution made by the SIA deficit * ΔT term. Given that the SIA deficit part of this product has already reached a maximum (as Sep SIA has declined to zero), we would expect hereon a warming SAT signal to cause this term to yield a negative ice production trend, as observed in the CESM-LE linear model (Figure 4.10b).

September SSTs have a fairly neutral influence overall; a result of the absence of a clear long-term trend (though there is a warming trend 2000–2020). The inverse snow depth * ΔT term causes marked interannual variability and a mildly positive trend overall: snow thinning only narrowly out-competes warming over this period in terms of promoting growth.

The contribution to ice production from the two divergent settings—the two divergence * ΔT terms—exhibit perhaps the strongest rises in the mid-part of the timeseries, out-competing atmospheric warming, until plateauing in the final c. 15 years, much like the overall ice production curve.

It is particularly notable that the recent warm Arctic winters of 2015/2016 and 2016/2017 (Boisvert et al., 2016; Ricker, Hendricks, Girard-Ardhuin, et al., 2017; Stroeve et al., 2018) are recovered as showing a steep drop-off in KL ice production, reaching lower values than exhibited since the mid-1990s.

4.3.5 Shifting patterns of winter ice production

Finally, we consider what these changes in the Kara and Laptev seas mean in terms of the regional patterns of ice production in the Arctic Ocean. In Figure 4.14, we show the spatial changes in the winter mean ice production across the Arctic Ocean relative to a reference period (1980–1999).

The map of ensemble mean ice production over the reference period (1980–1999) shows clearly

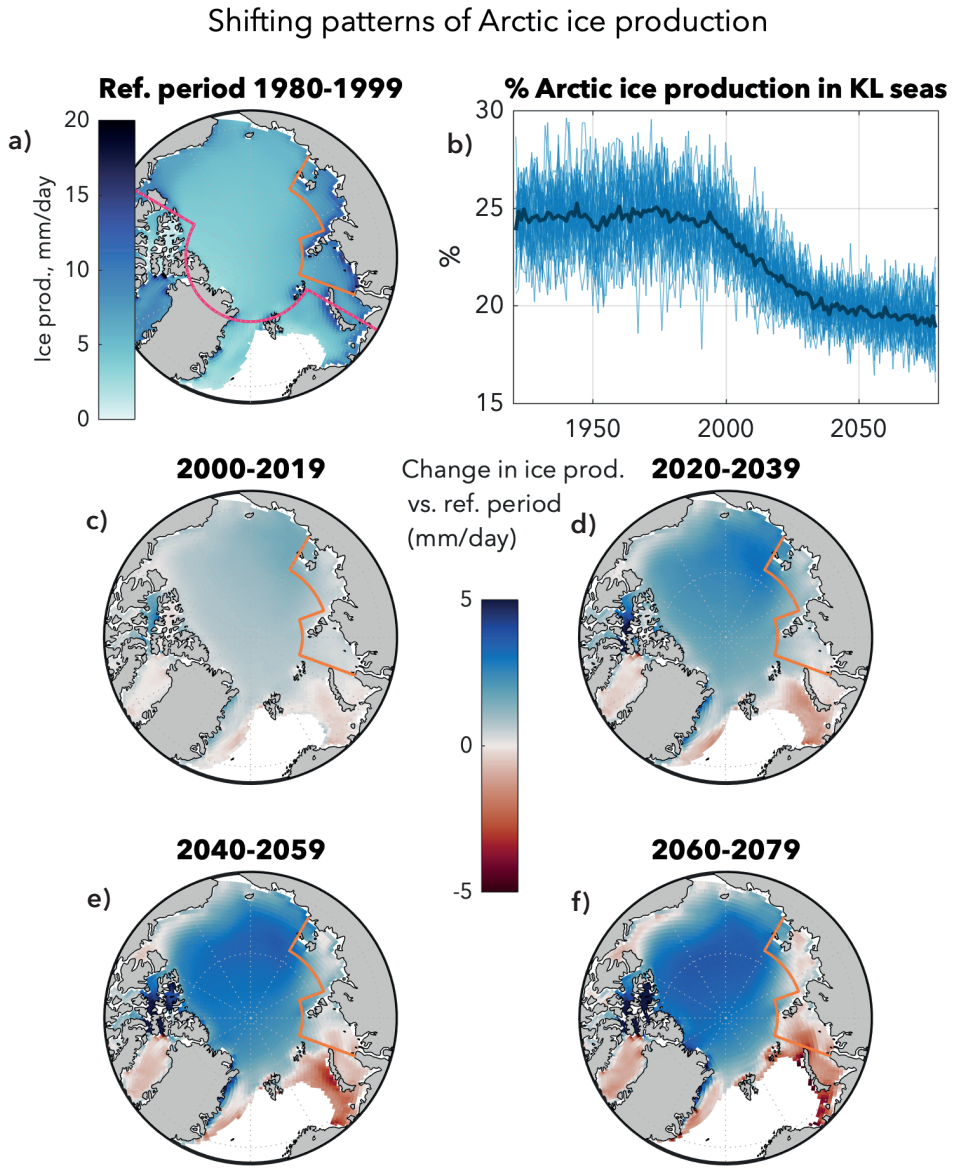


Figure 4.14: Shifting patterns of ensemble mean winter ice production in CESM-LE relative to a reference period 1980-1999 (a). b) shows the changing share of total Arctic ice production contributed by the KL seas. The Arctic region in question is enclosed by the magenta line in (a) and Bering Strait. Ensemble mean in (b) shown as darker line. Plots (c-f) show the spatial changes in ice production during sequential two-decade periods. Blue colour indicates more ice production; red indicates less. Ice production does not consider melting.

the outsized role of the Kara and Laptev seas in Arctic sea ice production. While only comprising 16% of the ocean area enclosed by the Arctic basin mask (indicated by magenta line in Figure 4.14, top left panel), the KL seas contribute a mean of c. 25% of the Arctic ice production until c. 1990. The share of ice production declines steeply during the first half of the 21st century, before following a shallower trend by c. 2040 to a value of 19% by 2080.

It might seem surprising that the share of ice production in the KL seas is in decline in the early 21st century even while the absolute ice production in the region is raised above mean 20th century values. Indeed, it can be seen in the spatial plots in Figure 4.14 that Kara and Laptev sea ice production is increased versus the reference period during the periods 2000-2019 (c) and 2020-2039 (d). But it can also be seen in these plots that this increase in ice production is generally less intense than that which is occurring elsewhere in the Arctic basin. (This trend of increasing ice production in the central basins is consistent with Petty et al. (2018), who document a rise in winter ice thickness in CESM-LE until c. 2060 in their western Arctic region.)

The underlying physics of sea ice growth are naturally the same in all regions, though the relative importance of different variables may vary. We may therefore extrapolate some of our findings from the Kara-Laptev seas to the central Arctic. Particularly, we would expect these increases in winter ice production in the Arctic basin to be driven primarily by the retreat of September sea ice, leaving a larger area of open water available for winter freeze-back. This is because these are areas that begin the RCP8.5 run with high concentrations of sea ice in September. We would also expect contributions to increased ice production from diminished snow cover and increased divergence. Unlike the Kara-Laptev seas, we would expect ocean-to-ice heat fluxes to be more important in the basin interior, particularly on the Eurasian Basin side, due to the presence of Atlantic Waters, and the prospect of a potentially weakening halocline. These ocean-to-ice heat fluxes should be easily accommodated in the regression model, as per Equation 4.1, though we leave expansion of this model to other areas of the Arctic to future work.

By 2040–2059 there are clear areas where reduction of ice production versus the reference period are evident in the KL seas (Figure 4.14e). This decrease in ice production is most intense in the Kara Sea, but also encompasses more or less the whole Laptev Sea by 2060–2079. This spatial pattern may be influenced in part by increasing ocean heat transport into the Kara Seas (Årthun et al., 2019).

4.4 Discussion

In CESM-LE, ensemble mean ice production in the Kara and Laptev seas passes a peak during 2010–2020. The timing of the turning point from rising to falling ice production appears to be primarily explained by the timing at which the September sea ice area approaches zero. After this point, the open water area available for freeze-back in the region cannot expand further, a fundamental upper limit on this negative feedback. Once this occurs, atmospheric warming means that the signal from the September open water setting (as captured in the linear model by the regressor: SIA deficit * ΔT) is one of declining ice production. We include the effect of sea ice divergence in terms of two variables: net area diverged * ΔT and compensated area diverged * ΔT. In both cases, continued increases in divergence balance warming until later in RCP8.5; warming begins to out-compete divergence after 2040–2050. Thinning snow cover is also a leading contributor to the rising ice production, but this negative feedback is also gradually overwhelmed by warming in the latter half of RCP8.5.

Physically, these first four explanatory variables are designed to capture the area and time-integrated growth rate or *efficiency*, while the September top 10 m ocean temperature captures the effect of decreasing *usage* of the ice factories: the shrinking growth season. We show in Section 4.3.2 that we can construct separate, skilful, linear models for the *usage* and *efficiency*, based on the different physics of these two different phenomena. This is what informs the construction of our model for winter ice production—which is a variable of wider climate and oceanographic interest.

The relative consistency of the ice production regression coefficients between the 20C and RCP8.5 runs (Figure 4.9) demonstrates that our linear model is physically useful in explaining changes in a range of climate settings. It would, however, break down when (or where) the assumption that the growth rate is primarily determined by F_c, not F_w, is violated. At this point oceanic heat fluxes would need to be included. While heat fluxes do increase in the region throughout RCP8.5 (Figure 4.11) these heat fluxes are statistically insignificant when inserted into our model during both 20C and RCP8.5.

The linear model for winter ice production is simple: it uses winter means and integrates over an area that includes contrasts in mean ocean and sea ice conditions. This makes it conceptually useful, but we note that more sophisticated models seeking even stronger statistical relationships could delve deeper into the seasonal and geographical structure of the variables. For instance, the monthly evolution of divergence and snow depth is undoubtedly important in determining the overall growth rate; given that thermodynamic changes in ice thickness go roughly with the square root of time, the early part of the season likely is most important for total ice production. A simple linear model that only considers winter means misses variability of this nature.

Nonetheless, the successful reconstruction of forced changes (Figure 4.10) means we can be confident of having isolated the key processes in a physically robust manner. This chapter thus builds on previous work by Stroeve et al. (2018) and Petty et al. (2018), who suggested that atmospheric and oceanic warming under anthropogenic climate change overwhelms negative feedbacks on sea ice loss based on changing correlations between surface air temperatures and ice growth.

Over the coming decades, we can expect ice production in the Kara and Laptev seas to decline. We can be confident of this because one of the leading negative feedbacks—the September open water area—has reached a limit and can no longer contribute additional ice production. In CESM-LE, this heralds the decline of the ice factories and we suspect the same will be true in the Arctic under continued warming.

We also expect the relative role of the KL ice factories in the Arctic sea ice budget to decline (Figure 4.14), as the September sea ice edge progressively migrates towards N Greenland and the pole, bringing negative feedbacks on sea ice loss into play in more central regions. In CESM-LE, the share of KL ice production in the Arctic basin declines from 25% in 20C to 19% by 2080 (it comprises 16% of the area; Figure 4.14b).

These shifting patterns of ice production may have implications for halocline stability in the Arctic. As ice production in the KL seas falls, we can expect halocline renewal via the 'advective mode' (Aagaard et al., 1981) to also decline. We can also expect sea ice import and accompanying summer melt in the Eurasian Basin and northern Barents Sea to fall. This decreased freshwater resupply should weaken the halocline as per the convective mechanism of halocline renewal (Lind et al., 2018; Rudels et al., 1994; Steele & Boyd, 1998). Furthermore, increasing ice production and brine rejection in the Eurasian basin interior may weaken the halocline by vigorous convection (Polyakov et al., 2020). We therefore suggest that this expected trend of decreasing on-shelf ice production and increasing off-shelf production should act to weaken the Eurasian Basin halocline, potentially favouring the development of deep convection during winter (Lique et al., 2018). How this effect will balance against increasing freshwater inputs from land (e.g. Zanowski et al., 2021) is uncertain. We discuss the implications of shifting patterns of ice production further in the Concluding Discussion (Section 6.4).

4.5 Conclusions

We offer our main conclusions below:

- Long term ice production in the Kara and Laptev seas can be understood through an idealised linear regression model including climate variables that are readily available from observation-based estimates
- The linear model assumes that growth rate is dominantly explained by conductive heat fluxes in the Arctic and that oceanic heat fluxes are negligible once freezing has begun.

This assumption appears to hold in the region in question up until at least 2080 in CESM-LE. September SSTs are invoked to explain a shortening growth season.

- The confounding correlation of surface air temperature with negative feedbacks is accounted for by constructing the conductive heat flux equation in a manner that reflects the growth rate equation, in which each of the regressors controlling growth rate has a linear dependence on the surface air temperature
- Once the September sea ice area approaches zero in CESM-LE, sea ice production begins to decline
- Application of the linear model to observation-based estimates suggests that ice production has peaked and is beginning to decline. Although these estimates carry significant uncertainty, the observation that SIA area in September has already approached zero adds credence to this suggestion.
- The relative importance of the Kara-Laptev shelf seas in Arctic ice production is expected to decrease. The shifting pattern of ice production towards the interior basins of the Arctic has potential implications for the stability of the Eurasian basin halocline.

Chapter 5

Effect of Wind-Driven Sea Ice Import/Export on Beaufort Gyre Adjustment

Abstract

The Beaufort Gyre (BG) is a wind-driven reservoir of freshwater situated beneath the climatological atmospheric anticyclone, the Beaufort Sea High, and is covered by mobile pack ice for most of the year. Liquid freshwater accumulation in and expulsion from this gyre is of critical interest to the climate modelling community, due to its potential to affect Atlantic ocean circulation. Here, we use forced model experiments to investigate whether wind-driven sea ice import to/export from the Beaufort Gyre region influences the gyre's processes of liquid freshwater accumulation or flushing under a stationary SLP forcing pattern. We suggest that differences between several models in simulated freshwater accumulation under a Beaufort High forcing pattern can be partially explained by the role of integrated wind-driven fluxes of ice across the region's boundaries. Using a regional setup of the MITgcm, we show with parallel experiments that freshwater changes are influenced by different ice import/export scenarios, which we bring about through an angular rotation of imposed wind over ice. Mechanistically, ice export and attendant thinning within the gyre is compensated by enhanced net thermodynamic ice growth within the gyre—a sink of liquid freshwater.

5.1 Introduction

The wind-driven Beaufort Gyre is the largest reservoir of liquid freshwater (FWC) in the Arctic (e.g. Carmack et al., 2016; Haine et al., 2015), storing a mean of 21,800 km^3 of FWC during 2003–2018 (Proshutinsky et al., 2019). During this 2003–2018 period, it has gained 6,400 km^3 of FWC, an increase of 40% relative to previous climatology (Proshutinsky et al., 2019). Its ability to store, and potentially discharge, significant volumes of freshwater makes its dynamics of key interest for climate modelling (Lique et al., 2016). This is because large fluxes of freshwater from the Arctic to the North Atlantic have the potential to impact global overturning circulation (e.g. Holliday et al., 2020; Jahn & Holland, 2013; H. Wang et al., 2018; Q. Yang et al., 2016), have been implicated in previous salinity anomalies in the subpolar North Atlantic (Belkin et al., 1998; Dickson et al., 1988), and are likely to increase in the future with climate change (Jahn & Laiho, 2020).

Here we investigate a hypothesis that is based on ideas presented in Chapter 3. Namely, that wind-driven import of ice into, or export from, the Beaufort Gyre may affect the liquid freshwater content of the gyre. This is because sea ice thickness is a key stabilising feedback on thermodynamic growth rate: thin ice grows faster than thick ice (e.g. Bitz & Roe, 2004). As such, we might expect sea ice import—which leads to dynamic thickening—to suppress ice growth and transfer of FWC from the liquid to solid reservoir, leading to a relative freshening of the ocean. Volumetric sea ice export, on the other hand, causes dynamic thinning, whether by divergence and the formation of (sea ice cracks under tension) or by advection of thinner ice into the region, and thicker ice out of the region. Sea ice export and attendant dynamic thinning should thus promote more rapid growth during the freezing season.

As we have seen in Chapter 3, the effect of the summer melt season must also be considered. The Beaufort Sea represents a region where ice often does not survive the summer (Stroeve et al., 2011, see also Chapter 3), and as such we might expect the summer changes to favour the proposed connection between sea ice export and liquid freshwater loss and sea ice import and liquid freshwater gain, rather than oppose them (as discussed in Chapter 3). This is because,

if the majority of sea ice melts in the region in the summer, thicker ice (due to sea ice import) can yield a greater melt volume; thinner ice (due to sea ice export), yields a lesser melt volume.

As illustrated schematically in Figure 5.1, sea ice import into/export from a region can occur under stationary, non-divergent, SLP patterns for three main reasons: a) ice motion does not follow isobars, resulting in divergence/convergence; or due to the wind forcing pattern projecting onto either b) ice mobility gradients or c) ice thickness gradients. Note that (b) and (c) do not hold if the region under consideration encompasses complete (closed) streamlines of ice. In this analysis though, these mechanisms are potentially relevant. There is a separate question of whether the choice of region is optimal for the physical processes under examination (Section 5.2.2). In the following, where we refer to sea ice export or import, we refer to the Beaufort Gyre region, and not the whole Arctic Ocean.

As sea ice characteristics in the Arctic change, we might expect trends in properties relevant for sea ice import/export: the angle of ice motion under geostrophic winds, gradients in mobility and thickness may all be expected to change. The role of sea ice import/export in affecting liquid FWC budget is therefore also subject to change. Future studies may be able to delve deeper into such changes and their implications for Beaufort Gyre freshwater adjustment.

We focus here on the response of the sea ice field to a stationary pattern of wind forcing that is designed to excite spin-up or spin-down of the Beaufort Gyre, and thus affecting its liquid FWC storage. Two such wind forcing patterns are used: the 'Beaufort Gyre Plus' (BGP) anticyclonic pattern and the 'Beaufort Gyre Minus' (BGM) cyclonic pattern. We rely on the experimental set up and collaborative effort proposed by J. Marshall et al. (2017).

We choose this experimental design because the representation of wind-driven freshwater changes in the Beaufort Gyre is a key modelling challenge, and this is the most direct route to understand if sea ice import/export may be a potential source of variability in simulations of such processes.

This chapter is structured as follows. In Section 5.1.1 we provide an introduction to the fresh-

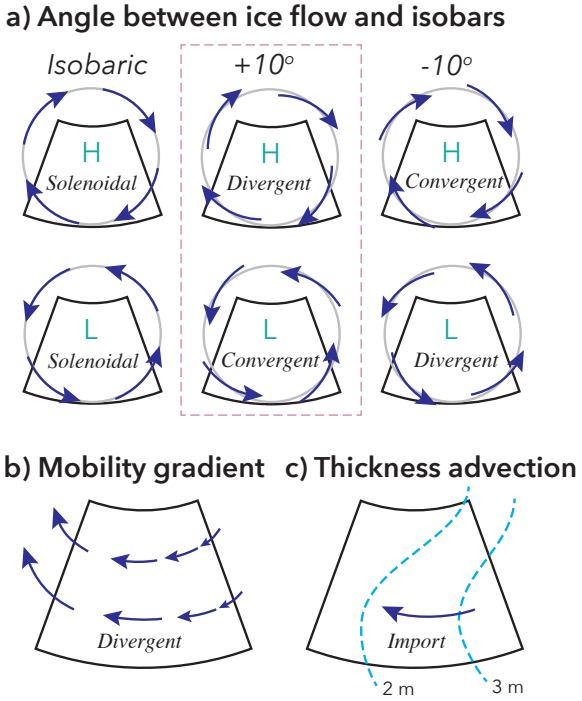


Figure 5.1: Possible mechanisms leading to sea ice export or import into the BG region (black box) under a stationary SLP anomaly. Blue arrows indicate ice motion. In (a), grey circles represents isobars, 'H' or 'L' indicate high or low SLP. Note that divergence corresponds to export and convergence to import in case (a). However in case (b) there may be confounding correlations with thickness advection. Dashed magenta line indicates the scenarios we attempt to induce in Section 5.3.

water dynamics of the Beaufort Gyre, before reviewing wind-driven sea ice motion in Section 5.1.2, which in our hypothesis is implicated in affecting liquid freshwater changes. In Section 5.2, we introduce a set of coordinated experiments led by J. Marshall et al. (2017) that focuses on isolating the response of freshwater in the Beaufort Gyre to the BGP and BGM forcing patterns. Using four different ice-ocean models, we assess the potential role of sea ice volume import/export in the intermodel spread in the simulated freshwater changes. In Section 5.3, we investigate the role of sea ice export/import on liquid FWC adjustment in one of the models in our ensemble (the MITgcm). We do this by performing parallel experiments with a 10° rotation of imposed wind forcing vectors over sea ice in order to trigger different ice volume flux scenarios. In Section 5.3.3, we introduce a simple source-sink model in order

to interpret these results in the context of theory. We then discuss the implications of our findings in Section 5.4 and offer conclusions in Section 5.5.

5.1.1 The Beaufort Gyre and its freshwater content

Above the core of the Atlantic Water layer, the water column structure in the Arctic Ocean is established by variations in salinity, rather than temperature; it is a so-called β-ocean (Carmack, 2007). As a result the Arctic Ocean, which receives an abundance of freshwater thanks to its position as a node of the global hydrological cycle (e.g. Carmack et al., 2016; Haine, 2020), is capped by a cold and relatively fresh layer of seawater, and the strong stratification across the halocline limits fluxes of heat from Atlantic waters below (e.g. Aagaard et al., 1981). In the Western Arctic, relatively fresh waters of a Pacific origin interleave between the surface mixed layer and Atlantic Waters, further strengthening the stratification and effectively isolating Atlantic Waters from the surface (McLaughlin et al., 2004; Steele et al., 2004). Because of their position at the surface of the water column, fresh waters receive vorticity and momentum from atmospheric winds, either directly or via sea ice.

The circulation of the Beaufort Gyre is sustained by the anticyclonic winds of the climatological Beaufort Sea High (Serreze & Barrett, 2011), driving Ekman convergence and halocline deepening within the gyre (Proshutinsky et al., 2002). Hydrographic data and satellite-derived measurements of sea surface height have revealed a substantial freshening of the Beaufort Gyre since the mid 1990s (Giles et al., 2012; Krishfield et al., 2014; Proshutinsky et al., 2009; Proshutinsky et al., 2019; Rabe et al., 2011). In particular, Proshutinsky et al. (2019) report an increase in FWC of 6,400 km^3 over their observational record of 2003–2018. Note that freshening of the gyre likely began in earnest around 2000 (Giles et al., 2012). These changes are thought to have been driven by a combination of a general increase in anticyclonic atmospheric circulation since the mid-1990s, increases in the surface anticyclonic stress due to a changing sea ice cover, the direct contribution of sea ice melt, and redirection of low salinity flows from the Mackenzie River and the Bering Strait by winds (Armitage et al., 2017; Giles

et al., 2012; Proshutinsky et al., 2019; Q. Wang et al., 2018). In tandem, the kinetic energy of the gyre has approximately doubled during the same period (Armitage et al., 2017; Regan, Lique, Talandier, et al., 2019).

While the winds over the Canada Basin vary on a range of timescales, the time-mean wind stress is anticyclonic and the resulting time-mean Ekman transport is convergent (e.g. Ma et al., 2017). One or more stabilising processes must thus exist to oppose perpetual Ekman-driven halocline deepening and freshwater accumulation (Manucharyan et al., 2016). Mesoscale eddies, activated by baroclinic instability, may act to flatten the slope of the halocline around a convergent lens (J. Marshall et al., 2002), and have been shown in eddy-resolving models to sustain a realistic Beaufort Gyre-like halocline (Manucharyan & Spall, 2016). The halocline depth and equilibration timescales are then inversely related to the mesoscale eddy diffusivity (Davis et al., 2014; Manucharyan & Spall, 2016). The other principal process opposing freshwater accumulation under anticyclonic winds arises from reductions (or reversals) of the anticyclonic ice-ocean shear. As the geostrophic circulation spins up, the relative stress imparted decreases (Zhong et al., 2018). During the winter, internal stresses within the pack ice can slow ice motion considerably, such that ice acts as a drag on the ocean currents and imparts cyclonic stress, even under anticyclonic winds (S. Dewey et al., 2018; Meneghello, Marshall, Timmermans, et al., 2018): a mechanism dubbed the *ice-ocean governor* (Meneghello, Marshall, Campin, et al., 2018). Doddridge et al. (2019) combine Ekman pumping, eddies and the *ice-ocean governor* in a single analytical model, and show that the adjustment timescale of the gyre to forcing is multi-year to decadal. In chapters 1 and 2, we determine a similar range of timescales for Arctic-wide adjustment of FWC from comprehensive couple climate models (Cornish et al., 2020; H. L. Johnson et al., 2018).

In recent years, the role of bathymetry in the dynamics of the Beaufort Gyre has begun to be elucidated. Using an eddy-resolving model, Manucharyan and Isachsen (2019) demonstrate—with reference to Eady (1949) theory—that the steep continental slopes bordering the gyre stabilise halocline slopes, favouring stronger circulation, a deeper halocline and prolonged

equilibration timescale. Similarly, Regan, Lique, Talandier, et al. (2019) show with a high-resolution regional model that the response of eddy kinetic energy to the intensification of the gyre is muted, because of the propensity of the gyre to expand outwards, thereby avoiding halocline deepening except for along the continental slopes where the gyre is constrained—and, halocline slopes are stabilised. Observations support this idea that the gyre is able to expand geographically and its centre wander in response to atmospheric forcing (Regan, Lique, & Armitage, 2019).

Hitherto un-explored, however, is the role that sea ice may play in redistributing freshwater into and out of the Beaufort Gyre, either in observations or models.

5.1.2 Sea ice motion and freshwater redistribution

By acting as a vector between locations of freeze and thaw, sea ice motion redistributes freshwater around the Arctic (Steele & Flato, 2000). Furthermore, the distribution of sea ice thickness on the surface of the ocean is a strong control on the local growth rate of ice, and therefore the local exchanges of freshwater with the ocean. This is because the growth rate of Arctic sea ice is dominantly explained by the conductive heat loss through the ice and overlying snow; a flux that is inversely proportional to the thicknesses of both layers (e.g. Petrich & Eicken, 2010, see also Chapter 4). This is especially true in the Canada Basin, where heat fluxes in the surface mixed layer to the underside of the ice are low, generally < 1 Wm^2 (Shaw et al., 2009). These heat fluxes are sustained predominantly by solar heating in the summer (Maykut & McPhee, 1995) because heat fluxes across the base of the surface mixed layer from warmer waters below are so low, associated with low vertical mixing (Fer, 2009; Shaw & Stanton, 2014; Timmermans et al., 2008).

Strain in the sea ice velocity field modifies the thermodynamic growth rate by affecting ice thickness. In leads, which form in zones of sea ice divergence, winter-time freezing and attendant heat fluxes to the atmosphere are enhanced by 2 orders of magnitude relative to multi-year ice (Alam & Curry, 1997; Hibler, 1979; Maykut, 1982), meanwhile sea ice convergence

suppresses these fluxes. On the other hand, sea ice divergence permits increased solar heating of the surface ocean during summer (Maykut & McPhee, 1995), which is the primary driver of summertime sea ice melting (Perovich et al., 2008; Perovich et al., 2011). In addition, simple advection can also modify the local thermodynamic growth rate by changing the local ice thickness. Volumetric sea ice import/export can involve contributions from both advection and strain in the ice velocity field.

The Beaufort Gyre region occupies a part of the Arctic Ocean that is characterised by a gradient in sea ice characteristics, from generally older, thicker and slower ice to the north and east, and more mobile, younger and thinner ice to the west. This gradient is seen in estimates of: a) thickness from CryoSAT-2 and ICESat (Kwok, 2018), b) multi-year ice coverage from QuikSCAT and ASCAT retrievals (Polyakov et al., 2012), and c) the relationship between geostrophic wind and sea ice motion (Kimura & Wakatsuchi, 2000; Kwok et al., 2013). With the retreat of multi-year sea ice towards the pole and northern sides of the CAA and Greenland, this gradient is also shifting (e.g. Maslanik et al., 2007; Maslanik et al., 2011). Strong wind forcing can, however, advect the multi-year ice pack over the Beaufort region, as observed during past (Stroeve et al., 2011) and recent (R. D. C. Mallett et al., 2021) anticyclonic AO conditions.

In this chapter, we investigate whether the simulated liquid freshwater balance of the Beaufort Gyre in climate models is sensitive to the representation of wind-driven sea ice export or import into the region. We speculate that such import/export may manifest in different ways (Figure 5.1), and affect liquid freshwater via the stabilising feedback of thickness on thermodynamic growth rate (Bitz & Roe, 2004). We pay particular attention to the angular relations between SLP contours, surface winds, and sea ice motion; relevant for mechanism (a) in Figure 5.1.

It is an oft-cited rule of thumb that sea ice in the northern hemisphere drifts at about 2% of the surface wind speed, and at an angle 30°–45° to the right of the surface winds (Colony & Thorndike, 1984; Nansen, 1902; Rigor et al., 2002; Thorndike & Colony, 1982). The surface wind is itself slower than the geostrophic wind and rotated approximately 30° to its left, such

that the sea ice drifts at approximately 1% of the speed of geostrophic winds, and in a direction that is generally somewhere between along isobars (isobaric) and 15° to the right of isobars (Kimura & Wakatsuchi, 2000; Thorndike & Colony, 1982). Indeed the atmospheric and oceanic boundary layers either side of the ice surface exhibit similar rotational dynamics, controlled by the same physics, as captured by Rossby similarity theory (McPhee, 1981, 2012; McPhee & Smith, 1976). Figure 5.2 illustrates one manifestation of these relationships (the angles can vary widely).

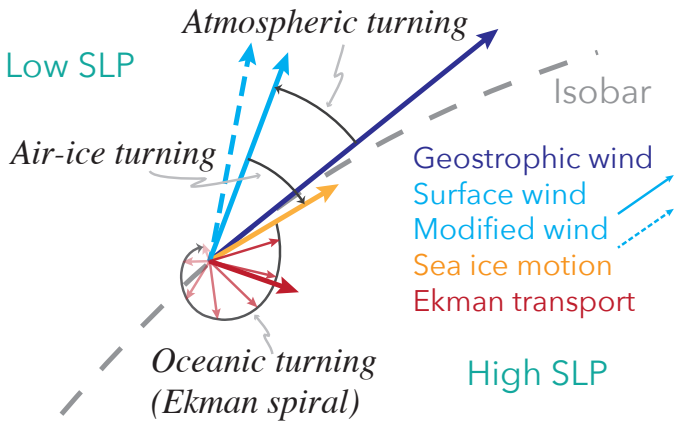


Figure 5.2: Plan-view schematic to illustrate the angular relationships between geostrophic winds, surface winds, sea ice motion and Ekman layer ocean velocities, in the absence of surface geostrophic ocean currents. The modified wind is used to trigger different sea ice export scenarios in Section 5.3.

While the drift of sea ice on short timescales (up to a month) can be predominantly explained by surface winds, a greater role for ocean currents emerges on longer timescales and at lower wind speeds (Colony & Thorndike, 1984; Thorndike & Colony, 1982). As such, tractions on the ice applied by the atmosphere and ocean are both dominant terms in the sea ice motion balance. However, a more complete description of sea ice motion can be obtained by including the forces arising from Earth's rotation, internal stresses, and the tilt of the sea surface (e.g. McPhee, 2012). The turning angle of ice relative to surface winds also varies substantially with these parameters (Park & Stewart, 2016), and indeed observations show a wide range of angular relationships, and a seasonal cycle with deviations further to the right of isobars in

the summer (Cole et al., 2017; Heorton et al., 2019; Thorndike & Colony, 1982).

While turning angles for sea ice motion relative to wind and ocean stresses may be prescribed based on empirical relationships (e.g. Hibler, 1979), more sophisticated models with coupled systems and sufficient vertical resolution to simulate the rotational physics may directly solve for these parameters. These models show a wide range of turning angles and often disagree markedly with observations (Girard et al., 2009; T. Martin & Gerdes, 2007). The angular deviation of ice motion from wind direction remains a key source of uncertainty in sea ice representation (e.g. McPhee, 2012).

5.2 Coordinated Climate Response Function (CRF) experiments

In this section we capitalise on a suite of existing simulations coordinated by J. Marshall et al. (2017). This series of Climate Response Function (CRF) experiments involves the participation of a number of modelling groups; a subset of which we have secured the additional parameters from necessary to investigate the subject matter of this chapter, namely exploring the implications of sea ice import/export for liquid FWC changes in the Beaufort Gyre. We first introduce the experimental rationale and design, the models involved and diagnostics we compute, before outlining results. These results motivate the experiments presented in Section 5.3.

5.2.1 CRF experiments: background

A CRF experiment involves observing how a model responds to an abrupt and sustained change in some aspect of model forcing. In Chapter 3, we also perform similar abrupt forcing experiments, and study the resulting 'anomalies' or 'responses'. Here, we use the terminology 'CRF' for consistency with the coordinated modelling effort (J. Marshall et al., 2017) that this chapter contributes towards. A CRF is necessarily a response to a sustained, abrupt change in forcing, whereas in chapter 3 we studied anomalies to a forcing after that forcing was 'switched

off', as well as when it was 'switched on'.

CRF experiments have proven useful in cleanly delineating relationships in the climate system, including responses to changes in: the concentration of greenhouse gases, ozone or aerosols; wind patterns; river or glacial meltwater runoff (e.g. Good et al., 2011; Good et al., 2013; Lambert et al., 2019; J. Marshall et al., 2014; Muilwijk et al., 2019). The CRF (or *step* response function) is the time integral of the characteristic *impulse* response function. The latter can be convolved with a time history of the forcing to estimate a time history of the response, as per linear response theory (e.g. Hasselmann et al., 1993). Linear response functions can also be derived directly from long control runs of fully coupled models (e.g. Kostov et al., 2017), and convolved with observationally-derived forcing timeseries in order to compare against nature (e.g. chapters 1 and 2; Cornish et al., 2020; H. L. Johnson et al., 2018). In model intercomparisons, climate response functions offer a means to go beyond comparing mean states and benchmark across models how climate variables respond to specific forcings. These comparisons can further provide the opportunity to identify the underlying causes of these differences, informing both model development and climate understanding.

We rely here on the coordinated CRF experiments designed by J. Marshall et al. (2017) to probe the behaviour of key "switches" in the Arctic Ocean; an effort in collaboration with modelling groups under the auspices of the Forum for Arctic Modelling and Observational Synthesis (FAMOS; Proshutinsky et al., 2016), the successor of AOMIP (Proshutinsky et al., 2011). The first such coordinated series of experiments is presented and analysed by Muilwijk et al. (2019), and focuses on ocean and sea ice responses to changes in the strength of the Greenland Sea Low. In this chapter, we present early results from experiments designed to understand the response of the Beaufort Gyre to abrupt wind-driven changes in the strength of the Beaufort High, an effort led by authors J. Marshall, G. Meneghello and J. Scott, as outlined in J. Marshall et al. (2017). We require additional parameters to the study led by Marshall et al., and rely on the output from CRF experiments conducted by four contributing modelling groups: Alberta, FESOM, MIT and NorESM.

5.2.2 Experimental setup

The four contributing ice-ocean models have different resolutions, domains and atmospheric forcing. The experimental procedure involved perturbing these models with exactly the same 10 m wind anomaly, by adding this perturbation pattern to the original forcing fields. Two anomaly patterns were used here: one that corresponds to a strong Beaufort Sea High (BGP, for Beaufort Gyre Plus), and one that corresponds to relatively lower pressure over the same region (BGM, for Beaufort Gyre Minus). The anomalies are centred on 77 °N, 149 °W, with a radius of influence on the order of 1000 km. This choice of location is based on analysis of 1948–2015 6 hourly NCAR/NCEP atmospheric reanalysis for centers of action and typical magnitudes (J. Marshall et al., 2017). The peak magnitude of the perturbations is 4 hPa, a magnitude chosen to be representative of multi-year to decadal trends. The 10 m winds are then computed using the relation to the geostrophic wind in Equation 5.1, as per Proshutinsky and Johnson (1997):

$$W_s = 0.7 \times \begin{bmatrix} \cos 30 & -\sin 30 \\ \sin 30 & \cos 30 \end{bmatrix} \times W_g \tag{5.1}$$

Note that in nature the angle and speed of the 10 m wind associated with a given geostrophic wind would vary in time and space according to factors such as the roughness of the ice surface (McPhee, 2012). The surface wind anomalies and associated SLP patterns are plotted in the lower panel in Figure 5.3.

Control runs were archived after some initial "spin up" time (J. Marshall et al., 2017). The perturbations were then applied abruptly to the control runs and sustained—in parallel–for 30 years. The CRFs are then given determined by the anomalies in the perturbed run versus the control run.

In all models, we compute diagnostics within a bounding box spanning 130 °W–170 °W and 70.5 °N–80.5 °N (see outline in Figure 5.3). This area definition corresponds closely to that

used in observational studies (Proshutinsky et al., 2009; Proshutinsky et al., 2019). There are drawbacks to this definition, however—not all forced ice-ocean models show a gyre that is tightly constrained within this area, (see, e.g. Ilicak et al., 2016). Indeed observations and models suggest that the gyre can expand toward the interior of the Arctic as it accumulates freshwater (Regan, Lique, & Armitage, 2019; Regan, Lique, Talandier, et al., 2019). Nonetheless, the centre of the perturbation pattern lies within this region and therefore our bounding box captures the centre of gyre intensification.

The principal diagnostics that we present here are: (1) the total freshwater content, as

$$\mathrm{FWC}(t) = \iiint_{z(S=S_{ref})}^{0} \frac{S_{ref} - S}{S_{ref}} dV \tag{5.2}$$

measured relative to a reference salinity (S_{ref}) of 34.8, as per Aagaard and Carmack (1989); (2) the sea ice volume; (3) sea ice export from the region. For the latter two diagnostics, snow is included after conversion to a sea ice volume equivalent using a conversion factor of 330 kgm^{-3}/910 kgm^{-3}, according to the assumed densities of snow and ice, respectively.

5.2.3 Models used

Basic information about the participating models is shown in Table 5.1. The University of Alberta group contribute a regional version of NEMO (Bourdallé-Badie et al., 2019); colleagues at AWI contribute the unstructured mesh model FESOM (Danilov et al., 2015; Danilov et al., 2004); the MIT group contribute a regional configuration of MITgcm (J. Marshall et al., 1997); and collaborators at the University of Bergen contribute simulations from NorESM (Bentsen et al., 2012).

The models are all ice-ocean models, with prescribed atmospheric forcing. The Alberta model uses a repeated 2002–2016 forcing, and FESOM uses a "normal year" forcing. Because 30 years are required for the CRF comparisons, these shorter climatologies must be repeated. The other models are forced by climatologies that exceed 30 years in length.

Table 5.1: Information about participating models

Group	Ocean model	Ice model	Horizontal res.	Domain/grid
Alberta	NEMOv3.4	LIM 2	Nominal 0.5°	Regional/tripolar ORCA05
FESOM	FESOM	FESIM	25 km Arctic	Global/unstructured
MIT	MITgcm	MITgcm	36 km	Regional/cubedsphere
NorESM	NorESM-O	CICE 4	Nominal 1°	Global/tripolar
	Forcing		Top cell	S restoring
Alberta	CGRF (Smith et al., 2014)		1.0225 m	No
FESOM	CORE normal yr. (Griffies et al., 2012)		10 m	No
MIT	JRA-25 (Onogi et al., 2007)		5 m	No
NorESM	20CR (He et al., 2016)		2.5–10 m	Yes

All models use a 0° turning angle in the ice-ocean stress. The implicit assumption in the use of this zero value is that the upper ocean vertical resolution is sufficient to resolve the dynamics of the ice-ocean boundary, without needing a prescribed adjustment to correct for the uppermost ocean cell vertically integrating too much of the Ekman spiral (consider Figure 5.2). The uppermost ocean grid cell vertical resolution is listed in Table 5.1 and gives us an indication of whether this assumption is fair.

5.2.4 Coordinated CRF experiment results

In Figure 5.3 we present the CRFs for each model under both the BGP and BGM wind forcings. The magnitude and timescale of freshwater accumulation is comparable between models, with less than a factor 2 difference between the maximum and minimum FWC anomalies at the end of 25 years. Here, we focus on the possible links between these freshwater CRFs and the CRFs of sea ice export/import, which is calculated as the net sea ice volume transport across the boundaries of the region (delineated by the black box on maps in Figure 5.3). More detailed analysis of other aspects of the freshwater CRFs, with more participating models, will be the subject of a subsequent study led by J. Marshall, G. Meneghello and J. Scott.

Two models show approximately no response in ice volume export or import under BGP: the Alberta model and the MITgcm, while the other two show ice export from the region. The

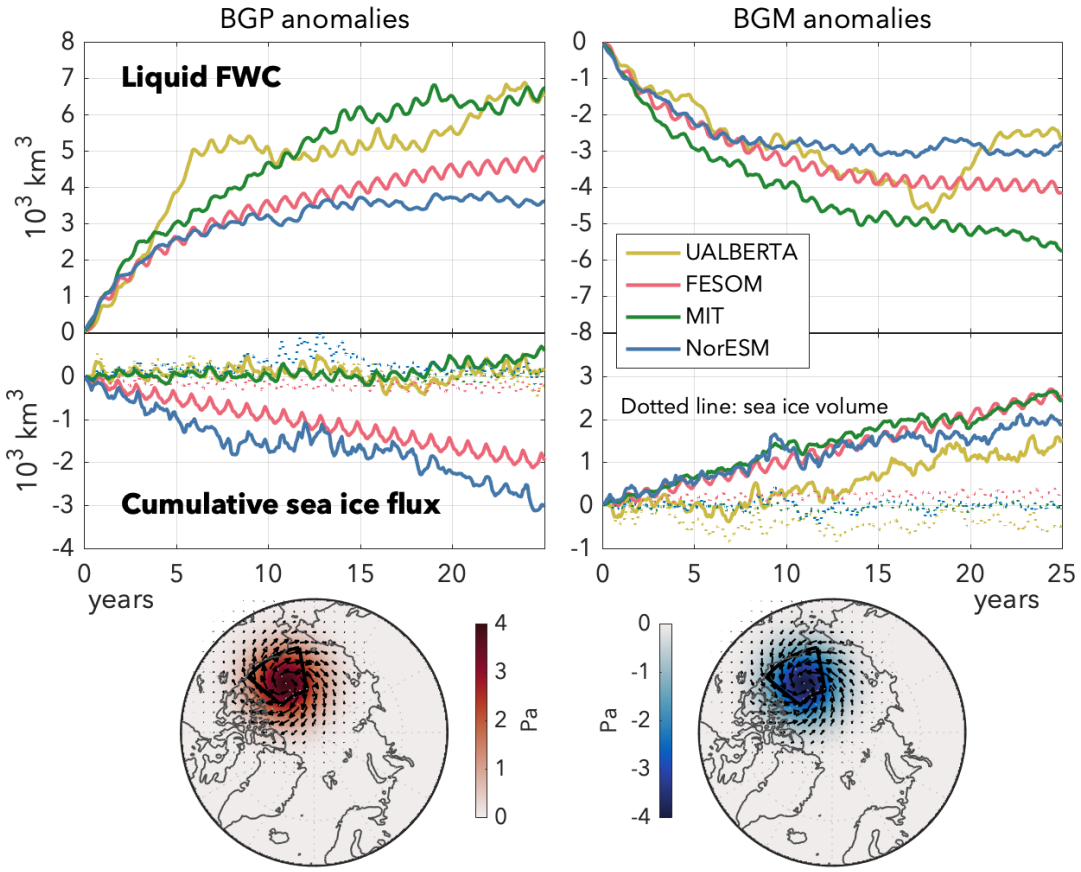


Figure 5.3: BGP and BGM CRFs for each model. Upper row: liquid FWC responses. Lower row: cumulative sea ice flux responses. Dotted lines correspond to sea ice volume responses. Lower panel: corresponding anomaly patterns, BGP on left and BGM on right.

cumulative sea ice export reaches 2,000 km^3 in FESOM and 3,000 km^3 in NorESM by the end of the 25 year comparison period. Meanwhile, both models show muted responses in sea ice volume within the region (as do all models). By mass conservation, the difference between sea ice volume and cumulative sea ice export must be balanced by sea ice growth—the influence of precipitation on ice is negligible (precipitation fields are unaltered and the ice area changes are small).

Because the growth rate of sea ice is inversely proportional to its thickness (e.g. Petrich & Eicken, 2010), ice export and attendant dynamic thinning should accelerate thermodynamic

sea ice growth during the freezing season (as we explore in chapters 3 and 4). Indeed, in an Arctic Ocean with a thinner ice pack, winter growth rates are higher (e.g. Petty et al., 2018). Enhanced winter sea ice growth rates constitute a sink of liquid FWC. As seen in Chapter 3, summertime melting may accentuate or reduce these changes, depending on the region in question. As described in Section 5.1, we have good reason to suspect that in the Beaufort Sea region, summertime melting may in fact act to reinforce the proposed link between sea ice export an liquid FWC. We propose that this may be the case due to lower sea ice availability due to dynamic thinning, which means—in a region where most sea ice melts—a smaller resupply of the liquid FWC reservoir by melting. Further investigation is required to confirm whether these seasonal dynamics are at play in these simulations.

We suggest that this proposed link between sea ice export and net thermodynamic ice growth rate is at play in NorESM and FESOM, and that persistent ice export represents a sustained sink of liquid freshwater, as freshwater is transferred from the liquid reservoir to the solid phase, then exported out of the region. These two models do indeed show weaker accumulation of FWC under the Beaufort high than the models with no net ice export, in line with this proposed mechanism.

All models show some ice import into the Beaufort Gyre area under the BGM. The Alberta model shows a muted response in the first ten years before exhibiting a similar rate of import to the other models, which show remarkably similar accumulations of ice within the region. Again, all models show a muted response in sea ice volume (the Alberta model shows a reduction, but this never exceeds 1,000 km^3). The difference between accumulated sea ice import and sea ice volume changes in these models can be reconciled by an overall reduction in growth rate. This is again in line with the operation of a stabilising feedback of sea ice thickness on growth rate. A reduction in sea ice growth rate implies a relative gain in liquid freshwater—in the case of BGM, a weaker freshwater loss. While this mechanism may be important in the individual models, its role in explaining differences between the models' BGM responses can only be small because the differences in ice import are small.

5.3 MITgcm modified wind experiments

In order to directly test the sensitivity of freshwater accumulation in the study region to wind-driven ice export/import, we perform dedicated experiments in the MITgcm model. In these experiments, we seek to actively perturb the sea ice trajectories by modifying the nature of the wind forcing. In this section, we first outline the methodology involved, before presenting results.

5.3.1 Method

We perform two parallel sets of experiments. Firstly, the original CRF experiment, as per Section 5.2.2, which is comprised of the model runs CTRL, BGP and BGM. Secondly, a CRF experiment with a modification to the angle of wind vectors by +10° (anticlockwise) over sea ice exclusively. This 'modified wind' is illustrated schematically in Figure 5.2 (dashed cyan arrow). This second experiment is comprised of runs named CTRL10, BGP10 and BGM10. CRFs are calculated using the respective control and perturbation runs for each experiment, as per Section 5.2.2. In following text, 'BGP' is—unless stated—shorthand for the response or CRF seen in BGP relative to CTRL, likewise for the other perturbation runs and their respective control runs.

In order to better understand the mechanisms at play, we explore the role of additional parameters here. As well as (1) freshwater content, (2) sea ice volume and (3) sea ice export, we also analyse: (4) liquid freshwater fluxes, (5) ice-to-ocean freshwater fluxes arising from melting and freezing, (6,7) precipitation on ice and ocean, respectively, and (8) sea ice thickness. Parameters (2,3,5,6,7) permit the construction of a complete freshwater budget for the ice component, while (8) allows us to see how the ice export/import relates to thickness changes. Gathering liquid freshwater fluxes is essential to understand whether editing the turning angle affects freshwater accumulation via Ekman transport. The inclusion of these fluxes also enables us to understand the results in terms of sources and sinks of freshwater, as we explore in Section 5.3.3.

5.3.2 Results

In Figure 5.4 we compare the two experiments described above. As expected, the BGP10 experiment shows ice export (dashed teal line) under the same wind forcing as the BGP experiment. This ice export is compensated by a commensurate change in the cumulative net thermodynamic ice-to-ocean freshwater exchange (orange line), drawing freshwater from the liquid reservoir and into the solid reservoir—maintaining the ice volume at a steady level (note the close match between lateral volume fluxes and ice-ocean fluxes in Figure 5.4). This ice-to-ocean exchange may be composed of contributions of both increased winter freezing and decreased summer melting; the lack of a clear seasonal cycle implies that both winter and summer seasons contribute in a relatively consistent manner to the response.

As expected via the mechanism described above, the liquid FWC accumulation is indeed somewhat weaker in the BGP10 experiment, due to the anomalous sea ice export (compare blue and dashed dark grey lines). This reduction in FWC accumulation can only be attributed to the change in cumulative ice-to-ocean fluxes ice export in BGP10. Liquid freshwater import (cyan line) actually increases subtly by up to 10% in BGP10 versus BGP and therefore cannot explain the reduction in FWC accumulation.

In BGM10, we see an increased sea ice import response relative to BGM (which also shows sea ice import). In both BGM and BGM10, this sea ice import (dashed teal line) is compensated by a net reduction in the thermodynamic growth rate (orange line), i.e. an increase in the cumulative ice-to-ocean freshwater fluxes. As noted above, this may be due to both suppressed winter freezing and enhanced summer melting; the lack of a clear seasonal cycle (especially relative to the other variables) implies that both seasons act relatively consistently regarding the change in net thermodynamic growth rate.

We next plot sea ice motion vectors and thickness fields in order to understand how ice import/export manifests and relates to regional sea ice characteristics and control run mean state. In Figure 5.5 we show the CTRL run ice motion vectors and thicknesses on the left side, and

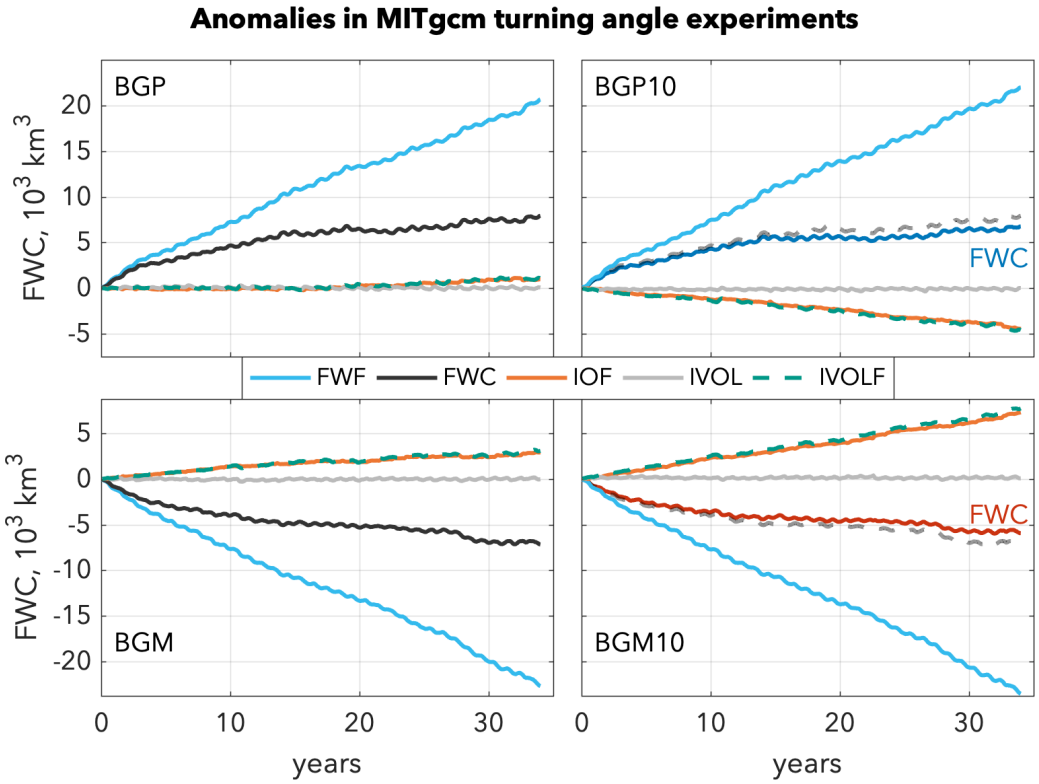


Figure 5.4: CRFs for different FWC budget terms in the regular CRF experiment (left side) and after +10° wind forcing modification (right side). Fluxes are positive when directed into the gyre. The FWC curves are coloured for compatibility with Figure 5.5. BGM and BGP FWC curves are overlain on BGM10 and BGP10 plots as dashed dark grey lines for ease of comparison. FWF = cumulative liquid freshwater flux across boundaries; FWC = liquid freshwater content; IOF = cumulative ice-to-ocean freshwater fluxes (positive into ocean); IVOL = sea ice volume; IVOLF = cumulative volume fluxes of sea ice across boundaries (import/export).

all anomalies on the right. In every case, we plot the time-mean of the first 30-years of the time period over which the responses are calculated.

The two CTRL states show a gradient in sea ice thickness from over 2 m to the north east of the region, to 1 m in the southwest. The thick ice north of the CAA is entrained into the region under the anticyclonic BGP perturbation, visible as a lobe of positive thickness anomaly in the southern part of the Beaufort Gyre, and wrapping around the edge of the region to the north. The overall balance, however, is one of minimal net import of ice in BGP (Figure 5.4), indeed the central, far southwestern and northeastern parts of the region show slight thinning. BGM

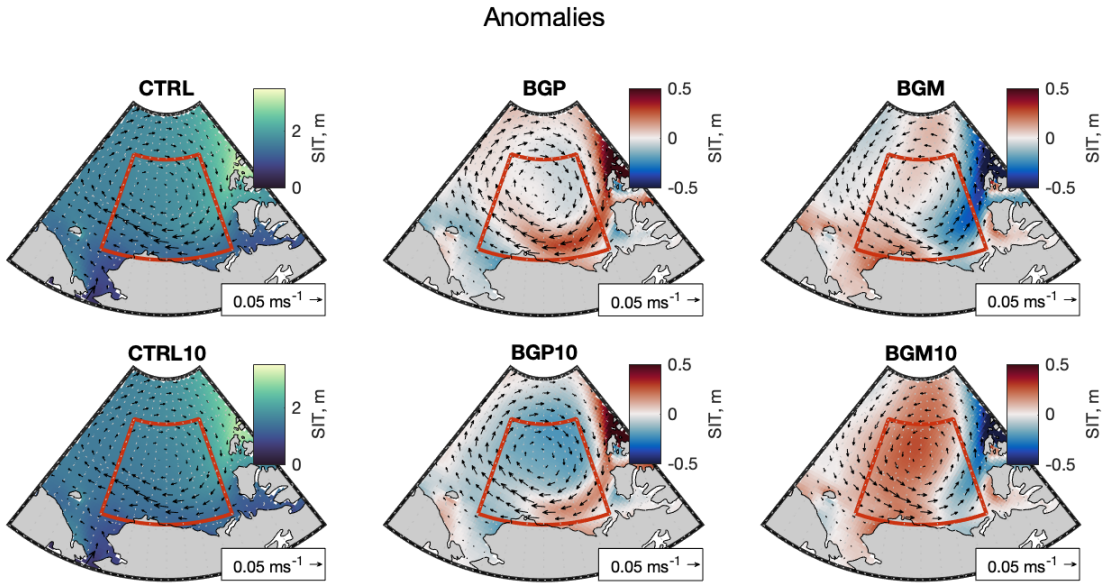


Figure 5.5: Maps showing sea ice thickness and velocity fields. Panels on the left show mean CTRL and CTRL10 conditions; panels on the right show the 30-year mean responses in those fields versus respective control periods.

by contrast shows a dipole in thickening across the region that can be interpreted as a slow-down of the usual anticyclonic flow, which normally brings in thicker ice through the eastern side of the region. Indeed, considering the full simulation rather than the anomaly, sea ice motion in the Beaufort Gyre region in BGM is relatively slow.

To investigate the differences made by the turning angle experiment, we compute differences between these parallel experiments, i.e. BGP10 - BGP and BGM10 - BGM. As shown in Figure 5.6, we find the differences between the respective responses of the sea ice velocity and thickness fields, as well as ice volume fluxes through each side (or 'gate') of the region.

Relative to BGP, BGP10 shows a thinning of ice in the region, consistent with the net ice volume export under BGP10. Similarly, BGM10 exhibits thickening relative to the BGM response; also expected due to the greater import under BGM10 than BGM. These thickness changes can be interpreted in terms of the expected angular changes to ice motion. The +10° modified wind should make the flow more divergent under BGP and more convergent under BGM (see ma-

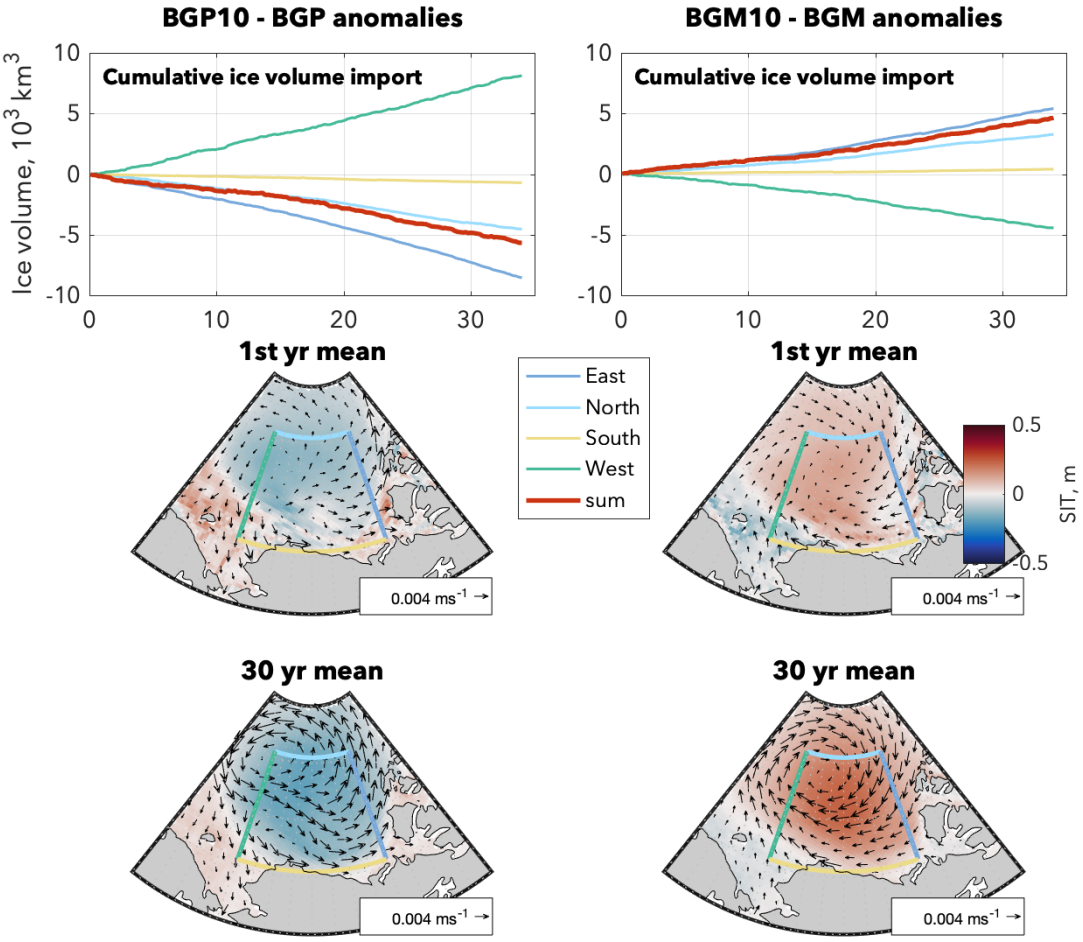


Figure 5.6: Difference between the ice volume fluxes through each gate of the BG region (upper panel; positive into gyre region), and velocity and thickness fields (lower panels) between the BGP and BGP10 responses, and BGM and BGM10 responses, respectively.

genta box in Figure 5.1). Indeed, in the first year of the perturbation experiments, we see a clear divergent pattern in the BGP10 - BGP velocity pattern and a convergent pattern in BGM10 - BGM. Over the 30-year mean, however, the difference in the ice velocities between the standard and modified (+10°) experiments appears more as an overall slowing or quickening of the anticyclonic ice circulation.

The breakdown of fluxes through the gates in Figure 5.6 shows that the changes in lateral

ice volume fluxes are all consistent with an overall slowing of the anticyclonic circulation in BGP10 versus BGP, and a quickening in BGM10 versus BGM. The CTRL run shows that the northern and eastern gates are inflow zones, while outflow occurs through the western gate (Figure 5.5). This slowing/quickening is harder to explain than the relative divergence/convergence triggered by the 10° modifications, but may be related to the fact that the angular deviation is small and any resulting differences in speed due to changing ice properties and the distribution of those properties might dominate the difference between vectors.

5.3.3 A simple source/sink balance

Having seen that the proposed mechanism connecting wind-driven ice volume export/import and liquid freshwater content holds—at least in the MITgcm—we next seek to understand the magnitude of FWC changes exhibited. In other words, why does a given ice export anomaly result in a given (and different) liquid FWC anomaly?

We have seen in Figure 5.4 that a tight compensation exists between ice volume export and ice growth, amounting to cumulative freshwater fluxes of approximately 150 km^3/yr. The corresponding change in liquid freshwater content, however, is more subtle. We seek here to understand this difference by considering the processes underpinning sinks and sources of freshwater in the gyre. In particular, that the sinks of freshwater in the gyre operate in a freshwater-dependent manner. In this section, we aim to describe the time-dependent evolution of liquid FWC in response to sources and sinks of FWC. As we shall argue in the following, the equation we seek has the following form:

$$\frac{dy}{dt} = s - ky^n \tag{5.3}$$

where y is the freshwater anomaly; $\frac{dy}{dt}$ is the rate of change of this anomaly; s is a constant (wind-driven) source/sink term; and ky^n is a FWC-dependent sink term, in which k is a constant and n is an exponent. We next consider the physical processes at play and their place in

the above equation.

We can see from Figure 5.4 that the cumulative liquid freshwater fluxes (FWF) and ice volume fluxes (IVOLF) across the BG region boundaries (i.e. import/export) are reasonably linear with time: the fluxes of volume/unit time are roughly constant. This suggests that they are independent of FWC, which changes through time, and is consistent with previous results (Manucharyan & Spall, 2016). It also reflects the fact that ocean velocities are much smaller than winds, thus the air-ocean stress (which drives Ekman convergence) is relatively independent of the oceanic state (e.g. Doddridge et al., 2019). We can therefore combine the wind-driven export/import of liquid freshwater (FWF) and ice (IVOLF) into one constant term that is independent of freshwater. This is our s in Equation 5.3.

The terms that we expect to depend on the liquid FWC state are sink terms: eddies and the ice-ocean governor. There must clearly be at least one sink process that depends on freshwater, in order for the freshwater accumulation curve to approach equilibrium (as identified by Manucharyan et al., 2016). These sink terms will be included as ky^n in Equation 5.3.

Previous work has related the time evolution of halocline depth, $\frac{\partial h_{\mathrm{halo}}}{\partial t}$ to these sink fluxes, and elucidated a dependence of these fluxes on depth of the halocline, h_{halo} (Doddridge et al., 2019; Manucharyan & Spall, 2016). In this formulation, if the radius of the gyre is assumed constant, $\frac{\partial h_{\mathrm{halo}}}{\partial t}$ the ice-ocean governor sink can be seen to be a function of h^2_{halo}, because of the dependence of ice-ocean stress on the square of the geostrophic velocity, which is a linear function of h_{halo} (see Doddridge et al., 2019, for more details). In eddy-resolving modelling, the eddy diffusivity depends on the square of the isopycnal slope (Manucharyan & Spall, 2016), meaning that the eddy sink should depend on h^3_{halo} (as can be seen from Doddridge et al., 2019, Equation 1). However, this relationship between eddy diffusivity and isopycnal slope will be model-dependent.

Here, however, we aim for a time-evolving equation not in terms of $\frac{\partial h_{\mathrm{halo}}}{\partial t}$ but in terms of $\frac{dy}{dt}$ (Equation 5.3), and we seek the dependence of the sink term on FWC, as per ky^n. An

analytical derivation of this equation is made complex—and subject to significant uncertainty—by considerations of the dependence of FWC, and the various sink terms, on h_{halo} and R, if R is allowed to vary as a function h_{halo} (c.f. Regan, Lique, Talandier, et al., 2019). As such, rather than analytically attempting to find n or k, we test different choices for n against the relevant CRF curves, and calculate k numerically as detailed below.

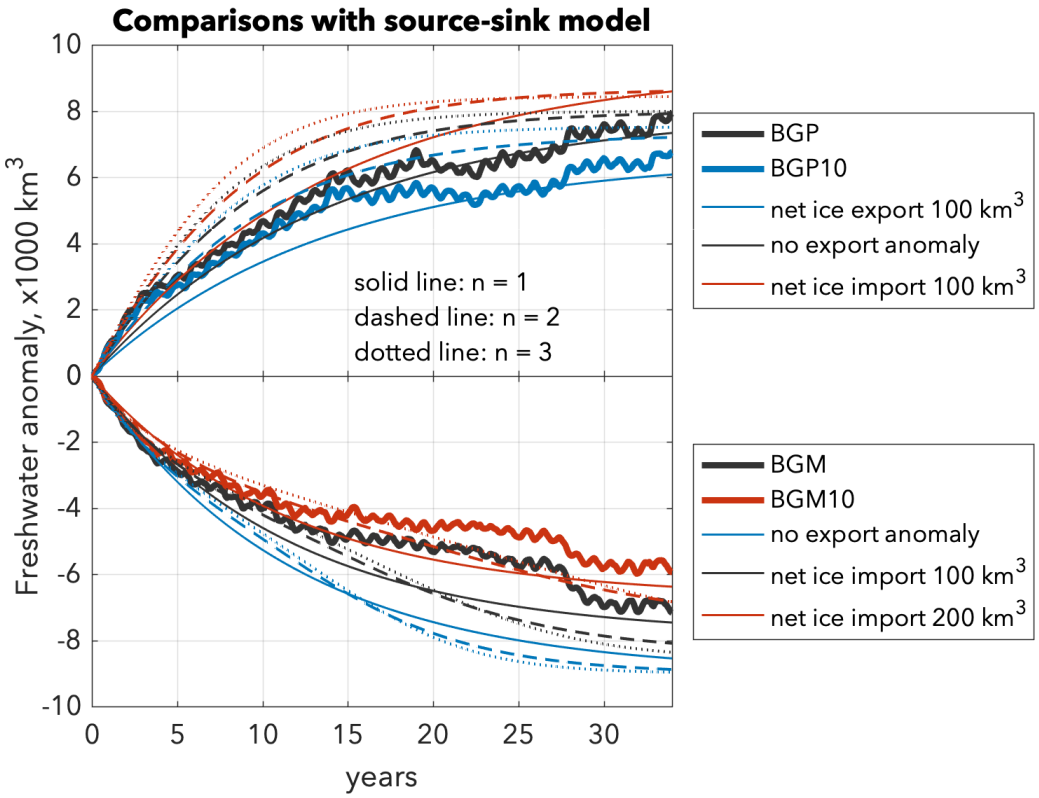


Figure 5.7: Comparison of liquid freshwater CRFs from the BGP, BGP10, BGM and BGM10 experiments (heavy lines), and time-evolving solutions for FWC from Equation 5.3 (thin solid/dashed/dotted lines).

To construct our idealised time-evolving solution for FWC ($\frac{dy}{dt}$), we do the following. We must first find the mean freshwater flux into the region in CTRL, as our anomaly values are measured relative to this, and we need to consider the total freshwater flux into the region in order that our idealised model captures the physics of the gyre in as accurate a way as possible.

We utilise the mean CTRL freshwater inflow as s_0. (This net inflow arises principally from net ice melting, balanced by precipitation on ice.) We then can estimate s as $s_0 + s_{\text{anom}}$, where

$s_{\text{anom}} = \text{FWF} + \text{IVOLF}$, and the latter two terms are taken from our CRFs (Figure 5.4). We can then constrain k by assuming an equilibrium value for the FWC CRFs as time goes to infinity, where $\frac{dy}{dt} = 0$ (this is a more sensitive approach than finding k from the CTRL state and s_0).

Our idealised model must consider the elevated state of the gyre above the surrounding ocean in order to best represent the physics. The MITgcm exhibits about 20 m of FWC in the BG versus a regional mean of 15 m. Conveniently, the dimensions of the gyre mean that this approximates 20,000 km^3, and we can view the CTRL state as sustaining a regional excess of 5,000 km^3. In our idealised model, then, y = 0 on the regional mean (an anomaly of -5,000 km^3). However, for plotting purposes, we show y as the anomaly against the CTRL state, consistent with the CRFs. This detail is relevant for explaining, for instance, the subtly different shapes of the resulting curves under BGM versus BGP conditions.

In Figure 5.7 we compare the BGP, BGP10, BGM and BGM10 curves to solutions for y as per Equation 5.3. We modify s to reflect changing freshwater fluxes into the region in each case, which arises on account of the differences in wind forcing. As an approximation of the CRFs, we choose 650 km^3/yr as the anomaly flux, s_{anom}, and modify this flux by plus or minus 100 km^3/yr in the BGP case. (Note that a slight change in FWF reduces the overall anomaly in s from what it would be if only IVOLF was modified.) In the BGM case, there is ice import under BGM, of approximately 100 km^3/yr; this is roughly doubled under BGM10. Our anomaly flux, s_{anom}, is therefore well described by 650 km^3/yr + 100 km^3/yr for BGM. The two scenarios either side of this anomaly are then 'no import' and net import of 200 km^3/yr, as shown in Figure 5.7.

We show three choices for n. In both forcing settings, the magnitude of difference made to y by a change in s of 100 km^3 are best described by the $n = 1$ curves, however the differences are small. The shapes of the curves also probably best represented by $n = 1$. It is worth noting that the assumptions about regional FWC levels, and the role of the sinks if/when FWC goes below these levels, make the BGM curves more subject to uncertainty; for instance, do the sinks become 'sources' once Beaufort Gyre FWC is at lower levels than the surrounding

ocean?

While of course not all details are captured, these results demonstrate on a simple level that a simple source/sink equation can help us understand the magnitude of changes seen in the CRFs (Figure 5.4). This provides a straightforward conceptual basis for considering the importance of freshwater fluxes arising from wind-driven liquid and solid transports. In the MITgcm simulations presented here, we tentatively suggest that the FWC sink terms are approximately linearly dependent on FWC.

5.4 Discussion

With parallel experiments in the MITgcm, we show that wind-driven ice volume export/import into the Beaufort Gyre region affects the adjustment of the freshwater reservoir to wind forcing. Further, it may help to explain differences in the simulated wind-driven FWC adjustment between different ice-ocean models. In MITgcm, we see that the tight compensation between ice import into/export from the region and ice-to-ocean fluxes within the region acts to maintain ice volume at a relatively constant level. As argued previously in this chapter and in Chapter 3, this balancing process can be understood by considering the effect of ice thickness on growth. And also, perhaps, by considering the changes in ice volume available to melt in the summer season. The Beaufort Sea is already an area where multi-year sea ice often does not survive the summer (e.g. Stroeve et al., 2011), and warm inflows through Bering Strait assist in melting the ice (e.g. Woodgate, 2018).

Are these relationships between ice import and net thermodynamic growth rate likely to hold in a warmer Beaufort Sea? In warmer conditions, we would still expect the sign of the annual-mean effect of sea ice import/divergence on thermodynamic growth rate to remain the same. If anything, the role of the summertime melt contribution becomes clearer: as all ice begins to melt away, regardless of thickness, a winter characterised by import preconditions a greater summer melt flux into the water column. Similarly, in a warmer winter, the dependence of sea

ice growth rate on the inverse of sea ice thickness still holds, however the ice production may of course exhibit forced changes, as investigated in Chapter 4.

Wind-driven export/import of ice can occur in several ways beneath a given stationary SLP pattern. One way, which we exploit in order to trigger the different export/import scenarios in the MITgcm, is via the divergence/convergence of ice that results from ice motion being angled outwards/inwards relative to SLP contours, which must be non-divergent (Figure 5.1a). Sea ice in the Arctic in the mean moves along isobars or shallowly to the right (Kimura & Wakatsuchi, 2000; Thorndike & Colony, 1982), implying subtle convergence under the Beaufort High. In the future, as ice properties change, we might expect drift characteristics typical of summertime to become increasingly relevant. The fact that drift angles are further to the right of isobars in summer implies that ice motion may become more convergent under the Beaufort High, and more divergent under low SLP anomalies. Our results (Figure 5.4) imply that the accompanying freshwater accumulation/flushing would become more extreme in magnitude.

Another scenario leading to sea ice export/import is the presence of a velocity gradient along streamlines of sea ice flow. This mechanism should be activated, therefore, when winds are directed along gradients in ice mobility. Indeed, in the Beaufort Gyre region, the SLP pattern that best explains sea ice (area) divergence in the Polar Pathfinder dataset is a dipole of high pressure to the north and low pressure to the south (Figure 5.8). This pattern directs easterly winds across the BG region, blowing down the ice thickness gradient and up the ice mobility gradient (compare with Kimura & Wakatsuchi, 2000; Kwok et al., 2013). This is scenario is represented schematically in Figure 5.1b.

The third scenario we consider involves the advection of ice in the presence of a thickness gradient (Figure 5.1c). Strong anticyclonic winds can sweep multi-year ice into the gyre (R. D. C. Mallett et al., 2021; Stroeve et al., 2011). This is something we also observe in the south of the region under BGP (Figure 5.5).

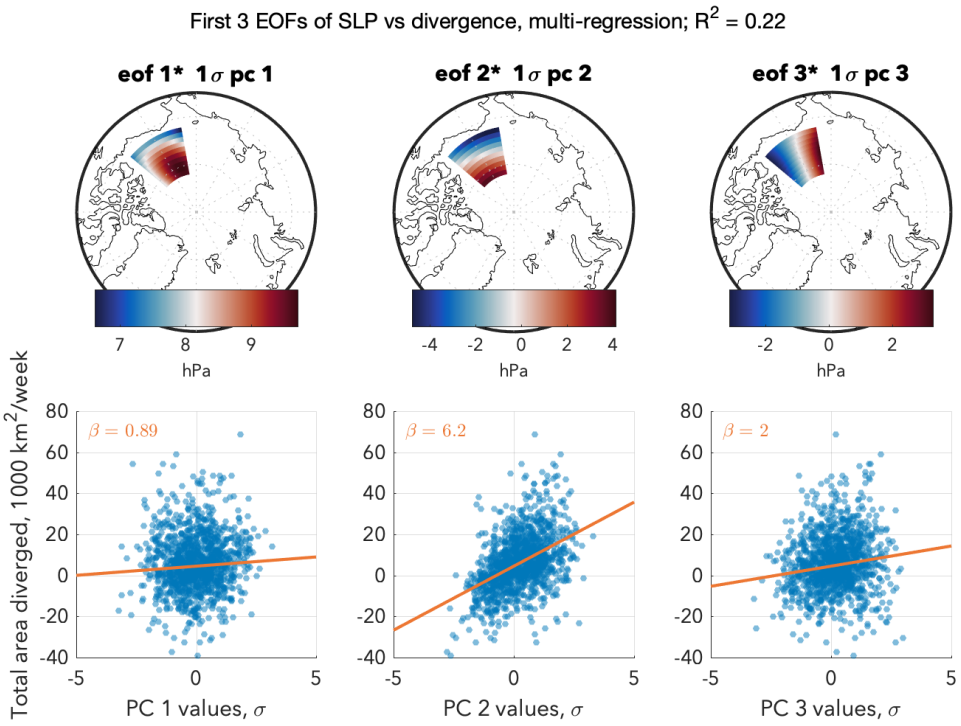


Figure 5.8: Multiple regression of the first three EOFs of SLP against ice divergence in the Beaufort gyre region from Polar Pathfinder. Comparison is on a weekly timescale. Upper panels show the EOF patterns, multiplied by 1 standard deviation of the corresponding principal component timeseries. The lower panels show the regressions.

As multiyear ice retreats towards the north of CAA and Greenland, the mobility of ice in the Beaufort region may become more uniform as it is increasingly characterised by first-year ice. Incursions of thicker ice may also become rarer, but potentially more impactful on the net thermodynamic growth rate when they do.

These mechanisms described above and illustrated in Figure 5.1, may be at play in forced ice-ocean model simulations of wind-driven Beaufort Gyre adjustment, such as the ones presented here (figures 5.3 and 5.4). It is not immediately clear which should dominate in determining ice import. However, in the response to a persistent, stationary, wind forcing anomaly, we suggest that scenario (a) in Figure 5.1 could be important. This is especially likely given the wide variability of angles between wind and ice velocities exhibited by models (Girard et al.,

2009; T. Martin & Gerdes, 2007). Furthermore, this scenario may have the greatest ability to cause sustained volume export/import: the gradients the other scenarios depend on may be eroded or altered by persistent wind-forcing.

One caveat to extrapolating our model-based results to nature comes from the choice of using ice-ocean models, which enable us to apply specific atmospheric forcings, but naturally do not represent atmospheric feedbacks. A potentially important feedback results from changing ice growth rate and accompanying vertical heat fluxes across sea ice. Winter sea ice thinning has been credited with contributing 37% of the relative warming of Arctic Amplification (Lang et al., 2017), due to the enhanced heat fluxes from ocean to atmosphere that occur over thin ice, particularly ice that is thinner than 0.4–0.5 m (Ford et al., 2021; Maykut, 1978). But these heat fluxes are an inextricable part of ice growth, and surface air temperatures are positively correlated with ice growth in coupled climate models (Petty et al., 2018, and as discussed in Chapter 4) in the contemporary and historical Arctic. We therefore do not expect that this lack of coupling in our model experiments leads to a meaningful difference in sea ice growth rates, versus a coupled scenario.

Given that wind-driven import or export of sea ice and liquid freshwater are relatively independent of the gyre's liquid FWC, we can understand their impact on the liquid FWC evolution by appealing to a simple source-sink model. The impact of a constant wind-driven flux of ice into or from the region on freshwater content is moderated by the effect of sink terms that are dependent on freshwater content, because they remove freshwater faster when there is excess freshwater in the system.

5.5 Concluding summary

We summarise our main conclusions below:

- Ice import/export to the Beaufort Gyre influences wind-driven liquid freshwater adjust-

ment in forced model experiments

- This mechanism may help to explain differences between model simulations with the same forcing
- The effect on freshwater is achieved by feedbacks of ice thickness on net thermodynamic growth rate
- The magnitude of the impact of wind-driven import/export of ice on freshwater changes can be understood in terms of a simple source-sink equation, in which the sink terms are dependent on freshwater

Chapter 6

Concluding Discussion

This section provides a concluding discussion to the thesis, beginning with a summary of key results, and followed by a discussion of themes that cross-cut the chapters above. An evaluation of different methodologies as pertains to the results is offered. Finally, a consideration of key research frontiers is given.

6.1 Summary of key results

In the first two chapters, we use linear response theory (e.g. Hasselmann et al., 1993) to isolate the relationship between Arctic freshwater content and sea-level pressure (SLP) patterns in coupled climate models. Our method captures the time-evolving response of freshwater content to an abrupt change in SLP forcing. Our results emphasise the importance of sea-level pressure variability in recent Arctic-wide freshwater changes; we are able to reconstruct a significant portion of recent trends using the model-derived response functions and SLP changes from atmospheric reanalysis. Through our statistical approach, we infer that coupled climate models generally show a positive freshwater response, evolving over a multi-year to decadal timescale, to an abrupt strengthening of the anticyclonic mode of the Arctic Oscillation (AO), the leading mode of SLP variability north of the tropics.

In Chapter 3, we explore the potential role for sea ice export in affecting Arctic-wide liquid freshwater content (FWC) changes. We employ forced model experiments to investigate the links between wind-driven ice dynamics and thermodynamics (thermodynamic growth and melt), and the effect of changes in net thermodynamics growth on liquid FWC. We find that the thermodynamic response of sea ice is highly dependent on the dynamic response of ice to the imposed wind forcing; in particular, the pattern of thickness changes driven by the winds. Accordingly, in some simulations, the dominant effect of increased sea ice export appears to be in accentuating the seasonal cycle of sea ice melt and growth, while in others, it drives an annual mean loss of liquid freshwater. Our results also show that, via upstream thinning, or dynamic preconditioning (Williams et al., 2016), winter Fram Strait sea ice export precipitates low sea ice area in the following September.

In Chapter 4, we seek to understand forced changes in sea ice production in the Kara and Laptev seas, which is important for the distribution of liquid Arctic freshwater and the strength of the Eurasian Basin halocline. Relying on model output from CESM-LE, we develop a simple linear model with insight from the ice growth rate equation. The model succeeds in explaining forced variations in ice production under climate change, allowing us to attribute the main physical drivers of trends. It furthermore permits use to reconstruct historical changes in ice production using observation-based estimates of the climate variables in question. Our results suggest that we may be passing the peak of winter ice production in the Kara and Laptev seas.

In Chapter 5 we focus on another key region for freshwater changes in the Arctic Ocean: the Beaufort Gyre. We ask whether wind-driven sea ice dynamics can affect freshwater accumulation in or flushing from the gyre, by the influence of dynamic changes in thickness (due to sea ice import or export) on the freshwater exchanges between ocean and ice as determined by the net thermodynamic growth rate. Capitalising on a set of existing coordinated experiments, we find differences in the simulated ice export between simulations that can plausibly explain part of the spread in simulated accumulation of liquid FWC under anticyclonic wind forcing. With dedicated model experiments in which we rotate the angle of imposed winds, we find

that different ice import scenarios affect the freshwater adjustment of the gyre. This effect is mediated by changes in the net thermodynamic growth rate. Our results suggest that sea ice import/export may play a significant role in modulating the multi-year to decadal wind-driven adjustment of the gyre.

6.2 Arctic-wide freshwater changes

The work in Chapter 1 and Chapter 2 identifies a strong role for SLP variability in pan-Arctic liquid FWC changes. This link is stronger and more dominant in the HiGEM model (Chapter 1) than any of the CMIP5 models (Chapter 2). The reasons for this difference are not obvious. HiGEM has a higher resolution (1/3°) ocean than most of the CMIP5 models, but it is not clear that this should result in a tighter SLP-FWC relationship. HiGEM has a considerably shorter control run, raising the possibility that part of the derived impulse response functions are based on overfitting, despite our attempts to mitigate this with segmentation of the run and varying the cutoff lag. We would need to apply the Monte Carlo statistical significance procedure that we developed in Chapter 2 (Section 2.2.5) to test what level of correlation we might expect from a random forcing timeseries.

A key finding from chapters 1 and 2 is that a reconstruction of Arctic FWC over recent decades, constructed through convolution of model-derived impulse response functions and SLP from reanalysis, can successfully capture part of the recent accumulation (1992–2012) of freshwater, and agrees well in terms of the timing of increase in the mid-late 1990s and apparent plateauing around 2010. Comparison of the HiGEM reconstruction with a longer data set from Polyakov et al. (2013) also yields similarity, but we note that the underlying data in the Polyakov et al. (2013) record are highly scattered; the smoothed timeseries is associated with substantial uncertainty and should not be treated as authoritative. The Rabe et al. (2014) record appears to be extended by two years to 2014 by Q. Wang et al. (2019), though this is not discussed in their paper. To our knowledge a pan-Arctic FWC record from hydrographic measurement beyond 2014 is not currently available. Freshwater monitoring in the Beaufort Gyre is available

up to 2018 (Proshutinsky et al., 2019), however other parts of the Arctic remain less well-sampled by in-situ measurement (Morison et al., 2021). Satellite measurements of dynamic ocean topography (Armitage et al., 2016) may help to fill this gap.

On the whole, though, our observational record of Arctic-wide FWC is spatially and temporally limited. Based on coupled climate model simulations, we expect Arctic Ocean FWC to exhibit a roughly decadal decorrelation timescale (Chapter 2, Table 2.2); as such it is effectively impossible to distinguish internal variability and forced changes due to anthropogenic climate change from the short observational record alone. Jahn and Laiho (2020) study a large ensemble of climate change and historical runs from the Large Ensemble of the Community Earth System Model; a setting that is ideally suited to discriminating between internal variability and forced changes. In CESM-LE, they find that a strong forced increase in Arctic liquid FWC emerges beyond the range of pre-industrial internal variability during the early 21st century. It might be tempting, then, to treat the recent accumulation of FWC as entirely comprised of a forced anthropogenic climate change signal. Our lack of an observational record describing internal variability perhaps increases the temptation. But the magnitude of the recent FWC accumulation (c. 10,000 km^3; Rabe et al., 2014) would not be uncommon in the CMIP5 or HiGEM pre-industrial control runs (figures 1.6 and 2.1).

What do our results contribute here? Our results suggest that SLP changes are responsible for a significant part of the recent FWC increase: 30–80% in the case of the CMIP5 models, and close to 100% (with a 1σ undertainty of c. 20%) in the case of HiGEM. But was this SLP change partly forced by anthropogenic climate change? We cannot answer this definitively, but if we restrict our attention to the first mode, the Arctic Oscillation (AO), we see that this mode contributed to the FWC increase thanks to a general predominance of the relatively anticyclonic, AO-, phase in the late 1990s until about 2010 (figures 1.7b and 2.15; note that the negative AO- is stronger in the positive y-axis direction in these plots). Given that most climate models suggest that the AO will become more cyclonic with climate change (Choi et al., 2010; R. L. Miller et al., 2006; Rind, 2005), it seems unlikely that this anticyclonic excursion was strengthened by climate

change—if anything, it ought to have been lessened. We suggest, therefore, that the recent accumulation of Arctic FWC was primarily driven by SLP changes that are within the range of natural (unforced) variability. This signal is most likely superimposed on a longer term and shallower positive trend in FWC due to an increasingly vigorous equator-to-pole hydrological cycle. Observations over the hitherto unreported last half-decade and next decade should help to clarify the characteristics of the recent FWC changes: we will see whether the recent FWC increase is part of a monotonic, sustained rise; simply part of decadal to multi-decadal variability; or—more likely—a combination of forced and unforced processes.

Should we expect the contribution of increased hydrological fluxes (runoff, precipitation) to be slow and roughly monotonic? We certainly see limited internal variability in accumulated fluxes from preciptation and runoff minus evaporation in the HiGEM pre-industrial control run (Figure 1.4). In addition, the response functions of cumulative runoff plus precipitation minus evaporation to the SLP modes are more than an order of magnitude smaller than the liquid FWC response functions (not shown). Intuitively, it seems likely that regional variability in precipitation over this landmass due to SLP variability would be averaged out on account of the rivers that enter the Arctic draining such a vast domain in both latitudinal and longitudinal dimensions. Indeed, Peterson et al. (2002) show that Eurasian river discharge, whilst showing a likely connection to the North Atlantic Oscillation, shows modest total discharge anomalies of order 50 km^3/yr in a ten-year running mean (a timescale on which we see significant FWC variability due to SLP in coupled models). Of course, atmospheric circulation also helps to determine the fate of river runoff. For instance, winds can modulate if Eurasian river plumes are directed towards the Beaufort Gyre, or if they are directed northwards into the Transpolar Drift, before exiting the Arctic (e.g. Morison et al., 2012; Proshutinsky et al., 2019; Steele & Ermold, 2004). In this manner SLP variability also helps to determine the effect that river runoff has on Arctic freshwater storage and distribution.

We next consider how future changes in SLP variability are likely to affect FWC variability. If the cyclonic mode of the AO does indeed become more dominant (Choi et al., 2010; R. L.

Miller et al., 2006; Rind, 2005), we would expect this to act to subtly reduce FWC, versus a scenario in which the AO showed no long-term trend. This effect may, of course, be captured in coupled model FWC projections (e.g. Jahn & Laiho, 2020; Shu et al., 2018; Zanowski et al., 2021), which nevertheless show increases in FWC; there is no suggestion that it will reverse the expected upwards trend. Changes in the Arctic Dipole (EOF2 of SLP in most coupled models and in ERA5 reanalysis) and the third mode of sea-level pressure variability may also be important; we see in HiGEM and some (but not all) of the CMIP5 models that these EOFs make important contributions to the overall FWC variability. Less is documented about how these other modes of atmospheric variability are expected to change on an annual mean basis (though projected changes in the summertime Arctic Dipole were studied by Cai et al., 2018). A final point to note on the role of different sea-level pressure patterns is that their manifestation is not stationary: for instance, the nodes of the AO and North Atlantic Oscillation (NAO) wander, with documented effects on sea ice export (Hilmer & Jung, 2000). We might expect such wandering to also affect liquid freshwater export.

Agnostic of how exactly SLP variability might change in the future, we can certainly expect changes in the relation of these patterns to FWC variability due to the changing character of sea ice. The decline in concentration, thickness, roughness, strength, and temporal coverage of sea ice is bound to modulate the transfer of stress from winds to the ocean. However, these relationships are complex and only partially understood. For instance, T. Martin et al. (2014) suggest that there is an 'optimal' concentration of sea ice that maximises the transfer of momentum at around 80-90%, and identify seasonality in surface ocean stress trends due to weakening of the ice pack in winter (increasing ocean surface stress) and increasing open water area in summer (decreasing ocean surface stress). T. Martin et al. (2016) show, however, that the trend of annual-mean ocean surface stress is subject to the way sea ice is simulated. In simulations with variable sea ice drag coefficients, as per Tsamados et al. (2014), T. Martin et al. (2016) find an overall decline in ocean surface stress of -0.002 $Nm^{-2}decade^{-1}$, whereas simulations with a single drag coefficient show an increase of 0.003 $Nm^{-2}decade^{-1}$. Given the complexity of the air-ice-ocean stress relationships (e.g. Cole et al., 2017; McPhee, 2012),

model projections of such trends should be treated with caution.

The spatial patterns of stress changes on the ocean surface are likely to be important for freshwater changes, however. Q. Wang et al. (2019) suggest that the decline of sea ice is partly responsible for diverging trends of FWC changes in the eastern and western Arctic (e.g. Armitage et al., 2016), primarily through changes in ocean surface stress and consequent changes in circulation patterns, rather than by the direct contribution of a reduction in net thermodynamic sea ice growth rate.

The decline of sea ice also has implications for freshwater content via the influence of sea ice on eddies. Eddies act, for instance, to oppose buildup of freshwater in the Beaufort Gyre (e.g. Davis et al., 2014; Manucharyan et al., 2016) and to transport heat and freshwater between the shelves and the basins (Spall, 2013; E. Watanabe, 2011). Meneghello et al. (2021) show that eddies in Canada Basin are damped above about 50 m by the action of friction with sea ice, but persist in the subsurface (50–250 m), maintained by baroclinic instability. They surmise that a thinner and less extensive sea ice cover would permit the vigorous surface eddy activity observed in summer to persist for more of the annual cycle. Similarly, Armitage et al. (2020) report enhanced eddy activity due to sea ice loss since 2007 and suggest that sea ice decline will lead to a more energetic Beaufort Gyre in which eddies play a greater role in stabilisation—as opposed to the *ice-ocean governor* (Meneghello, Marshall, Campin, et al., 2018; Meneghello, Marshall, Timmermans, et al., 2018, described in sections 1.1.1 and 5.1.1).

The ice-ocean governor mechanism acts as a brake on the geostrophic current and causes Ekman divergence. If this mechanism becomes absent, we might expect longer equilibration timescales in the Beaufort Gyre and larger storage (Doddridge et al., 2019). In tandem, we would expect a lengthening of time that the gyre retains the imprint of past atmospheric circulation. If the Beaufort Gyre does become able to accommodate larger freshwater volumes, it seems highly likely that the risk of large flushing events should increase. An open question, therefore, is: will Beaufort Gyre freshwater variability be greater in the future? And, in terms of its downstream effects: is the overturning circulation sensitive to rapid freshwater flushing

events, or is it the longer-term trend in freshwater fluxes from the Arctic that matter?

Given that Arctic FWC changes are not spatially uniform, and the Beaufort Gyre can experience freshening at the same time as salinification in the Eurasian Basin is causing episodic weakening of the halocline (Polyakov et al., 2017; Proshutinsky et al., 2019), one might ask if it is most apt to study pan-Arctic FWC as an integrated measure. We would contend that it makes an obvious starting point for the novel coupled climate model analyses we have performed, and furthermore is a quantity that relates explicitly to freshwater fluxes in and out of the Arctic Ocean, something of clear interest given the potential for freshwater fluxes to influence Atlantic circulation.

However, freshwater export to the subpolar North Atlantic is not the only flux at play; trends might be driven instead by changes in Bering Strait inflow, for instance. The Arctic Ocean can approximately be divided in two along the Transpolar Drift, which separates anticylonic vorticity in the western Arctic from cyclonic vorticity in the eastern Arctic (e.g. Armitage et al., 2016; Morison et al., 2021), though the physical division naturally varies in space over time. Given that the two parts of the Arctic Ocean have contrasting mean freshwater states, and are sensitive in different ways to freshwater changes, this division might prove an instructive 'next step' to granularise the Arctic Ocean. We note, for instance, that freshwater transfer from the Eurasian side to the Canada basin could cause significant hydrological changes due to the suspected instability of the Eurasian halocline, but would not be detected in a pan-Arctic spatial integral.

Finally, what will be the consequences of freshening on the Arctic Ocean itself? This in large part depends on how this expected freshwater increase will be distributed. Shu et al. (2018) show that in the CMIP5 multi-model mean, under RCP8.5 forcing, the strongest freshening is in the western Arctic, with little change in the eastern Arctic. In the $4\times CO_2$ model simulation of the coupled climate model HiGEM, Lique et al. (2018) report that western Arctic freshens while the Eurasian Basin salinifies. Further, they find that the weakening of the stratification in the Eurasian Basin leads to deep convection near to the ice-edge, with the mixed layer

deepening episodically to depths of 1,000 m.

The recent trend has, similarly, been one of strong freshening in the western Arctic and a slight salinification in the eastern Arctic (e.g. Armitage et al., 2016). Athanase et al. (2020) provide evidence that episodic mixed layer deepening over the Yermak Plateau-Sofia Deep and continental slope northeast of Svalbard down to 300 m occurred during ice-free conditions in the winters 2017/2018 and 2012/2013, respectively. This is in addition to the episodic winter-time shoaling of the Atlantic Water in the Eurasian Basin documented by Polyakov et al. (2020).

In concert with hydrographic changes, the Barents Sea-Eurasian Basin region appears to be experiencing potentially significant ecological changes, characterised by poleward shifts in previously boreal fish communities (Fossheim et al., 2015) and increasing coccolithophore and *phaeocystis* blooms (Orkney et al., 2020). Frainer et al. (2021) warn that the presently observed increase in species richness and functional diversity in the region may be a harbinger of an ecological transition in which Arctic species are out-competed or preyed upon; likely to ultimately lead, they suggest, to a decline in functional diversity.

Across most of the Arctic Ocean, net primary production has been increasing over recent decades due to increasing sunlight availability (Arrigo & van Dijken, 2015), including in the western Arctic. Here, however, Zhuang et al. (2021) conclude that nutrient availability has been declining over the past three decades. They posit that this is due to the compound effects of reduced resupply from depth due to the freshening and strengthened stratification, and increased utilisation by primary producers.

Arctic freshwater changes clearly, therefore, have implications for ecology that vary across the basin, just as the physical impacts are likely to vary. When it is only Arctic-wide freshwater changes that are reported from climate models, valuable information about these cross-Arctic differences is missed.

6.3 Sea ice export variability and upstream effects

In order for increased sea ice export to drive a predictable depletion of liquid FWC, sea ice volume losses through Fram Strait must be compensated by upstream net thermodynamic sea ice growth. In Chapter 3, we show that both the winter and summertime responses of net thermodynamic growth rate are sensitive to the nature of the wind forcing and the dynamic response of ice to that wind forcing, the latter of which is model dependent. When sea ice divergence occurs within the interior basins of the Arctic, this preconditions a low sea ice anomaly in September. In the CREG025 simulations, the area diverged also corresponds closely in magnitude to the September sea ice area anomaly. This is experimental support for the observational inference of dynamic preconditioning of September sea ice extent (Williams et al., 2016), however it also demonstrates that this connection is dependent on the pattern of sea ice divergence. It is also important to note that the net sea ice area diverged in the Arctic can exceed the Fram Strait sea ice area export due to areal expansion of the ice pack within the Arctic basin and via export through other gateways (particularly into the Barents Sea). This might help to explain how relatively small area anomalies in Fram Strait export may be related to larger anomalies in Arctic-wide September sea ice area. In models that capture the physics of melt ponds, further amplification of a thinning signal might be expected, possibly leading to larger anomalies in September sea ice area associated with the preceding winter Fram Strait ice export (as per Landy et al., 2015).

We now focus on the overall exchanges of freshwater between ice and ocean (i.e., the net thermodynamic growth rate). We see in Chapter 3 that the connection between sea ice export through Fram Strait and thermodynamic sea ice growth rate is mediated by the spatial pattern and magnitude of upstream ice divergence; something that is dictated by a combination of the dominant wind patterns, the coastal geometry of the Arctic Ocean, and the response of the sea ice velocity field to winds. The nature of the dynamic response of sea ice influences the thermodynamics during both winter and summer.

The effect of dynamic thinning of sea ice within the Arctic Ocean is to increase the winter

sea ice growth rate in most areas. We identify exceptions in the MITgcm simulations in areas where Atlantic heat may be able to interfere with ice growth, though more work is needed to confirm this. In the summer, the effect of thinning on sea ice melting varies spatially in our simulations. Generally speaking, over the shelf seas, a thinner sea ice cover leads to less melting. These are regions that are generally ice-free in September in recent Arctic conditions—even relatively thick sea ice is unlikely to survive the summer (Maslanik et al., 2011; Stroeve et al., 2011). By contrast, dynamic thinning in the basins leads to substantial increases in melting, which we contend is due to earlier breakup of the pack ice and earlier propagation of sunlight into the water column, leading to accelerated melting (e.g. Perovich et al., 2011; Steele et al., 2010; Steele & Dickinson, 2016).

In the summer following anomalous Arctic Dipole forcing during winter, the model CREG025 exhibits a strong melting anomaly, which is then partially offset by rapid ice growth at the onset of freezing. In this way, the effect of the Arctic Dipole pattern—imposed during winter in this model—is to enhance the seasonal cycle of sea ice volume and freshwater exchange between phases within the Arctic Ocean. The summertime melting is preconditioned by wintertime dynamic thinning in the central basins. Simulations run beyond one annual cycle are needed to investigate the longer-term response of a sustained Arctic Dipole forcing. It remains to be seen if the net loss in sea ice volume over the first year continues, or if there is a recovery, which would drain the liquid freshwater reservoir, and connect sea ice export to freshwater changes more directly. A potential mechanism for this is through decreasing thickness of export fluxes in response to net sea ice loss—the thinner the exported ice is, the more likely newly grown first-year ice is able to compensate its loss.

In the MITgcm, by comparison, the winter Arctic Dipole forcing yields reduced melting in the summer months, and as a consequence, the effect of export over the whole annual cycle is to drain the liquid reservoir. The difference versus CREG025 appears to be primarily caused by the pattern of dynamic sea ice thickness changes during the winter. In CREG025, the dynamic thinning occurs in the basins, with thickening in the shelf seas east of the New Siberian Is-

lands. In the MITgcm, on the other hand, there is thinning on the shelves and thickening in the central Arctic. This combination leads to relatively low melting in the MITgcm simulation during summertime, especially in the shelf seas. While the dynamic responses of sea ice are markedly different between the two models, the pattern of the thermodynamic response during summertime in response to the redistribution of ice thickness shows marked similarity. Both models show increases in melting when sea ice is thickened in the shelf seas, and increases in melting when sea ice is thinned in the central basins.

Although we did not simulate its effect, we can consider the influence of the Arctic Oscillation on the redistribution and export of sea ice, and its impact on the seasonal cycle of growth and melt. Historical observations have indicated a positive correlation between the (positive) cyclonic mode of the Arctic Oscillation (or North Atlantic Oscillation) and sea ice export (e.g. Kwok & Rothrock, 1999; Kwok et al., 2004; Rigor et al., 2002), though this relationship is modulated by the position of the Icelandic low (Hilmer & Jung, 2000). Rigor et al. (2002) furthermore show that the cyclonic AO enhances the ice export away from the East Siberian and Laptev seas, dynamically thinning the sea ice cover. The authors show a connection to the following summer sea ice concentration that indicates that this thinning enhances sea ice melting. Hence, a positive AO during winter has historically been associated with a low sea ice extent the following September (Rigor et al., 2002; Williams et al., 2016).

Stroeve et al. (2011) argue that historical relationship has begun to break down, however—and this is also detectable in Figure 4 of Williams et al. (2016). One apparently key reason for this is that the negative AO acts to move thick, multi-year ice into the Beaufort and Chukchi Seas, and in recent years, this ice has been vulnerable to completely melting away. Indeed, our results from the summer of 2010 show that thicker ice in the Beaufort Sea leads to greater melting, while thinning in the shelf seas limits melting due to reduced freshwater availability. The winter of 2020/2021 has been characterised by record-breaking anticyclonic winds over the Arctic sea ice, leading to an unusually high proportion of multi-year sea ice being stored in the Beaufort and Chukchi seas (R. D. C. Mallett et al., 2021). Meanwhile, the ice is relatively

thin in the central basins, despite it being a fairly low year for sea ice export (R. D. C. Mallett et al., 2021). If the pattern of thin sea ice in the basins and thicker sea ice on the shelves is indeed a recipe for enhanced sea ice melting—as it is in our simulations—then the conditions may be in place for anomalously low September sea ice volume in 2021. If this occurs, it will be in opposition to the historical correlation involving the AO (Rigor et al., 2002).

6.4 Shifting patterns of ice production

In Chapter 4, we analyse changes in sea ice production in the Kara and Laptev seas using CESM-LE. We construct an idealised linear model from the internal variability in the model ensemble that can explain both the rise (c. 1980–2020) and fall (2020 onward) in ensemble-mean ice production, due to anthropogenic climate change. These changes are part of wider shifts in the patterns of sea ice production. With future warming, winter sea ice production in CESM-LE shows a decline in the traditional 'ice factory' regions of the Kara and Laptev Sea flaw polynyas, while an increase in ice production characterises the interior basins of the Arctic. These diverging trends are also seen in the CREG025 historical run over 1980–2018 (not shown).

After considering previous work on the effects of ice production in the shelf seas and within the Eurasian Basin, we argue in Chapter 4 that ice production on the shallow shelf seas overall acts to stabilise the halocline. For one thing, Atlantic Waters (AW) are rarely present in the shallow seas (Janout et al., 2017), so the waters there are not in danger of AW shoaling in response to convection driven by brine rejection; the convection can at most propagate to the seafloor. Secondly, the modification of fresh shelf waters by brine rejection provides more saline waters that may feed into—and strengthen—the halocline of the Eurasian Basin by lateral advection (Aagaard et al., 1981). Thirdly, the sea ice created in the shelf regions can advect into the Eurasian Basin and Northern Barents Sea, and melt there during summer, replenishing the surface freshwater layer (Rudels et al., 1994).

The intensification of ice production in the Eurasian Basin, on the other hand, seems to weaken the halocline; winter freezing causes convective mixing that may lead to halocline shoaling (Polyakov et al., 2020). Moreover, if ice production in the shelf seas is reduced (as per the projections in CESM-LE), this should mean a reduction in freshwater resupply by summertime melt of ice derived from the shelf regions. Evidently, it is not only the shifting patterns of winter-time ice production that need to be mapped and interpreted, but also the shifting patterns of summertime melting. In other words, the changing patterns of net thermodynamic ice-ocean freshwater exchange need to be understood. We suggest that this should be a research priority given the prospects of 'Atlantification' and deep winter convection in the Eurasian Basin (e.g. Lique et al., 2018; Polyakov et al., 2018).

Sea ice-mediated redistribution of freshwater is just one process in determining local freshwater abundance, but it is undoubtedly important: the seasonal exchange of freshwater between solid and liquid phases in the Arctic Ocean is vast: c. 13,000 km^3, roughly 4,000 km^3 greater than the net annual freshwater inflows/outflows (Haine et al., 2015). In turn, freshwater abundance is a dominant factor in setting the stratification and establishing halocline stability.

We therefore suggest a focus on the freshwater redistribution mechanism of sea ice growth, drift and melt (as summarised by the net annual thermodynamic growth rate) for the purposes of anticipating halocline stability changes, with several reasons in mind. Firstly, sea ice growth and melt patterns are obviously changing, and the long-term changes should be predictable. Secondly, these patterns should be relatively easy to infer from observations thanks to satellite retrievals of sea ice thickness in winter and sea ice drift and concentration all year-round (though there are issues with the quality of sea ice thickness products, as we discuss in Section 6.7.1). Hydrographic observations of the halocline, however, are still sparse in time and space, and costly to obtain. Thirdly, net thermodynamic growth rate is a computationally efficient variable to work with from climate model output as it is a two-dimensional field. Hydrographic fields, by comparison, are much more storage-intensive owing to the depth dimension. Fourthly, it would be unwise to solely focus on simulated changes in halocline stability under

future scenarios; model representation of halocline dynamics may not be representative of the Arctic. We note, for example, that there are clear differences between the characteristics of the CESM-LE halocline and the halocline inferred from hydrographic observations. Put simply, CESM-LE does not exhibit the classical 'cold halocline' (e.g. Aagaard et al., 1981), but rather exhibits warming downwards across the halocline; its response to future changes might be biased by this difference. It is worthwhile, therefore, to investigate how the conditions that set the stratification are likely to change (i.e. freshwater abundance), regardless of how the halocline itself and mixing across it is simulated. Of course, simulated sea ice dynamics are also subject to model bias, but these fields are more readily comparable to observations and other models.

A final argument for the importance of studying shifting patterns of sea ice production is that the origin and fate of sea ice is also important for the transport of pollutants, sediments and trace gases (Krumpen et al., 2019; Peeken et al., 2018).

6.5 Sea ice thermodynamic growth rate and Beaufort Gyre freshwater

In Chapter 5, we show that sea ice import or export can affect the response of liquid freshwater in the gyre to wind forcing in the Beaufort Gyre. Using simulations with the MITgcm, we find that anomalies in import or export are compensated by changes in the net thermodynamic growth rate of sea ice, meaning that sea ice import/export anomalies are communicated directly to the liquid freshwater reservoir by modulation of ice-ocean freshwater exchanges.

The physical explanation for this relationship appears to be as follows. Wind-driven sea ice import or export to the region constitutes a dynamic change in thickness. This dynamic change in ice thickness can impact the winter thermodynamic growth rate, because the growth rate of ice is inversely proportional to its thickness. Dynamic changes in ice thickness can also lead to summertime melting anomalies. As examined in Chapter 3, the nature of these anomalies

appears to depend largely on the location within the Arctic Ocean.

The Beaufort Sea may be becoming a region where even thick, multi-year ice does not survive the summer (Stroeve et al., 2011). Enhanced summertime melting is attributable in the main to increased solar heating of the upper ocean due to a general reduction of summer sea ice concentration (e.g. Perovich et al., 2008). But even absent of sea ice area reduction, increasing warm Pacific summer inflow (Serreze et al., 2016; Woodgate, 2018; Woodgate et al., 2010; Woodgate et al., 2012) are likely to make thick ice more vulnerable to summer melting than otherwise. In addition, increasingly warm Pacific-origin waters are subducting into the Canada Basin halocline via isopycnals that outcrop in the Chukchi Sea, leading to increased heat storage in the halocline (Timmermans et al., 2017; Timmermans et al., 2018). However, it is not obvious if this subsurface stored heat should affect summer melting.

If it is indeed the case that summer melting is positively correlated with dynamic changes in ice thickness in the Beaufort Gyre region, this would mean that the response of net thermodynamic growth rate to dynamic thickness changes (by ice import/export) would be consistent between summer and winter. Dynamically thicker ice (due to ice import) would result in less winter freezing, and more summer melting; and the reverse for dynamically thinned ice (due to ice export). Given the latitudinal extent of the gyre region (70.5–80.5 °N), it is likely that there is variation in this relationship between thickness and melt across the region. Indeed, this is what we can infer from examining Figure 3.15.

We note in Chapter 5 that there are several ways in which dynamic thickness changes in the gyre could be realised. The most obvious way to dynamically change sea ice thickness in the Beaufort Gyre is through the action of wind-driven sea ice advection. (Our use of the term 'dynamic' is predicated on the sea ice thickness changes we are concerned with being local; considering larger scales, advection merely redistributes sea ice thickness.) An atmospheric anticyclone centred over the north pole—consider the AO- pattern, for instance—would sweep multi-year sea ice into the region, causing thickening (Stroeve et al., 2011). Southerly winds by contrast would cause coastal divergence and sweep thin ice into the gyre (or shift the ice

edge northwards). The cyclonic AO would also likely thin the ice in the region.

If we envision a single winter of strong AO- forcing, we may find that the impact of the winds on ice thickness varies throughout the season, owing to the mobility and thickness gradient in the pack ice. We might expect divergence within the Beaufort Gyre region in the early part of the winter, because the winds blow from a region of low-mobility sea ice towards a region of higher mobility (e.g. Kimura & Wakatsuchi, 2000). Indeed we see that this pattern of winds drives sea ice divergence in the gyre region (Figure 5.8). However, this divergence is likely to be offset in its impact on sea ice thickness over the course of the winter by the advection of that lower mobility, thicker ice into the region. This thickening should limit ice growth in the winter, causing a relative freshening in the ocean. In the summer months, this thick sea ice anomaly could potentially cause excess melting and freshening, as discussed above. On the other hand, a large fraction of the melting in the Canada Basin appears to be driven by solar heating of the mixed layer (Steele et al., 2010). A thick anomaly could delay and suppress this effect, possibly leading to reduced melting.

As we saw in Chapter 3, the summertime dynamics are crucial for the annual mean freshwater balance in the region under consideration. The fact that the MITgcm simulations do not show any significant seasonality in the anomalous ice-ocean freshwater exchange indicates that there is a fairly consistent area-mean relationship between thermodynamic growth rate (freezing/melting) and dynamic thickening across the winter and summer seasons. Further work is needed to confirm this. If true, this positive relationship between dynamic thickening and summer melting stands in contrast to the CREG025 pan-Arctic results in Chapter 3, showing enhanced net summer melting after anomalous winter ice export (Figure 3.13c). However, the proposed positive relationship is consistent with the findings for most shelf regions, where summer melting correlates positively with preceding dynamic thickness changes (Figure 3.15).

Our experiments in Chapter 5 involve a stationary wind perturbation that either enhances or suppresses the Beaufort Sea High. We further modified the angle of the surface wind with respect to hypothetical geostrophic wind in order to drive anomalous divergence or conver-

gence of the ice pack. As such, the mechanism of dynamic thickness change that our simulations most directly involve is that which derives from the angular relationship between sea ice velocities and the geostrophic wind (Figure 5.1a). Given that the angle between wind and sea ice motion is affected by characteristics of sea ice that are changing (e.g. thickness and concentration; Park & Stewart, 2016), it is likely that there will be systematic changes in the turning angle with climate change. These may already be detectable, but have not been studied in studies of the relationship between geostrophic winds and sea ice velocities (Kimura & Wakatsuchi, 2000; Kwok et al., 2013). This is a clear research priority that we hope future work will address, and our study provides a physical rationale for doing so.

6.6 Evaluation of materials and methods

Here we consider the strengths and weakness of the techniques used in this thesis, and the robustness of our results in light of these limitations.

6.6.1 Linear response functions from coupled climate models

In Chapter 2, we explore in some detail the caveats and strengths of using linear response functions from coupled climate models; we will summarise here and offer a little further discussion. This is a technique that is most useful when one seeks the relationship between a 'forcing' timeseries that is white noise or shows a relatively short decorrelation timescale, and a 'target' timeseries that is red noise: simple zero-lag correlations would not adequately describe this relationship. The technique works best when: a) the timeseries available is very long compared to the decorrelation timescale of the 'target' timeseries; b) there is a strong relationship between the two variables; c) the response function cutoff lag is longer than the 'target' decorrelation timescale ; d) the relationship sought can be fairly approximated as linear. Additionally, error goes up as the decorrelation timescale of the 'target' increases.

When is this linearity assumption valid? If the reconstructions using the derived response functions are skilful, the linearity assumption is likely fair. If the system under study can be

reduced to some fundamental physical equations, this might offer insight. In addition, natural variability in a given non-linear system may remain in a sufficiently limited parameter space that it resembles a nearly-linear regime (i.e., the amplitude of variability is small relative to the scales over which the system exhibits significant non-linearity). The applicability of linear response theory can be further tested with accompanying forced model experiments.

The key strengths of this technique are that it permits the equivalent of a model perturbation experiment in state-of-the-art coupled climate models, and that it is computationally efficient, only requiring the output data of control simulations, which are relatively accessible. Multiple models can be assessed using this approach, as we demonstrated in Chapter 2. Through convolution of the derived response functions with reanalysis 'forcing' data, it is possible to undertake novel historical reconstructions.

Because this is a statistical technique, it is never possible to have complete certainty over the nature of the inferred relationships. The challenge is in best constraining the uncertainty around those inferred relationships, something for which we develop a robust technique in Chapter 2.

The FWC variability of CMIP5 models in long, unforced, pre-industrial control runs is an appropriate setting in which to study employ linear response functions. However, the insight the technique could offer was limited in Chapter 2 by the fact that the derived relationships were often quite weak, resulting in greater uncertainty. Due to the fact that we developed the response functions in a pre-industrial control run, it is not necessarily clear that the derived relationships should hold in a warmer Arctic with reduced sea ice concentration and thickness, for instance. Indeed, the derived relationships were often unsuccessful in reconstructing FWC variability in the historical runs of their respective models.

6.6.2 Model perturbation experiments with ice-ocean models

Computing step response functions from model perturbation experiments where atmospheric forcing is perturbed confers several advantages over the linear approach described above. Firstly, the response of a range of variables (and spatial fields rather than one-dimensional timeseries) can be easily investigated. Secondly, there is no ambiguity in the response: causality is clear and only one time-evolving solution is available. Thirdly, non-linearity in the response can be resolved.

The drawbacks to the technique, however, are several. All time-evolving solutions are approximations of the true underlying response function; in order to fairly estimate this, multiple experiments would be needed set against different states of background variability. However, it is computationally expensive to perform new runs of climate models, and results in the creation of a large amount of new data. Compromises may need to be made in order to minimise costs; for instance one might choose to limit the length of the run, or perform fewer experiments than would be sought in the absence of such limitations. In addition, because model perturbation experiments are always model-dependent, it can be most insightful to use multiple models. This can be achieved through the coordination of multiple modelling groups, as per the effort led by J. Marshall et al. (2017) and the results presented in Chapter 5.

In our experiments in Chapter 3, we used two different models, and discovered some significant model differences in the resulting anomalies—for instance, the pattern and magnitude of sea ice divergence triggered by the same wind anomaly. However, there are robust similarities, especially in the relationships between different variables within each model (e.g. between wintertime dynamic thickness changes and summertime melting), which convey important physical information. We were not able to investigate the effect of different climatological background states; to increase the confidence in our results we would need to repeat our experiments in different years. Furthermore, we chose to run short experiments, constraining our focus to the annual timescale of response. Though this carries a lot of important information about what we would expect on longer timescales, the ultimate test would be to repeat

the experiments over a longer period. This would also enable a fairer comparison with the responses inferred from HiGEM, described in Chapter 3, Section 3.2.1.

6.6.3 Large ensembles of coupled climate models

Large ensembles, such as CESM-LE provide the opportunity to investigate—and separate—internal variability and forced changes (e.g. Kay et al., 2015). As we have shown in Chapter 4, they also make apposite settings to advance physical understanding through the development of simple linear models.

An important caveat is that large ensembles only comprise one model—they are subject to the same biases and drawbacks as other single coupled climate models. As such, while our idealised ice production model (Chapter 4) is representative of CESM-LE, different relationships may exist in nature, and in other coupled models. Another drawback of using large ensembles is that data handling can become an issue if three-dimensional variables are required. This is something we mitigate in Chapter 4 through a focus on two-dimensional variables.

6.6.4 Satellite products

The Arctic Ocean is sparsely observed in-situ, but well observed by satellites following a polar orbit. A wide array of products exist to translate the raw satellite observations into estimates of physical variables. The products generally begin around 1979, the start of the so-called satellite era. The satellite instrumentation and methodology they rely on are not constant however, raising the possibility of systematic biases and spurious shifts in the collected time-series. This is one reason why our historical ice production reconstruction in Chapter 4 is subject to significant uncertainty.

The satellite record spans the period of major change in the Arctic sea ice cover, and is long enough to permit a range of statistical investigations. This period is not long enough, however, to robustly investigate multi-year to decadal internal variability, however.

In-situ measurement is essential in order to 'ground-truth' satellite products, but is also logistically challenging and subject to sampling error and biases. This is where projects like MOSAiC (e.g. Krumpen et al., 2020) provide opportunity for testing and improvement of satellite products.

Estimates of thickness from satellite retrievals, for instance, are associated with significant uncertainty, but have the potential to greatly assist our understanding of many of the questions tackled in this thesis. If a longer, and less uncertain record of satellite thickness was available, we would have been able to augment our analysis in Chapter 4 with a record of inferred ice production based on satellite retrievals. In the following section we describe some of the challenges in more detail (Section 6.7.1).

A source of uncertainty in our idealised linear model in Chapter 4 and our investigations in Chapter 3, Section 3.3, comes from sea ice drift estimates. Namely, any noise in the sea ice drift field is counted in our calculations that rely on integrating the positive part of the divergence signal. As such, the 'compensated divergence' signal that this analysis yields, is subject to overestimation. However, we note that there is good agreement between the compensated area diverged as derived from a satellite drift product (Polar Pathfinder) and CESM-LE (which, as a model, provides no instrumental or measurement error). On the other hand, the net sea ice area diverged from Polar Pathfinder—which should not be as biased by noise—is lower than its equivalent in CESM-LE; an indication that there may indeed be some overestimation in the compensated divergence (Figure 4.8c,d).

6.7 Related research frontiers

This section summarises key areas of necessary advancement in order to further our understanding of Arctic freshwater changes and the impacts of these changes.

6.7.1 Satellite estimates of sea ice thickness

Estimates of sea ice thickness from satellite retrievals offer great potential benefit to the understanding of sea ice dynamics and thermodynamics, and the interactions between the two. As explored in chapters 3, 4 and 5, this interplay between sea ice dynamics and thermodynamics is of great importance for the distribution and abundance of liquid freshwater in the Arctic Ocean. However, such estimates have not yet matured. Below, we briefly examine some of the challenges associated with estimating sea ice thickness from satellite data.

The satellite CryoSat-2, launched in 2010, monitors the polar ocean with near complete coverage, and its multi-look synthetic aperture radar (SAR) enables the measurement of freeboard at a greater precision and resolution than previous altimeters (Wingham et al., 2006). A key assumption in CryoSat-2 retrievals is that its Ku-band radar penetrates through snow and backscatters from the snow-ice interface. The freeboard measurement is then converted to sea ice thickness with estimates of sea ice density from the literature—and, in most state-of-the-art products—snow thicknesses and density from the Warren et al. (1999) climatology (Kwok & Cunningham, 2015; Laxon et al., 2013).

When this climatology is replaced with new data with more realistic variability and trends, the results are very different. R. D. Mallett et al. (2021) show that, upon replacing the Warren climatology with snow estimates from SnowModel-LG (Liston et al., 2020; Stroeve et al., 2020), the sea ice thickness in four of the Arctic's seven marginal seas is found to decline 60–100% faster. The trend is steeper because the assumed weight of snow on ice is allowed to decrease, meaning a smaller thickness of positively buoyant subsurface ice is needed to support the above surface weight (by hydrostasy). Error is also introduced by assumptions involving the speed of radar propagation through snow (R. D. Mallett et al., 2020). In addition, variable sea ice roughness introduces an uncertainty equivalent to 20% of first-year ice thickness and 30% of multi-year ice thickness (Landy et al., 2020). Finally, the underlying assumption that the radar entirely penetrates the snow cover is uncertain, and neglects considerable variation in the properties of snow (King et al., 2018; Nandan et al., 2017; Willatt et al., 2011). This is

important because errors in the freeboard measurement are amplified by roughly ten times in the calculation of the sea ice thickness (Landy et al., 2020).

One possibly complementary alternative is to use laser altimetry that explicitly measures the top surface of the snow, but this still requires knowledge of the underlying dynamic snow field for estimates of sea ice thickness. With the advent of ICESat-2, a new sea ice thickness product using laser altimetry is on the horizon (Petty et al., 2020).

Reducing uncertainty in satellite-derived sea ice thickness estimates is crucial for improving our understanding of sea ice mass balance. By coupling sea ice thickness and drift estimates, it is possible to approximate freshwater exchanges across the Arctic basin due to sea ice growth and melt. For instance, in relation to Chapter 4, it would be possible to estimate ice production in the Kara and Laptev seas, export from these seas into the Eurasian Basin, and the magnitude of summertime melt in the Eurasian Basin. As explored above (Section 6.4), this is of crucial importance for the hydrography of the region and stability of the halocline.

6.7.2 Modelling the (coupled) climate system

Given the sparsity of observations in time and space in the Arctic Ocean, climate models are a powerful tool to develop understanding of the Arctic's climate dynamics. Coupled models, in particular, offer the opportunity to investigate the interactions in multiple directions between the different parts of the Arctic climate system. However, the connections between these systems are complex, and the underlying processes are often poorly resolved or parameterised by models (e.g. Lique et al., 2016).

For instance—in the ocean domain—eddies in the Arctic are ubiquitous in the subsurface, the open ocean and marginal ice zone (Kozlov et al., 2019; Meneghello, Marshall, Timmermans, et al., 2018; M. Zhao et al., 2016). Owing to its high-latitude location and often shallow depth scales, eddies tend to be small in the Arctic Ocean. Indeed, Kozlov et al. (2019) find that eddies can range in size from 100 km to as little as 0.5 km, scales that most models cannot resolve.

However, progress in simulating the ocean at increasingly higher resolutions is rapid (Haine et al., 2021), and high resolution regional models have recently provided key insight into eddy dynamics in the Arctic, resolving horizontal scales of 3–4 km (Meneghello et al., 2021; Regan, Lique, Talandier, et al., 2019). Previously, eddy-resolving models were, by necessity, highly idealised (e.g. Manucharyan & Spall, 2016).

The two-way coupling between atmosphere and ocean can only be represented by coupled models, however, and there are further challenges that are unique to the high latitude environment. For instance, simulating the exchanges of heat and momentum between the atmosphere and ocean, via highly heterogeneous sea ice and its dynamic snow cover, is a modelling challenge that is key to representing Arctic climate.

The physical system is also affected by biology, in sometimes surprising ways. For instance, marine phytoplankton blooms from Bering Strait can—via storms—provide ice-nucleating particles that contribute to cloud formation in the Arctic (Creamean et al., 2019), with potentially important effects for the radiative budget.

Multi-disciplinary campaigns such as SHEBA (Uttal et al., 2002) and MOSAiC (e.g. Krumpen et al., 2020) are crucial to advance basic knowledge of the nature of couplings between elements of the climate system and improve model representations. Model studies are of course essential to interpret and compare coupled model outputs; this is something we contribute to in Chapter 2.

Improvements to coupled models would provide greater confidence in their future projections for Arctic freshwater changes under anthropogenic climate change. Improved coupled models should also provide us with more insight into climate dynamics through interrogation of their internal variability. This is important, because scientific investigation with coupled climate models (e.g. in chapters 1, 2 and 4) is not motivated only for the sake of summarising the nature of those models, but is also aimed at understanding something new about the real physical climate system.

6.7.3 Effect of sea ice changes on ocean-atmosphere coupling

As the Arctic ice cover recedes in spatiotemporal extent and thickness, becomes smoother and is overlain by thinner snow, we can expect profound changes in the nature of ocean-atmosphere coupling—these changes are already well underway, of course. There are clear implications for heat fluxes, momentum transfer, gas exchange and aerosol transfer. Freshwater distribution, additionally, appears to be directly affected by stress changes on the ocean surface due to reductions in sea ice cover (Q. Wang et al., 2019).

Advancements in sea ice modelling schemes have resulted in key improvements of the spatial representations of ice cover (e.g. Tsamados et al., 2014) and changes in the trends of variables such as ice-ocean stress (T. Martin et al., 2016); one might imagine that future advances will yield further changes. Again, campaigns such as MOSAiC and SHEBA, which explicitly capture above and below ice conditions simultaneously at a number of sites of different ice characteristics, have great potential to advance the basic knowledge that should assist model development.

6.7.4 Atlantification

'Atlantification' has become a well-known term used to describe the increasing influence of Atlantic Waters in the Arctic Ocean (e.g. Årthun et al., 2012; Asbjørnsen et al., 2020; Polyakov et al., 2017; Simmonds et al., 2008). This is a topic that connects Arctic and North Atlantic variability, and thus we must consider physical dynamics both within and beyond the Arctic in assessing likely changes in the patterns and mechanisms of Atlantification in the future.

For instance, the Atlantic Water heat transport into the Arctic Ocean is associated with changes in both its flow and temperature. Upstream variability in these variables are related to the AMOC, but there are also important roles for local forcings. For instance, winds in the Nordic Seas significantly affect inflow (Årthun et al., 2019; Muilwijk et al., 2019), and atmospheric conditions in the Barents Sea affect heat loss (e.g. Skagseth et al., 2020).

As such, the future impact of Atlantification appears to be sensitive to the interplay between a changing AMOC, and changing regional and large-scale atmospheric circulation and temperatures; as well as the Arctic conditions discussed in this thesis—which concern freshwater distribution and halocline stability.

In addition, Atlantification appears to go hand-in-hand with deep water formation moving into the Arctic Ocean (e.g. Athanase et al., 2020; Lique et al., 2018), with possible implications for the AMOC itself.

6.7.5 Increasing ocean heat from the Pacific

Heat transport through the Bering Strait increased by 60% during 2001–2015; a result of both volume flux and temperature increases (Woodgate, 2018); the Chukchi Sea is additionally warming due to increased solar absorption (Steele et al., 2010; Timmermans et al., 2018).

The primary reservoir of heat in the western Arctic above c. 200 m depth is Pacific Summer Water (Timmermans et al., 2014), which defines the 'warm halocline' of the Beaufort Gyre at depths c. 30–130 m (Timmermans et al., 2017). Between 1987–2017, ocean measurements reveal a near doubling of ocean heat content relative to the freezing temperature in the Beaufort Gyre halocline, raising questions about potential impacts on sea ice: if all of that heat was mixed upwards, it could melt 1 m of ice across the Beaufort Gyre (Timmermans et al., 2018).

In the summer months, there is a lateral density contrast found at the surface of the Chukchi Sea, separating the warmer, saltier, Pacific Summer Water from the fresher surface waters of the Canada Basin. In order for the Pacific Summer Water to subduct and ventilate the warm halocline, geostrophic balance along the divide must be broken—such that the pressure gradient force at the front is not simply balanced by the coriolis force acting on the flows along the front (MacKinnon et al., 2021). This may occur through wind-driven Ekman pumping (Timmermans et al., 2014; Timmermans et al., 2017), but the warmest inflows appear to be emanating from Barrow Canyon (MacKinnon et al., 2021). Recent high-resolution hydrographic

surveying shows that the meandering of a warm jet originating from Barrow Canyon (MacKinnon et al., 2021) leads to filamented parcels of warm Pacific Summer Water being sequestered into the Beaufort Gyre halocline. The processes involved operate on the sub-mesoscale; scales not captured by even high-resolution regional models, never mind relatively coarse coupled climate models.

It is not clear what the fate of this sequestered heat—insulated beneath Beaufort Gyre freshwater, and seasonally isolated from ventilation—will be (MacKinnon et al., 2021; Timmermans et al., 2018). Improved understanding of both upward vertical mixing and lateral stirring in the region is required to understand its implications for the ice cover, for instance. Nor is it clear what the future of the processes of ventilation will be; density contrasts along the front in the Chukchi Sea may weaken as the water masses warm (Timmermans & Jayne, 2016). These are questions of important relevance for the sea ice cover of the western Arctic, and questions that interface directly with those regarding freshwater changes.

6.7.6 Impact of Arctic Ocean changes on mid-latitude weather

Of key interest to the scientific community is the potential for Arctic warming and sea ice retreat to impact mid-latitude weather and climate. Francis and Vavrus (2012) hypothesise that weaker meridional gradients in the thickness of the 1,000-500 hPa atmospheric layer cause slower zonal winds, and that enhanced Arctic warming causes 500 hPa heights to rise more near the pole than in mid-latitudes, elongating the peaks of high-pressure ridges northward and increasing wave amplitude. Both effects, they argue, should slow eastward upper-level wave propagation, and result in longer and more severe weather extremes at mid-latitudes. Other mechanisms have since been suggested that link Arctic Amplification and mid-latitude weather. Though all interconnected, Cohen et al. (2014) summarise these mechanisms as follows: a) changes in storm tracks in the North Atlantic sector; b) changes in the characteristics of the jet stream; and c) changes in planetary wave configurations.

Certain periods over the last several decades appear to support the idea that Arctic Amplifica-

tion may promote extreme mid-latitude weather (e.g. Cohen et al., 2014; Mori et al., 2019), however Blackport and Screen (2020) argue that much of this evidence arises from internal variability, and is not supported by longer-term trends. Indeed, modelling studies (e.g. Dai & Song, 2020) have recently suggested the influence of Arctic warming on mid-latitude weather is limited. Understanding the prospects of Arctic Amplification for extreme mid-latitude weather clearly has vast societal and economic implications, and will remain a key frontier in Arctic research.

In the other direction, the impact of warm and moist air intrusions into the Arctic from mid-latitudes also has important implications for Arctic climate and sea ice conditions (e.g. Wernli & Papritz, 2018; Woods & Caballero, 2016).

6.7.7 Arctic freshwater export and the AMOC

The last two decades have seen major advances in theoretical understanding of the AMOC (H. L. Johnson et al., 2019) and in its observation, thanks largely to the introduction of observational arrays at 26.5 N (the RAPID-MOCHA array; Cunningham et al., 2007) and in the subpolar N. Atlantic (the OSNAP array; Lozier et al., 2019). Coupled climate models generally predict a slowdown of the AMOC under greenhouse gas forcing (e.g. Meehl et al., 2012; Weaver et al., 2012), due to surface freshening in the subpolar N. Atlantic (e.g. Jahn & Holland, 2013), which implicates the role Arctic freshwater variability, and Greenland runoff (e.g. Shepherd et al., 2020). Debate is active over whether or not recently observed decreases in the overturning are driven by anthropogenic climate change (Rahmstorf et al., 2015), or consistent with internal variability (Jackson et al., 2016).

A key motivation behind modelling and observational efforts to better describe Arctic freshwater variability is the understanding that freshwater fluxes from the Arctic to the subpolar North Atlantic may impact the overturning circulation (Lique et al., 2016). The AMOC plays a vital role in global ocean circulation and climate. Moreover, it is theorised to exhibit multiple stable states, with the transition between them possibly determined by freshwater input (e.g.

Broecker, 1997; Broecker et al., 1985). Naturally, therefore, the question of how Arctic freshwater outflows may impact the AMOC is of considerable interest—and how these effects may be sensitive to different emissions scenarios.

It seems likely that it is not only the quantities of Arctic freshwater exported to the subpolar seas that is important for deepwater formation, but also the pathways taken by this freshwater and the patterns of mixing with the ambient ocean (e.g. de Steur et al., 2018; Holliday et al., 2020; H. Wang et al., 2018). However, simulations of these processes are model dependent (e.g. H. Wang et al., 2018) and our observational record remains short; coordinated efforts to improve both simulations and observations are needed.

6.8 Concluding remarks

It may be tempting to view the recent freshening of the Arctic Ocean as entirely a forced signal of climate change. Indeed, internal variability in the climate system is often underappreciated (e.g. Tebaldi et al., 2011). It would be unwise to do so; we have good evidence that the signal has been largely wind-driven (chapters 1 and 2), and it is likely that a significant part of the signal has arisen from internal variability. In an Arctic that is expected to exhibit forced changes towards a fresher state, we should still expect significant multi-year to multi-decadal variability. Indeed, if the mean state of the Arctic is fresher, we may expect greater variability in fluxes too; there are some signs of this in CMIP6 models (Zanowski et al., 2021).

As the pack ice becomes progressively weaker, the freshwater balance of the Beaufort Gyre should depend primarily on eddies and Ekman pumping, with the consequence that the gyre should hold more freshwater and adjust over a longer timescale (Doddridge et al., 2019; Timmermans & Marshall, 2020). Exchanges of freshwater with the dynamic overlying ice pack (Chapter 5) should be considered alongside exchanges of momentum (i.e., the 'ice ocean governor'; Meneghello, Marshall, Timmermans, et al., 2018).

On the eastern side of the Arctic, meanwhile, shifting patterns of ice production (Chapter

4) are likely to mean that the Eurasian halocline is increasingly unstable during the winter. Coupled with warming Atlantic inflows beneath, we may see increasing events of halocline collapse and deep convection, releasing heat from the Atlantic Waters to the surface (Lique et al., 2016; Polyakov et al., 2020). As sea ice import into the Eurasian Basin from the shelf seas declines, the freshwater content of the region will become more dependent on the pathways of the Eurasian river plumes. The long-term stability of winter sea ice in the Eurasian Basin depends on halocline stability and, therefore, freshwater.

It is possible that the east-west Arctic freshwater divide will steepen (e.g. Lique et al., 2016). This raises further questions for ocean dynamics: will this increase the baroclinicity of the interior, and result in a richer eddy field? Will this steepen east-west property gradients along the Transpolar Drift (e.g. Morison et al., 1998), potentially spinning up the flow and increasing freshwater fluxes out of the Arctic through Fram Strait?

This thesis has emphasised the primary importance of wind forcing for freshwater changes, but how will this atmospheric circulation change in the future? Will the Icelandic Low deepen, and the Beaufort Sea High weaken (as discussed by Moore et al., 2018; Timmermans & Marshall, 2020)? Such changes have obvious implications for the surface sea ice and geostrophic circulation of the ocean, and may influence Atlantic variability. As we have seen, the response of sea ice thermodynamics to winds can be rather different between the seasons (Chapter 3); it is not just the annual mean atmospheric circulation changes that we are concerned with, but the seasonal characteristics of change.

In an Arctic with a weaker, more mobile ice pack, patterns of divergence and convergence will be more intense. As such, it seems likely that there will be a greater role for atmospheric circulation in shaping the variability of the sea ice thickness, via dynamic thickness changes. We have seen that dynamic thickness changes have important implications for the thermodynamic exchanges of freshwater between ocean and ice, with seasonal characteristics that vary between the interior basins and marginal shelves (chapters 3 and 5). The variability in the sea ice thickness distribution—as shaped by winds, often in winter—is likely to play a key role in

the variability of summer sea ice melting and September sea ice extent and volume.

In a spatially and temporally variable manner, the future Arctic Ocean will most likely be warmer, fresher, more energetic in its surface eddy field, and covered with weaker, more mobile and increasingly seasonal sea ice. With ever warming inflows, the stability of the halocline—dependent on freshwater abundance—will be crucial for the long-term stability of winter sea ice. Larger volumes of freshwater, on the other hand, have greater potential to impact the AMOC if flushed from the Arctic. As the ecological make-up of the Arctic Ocean changes, nutrient limitation due to stratification may become increasingly important as solar irradiation increases. The understanding of freshwater changes in the Arctic Ocean will only become more essential in a warming world.

References

Aagaard, K., Swift, J. H., & Carmack, E. C. (1985). Thermohaline circulation in the Arctic Mediterranean Seas. *Journal of Geophysical Research*, *90*(C3), 4833.

Aagaard, K., & Carmack, E. C. (1989). The role of sea ice and other fresh water in the Arctic circulation. *Journal of Geophysical Research*, *94*(C10), 14485–14498.

Aagaard, K., Coachman, L. K., & Carmack, E. C. (1981). On the halocline of the Arctic Ocean. *Deep Sea Research Part A, Oceanographic Research Papers*, *28*(6), 529–545.

Alam, A., & Curry, J. A. (1997). Determination of surface turbulent fluxes over leads in Arctic sea ice. *Journal of Geophysical Research: Oceans*, *102*(C2), 3331–3343.

Alexandrov, V. Y., Martin, T., Kolatschek, J., Eicken, H., Kreyscher, M., & Makshtas, A. P. (2000). Sea ice circulation in the Laptev Sea and ice export to the Arctic Ocean: Results from satellite remote sensing and numerical modeling. *Journal of Geophysical Research: Oceans*, *105*(C7), 17143–17159.

Alkire, M. B., Falkner, K. K., Rigor, I. G., Steele, M., & Morison, J. (2007). The return of Pacific waters to the upper layers of the central Arctic Ocean. *Deep-Sea Research Part I: Oceanographic Research Papers*, *54*(9), 1509–1529.

Armitage, T. W., Bacon, S., Ridout, A. L., Thomas, S. F., Aksenov, Y., & Wingham, D. J. (2016). Arctic sea surface height variability and change from satellite radar altimetry and GRACE, 2003-2014. *Journal of Geophysical Research: Oceans*, *121*(6), 4303–4322.

Armitage, T. W., Bacon, S., Ridout, A. L., Petty, A. A., Wolbach, S., & Tsamados, M. (2017). Arctic Ocean surface geostrophic circulation 2003-2014. *Cryosphere*, *11*(4), 1767–1780.

Armitage, T. W., Bacon, S., & Kwok, R. (2018). Arctic Sea Level and Surface Circulation Response to the Arctic Oscillation. *Geophysical Research Letters*, *45*(13), 6576–6584.

Armitage, T. W., Manucharyan, G. E., Petty, A. A., Kwok, R., & Thompson, A. F. (2020). Enhanced eddy activity in the Beaufort Gyre in response to sea ice loss. *Nature Communications*, *11*(1), 1–8.

Arrhenius, S. (1896). On the influence of carbonic acid in the air upon the temperature of the ground. *The London, Edinburgh, and Dublin Philosophical Magazine and Journal of Science*, *41*(251), 237–276.

Arrigo, K. R., & van Dijken, G. L. (2015). Continued increases in Arctic Ocean primary production. *Progress in Oceanography*, *136*, 60–70.

Årthun, M., Eldevik, T., Smedsrud, L. H., Skagseth, & Ingvaldsen, R. B. (2012). Quantifying the influence of atlantic heat on barents sea ice variability and retreat. *Journal of Climate*, *25*(13), 4736–4743.

Årthun, M., Eldevik, T., & Smedsrud, L. H. (2019). The role of Atlantic heat transport in future Arctic winter sea ice loss. *Journal of Climate*, *32*(11), 3327–3341.

Asbjørnsen, H., Årthun, M., Skagseth, Ø., & Eldevik, T. (2020). Mechanisms Underlying Recent Arctic Atlantification. *Geophysical Research Letters*, *47*(15).

Athanase, M., Provost, C., Pérez-Hernández, M. D., Sennéchael, N., Bertosio, C., Artana, C., Garric, G., & Lellouche, J. M. (2020). Atlantic Water Modification North of Svalbard in the Mercator Physical System From 2007 to 2020. *Journal of Geophysical Research: Oceans*, *125*(10), 1–26.

Barnhart, K. R., Miller, C. R., Overeem, I., & Kay, J. E. (2016). Mapping the future expansion of Arctic open water. *Nature Climate Change*, *6*(3), 280–285.

Barnier, B., Madec, G., Penduff, T., Molines, J.-M., Treguier, A. M., Le Sommer, J., Beckmann, A., Biastoch, A., Böning, C., Dengg, J., Derval, C., Durand, E., Gulev, S., Remy, E., Talandier, C., Theetten, S., Maltrud, M., McClean, J., & De Cuevas, B. (2006). Impact of partial steps and momentum advection schemes in a global ocean circulation model at eddy-permitting resolution. *Ocean Dynamics*, *56*(5-6), 543–567.

Barton, B. I., Lenn, Y.-D., & Lique, C. (2018). Observed Atlantification of the Barents Sea Causes the Polar Front to Limit the Expansion of Winter Sea Ice. *Journal of Physical Oceanography*, *48*(8), 1849–1866.

Bathiany, S., Notz, D., Mauritsen, T., Raedel, G., & Brovkin, V. (2016). On the potential for abrupt Arctic winter sea ice loss. *Journal of Climate*, *29*(7), 2703–2719.

Bekryaev, R. V., Polyakov, I. V., & Alexeev, V. A. (2010). Role of polar amplification in long-term surface air temperature variations and modern arctic warming. *Journal of Climate*, *23*(14), 3888–3906.

Belkin, I. M., Levitus, S., Antonov, J., & Malmberg, S. A. (1998). 'Great Salinity Anomalies' in the North Atlantic. *Progress in Oceanography*, *41*(1), 1–68.

Belleflamme, A., Fettweis, X., & Erpicum, M. (2015). Recent summer Arctic atmospheric circulation anomalies in a historical perspective. *The Cryosphere*, *9*(1), 53–64.

Bentsen, M., Bethke, I., Debernard, J. B., Iversen, T., Kirkevåg, A., Seland, Ø., Drange, H., Roelandt, C., Seierstad, I. A., Hoose, C., & Kristjánsson, J. E. (2012). The Norwegian Earth System Model, NorESM1-M – Part 1: Description and basic evaluation. *Geoscientific Model Development Discussions*, *5*(3), 2843–2931.

Berrisford, P., Dee, D., Poli, P., Brugge, R., Fielding, M., Fuentes, M., Kållberg, P., Kobayashi, S., Uppala, S., & Simmons, A. (2001). *The ERA-Interim Archive ERA Report Series No.1 Version 2.0 i* (tech. rep.). ECMWF. Reading, UK.

Bigdeli, A., Nguyen, A. T., Pillar, H. R., Ocaña, V., & Heimbach, P. (2020). Atmospheric Warming Drives Growth in Arctic Sea Ice: A Key Role for Snow. *Geophysical Research Letters*, *47*(20), 1–10.

Bintanja, R., Graversen, R. G., & Hazeleger, W. (2011). Arctic winter warming amplified by the thermal inversion and consequent low infrared cooling to space. *Nature Geoscience*, *4*(11), 758–761.

Bitz, C. M., & Roe, G. H. (2004). A mechanism for the high rate of sea ice thinning in the Arctic Ocean. *Journal of Climate*, *17*(18), 3623–3632.

Blackport, R., & Screen, J. A. (2020). Weakened evidence for mid-latitude impacts of Arctic warming. *Nature Climate Change*, *10*(12), 1065–1066.

Block, K., Schneider, F. A., Mülmenstädt, J., Salzmann, M., & Quaas, J. (2020). Climate models disagree on the sign of total radiative feedback in the Arctic. *Tellus, Series A: Dynamic Meteorology and Oceanography*, *72*(1), 1–14.

Boisvert, L. N., Petty, A. A., & Stroeve, J. C. (2016). The impact of the extreme winter 2015/16 arctic cyclone on the Barents-Kara Seas. *Monthly Weather Review*, *144*(11), 4279–4287.

Bourdallé-Badie, R., Bell, M., Chanut, J., Clementi, E., Coward, A., Drudi, M., Éthé, C., Iovino, D., Lea, D., Lévy, C., Madec, G., Martin, N., Masson, S., Mathiot, P., Mocavero, S., Müller, S., Nurser, G., Samson, G., & Storkey, D. (2019). NEMO ocean engine.

Box, J. E., Colgan, W. T., Christensen, T. R., Schmidt, N. M., Lund, M., Parmentier, F. J. W., Brown, R., Bhatt, U. S., Euskirchen, E. S., Romanovsky, V. E., Walsh, J. E., Overland, J. E., Wang, M., Corell, R. W., Meier, W. N., Wouters, B., Mernild, S., Mård, J., Pawlak, J., & Olsen, M. S. (2019). Key indicators of Arctic climate change: 1971-2017. *Environmental Research Letters*, *14*(4).

Boyer, T., Levitus, S., Garcia, H., Locarnini, R. A., Stephens, C., & Antonov, J. (2005). Objective analyses of annual, seasonal, and monthly temperature and salinity for the World Ocean on a 0.25° grid. *International Journal of Climatology*, *25*(7), 931–945.

Brodeau, L., Barnier, B., Treguier, A. M., Penduff, T., & Gulev, S. (2010). An ERA40-based atmospheric forcing for global ocean circulation models. *Ocean Modelling*, *31*(3-4), 88–104.

Broecker, W. S. (1997). Thermohaline circulation, the achilles heel of our climate system: Will man-made CO2 upset the current balance? *Science*, *278*(5343), 1582–1588.

Broecker, W. S., Peteet, D. M., & Rind, D. (1985). Does the ocean-atmosphere system have more than one stable mode of operation? *Nature*, *315*(6014), 21–26.

Bulgakov, N. P. (1962). The role of convection in the mechanism of heat transfer of deep Atlantic water. *Deep-Sea Research and Oceanographic Abstracts*, *9*(5-6), 233–239.

Cai, L., Alexeev, V. A., Walsh, J. E., & Bhatt, U. S. (2018). Patterns, impacts, and future projections of summer variability in the arctic from CMIP5 models. *Journal of Climate*, *31*(24), 9815–9833.

Carmack, E. C. (2007). The alpha/beta ocean distinction: A perspective on freshwater fluxes, convection, nutrients and productivity in high-latitude seas. *Deep-Sea Research Part II: Topical Studies in Oceanography*, *54*(23-26), 2578–2598.

Carmack, E. C., & Wassmann, P. (2006). Food webs and physical-biological coupling on pan-Arctic shelves: Unifying concepts and comprehensive perspectives. *Progress in Oceanography*, *71*(2-4), 446–477.

Carmack, E. C., Polyakov, I., Padman, L., Fer, I., Hunke, E., Hutchings, J., Jackson, J., Kelley, D., Kwok, R., Layton, C., Melling, H., Perovich, D. K., Persson, O., Ruddick, B., Timmermans, M.-L., Toole, J. M., Ross, T., Vavrus, S., & Winsor, P. (2015). Toward quantifying the increasing role of oceanic heat in sea ice loss in the new arctic. *Bulletin of the American Meteorological Society*, *96*(12), 2079–2105.

Carmack, E. C., Yamamoto-Kawai, M., Haine, T. W. N., Bacon, S., Bluhm, B. A., Lique, C., Melling, H., Polyakov, I. V., Straneo, F., Timmermans, M.-L., & Williams, W. J. (2016). Freshwater and its role in the Arctic Marine System: Sources, disposition, storage, export, and physical and biogeochemical consequences in the Arctic and global oceans. *Journal of Geophysical Research G: Biogeosciences*, *121*(3), 675–717.

Cavalieri, D. J., & Martin, S. (1994). The contribution of Alaskan, Siberian, and Canadian coastal polynyas to the cold halocline layer of the Arctic Ocean. *Journal of Geophysical Research*, *99*(C9).

Cavalieri, D. J., & Parkinson, C. L. (2012). Arctic sea ice variability and trends, 1979-2010. *Cryosphere*, *6*(4), 881–889.

Choi, D. H., Kug, J. S., Kwon, W. T., Jin, F. F., Baek, H. J., & Min, S. K. (2010). Arctic Oscillation responses to greenhouse warming and role of synoptic eddy feedback. *Journal of Geophysical Research Atmospheres*, *115*(17), 1–9.

Chylek, P., Li, J., Dubey, M. K., Wang, M., & Lesins, G. (2011). Observed and model simulated 20th century Arctic temperature variability: Canadian Earth System Model CanESM2. *Atmospheric Chemistry and Physics Discussions*, *11*(8), 22893–22907.

Chylek, P., Folland, C. K., Lesins, G., Dubey, M. K., & Wang, M. (2009). Arctic air temperature change amplification and the Atlantic Multidecadal Oscillation. *Geophysical Research Letters*, *36*(14), 2–6.

Close, S., Houssais, M.-N., & Herbaut, C. (2017). The Arctic Winter Sea Ice Quadrupole Revisited. *Journal of Climate*, *30*(9), 3157–3167.

Cohen, J., Screen, J. A., Furtado, J. C., Barlow, M., Whittleston, D., Coumou, D., Francis, J. A., Dethloff, K., Entekhabi, D., Overland, J. E., & Jones, J. (2014). Recent Arctic amplification and extreme mid-latitude weather.

Cohen, J., Zhang, X., Francis, J. A., Jung, T., Kwok, R., Overland, J. E., Tayler, P. C., Lee, S., Laliberte, F., Feldstein, S., Maslowski, G., Henderson, G., Stroeve, J. C., Coumou, D., Handorf, D., Semmler, T., Ballinger, T., Hell, M., Kretschmer, M., … Blackport, R. (2018). Arctic change and possible influence on mid-latitude climate and weather. *US CLIVAR Report 2018-1*, (March), 41.

Cole, S. T., Toole, J. M., Lele, R., Timmermans, M.-L., Gallaher, S. G., Stanton, T. P., Shaw, W. J., Hwang, B., Maksym, T., Wilkinson, J. P., Ortiz, M., Graber, H., Rainville, L., Petty, A. A., Farrell, S. L., Richter-Menge, J. A., Haas, C., Deming, J. W., & Thomson, J. (2017). Ice and ocean velocity in the Arctic marginal ice zone: Ice roughness and momentum transfer. *Elem Sci Anth*, *5*.

Colony, R., & Thorndike, A. S. (1984). An estimate of the mean field of Arctic sea ice motion. *Journal of Geophysical Research*, *89*(C6), 10623.

Comiso, J. C., Cavalieri, D. J., Parkinson, C. L., & Gloersen, P. (1997). Passive microwave algorithms for sea ice concentration: A comparison of two techniques. *Remote Sensing of Environment*, *60*(3), 357–384.

Cornish, S. B., Kostov, Y., Johnson, H. L., & Lique, C. (2020). Response of Arctic freshwater to the Arctic Oscillation in coupled climate models. *Journal of Climate*, *33*(7), 2533–2555.

Creamean, J. M., Cross, J. N., Pickart, R., McRaven, L., Lin, P., Pacini, A., Hanlon, R., Schmale, D. G., Ceniceros, J., Aydell, T., Colombi, N., Bolger, E., & DeMott, P. J. (2019). Ice Nucleating Particles Carried From Below a Phytoplankton Bloom to the Arctic Atmosphere. *Geophysical Research Letters*, *46*(14), 8572–8581.

Cunningham, S. A., Kanzow, T., Rayner, D., Baringer, M. O., Johns, W. E., Marotzke, J., Longworth, H. R., Grant, E. M., Hirschi, J. J.-M., Beal, L. M., Meinen, C. S., & Bryden, H. L. (2007). Temporal Variability of the Atlantic Meridional Overturning Circulation at 26.5 N. *Science*, *317*(5840), 935–938.

Curry, B., Lee, C. M., & Petrie, B. (2011). Volume, Freshwater, and Heat Fluxes through Davis Strait, 2004–05*. *Journal of Physical Oceanography*, *41*(3), 429–436.

Curry, J. A., Schramm, J. L., Rossow, W. B., & Randall, D. (1996). Overview of Arctic Cloud and Radiation Characteristics. *Journal of Climate*, *9*(8), 1731–1764.

Curry, R., & Mauritzen, C. (2005). Dilution of the Northern North Atlantic Ocean in recent decades. *Science*, *308*(5729), 1772–1774.

Dai, A., & Trenberth, K. E. (2002). Estimates of freshwater discharge from continents: Latitudinal and seasonal variations. *Journal of Hydrometeorology*, *3*(6), 660–687.

Dai, A., Luo, D., Song, M., & Liu, J. (2019). Arctic amplification is caused by sea-ice loss under increasing CO 2. *Nature Communications*, *10*(1), 1–13.

Dai, A., & Song, M. (2020). Little influence of Arctic amplification on mid-latitude climate. *Nature Climate Change*, *10*(3), 231–237.

Danilov, S., Wang, Q., Timmermann, R., Iakovlev, N., Sidorenko, D., Kimmritz, M., Jung, T., & Schröter, J. (2015). Finite-Element Sea Ice Model (FESIM), version 2. *Geoscientific Model Development*, *8*(6), 1747–1761.

Danilov, S., Kivman, G., & Schröter, J. (2004). A finite-element ocean model: principles and evaluation. *Ocean Modelling*, *6*(2), 125–150.

Davis, P. E. D., Lique, C., & Johnson, H. L. (2014). On the link between arctic sea ice decline and the freshwater content of the beaufort gyre: Insights from a simple process model. *Journal of Climate*, *27*(21), 8170–8184.

Davis, P. E. D., Lique, C., Johnson, H. L., & Guthrie, J. D. (2016). Competing Effects of Elevated Vertical Mixing and Increased Freshwater Input on the Stratification and Sea Ice Cover in a Changing Arctic Ocean. *Journal of Physical Oceanography*, *46*(5), 1531–1553.

Dee, D. P., Uppala, S. M., Simmons, A. J., Berrisford, P., Poli, P., Kobayashi, S., Andrae, U., Balmaseda, M. A., Balsamo, G., Bauer, P., Bechtold, P., Beljaars, A. C. M., van de Berg, L., Bidlot, J., Bormann, N., Delsol, C., Dragani, R., Fuentes, M., Geer, A. J., … Vitart, F. (2011). The ERA-Interim reanalysis: configuration and performance of the data assimilation system. *Quarterly Journal of the Royal Meteorological Society*, *137*(656), 553–597.

de Lavergne, C., Falahat, S., Madec, G., Roquet, F., Nycander, J., & Vic, C. (2019). Toward global maps of internal tide energy sinks. *Ocean Modelling*, *137*, 52–75.

DeRepentigny, P., Tremblay, L. B., Newton, R., & Pfirman, S. (2016). Patterns of Sea Ice Retreat in the Transition to a Seasonally Ice-Free Arctic. *Journal of Climate*, *29*(19), 6993–7008.

Deser, C. (2000). On the teleconnectivity of the 'Arctic Oscillation'. *Geophysical Research Letters*, *27*(6), 779–782.

de Steur, L., Peralta-Ferriz, C., & Pavlova, O. (2018). Freshwater Export in the East Greenland Current Freshens the North Atlantic. *Geophysical Research Letters*, *45*(24), 359–13.

Dewey, R., Muench, R., & Gunn, J. (1999). Mixing and vertical heat flux estimates in the Arctic Eurasian Basin. *Journal of Marine Systems*, *21*(1-4), 199–205.

Dewey, S., Morison, J., Kwok, R., Dickinson, S., Morison, D., & Andersen, R. (2018). Arctic Ice-Ocean Coupling and Gyre Equilibration Observed With Remote Sensing. *Geophysical Research Letters*, *45*(3), 1499–1508.

Dickson, R. R., Meincke, J., Malmberg, S.-A., & Lee, A. J. (1988). The 'Great Salinity Anomaly' in the northern North Atlantic 1968-1982. Progress in Oceanography. *Progress in Oceanography*, *20*, 103–151.

Dickson, R. R., Rudels, B., Dye, S., Karcher, M., Meincke, J., & Yashayaev, I. (2007). Current estimates of freshwater flux through Arctic and subarctic seas. *Progress in Oceanography*, *73*(3-4), 210–230.

Ding, Y., Carton, J. A., Chepurin, G. A., Steele, M., & Hakkinen, S. (2016). Seasonal heat and freshwater cycles in the Arctic Ocean in CMIP5 coupled models. *Journal of Geophysical Research: Oceans*, *121*(4), 2043–2057.

Dix, M., Vohralik, P., Bi, D., Rashid, H., Marsland, S., O'Farrell, S., Uotila, P., Hirst, T., Kowalczyk, E., Sullivan, A., Yan, H., Franklin, C., Sun, Z., Watterson, I., Collier, M., Noonan, J., Rotstayn, L., Stevens, L., Uhe, P., & Puri, K. (2013). The ACCESS coupled model: documentation of core CMIP5 simulations and initial results. *Australian Meteorological and Oceanographic Journal*, *63*(1), 83–99.

Dmitrenko, I. A., Tyshko, K. N., Kirillov, S. A., Eicken, H., Hölemann, J. A., & Kassens, H. (2005). Impact of flaw polynyas on the hydrography of the Laptev Sea. *Global and Planetary Change*, *48*(1-3 SPEC. ISS.), 9–27.

Doddridge, E. W., Meneghello, G., Marshall, J., Scott, J., & Lique, C. (2019). A Three-way Balance in The Beaufort Gyre: The Ice-Ocean Governor, Wind Stress, and Eddy Diffusivity. *Journal of Geophysical Research: Oceans*, 2018JC014897.

Dufresne, J.-L., Foujols, M.-A., Denvil, S., Caubel, A., Marti, O., Aumont, O., Balkanski, Y., Bekki, S., Bellenger, H., Benshila, R., Bony, S., Bopp, L., Braconnot, P., Brockmann, P., Cadule, P., Cheruy, F., Codron, F., Cozic, A., Cugnet, D., … Vuichard, N. (2013). Climate change projections using the IPSL-CM5 Earth System Model: from CMIP3 to CMIP5. *Climate Dynamics*, *40*(9-10), 2123–2165.

Dunne, J. P., John, J. G., Adcroft, A. J., Griffies, S. M., Hallberg, R. W., Shevliakova, E., Stouffer, R. J., Cooke, W., Dunne, K. A., Harrison, M. J., Krasting, J. P., Malyshev, S. L., Milly, P. C. D., Phillipps, P. J., Sentman, L. T., Samuels, B. L., Spelman, M. J., Winton, M., Wittenberg, A. T., & Zadeh, N. (2012). GFDL's ESM2 Global Coupled Climate–Carbon Earth System Models. Part I: Physical Formulation and Baseline Simulation Characteristics. *Journal of Climate*, *25*(19), 6646–6665.

Dupont, F., Higginson, S., Bourdallé-Badie, R., Lu, Y., Roy, F., Smith, G. C., Lemieux, J.-F., Garric, G., & Davidson, F. (2015). A high-resolution ocean and sea-ice modelling system for the Arctic and North Atlantic oceans. *Geoscientific Model Development*, *8*(5), 1577–1594.

Eady, E. T. (1949). Long Waves and Cyclone Waves. *Tellus*, *1*(3), 33–52.

ECCO Consortium, Fukumori, I., Wang, O., Fenty, I., Forget, G., Heimbach, P., & Ponte, R. M. (2021). Synopsis of the ECCO Central Production Global Ocean and Sea-Ice State Estimate (Version 4 Release 4).

Eisenman, I., & Wettlaufer, J. S. (2009). Nonlinear threshold behavior during the loss of Arctic sea ice. *Proceedings of the National Academy of Sciences of the United States of America*, *106*(1), 28–32.

England, M., Jahn, A., & Polvani, L. (2019). Nonuniform Contribution of Internal Variability to Recent Arctic Sea Ice Loss. *Journal of Climate*, *32*(13), 4039–4053.

Fer, I. (2009). Weak Vertical Diffusion Allows Maintenance of Cold Halocline in the Central Arctic. *Atmospheric and Oceanic Science Letters*, *2*(3), 148–152.

Fetterer, F., Knowles, K., Meier, W. N., Savoie, M. H., & Windnagel, A. K. (2017). Sea Ice Index, Version 3 [1979-2020].

Ford, V. L., Frauenfeld, O. W., Nowotarski, C. J., & Bombardi, R. J. (2021). Effective sea ice area based on a thickness threshold. *Climate Dynamics*, (January).

Forget, G., Campin, J.-M., Heimbach, P., Hill, C. N., Ponte, R. M., & Wunsch, C. (2015). ECCO version 4: an integrated framework for non-linear inverse modeling and global ocean state estimation. *Geoscientific Model Development*, *8*(10), 3071–3104.

Fossheim, M., Primicerio, R., Johannesen, E., Ingvaldsen, R. B., Aschan, M. M., & Dolgov, A. V. (2015). Recent warming leads to a rapid borealization of fish communities in the Arctic. *Nature Climate Change*, *5*(7), 673–677.

Frainer, A., Primicerio, R., Dolgov, A., Fossheim, M., Johannesen, E., Lind, S., & Aschan, M. (2021). Increased functional diversity warns of ecological transition in the Arctic.

Francis, J. A., & Vavrus, S. J. (2012). Evidence linking Arctic amplification to extreme weather in mid-latitudes. *Geophysical Research Letters*, *39*(6).

Francis, J. A., & Skific, N. (2015). Evidence linking rapid Arctic warming to mid-latitude weather patterns. *Philosophical Transactions of the Royal Society A: Mathematical, Physical and Engineering Sciences*, *373*(2045).

Fučkar, N. S., Guemas, V., Johnson, N. C., Massonnet, F., & Doblas-Reyes, F. J. (2016). Clusters of interannual sea ice variability in the northern hemisphere. *Climate Dynamics*, *47*(5-6), 1527–1543.

Gawarkiewicz, G., & Plueddemann, A. J. (1995). Topographic control of thermohaline frontal structure in the Barents Sea Polar Front on the south flank of Spitsbergen Bank. *Journal of Geophysical Research*, *100*(C3), 4509.

Gent, P. R., & McWilliams, J. C. (1990). Isopycnal Mixing in Ocean Circulation Models. *Journal of Physical Oceanography*, *20*(1), 150–155.

Gent, P. R., Danabasoglu, G., Donner, L. J., Holland, M. M., Hunke, E. C., Jayne, S. R., Lawrence, D. M., Neale, R. B., Rasch, P. J., Vertenstein, M., Worley, P. H., Yang, Z.-L., & Zhang, M. (2011). The Community Climate System Model Version 4. *Journal of Climate*, *24*(19), 4973–4991.

Giles, K. A., Laxon, S. W., Ridout, A. L., Wingham, D. J., & Bacon, S. (2012). Western Arctic Ocean freshwater storage increased by wind-driven spin-up of the Beaufort Gyre. *Nature Geoscience*, *5*(3), 194–197.

Gill, A. E. (1973). Circulation and bottom water production in the Weddell Sea. *Deep-Sea Research and Oceanographic Abstracts*, *20*(2), 111–140.

Gillard, L. C., Hu, X., Myers, P. G., & Bamber, J. L. (2016). Meltwater pathways from marine terminating glaciers of the Greenland ice sheet. *Geophysical Research Letters*, *43*(20), 873–10.

Giorgetta, M. A., Jungclaus, J., Reick, C. H., Legutke, S., Bader, J., Böttinger, M., Brovkin, V., Crueger, T., Esch, M., Fieg, K., Glushak, K., Gayler, V., Haak, H., Hollweg, H.-D., Ilyina, T., Kinne, S., Kornblueh, L., Matei, D., Mauritsen, T., … Stevens, B. (2013). Climate and carbon cycle changes from 1850 to 2100 in MPI-ESM simulations for the Coupled Model Intercomparison Project phase 5. *Journal of Advances in Modeling Earth Systems*, *5*(3), 572–597.

Girard, L., Weiss, J., Molines, J. M., Barnier, B., & Bouillon, S. (2009). Evaluation of high-resolution sea ice models on the basis of statistical and scaling properties of Arctic sea ice drift and deformation. *Journal of Geophysical Research*, *114*(C8), 1–15.

Good, P., Gregory, J. M., & Lowe, J. A. (2011). A step-response simple climate model to reconstruct and interpret AOGCM projections. *Geophysical Research Letters*, *38*(1), 1–5.

Good, P., Gregory, J. M., Lowe, J. A., & Andrews, T. (2013). Abrupt CO2 experiments as tools for predicting and understanding CMIP5 representative concentration pathway projections. *Climate Dynamics*, *40*(3-4), 1041–1053.

Gordeev, V. V., Martin, J. M., Sidorov, I. S., & Sidorova, M. V. (1996). A reassessment of the Eurasian river input of water, sediment, major elements, and nutrients to the Arctic Ocean. *American Journal of Science*, *296*(6), 664–691.

Graham, R. M., Cohen, L., Petty, A. A., Boisvert, L. N., Rinke, A., Hudson, S. R., Nicolaus, M., & Granskog, M. A. (2017). Increasing frequency and duration of Arctic winter warming events. *Geophysical Research Letters*, *44*(13), 6974–6983.

Graversen, R. G., & Wang, M. (2009). Polar amplification in a coupled climate model with locked albedo. *Climate Dynamics*, *33*(5), 629–643.

Griffies, S. M., Gnanadesikan, A., Pacanowski, R. C., Larichev, V. D., Dukowicz, J. K., & Smith, R. D. (1998). Isoneutral Diffusion in a z -Coordinate Ocean Model. *Journal of Physical Oceanography*, *28*(5), 805–830.

Griffies, S. M., Winton, M., Donner, L. J., Horowitz, L. W., Downes, S. M., Farneti, R., Gnanadesikan, A., Hurlin, W. J., Lee, H.-C., Liang, Z., Palter, J. B., Samuels, B. L., Wittenberg, A. T., Wyman, B. L., Yin, J., & Zadeh, N. (2011). The GFDL CM3 Coupled Climate Model: Characteristics of the Ocean and Sea Ice Simulations. *Journal of Climate*, *24*(13), 3520–3544.

Griffies, S. M., Winton, M., Samuels, B., Danabasoglu, G., Yeager, S. G., Marlsand, S., Drange, H., & Bentsen, M. (2012). Datasets and protocol for the CLIVAR WGOMD Coordinated Ocean-sea ice Reference Experiments (COREs). *ICPO Publication Series*, (184), 21.

Guthrie, J. D., Morison, J. H., & Fer, I. (2013). Revisiting internal waves and mixing in the Arctic Ocean. *Journal of Geophysical Research: Oceans*, *118*(8), 3966–3977.

Haas, C. (2010). Dynamics versus Thermodynamics: The Sea Ice Thickness Distribution. In D. N. Thomas & G. S. Dieckmann (Eds.), *Sea ice* (2nd ed., pp. 113–153). Wiley-Blackwell.

Haine, T. W. N. (2020). Arctic Ocean Freshening Linked to Anthropogenic Climate Change: All Hands on Deck. *Geophysical Research Letters*, *47*(22), 1–5.

Haine, T. W. N., Curry, B., Gerdes, R., Hansen, E., Karcher, M., Lee, C., Rudels, B., Spreen, G., de Steur, L., Stewart, K. D., & Woodgate, R. (2015). Arctic freshwater export: Status, mechanisms, and prospects.

Haine, T. W. N., Gelderloos, R., Jimenez-Urias, M. A., Siddiqui, A. H., Lemson, G., Medvedev, D., Szalay, A., Abernathey, R. P., Almansi, M., & Hill, C. N. (2021). Is Computational Oceanography Coming of Age? *Bulletin of the American Meteorological Society*, 1–33.

Hall, A. (2004). The role of surface albedo feedback in climate. *Journal of Climate*, *17*(7), 1550–1568.

Hasselmann, K., Sausen, R., Maier-Reimer, E., & Voss, R. (1993). On the cold start problem in transient simulations with coupled atmosphere-ocean models. *Climate Dynamics*, *9*(2), 53–61.

He, Y.-C., Drange, H., Gao, Y., & Bentsen, M. (2016). Simulated Atlantic Meridional Overturning Circulation in the 20th century with an ocean model forced by reanalysis-based atmospheric data sets. *Ocean Modelling*, *100*, 31–48.

Heorton, H. D., Tsamados, M., Cole, S. T., Ferreira, A. M., Berbellini, A., Fox, M., & Armitage, T. W. (2019). Retrieving Sea Ice Drag Coefficients and Turning Angles From In Situ and Satellite Observations Using an Inverse Modeling Framework. *Journal of Geophysical Research: Oceans*, *124*(8), 6388–6413.

Hersbach, H., Bell, B., Berrisford, P., Hirahara, S., Horányi, A., Muñoz-Sabater, J., Nicolas, J., Peubey, C., Radu, R., Schepers, D., Simmons, A., Soci, C., Abdalla, S., Abellan, X., Balsamo, G., Bechtold, P., Biavati, G., Bidlot, J., Bonavita, M., … Thépaut, J. N. (2020). The

ERA5 global reanalysis. *Quarterly Journal of the Royal Meteorological Society*, *146*(730), 1999–2049.

Hibler, W. D. (1979). A Dynamic Thermodynamic Sea Ice Model. *Journal of Physical Oceanography*, *9*(4), 815–846.

Hilmer, M., & Jung, T. (2000). Evidence for a recent change in the link between the North Atlantic Oscillation and Arctic sea ice export. *Geophysical Research Letters*, *27*(7), 989–992.

Holland, M. M., & Bitz, C. M. (2003). Polar amplification of climate change in coupled models. *Climate Dynamics*, *21*(3-4), 221–232.

Holland, M. M., Finnis, J., & Serreze, M. C. (2006). Simulated Arctic Ocean freshwater budgets in the twentieth and twenty-first centuries. *Journal of Climate*, *19*(23), 6221–6242.

Holland, M. M., Finnis, J., Barrett, A. P., & Serreze, M. C. (2007). Projected changes in Arctic Ocean freshwater budgets. *Journal of Geophysical Research: Biogeosciences*, *112*(4).

Holland, M. M., & Stroeve, J. C. (2011). Changing seasonal sea ice predictor relationships in a changing Arctic climate. *Geophysical Research Letters*, *38*(18), 1–6.

Holland, M. M., Bailey, D. A., Briegleb, B. P., Light, B., & Hunke, E. (2012). Improved Sea Ice Shortwave Radiation Physics in CCSM4: The Impact of Melt Ponds and Aerosols on Arctic Sea Ice. *Journal of Climate*, *25*(5), 1413–1430.

Holliday, N. P., Bersch, M., Berx, B., Chafik, L., Cunningham, S. A., Florindo-López, C., Hátún, H., Johns, W., Josey, S. A., Larsen, K. M. H., Mulet, S., Oltmanns, M., Reverdin, G., Rossby, T., Thierry, V., Valdimarsson, H., & Yashayaev, I. (2020). Ocean circulation causes the largest freshening event for 120 years in eastern subpolar North Atlantic. *Nature Communications*, *11*(1).

Holmes, R. M., Shiklomanov, A. I., A., S., Tretiakov, M., McClelland, J. W., Spencer, R. G. M., & Tank, S. E. (2018). River Discharge. *Arctic Report Card 2018*.

Houssais, M.-N., & Herbaut, C. (2011). Atmospheric forcing on the Canadian Arctic Archipelago freshwater outflow and implications for the Labrador Sea variability. *Journal of Geophysical Research*, *116*, C00D02.

Hunke, E. C., & Dukowicz, J. K. (1997). An Elastic–Viscous–Plastic Model for Sea Ice Dynamics. *Journal of Physical Oceanography*, *27*(9), 1849–1867.

Ilicak, M., Drange, H., Wang, Q., Gerdes, R., Aksenov, Y., Bailey, D., Bentsen, M., Biastoch, A., Bozec, A., Böning, C., Cassou, C., Chassignet, E., Coward, A. C., Curry, B., Danabasoglu, G., Danilov, S., Fernandez, E., Fogli, P. G., Fujii, Y., … Yeager, S. G. (2016). An assessment of the Arctic Ocean in a suite of interannual CORE-II simulations. Part III: Hydrography and fluxes. *Ocean Modelling*, *100*, 141–161.

Ionita, M., Scholz, P., Lohmann, G., Dima, M., & Prange, M. (2016). Linkages between atmospheric blocking, sea ice export through Fram Strait and the Atlantic Meridional Overturning Circulation. *Scientific Reports*, *6*(September), 1–10.

Ivanova, D. P., Gleckler, P. J., Taylor, K. E., Durack, P. J., & Marvel, K. D. (2016). Moving beyond the total sea ice extent in gauging model biases. *Journal of Climate*, *29*(24), 8965–8987.

Jackson, L. C., Peterson, K. A., Roberts, C. D., & Wood, R. A. (2016). Recent slowing of Atlantic overturning circulation as a recovery from earlier strengthening. *Nature Geoscience*, *9*(7), 518–522.

Jahn, A. (2018). Reduced probability of ice-free summers for 1.5 °C compared to 2 °C warming. *Nature Climate Change*, *8*(5), 409–413.

Jahn, A., Tremblay, B., Mysak, L. A., & Newton, R. (2010). Effect of the large-scale atmospheric circulation on the variability of the Arctic Ocean freshwater export. *Climate Dynamics*, *34*(2-3), 201–222.

Jahn, A., & Holland, M. M. (2013). Implications of Arctic sea ice changes for North Atlantic deep convection and the meridional overturning circulation in CCSM4-CMIP5 simulations. *Geophysical Research Letters*, *40*(6), 1206–1211.

Jahn, A., Kay, J. E., Holland, M. M., & Hall, D. M. (2016). How predictable is the timing of a summer ice-free Arctic? *Geophysical Research Letters*, *43*(17), 9113–9120.

Jahn, A., & Laiho, R. (2020). Forced Changes in the Arctic Freshwater Budget Emerge in the Early 21st Century. *Geophysical Research Letters*, *47*(15), 1–10.

Janout, M. A., Hölemann, J., Timokhov, L., Gutjahr, O., & Heinemann, G. (2017). Circulation in the northwest Laptev Sea in the eastern Arctic Ocean: Crossroads between Siberian River water, Atlantic water and polynya-formed dense water. *Journal of Geophysical Research: Oceans*, *122*(8), 6630–6647.

Johns, T. C., Durman, C. F., Banks, H. T., Roberts, M. J., McLaren, A. J., Ridley, J. K., Senior, C. A., Williams, K. D., Jones, A., Rickard, G. J., Cusack, S., Ingram, W. J., Crucifix, M., Sexton, D. M. H., Joshi, M. M., Dong, B.-W., Spencer, H., Hill, R. S. R., Gregory, J. M., … Searl, Y. (2006). The New Hadley Centre Climate Model (HadGEM1): Evaluation of Coupled Simulations. *Journal of Climate*, *19*(7), 1327–1353.

Johnson, H. L., Cornish, S. B., Kostov, Y., Beer, E., & Lique, C. (2018). Arctic Ocean Freshwater Content and Its Decadal Memory of Sea-Level Pressure. *Geophysical Research Letters*, *45*(10), 4991–5001.

Johnson, H. L., Cessi, P., Marshall, D. P., Schloesser, F., & Spall, M. A. (2019). Recent contributions of theory to our understanding of the Atlantic Meridional Overturning Circulation. *Journal of Geophysical Research: Oceans*, 1–24.

Johnson, M. A., & Polyakov, I. V. (2001). The Laptev Sea as a source for recent Arctic Ocean salinity changes. *Geophysical Research Letters*, *28*(10), 2017–2020.

Jones, E. P., & Anderson, L. G. (1986). On the origin of the chemical properties of the Arctic Ocean halocline. *Journal of Geophysical Research*, *91*(C9), 10759.

Kay, J. E., Deser, C., Phillips, A., Mai, A., Hannay, C., Strand, G., Arblaster, J. M., Bates, S. C., Danabasoglu, G., Edwards, J., Holland, M., Kushner, P., Lamarque, J. F., Lawrence, D., Lindsay, K., Middleton, A., Munoz, E., Neale, R., Oleson, K., … Vertenstein, M. (2015). The community earth system model (CESM) large ensemble project : A community resource for studying climate change in the presence of internal climate variability. *Bulletin of the American Meteorological Society*, *96*(8), 1333–1349.

Kimura, N., & Wakatsuchi, M. (2000). Relationship between sea-ice motion and geostrophic wind in the northern hemisphere. *Geophysical Research Letters*, *27*(22), 3735–3738.

King, J., Skourup, H., Hvidegaard, S. M., Rösel, A., Gerland, S., Spreen, G., Polashenski, C., Helm, V., & Liston, G. E. (2018). Comparison of Freeboard Retrieval and Ice Thickness Calculation From ALS, ASIRAS, and CryoSat-2 in the Norwegian Arctic to Field Measurements Made During the N-ICE2015 Expedition. *Journal of Geophysical Research: Oceans*, *123*(2), 1123–1141.

Kostov, Y., Marshall, J., Hausmann, U., Armour, K. C., Ferreira, D., & Holland, M. M. (2017). Fast and slow responses of Southern Ocean sea surface temperature to SAM in coupled climate models. *Climate Dynamics*, *48*(5-6), 1595–1609.

Kostov, Y., Ferreira, D., Armour, K. C., & Marshall, J. (2018). Contributions of Greenhouse Gas Forcing and the Southern Annular Mode to Historical Southern Ocean Surface Temperature Trends. *Geophysical Research Letters*, *45*(2), 1086–1097.

Kozlov, I. E., Artamonova, A. V., Manucharyan, G. E., & Kubryakov, A. A. (2019). Eddies in the Western Arctic Ocean From Spaceborne SAR Observations Over Open Ocean and Marginal Ice Zones. *Journal of Geophysical Research: Oceans*, *124*(9), 6601–6616.

Krishfield, R. A., Proshutinsky, A., Tateyama, K., Williams, W. J., Carmack, E. C., McLaughlin, F. A., & Timmermans, M.-L. (2014). Deterioration of perennial sea ice in the Beaufort Gyre from 2003 to 2012 and its impact on the oceanic freshwater cycle. *Journal of Geophysical Research: Oceans*, *119*(2), 1271–1305.

Krumpen, T., Belter, H. J., Boetius, A., Damm, E., Haas, C., Hendricks, S., Nicolaus, M., Nöthig, E. M., Paul, S., Peeken, I., Ricker, R., & Stein, R. (2019). Arctic warming interrupts the Transpolar Drift and affects long-range transport of sea ice and ice-rafted matter. *Scientific Reports*, *9*(1), 1–9.

Krumpen, T., Birrien, F., Kauker, F., Rackow, T., von Albedyll, L., Angelopoulos, M., Belter, H. J., Bessonov, V., Damm, E., Dethloff, K., Haapala, J., Haas, C., Hendricks, S., Hoelemann, J., Hoppmann, M., Kaleschke, L., Karcher, M., Kolabutin, n., Lenz, J., … Tsamados, M. (2020). The MOSAiC ice floe: sediment-laden survivor from the Siberian shelf. *The Cryosphere Discussions*, 1–20.

Kurtz, N., & Harbeck, J. (2017). CryoSat-2 Level-4 Sea Ice Elevation, Freeboard, and Thickness, Version 1.

Kwok, R. (2018). Arctic sea ice thickness, volume, and multiyear ice coverage: Losses and coupled variability (1958-2018). *Environmental Research Letters*, *13*(10).

Kwok, R., Cunningham, G. F., & Yueh, S. (1999). Area balance of the Arctic Ocean perennial ice zone: October 1996 to April 1997. *Journal of Geophysical Research*, *104*(C11), 747–25.

Kwok, R., & Rothrock, D. A. (1999). Variability of Fram Strait ice flux and North Atlantic Oscillation. *Journal of Geophysical Research*, *104*(1998), 5177–5189.

Kwok, R., Cunningham, G. F., & Pang, S. S. (2004). Fram Strait sea ice outflow. *Journal of Geophysical Research: Oceans*, *109*(1), 1–14.

Kwok, R., & Rothrock, D. A. (2009). Decline in Arctic sea ice thickness from submarine and ICESat records: 1958-2008. *Geophysical Research Letters*, *36*(15), 1–5.

Kwok, R., Spreen, G., & Pang, S. (2013). Arctic sea ice circulation and drift speed: Decadal trends and ocean currents. *Journal of Geophysical Research: Oceans*, *118*(5), 2408–2425.

Kwok, R., & Cunningham, G. F. (2015). Variability of arctic sea ice thickness and volume from CryoSat-2. *Philosophical Transactions of the Royal Society A: Mathematical, Physical and Engineering Sciences*, *373*(2045).

Kwok, R. (2009). Outflow of Arctic Ocean sea ice into the Greenland and Barent Seas: 1979-2007. *Journal of Climate*, *22*(9), 2438–2457.

Labe, Z., Magnusdottir, G., & Stern, H. (2018). Variability of Arctic sea ice thickness using PIOMAS and the CESM large ensemble. *Journal of Climate*, *31*(8), 3233–3247.

Lamarque, J.-F., Bond, T. C., Eyring, V., Granier, C., Heil, A., Klimont, Z., Lee, D., Liousse, C., Mieville, A., Owen, B., Schultz, M. G., Shindell, D., Smith, S. J., Stehfest, E., Van Aardenne, J., Cooper, O. R., Kainuma, M., Mahowald, N., McConnell, J. R., … van Vuuren, D. P. (2010). Historical (1850–2000) gridded anthropogenic and biomass burning emissions of reactive gases and aerosols: methodology and application. *Atmospheric Chemistry and Physics*, *10*(15), 7017–7039.

Lambert, E., Nummelin, A., Pemberton, P., & Ilıcak, M. (2019). Tracing the Imprint of River Runoff Variability on Arctic Water Mass Transformation. *Journal of Geophysical Research: Oceans*, *124*(1), 302–319.

Lammers, R. B., Shiklomanov, A. I., Vörösmarty, C. J., Fekete, B. M., & Peterson, B. J. (2001). Assessment of contemporary Arctic river runoff based on observational discharge records. *Journal of Geophysical Research Atmospheres*, *106*(D4), 3321–3334.

Landy, J. C., Ehn, J. K., & Barber, D. G. (2015). Albedo feedback enhanced by smoother Arctic sea ice. *Geophysical Research Letters*, *42*(24), 10714–10720.

Landy, J. C., Petty, A. A., Tsamados, M., & Stroeve, J. C. (2020). Sea Ice Roughness Overlooked as a Key Source of Uncertainty in CryoSat-2 Ice Freeboard Retrievals. *Journal of Geophysical Research: Oceans*, *125*(5), 1–18.

Lang, A., Yang, S., & Kaas, E. (2017). Sea ice thickness and recent Arctic warming. *Geophysical Research Letters*, *44*(1), 409–418.

Laxon, S. W., Giles, K. A., Ridout, A. L., Wingham, D. J., Willatt, R., Cullen, R., Kwok, R., Schweiger, A., Zhang, J., Haas, C., Hendricks, S., Krishfield, R., Kurtz, N., Farrell, S., & Davidson, M. (2013). CryoSat-2 estimates of Arctic sea ice thickness and volume. *Geophysical Research Letters*, *40*(4), 732–737.

Ledley, T. S. (1991). Snow on sea ice: competing effects in shaping climate. *Journal of Geophysical Research*, *96*(D9).

Lenn, Y. D., Wiles, P. J., Torres-Valdes, S., Abrahamsen, E. P., Rippeth, T. P., Simpson, J. H., Bacon, S., Laxon, S. W., Polyakov, I., Ivanov, V., & Kirillov, S. (2009). Vertical mixing at intermediate depths in the Arctic boundary current. *Geophysical Research Letters*, *36*(5), 1–5.

Lincoln, B. J., Rippeth, T. P., Lenn, Y.-D., Timmermans, M.-L., Williams, W. J., & Bacon, S. (2016). Wind-driven mixing at intermediate depths in an ice-free Arctic Ocean. *Geophysical Research Letters*, *43*(18), 9749–9756.

Lind, S., Ingvaldsen, R. B., & Furevik, T. (2018). Arctic warming hotspot in the northern Barents Sea linked to declining sea-ice import. *Nature Climate Change*, *8*(7), 634–639.

Lindsay, R., Wensnahan, M., Schweiger, A., & Zhang, J. (2014). Evaluation of Seven Different Atmospheric Reanalysis Products in the Arctic. *Journal of Climate*, *27*(7), 2588–2606.

Lindsay, R., & Schweiger, A. (2015). Arctic sea ice thickness loss determined using subsurface, aircraft, and satellite observations. *Cryosphere*, *9*(1), 269–283.

Lique, C., Treguier, A. M., Scheinert, M., & Penduff, T. (2009). A model-based study of ice and freshwater transport variability along both sides of Greenland. *Climate Dynamics*, *33*(5), 685–705.

Lique, C., Treguier, A. M., Blanke, B., & Grima, N. (2010). On the origins of water masses exported along both sides of Greenland: A Lagrangian model analysis. *Journal of Geophysical Research: Oceans*, *115*(5), 1–20.

Lique, C., & Johnson, H. L. (2015). Is there any imprint of the wind variability on the Atlantic Water circulation within the Arctic Basin? *Geophysical Research Letters*, *42*(22), 9880–9888.

Lique, C., Johnson, H. L., & Davis, P. E. D. (2015). On the Interplay between the Circulation in the Surface and the Intermediate Layers of the Arctic Ocean. *Journal of Physical Oceanography*, *45*(5), 1393–1409.

Lique, C., Holland, M. M., Dibike, Y. B., Lawrence, D. M., & Screen, J. A. (2016). Modeling the Arctic freshwater system and its integration in the global system: Lessons learned and future challenges.

Lique, C., Johnson, H. L., & Plancherel, Y. (2018). Emergence of deep convection in the Arctic Ocean under a warming climate. *Climate Dynamics*, *50*(9-10), 3833–3847.

Liston, G. E., Itkin, P., Stroeve, J. C., Tschudi, M. A., Stewart, J. S., Pedersen, S. H., Reinking, A. K., & Elder, K. (2020). A Lagrangian Snow-Evolution System for Sea-Ice Applications (SnowModel-LG): Part I—Model Description. *Journal of Geophysical Research: Oceans*, *125*(10).

Losch, M., Menemenlis, D., Campin, J.-M., Heimbach, P., & Hill, C. (2010). On the formulation of sea-ice models. Part 1: Effects of different solver implementations and parameterizations. *Ocean Modelling*, *33*(1-2), 129–144.

Lozier, M. S., Li, F., Bacon, S., Bahr, F., Bower, A. S., Cunningham, S. A., De Jong, M. F., De Steur, L., DeYoung, B., Fischer, J., Gary, S. F., Greenan, B. J., Holliday, N. P., Houk, A., Houpert, L., Inall, M. E., Johns, W. E., Johnson, H. L., Johnson, C., … Zhao, J. (2019). A sea change in our view of overturning in the subpolar North Atlantic. *Science*, *363*(6426), 516–521.

Lund, I. A. (1970). A Monte Carlo Method for Testing the Statistical Significance of a Regression Equation. *Journal of Applied Meteorology*, *9*, 330–332.

Luneva, M. V., Willmott, A. J., & Maqueda, M. A. M. (2012). Geostrophic adjustment problems in a polar basin. *Atmosphere - Ocean*, *50*(2), 134–155.

Ma, B., Steele, M., & Lee, C. M. (2017). Ekman circulation in the Arctic Ocean: Beyond the Beaufort Gyre. *Journal of Geophysical Research: Oceans*, *122*(4), 3358–3374.

MacKinnon, J. A., Simmons, H. L., Hargrove, J., Thomson, J., Peacock, T., Alford, M. H., Barton, B. I., Boury, S., Brenner, S. D., Couto, N., Danielson, S. L., Fine, E. C., Graber, H. C., Guthrie, J., Hopkins, J. E., Jayne, S. R., Jeon, C., Klenz, T., Lee, C. M., … Wood, K. R. (2021). A warm jet in a cold ocean. *Nature Communications*, *12*(1), 2418.

Mahlstein, I., Knutti, R., Solomon, S., & Portmann, R. W. (2011). Early onset of significant local warming in low latitude countries. *Environmental Research Letters*, *6*(3).

Mallett, R. D. C., Stroeve, J. C., Cornish, S. B., Crawford, A. D., Lukovich, J. V., Serreze, M. C., Barrett, A. P., Meier, W. N., Heorton, H. D. B. S., & Tsamados, M. (2021). Record winter winds in 2020/21 drove exceptional Arctic sea ice transport. *Communications Earth & Environment*, *2*(1), 17–22.

Mallett, R. D., Lawrence, I. R., Stroeve, J. C., Landy, J. C., & Tsamados, M. (2020). Brief communication: Conventional assumptions involving the speed of radar waves in snow introduce systematic underestimates to sea ice thickness and seasonal growth rate estimates. *Cryosphere*, *14*(1), 251–260.

Mallett, R. D., Stroeve, J. C., Tsamados, M., Landy, J. C., Willatt, R., Nandan, V., & Liston, G. E. (2021). Faster decline and higher variability in the sea ice thickness of the marginal Arctic seas. *The Cryosphere Discussions (accepted)*.

Manabe, S., & Stouffer, R. J. (1980). Sensitivity of a global climate model to an increase of CO2 concentration in the atmosphere. *Journal of Geophysical Research*, *85*(C10), 5529–5554.

Manabe, S., & Wetherald, R. T. (1975). The Effects of Doubling the CO 2 Concentration on the climate of a General Circulation Model. *Journal of the Atmospheric Sciences*, *32*(1), 3–15.

Manucharyan, G. E., Spall, M. A., & Thompson, A. F. (2016). A theory of the wind-driven beaufort gyre variability. *Journal of Physical Oceanography*, *46*(11), 3263–3278.

Manucharyan, G. E., & Spall, M. A. (2016). Wind-driven freshwater buildup and release in the Beaufort Gyre constrained by mesoscale eddies. *Geophysical Research Letters*, *43*(1), 273–282.

Manucharyan, G. E., & Isachsen, P. E. (2019). Critical Role of Continental Slopes in Halocline and Eddy Dynamics of the Ekman-Driven Beaufort Gyre. *Journal of Geophysical Research: Oceans*, *124*(4), 2679–2696.

Marshall, J., Adcroft, A., Hill, C., Perelman, L., & Heisey, C. (1997). A finite-volume, incompressible Navier Stokes model for studies of the ocean on parallel computers. *Journal of Geophysical Research: Oceans*, *102*(C3), 5753–5766.

Marshall, J., Jones, H., Karsten, R., & Wardle, R. (2002). Can eddies set ocean stratification? *Journal of Physical Oceanography*, *32*(1), 26–38.

Marshall, J., Armour, K. C., Scott, J. R., Kostov, Y., Hausmann, U., Ferreira, D., Shepherd, T. G., & Bitz, C. M. (2014). The ocean's role in polar climate change: Asymmetric Arctic and Antarctic responses to greenhouse gas and ozone forcing. *Philosophical Transactions of the Royal Society A: Mathematical, Physical and Engineering Sciences*, *372*(2019).

Marshall, J., Scott, J., & Proshutinsky, A. (2017). Climate response functions for the Arctic Ocean: A proposed coordinated modelling experiment. *Geoscientific Model Development*, *10*(7), 2833–2848.

Martin, S., & Cavalieri, D. J. (1989). Contributions of the siberian shelf polynyas to the arctic ocean intermediate and deep water. *Journal of Geophysical Research: Oceans*, *94*(C9), 725–738.

Martin, T., & Gerdes, R. (2007). Sea ice drift variability in Arctic Ocean Model Intercomparison Project models and observations. *Journal of Geophysical Research: Oceans*, *112*(4), 1–13.

Martin, T., Steele, M., & Zhang, J. (2014). Seasonality and long-term trend of Arctic Ocean surface stress in a model. *Journal of Geophysical Research: Oceans*, *119*(3), 1723–1738.

Martin, T., Tsamados, M., Schroeder, D., & Feltham, D. L. (2016). The impact of variable sea ice roughness on changes in Arctic Ocean surface stress: A model study. *Journal of Geophysical Research: Oceans*, *121*(3), 1931–1952.

Martinson, D. G., & Steele, M. (2001). Future of the Arctic sea ice cover: Implications of an Antarctic analog. *Geophysical Research Letters*, *28*(2), 307–310.

Maslanik, J. A., Fowler, C., Stroeve, J. C., Drobot, S., Zwally, J., Yi, D., & Emery, W. (2007). A younger, thinner Arctic ice cover: Increased potential for rapid, extensive sea-ice loss. *Geophysical Research Letters*, *34*(24), 2004–2008.

Maslanik, J. A., Stroeve, J. C., Fowler, C., & Emery, W. (2011). Distribution and trends in Arctic sea ice age through spring 2011. *Geophysical Research Letters*, *38*(13), 2–7.

Maykut, G. A. (1982). Large-scale heat exchange and ice production in the central Arctic. *Journal of Geophysical Research*, *87*(C10), 7971–7984.

Maykut, G. A., & McPhee, M. G. (1995). Solar heating of the Arctic mixed layer. *Journal of Geophysical Research*, *100*(C12).

Maykut, G. A. (1978). Energy exchange over young sea ice in the central Arctic. *Journal of Geophysical Research*, *83*(C7), 3646.

McClelland, J. W., Déry, S. J., Peterson, B. J., Holmes, R. M., & Wood, E. F. (2006). A pan-arctic evaluation of changes in river discharge during the latter half of the 20th century. *Geophysical Research Letters*, *33*, 2–5.

McLaughlin, F. A., Carmack, E., Macdonald, R., Melling, H., Swift, J., Wheeler, P., Sherr, B., & Sherr, E. (2004). The joint roles of Pacific and Atlantic-origin waters in the Canada Basin, 1997–1998. *Deep Sea Research Part I: Oceanographic Research Papers*, *51*(1), 107–128.

McLaughlin, F. A., & Carmack, E. C. (2010). Deepening of the nutricline and chlorophyll maximum in the Canada Basin interior, 2003-2009. *Geophysical Research Letters*, *37*(24).

McPhee, M. G., Proshutinsky, A., Morison, J. H., Steele, M., & Alkire, M. B. (2009). Rapid change in freshwater content of the Arctic Ocean. *Geophysical Research Letters*, *36*(10).

McPhee, M. G. (1981). An analytic similarity theory for the planetary boundary layer stabilized by surface buoyancy. *Boundary-Layer Meteorology*, *21*(3), 325–339.

McPhee, M. G. (2012). Advances in understanding ice-ocean stress during and since AIDJEX. *Cold Regions Science and Technology*, *76-77*, 24–36.

McPhee, M. G., & Smith, J. D. (1976). Measurements of the Turbulent Boundary Layer under Pack Ice. *Journal of Physical Oceanography*, *6*(5), 696–711.

Meehl, G. A., Washington, W. M., Arblaster, J. M., Hu, A., Teng, H., Tebaldi, C., Sanderson, B. N., Lamarque, J.-F., Conley, A., Strand, W. G., & White, J. B. (2012). Climate System Response to External Forcings and Climate Change Projections in CCSM4. *Journal of Climate*, *25*(11), 3661–3683.

Meier, W. N., Fetterer, F., Savoie, M. H., Mallory, S., Duerr, R., & Stroeve, J. C. (2017). NOAA/NSIDC Climate Data Record of Passive Microwave Sea Ice Concentration, Version 3. [1978-2019].

Meinshausen, M., Smith, S. J., Calvin, K., Daniel, J. S., Kainuma, M. L. T., Lamarque, J.-F., Matsumoto, K., Montzka, S. A., Raper, S. C. B., Riahi, K., Thomson, A., Velders, G. J. M., & van Vuuren, D. P. (2011). The RCP greenhouse gas concentrations and their extensions from 1765 to 2300. *Climatic Change*, *109*(1-2), 213–241.

Melling, H., Johnston, P. H., & Riedel, D. A. (1995). Measurements of the Underside Topography of Sea Ice by Moored Subsea Sonar. *Journal of Atmospheric and Oceanic Technology*, *12*(3), 589–602.

Meneghello, G., Marshall, J., Campin, J. M., Doddridge, E., & Timmermans, M.-L. (2018). The Ice-Ocean Governor: Ice-Ocean Stress Feedback Limits Beaufort Gyre Spin-Up. *Geophysical Research Letters*, *45*(20), 293–11.

Meneghello, G., Marshall, J., Timmermans, M.-L., & Scott, J. (2018). Observations of Seasonal Upwelling and Downwelling in the Beaufort Sea Mediated by Sea Ice. *Journal of Physical Oceanography*, *48*(4), 795–805.

Meneghello, G., Marshall, J., Lique, C., Isachsen, P. E., Doddridge, E., Campin, J.-M., Regan, H., & Talandier, C. (2021). Genesis and Decay of Mesoscale Baroclinic Eddies in the Seasonally Ice-Covered Interior Arctic Ocean. *Journal of Physical Oceanography*, *51*(1), 115–129.

Merkouriadi, I., Cheng, B., Graham, R. M., Rösel, A., & Granskog, M. A. (2017). Critical Role of Snow on Sea Ice Growth in the Atlantic Sector of the Arctic Ocean. *Geophysical Research Letters*, *44*(20), 479–10.

Miller, G. H., Alley, R. B., Brigham-Grette, J., Fitzpatrick, J. J., Polyak, L., Serreze, M. C., & White, J. W. (2010). Arctic amplification: Can the past constrain the future? *Quaternary Science Reviews*, *29*(15-16), 1779–1790.

Miller, R. L., Schmidt, G. A., & Shindell, D. T. (2006). Forced annular variations in the 20th century Intergovernmental Panel on Climate Change Fourth Assessment Report models. *Journal of Geophysical Research Atmospheres*, *111*(18), 1–17.

Moore, G. W., Renfrew, I. A., & Pickart, R. S. (2013). Multidecadal mobility of the north atlantic oscillation. *Journal of Climate*, *26*(8), 2453–2466.

Moore, G. W., Schweiger, A., Zhang, J., & Steele, M. (2018). Collapse of the 2017 Winter Beaufort High: A Response to Thinning Sea Ice? *Geophysical Research Letters*, *45*(6), 2860–2869.

Morales Maqueda, M. A., Willmott, A. J., & Biggs, N. R. (2004). Polynya dynamics: A review of observations and modeling. *Reviews of Geophysics*, *42*(1).

Mori, M., Kosaka, Y., Watanabe, M., Nakamura, H., & Kimoto, M. (2019). A reconciled estimate of the influence of Arctic sea-ice loss on recent Eurasian cooling.

Morison, J., Steele, M., Kikuchi, T., Falkner, K., & Smethie, W. (2006). Relaxation of central Arctic Ocean hydrography to pre-1990s climatology. *Geophysical Research Letters*, *33*(17), 1–5.

Morison, J., Steele, M., & Andersen, R. (1998). Hydrography of the upper Arctic Ocean measured from the nuclear submarine U.S.S. Pargo. *Deep Sea Research Part I: Oceanographic Research Papers*, *45*(1), 15–38.

Morison, J., Kwok, R., Peralta-Ferriz, C., Alkire, M. B., Rigor, I. G., Andersen, R., & Steele, M. (2012). Changing Arctic Ocean freshwater pathways. *Nature*, *481*(7379), 66–70.

Morison, J., Kwok, R., Dickinson, S., Andersen, R., Peralta-Ferriz, C., Morison, D., Rigor, I., Dewey, S., & Guthrie, J. (2021). The Cyclonic Mode of Arctic Ocean Circulation. *Journal of Physical Oceanography*.

Morrison, A. L., Kay, J. E., Frey, W. R., Chepfer, H., & Guzman, R. (2019). Cloud Response to Arctic Sea Ice Loss and Implications for Future Feedback in the CESM1 Climate Model. *Journal of Geophysical Research: Atmospheres*, *124*(2), 1003–1020.

Muilwijk, M., Smedsrud, L. H., Ilicak, M., & Drange, H. (2018). Atlantic Water Heat Transport Variability in the 20th Century Arctic Ocean From a Global Ocean Model and Observations. *Journal of Geophysical Research: Oceans*, *123*(11), 8159–8179.

Muilwijk, M., Ilicak, M., Cornish, S. B., Danilov, S., Gelderloos, R., Gerdes, R., Haid, V., Haine, T. W. N., Johnson, H. L., Kostov, Y., Kovács, T., Lique, C., Marson, J. M., Myers, P. G., Scott, J., Smedsrud, L. H., Talandier, C., & Wang, Q. (2019). Arctic Ocean response to Greenland Sea wind anomalies in a suite of model simulations. *Journal of Geophysical Research: Oceans*, 2019JC015101.

Nandan, V., Geldsetzer, T., Yackel, J., Mahmud, M., Scharien, R., Howell, S., King, J., Ricker, R., & Else, B. (2017). Effect of Snow Salinity on CryoSat-2 Arctic First-Year Sea Ice Freeboard Measurements. *Geophysical Research Letters*, *44*(20), 419–10.

Nansen, F. (1902). *The oceanography of the North Polar Basin. The Norwegian North Polar Expedition 1893-1896. Scientific Results, 3(9).* Longmans, Green, co.

Newton, R., Schlosser, P., Martinson, D. G., & Maslowski, W. (2008). Freshwater distribution in the Arctic Ocean: Simulation with a highresolution model and model-data comparison. *Journal of Geophysical Research: Oceans*, *113*(5), 1–15.

Niederdrenk, A. L., Sein, D. V., & Mikolajewicz, U. (2016). Interannual variability of the Arctic freshwater cycle in the second half of the twentieth century in a regionally coupled climate model. *Climate Dynamics*, *47*(12), 3883–3900.

North, G. R., Bell, T. L., Cahalan, R. F., & Moeng, F. J. (1982). Sampling Errors in the Estimation of Empirical Orthogonal Functions. *Monthly Weather Review*, *110*(7), 699–706.

Notz, D. (2009). The future of ice sheets and sea ice: Between reversible retreat and unstoppable loss. *Proceedings of the National Academy of Sciences of the United States of America*, *106*(49), 20590–20595.

Notz, D., & Stroeve, J. C. (2016). Observed Arctic sea-ice loss directly follows anthropogenic CO2 emission. *Science*, *354*(6313), 747–750.

Nummelin, A., Ilicak, M., Li, C., & Smedsrud, L. H. (2016). Consequences of future increased Arctic runoff on Arctic Ocean stratification, circulation, and sea ice cover. *Journal of Geophysical Research: Oceans*, *121*(1), 617–637.

Olason, E., & Notz, D. (2014). Drivers of variability in Arctic sea-ice drift speed. *Journal of Geophysical Research: Oceans*, *119*(9), 5755–5775.

O'Neill, B. C., Tebaldi, C., van Vuuren, D. P., Eyring, V., Friedlingstein, P., Hurtt, G., Knutti, R., Kriegler, E., Lamarque, J.-F., Lowe, J., Meehl, G. A., Moss, R., Riahi, K., & Sanderson, B. M. (2016). The Scenario Model Intercomparison Project (ScenarioMIP) for CMIP6. *Geoscientific Model Development*, *9*(9), 3461–3482.

Onogi, K., Tsutsui, J., Koide, H., Sakamoto, M., Kobayashi, S., Hatsushika, H., Matsumoto, T., Yamazaki, N., Kamahori, H., Takahashi, K., Kadokura, S., Wada, K., Kato, K., Oyama, R., Ose, T., Mannoji, N., & Taira, R. (2007). The JRA-25 Reanalysis. *Journal of the Meteorological Society of Japan. Ser. II*, *85*(3), 369–432.

Orkney, A., Platt, T., Narayanaswamy, B. E., Kostakis, I., & Bouman, H. A. (2020). Bio-optical evidence for increasing Phaeocystis dominance in the Barents Sea: Increasing Phaeocystis in Barents Sea. *Philosophical Transactions of the Royal Society A: Mathematical, Physical and Engineering Sciences*, *378*(2181).

Osadchiev, A. A., Pisareva, M. N., Spivak, E. A., Shchuka, S. A., & Semiletov, I. P. (2020). Freshwater transport between the Kara, Laptev, and East-Siberian seas. *Scientific Reports*, *10*(1).

Overland, J. E., & Wang, M. (2010). Large-scale atmospheric circulation changes are associated with the recent loss of Arctic sea ice. *Tellus, Series A: Dynamic Meteorology and Oceanography*, *62*(1), 1–9.

Overland, J. E., Dunlea, E., Box, J. E., Corell, R., Forsius, M., Kattsov, V., Olsen, M. S., Pawlak, J., Reiersen, L. O., & Wang, M. (2019). The urgency of Arctic change. *Polar Science*, *21*(July 2018), 6–13.

Padman, L., & Dillon, T. M. (1991). Turbulent mixing near the Yermak Plateau during the Coordinated Eastern Arctic Experiment. *Journal of Geophysical Research*, *96*(C3), 4769.

Park, H. S., & Stewart, A. L. (2016). An analytical model for wind-driven Arctic summer sea ice drift. *Cryosphere*, *10*(1), 227–244.

Payne, A. E., Jansen, M. F., & Cronin, T. W. (2015). Conceptual model analysis of the influence of temperature feedbacks on polar amplification. *Geophysical Research Letters*, *42*(21), 9561–9570.

Peeken, I., Primpke, S., Beyer, B., Gütermann, J., Katlein, C., Krumpen, T., Bergmann, M., Hehemann, L., & Gerdts, G. (2018). Arctic sea ice is an important temporal sink and means of transport for microplastic. *Nature Communications*, *9*(1), 1505.

Pemberton, P., Nilsson, J., & Meier, H. E. (2014). Arctic ocean freshwater composition, pathways and transformations from a passive tracer simulation. *Tellus, Series A: Dynamic Meteorology and Oceanography*, *66*(1).

Peng, G., Meier, W. N., Scott, D. J., & Savoie, M. H. (2013). A long-term and reproducible passive microwave sea ice concentration data record for climate studies and monitoring. *Earth System Science Data*, *5*(2), 311–318.

Perovich, D. K., Richeter-Menge, J. A., Jones, K. F., & Light, B. (2008). Sunlight, water, and ice: Extreme Arctic sea ice melt during the summer of 2007. *Geophysical Research Letters*, *35*(11), 2–5.

Perovich, D. K., Richter-Menge, J. A., Jones, K. F., Light, B., Elder, B. C., Polashenski, C., Laroche, D., Markus, T., & Lindsay, R. (2011). Arctic sea-ice melt in 2008 and the role of solar heating. *Annals of Glaciology*, *52*(57), 355–359.

Peters, G. P., Andrew, R. M., Boden, T., Canadell, J. G., Ciais, P., Le Quéré, C., Marland, G., Raupach, M. R., & Wilson, C. (2013). The challenge to keep global warming below 2C. *Nature Climate Change*, *3*(1), 4–6.

Peterson, B. J., Holmes, R. M., McClelland, J. W., Vörösmarty, C. J., Lammers, R. B., Shiklomanov, A. I., Shiklomanov, I. A., & Rahmstorf, S. (2002). Increasing river discharge to the Arctic Ocean. *Science*, *298*(5601), 2171–2173.

Petrich, C., & Eicken, H. (2010). Growth, Structure and Properties of Sea Ice. In D. N. Thomas & G. S. Dieckmann (Eds.), *Sea ice* (pp. 79–113). Wiley-Blackwell.

Petty, A. A., Hutchings, J. K., Richter-Menge, J. A., & Tschudi, M. A. (2016). Sea ice circulation around the Beaufort Gyre: The changing role of wind forcing and the sea ice state. *Journal of Geophysical Research: Oceans*, *121*(5), 3278–3296.

Petty, A. A., Holland, M. M., Bailey, D. A., & Kurtz, N. T. (2018). Warm Arctic, Increased Winter Sea Ice Growth? *Geophysical Research Letters*, *45*(23), 922–12.

Petty, A. A., Kurtz, N. T., Kwok, R., Markus, T., & Neumann, T. A. (2020). Winter Arctic Sea Ice Thickness From ICESat-2 Freeboards. *Journal of Geophysical Research: Oceans*, *125*(5), 1–28.

Pickart, R. S., & Spall, M. A. (2007). Impact of Labrador Sea convection on the North Atlantic meridional overturning circulation. *Journal of Physical Oceanography*, *37*(9), 2207–2227.

Pithan, F., & Mauritsen, T. (2014). Arctic amplification dominated by temperature feedbacks in contemporary climate models. *Nature Geoscience*, *7*(3), 181–184.

Pnyushkov, A. V., Polyakov, I. V., Ivanov, V. V., Aksenov, Y., Coward, A. C., Janout, M., & Rabe, B. (2015). Structure and variability of the boundary current in the Eurasian Basin of the Arctic Ocean. *Deep-Sea Research Part I: Oceanographic Research Papers*, *101*, 80–97.

Poli, P., Hersbach, H., Dee, D. P., Berrisford, P., Simmons, A. J., Vitart, F., Laloyaux, P., Tan, D. G., Peubey, C., Thépaut, J. N., Trémolet, Y., Hólm, E. V., Bonavita, M., Isaksen, L., & Fisher, M. (2016). ERA-20C: An atmospheric reanalysis of the twentieth century. *Journal of Climate*, *29*(11), 4083–4097.

Polyakov, I. V., Beszczynska, A., Carmack, E. C., Dmitrenko, I. A., Fahrbach, E., Frolov, I. E., Gerdes, R., Hansen, E., Holfort, J., Ivanov, V. V., Johnson, M. A., Karcher, M., Kauker, F., Morison, J., Orvik, K. A., Schauer, U., Simmons, H. L., Skagseth, Ø., Sokolov, V. T., … Walsh, J. E. (2005). One more step toward a warmer Arctic. *Geophysical Research Letters*, *32*(17), 1–4.

Polyakov, I. V., Alexeev, V. A., Belchansky, G. I., Dmitrenko, I. A., Ivanov, V. V., Kirillov, S. A., Korablev, A. A., Steele, M., Timokhov, L. A., & Yashayaev, I. (2008). Arctic Ocean freshwater changes over the past 100 years and their causes. *Journal of Climate*, *21*(2), 364–384.

Polyakov, I. V., Walsh, J. E., & Kwok, R. (2012). Recent changes of Arctic multiyear sea ice coverage and the likely causes. *Bulletin of the American Meteorological Society*, *93*(2), 145–151.

Polyakov, I. V., Bhatt, U. S., Walsh, J. E., Abrahamsen, E. P., Pnyushkov, A. V., & Wassmann, P. F. (2013). Recent oceanic changes in the Arctic in the context of long-term observations. *Ecological Applications*, *23*(8), 1745–1764.

Polyakov, I. V., Pnyushkov, A. V., Alkire, M. B., Ashik, I. M., Baumann, T. M., Carmack, E. C., Goszczko, I., Guthrie, J., Ivanov, V. V., Kanzow, T., Krishfield, R., Kwok, R., Sundfjord, A., Morison, J., Rember, R., & Yulin, A. (2017). Greater role for Atlantic inflows on sea-ice loss in the Eurasian Basin of the Arctic Ocean. *Science*, *356*(6335), 285–291.

Polyakov, I. V., Pnyushkov, A. V., & Carmack, E. C. (2018). Stability of the arctic halocline: A new indicator of arctic climate change. *Environmental Research Letters*, *13*(12).

Polyakov, I. V., Rippeth, T. P., Fer, I., Alkire, M. B., Baumann, T. M., Carmack, E. C., Ingvaldsen, R., Ivanov, V. V., Janout, M., Lind, S., Padman, L., Pnyushkov, A. V., & Rember, R. (2020).

Weakening of cold halocline layer exposes sea ice to oceanic heat in the eastern arctic ocean. *Journal of Climate*, *33*(18), 8107–8123.

Proshutinsky, A., Steele, M., & Timmermans, M.-L. (2016). Forum for Arctic Modeling and Observational Synthesis (FAMOS): Past, current, and future activities. *Journal of Geophysical Research: Oceans*, *121*(6), 3803–3819.

Proshutinsky, A., & Johnson, M. A. (1997). Two circulation regimes of the wind-driven Arctic Ocean. *Journal of Geophysical Research: Oceans*, *102*(C6), 12493–12514.

Proshutinsky, A., Bourke, R. H., & McLaughlin, F. A. (2002). The role of the Beaufort Gyre in Arctic climate variability: Seasonal to decadal climate scales. *Geophysical Research Letters*, *29*(23), 15–1.

Proshutinsky, A., Krishfield, R., Timmermans, M.-L., Toole, J. M., Carmack, E. C., McLaughlin, F. A., Williams, W. J., Zimmermann, S., Itoh, M., & Shimada, K. (2009). Beaufort Gyre freshwater reservoir: State and variability from observations. *Journal of Geophysical Research*, *114*.

Proshutinsky, A., Aksenov, Y., Clement Kinney, J., Gerdes, R., Golubeva, E., Holland, D., Holloway, G., Jahn, A., Johnson, M., Popova, E., Steele, M., & Watanabe, E. (2011). Recent Advances in Arctic Ocean Studies Employing Models from the Arctic Ocean Model Intercomparison Project. *Oceanography*, *24*(3), 102–113.

Proshutinsky, A., Krishfield, R., Toole, J. M., Timmermans, M.-L., Williams, W., Zimmermann, S., Yamamoto-Kawai, M., Armitage, T. W., Dukhovskoy, D., Golubeva, E., Manucharyan, G. E., Platov, G., Watanabe, E., Kikuchi, T., Nishino, S., Itoh, M., Kang, S. H., Cho, K. H., Tateyama, K., & Zhao, J. (2019). Analysis of the Beaufort Gyre Freshwater Content in 2003–2018. *Journal of Geophysical Research: Oceans*, *124*(12), 9658–9689.

Rabe, B., Dodd, P. A., Hansen, E., Falck, E., Schauer, U., MacKensen, A., Beszczynska-Möller, A., Kattner, G., Rohling, E. J., & Cox, K. (2013). Liquid export of Arctic freshwater components through the Fram Strait 1998–2011. *Ocean Science*, *9*(1), 91–109.

Rabe, B., Karcher, M., Kauker, F., Schauer, U., Toole, J. M., Krishfield, R. A., Pisarev, S., Kikuchi, T., & Su, J. (2014). Arctic Ocean basin liquid freshwater storage trend 1992-2012. *Geophysical Research Letters*, *41*(3), 961–968.

Rabe, B., Karcher, M., Schauer, U., Toole, J. M., Krishfield, R. A., Pisarev, S., Kauker, F., Gerdes, R., & Kikuchi, T. (2011). An assessment of Arctic Ocean freshwater content changes from the 1990s to the 2006-2008 period. *Deep-Sea Research Part I: Oceanographic Research Papers*, *58*(2), 173–185.

Rahmstorf, S., Box, J. E., Feulner, G., Mann, M. E., Robinson, A., Rutherford, S., & Schaffernicht, E. J. (2015). Exceptional twentieth-century slowdown in Atlantic Ocean overturning circulation. *Nature Climate Change*, *5*(5), 475–480.

Rampal, P., Weiss, J., & Marsan, D. (2009). Positive trend in the mean speed and deformation rate of Arctic sea ice, 1979-2007. *Journal of Geophysical Research: Oceans*, *114*(5), 1–14.

Regan, H. C., Lique, C., & Armitage, T. W. (2019). The Beaufort Gyre Extent, Shape, and Location Between 2003 and 2014 From Satellite Observations. *Journal of Geophysical Research: Oceans*.

Regan, H. C., Lique, C., Talandier, C., & Meneghello, G. (2019). Response of Total and Eddy Kinetic Energy to the recent spin up of the Beaufort Gyre. *Journal of Physical Oceanography*, 575–594.

Reimnitz, E., Dethleff, D., & Nürnberg, D. (1994). Contrasts in Arctic shelf sea-ice regimes and some implications: Beaufort Sea versus Laptev Sea. *Marine Geology*, *119*(3-4), 215–225.

Reynolds, R. W., Rayner, N. A., Smith, T. M., Stokes, D. C., & Wang, W. (2002). An improved in situ and satellite SST analysis for climate. *Journal of Climate*, *15*(13), 1609–1625.

Ricker, R., Hendricks, S., Girard-Ardhuin, F., Kaleschke, L., Lique, C., Tian-Kunze, X., Nicolaus, M., & Krumpen, T. (2017). Satellite-observed drop of Arctic sea ice growth in winter 2015–2016. *Geophysical Research Letters*, *44*(7), 3236–3245.

Ricker, R., Hendricks, S., Kaleschke, L., Tian-Kunze, X., King, J., & Haas, C. (2017). A weekly Arctic sea-ice thickness data record from merged CryoSat-2 and SMOS satellite data. *The Cryosphere*, *11*(4), 1607–1623.

Ricker, R., Girard-Ardhuin, F., Krumpen, T., & Lique, C. (2018). Satellite-derived sea ice export and its impact on Arctic ice mass balance. *Cryosphere*, *12*(9), 3017–3032.

Rigor, I. G., & Colony, R. (1997). Sea-ice production and transport of pollutants in the Laptev Sea, 1979- 1993. *Science of the Total Environment*, *202*(1-3), 89–110.

Rigor, I. G., Wallace, J. M., & Colony, R. L. (2002). Response of sea ice to the Arctic Oscillation. *Journal of Climate*, *15*(18), 2648–2663.

Rind, D. (2005). AO/NAO response to climate change: 1. Respective influences of stratospheric and tropospheric climate changes. *Journal of Geophysical Research*, *110*(D12), D12107.

Roberts, M., & Marshall, D. P. (1998). Do We Require Adiabatic Dissipation Schemes in Eddy-Resolving Ocean Models? *Journal of Physical Oceanography*, *28*(10), 2050–2063.

Rousset, C., Vancoppenolle, M., Madec, G., Fichefet, T., Flavoni, S., Barthélemy, A., Benshila, R., Chanut, J., Levy, C., Masson, S., & Vivier, F. (2015). The Louvain-La-Neuve sea ice model LIM3.6: global and regional capabilities. *Geoscientific Model Development*, *8*(10), 2991–3005.

Rudels, B. (1986). The T-S relations in the northern seas: Implications for the deep circulation. *Polar Research*, *4*(2), 133–159.

Rudels, B. (2015). Arctic Ocean circulation, processes and water masses: A description of observations and ideas with focus on the period prior to the International Polar Year 2007-2009. *Progress in Oceanography*, *132*, 22–67.

Rudels, B., Jones, E. P., Anderson, L. G., & Kattner, G. (1994). On the Intermediate Depth Waters of the Arctic Ocean. In O. Johannessen, R. Muench, & J. Overland (Eds.), *The polar oceans and their role in shaping the global environment: The nansen centennial volume, geophysical monograph series, vol. 85* (pp. 33–46). AGU.

Rudels, B., Friedrich, H. J., & Quadfasel, D. (1999). The arctic circumpolar boundary current. *Deep-Sea Research Part II: Topical Studies in Oceanography*, *46*(6-7), 1023–1062.

Rudels, B., Jones, E. P., Schauer, U., & Eriksson, P. (2004). Atlantic sources of the Arctic Ocean surface and halocline waters. *Polar Research*, *23*(2), 181–208.

Schauer, U., & Losch, M. (2019). "FRESHWATER" IN THE OCEAN IS NOT A USEFUL PARAMETER IN CLIMATE RESEARCH. *Journal of Physical Oceanography*, *49*(9), 2309–2321.

Schmith, T., & Hansen, C. (2003). Fram Strait Ice Export during the Nineteenth and Twentieth Centuries Reconstructed from a Multiyear Sea Ice Index from Southwestern Greenland. *Journal of Climate*, *16*(16), 2782–2791.

Schreiber, T., & Schmitz, A. (2000). Surrogate time series. *Physica D: Nonlinear Phenomena*, *142*(3-4), 346–382.

Schwalm, C. R., Glendon, S., & Duffy, P. B. (2020). RCP8.5 tracks cumulative CO2 emissions. *Proceedings of the National Academy of Sciences of the United States of America*, *117*(33), 19656–19657.

Schweiger, A., Lindsay, R., Zhang, J., Steele, M., Stern, H., & Kwok, R. (2011). Uncertainty in modeled Arctic sea ice volume. *Journal of Geophysical Research: Oceans*, *116*(9), 1–21.

Schweiger, A., Wood, K. R., & Zhang, J. (2019). Arctic sea ice volume variability over 1901–2010: A model-based reconstruction. *Journal of Climate*, *5*, 19–0008.

Screen, J. A., & Simmonds, I. (2010). The central role of diminishing sea ice in recent Arctic temperature amplification. *Nature*, *464*(7293), 1334–1337.

Serreze, M. C., Barrett, A. P., Slater, A. G., Woodgate, R. A., Aagaard, K., Lammers, R. B., Steele, M., Moritz, R., Meredith, M., & Lee, C. M. (2006). The large-scale freshwater cycle of the Arctic. *Journal of Geophysical Research: Oceans*, *111*(11).

Serreze, M. C., Barrett, A. P., Stroeve, J. C., Kindig, D. N., & Holland, M. M. (2009). The emergence of surface-based Arctic amplification. *Cryosphere*, *3*(1), 11–19.

Serreze, M. C., & Barrett, A. P. (2011). Characteristics of the Beaufort Sea high. *Journal of Climate*, *24*(1), 159–182.

Serreze, M. C., & Barry, R. G. (2011). Processes and impacts of Arctic amplification: A research synthesis. *Global and Planetary Change*, *77*(1-2), 85–96.

Serreze, M. C., Crawford, A. D., Stroeve, J. C., Barrett, A. P., & Woodgate, R. A. (2016). Variability, trends, and predictability of seasonal sea ice retreat and advance in the Chukchi Sea. *Journal of Geophysical Research: Oceans*, *121*(10), 7308–7325.

Shaffrey, L. C., Stevens, I., Norton, W. A., Roberts, M. J., Vidale, P. L., Harle, J. D., Jrrar, A., Stevens, D. P., Woodage, M. J., Demory, M. E., Donners, J., Clark, D. B., Clayton, A., Cole, J. W., Wilson, S. S., Connolley, W. M., Davies, T. M., Iwi, A. M., Johns, T. C., … Martin, G. M. (2009). U.K. HiGEM: The new U.K. high-resolution global environment model - Model description and basic evaluation. *Journal of Climate*, *22*(8), 1861–1896.

Shaw, W. J., Stanton, T. P., McPhee, M. G., Morison, J. H., & Martinson, D. G. (2009). Role of the upper ocean in the energy budget of Arctic sea ice during SHEBA. *Journal of Geophysical Research: Oceans*, *114*(6), 1–21.

Shaw, W. J., & Stanton, T. P. (2014). Vertical diffusivity of the Western Arctic Ocean halocline. *Journal of Geophysical Research: Oceans*, *119*(8), 5017–5038.

Shepherd, A., Ivins, E., Rignot, E., Smith, B., van den Broeke, M., Velicogna, I., Whitehouse, P., Briggs, K., Joughin, I., Krinner, G., Nowicki, S., Payne, T., Scambos, T., Schlegel, N., A, G., Agosta, C., Ahlstrøm, A., Babonis, G., Barletta, V. R., … Wuite, J. (2020). Mass balance of the Greenland Ice Sheet from 1992 to 2018. *Nature*, *579*(7798), 233–239.

Shu, Q., Qiao, F., Song, Z., Zhao, J., & Li, X. (2018). Projected Freshening of the Arctic Ocean in the 21st Century. *Journal of Geophysical Research: Oceans*, *123*(12), 9232–9244.

Simmonds, I., Burke, C., & Keay, K. (2008). Arctic Climate Change as Manifest in Cyclone Behavior. *Journal of Climate*, *21*(22), 5777–5796.

Simmons, A. J., & Poli, P. (2015). Arctic warming in ERA-Interim and other analyses. *Quarterly Journal of the Royal Meteorological Society*, *141*(689), 1147–1162.

Sirevaag, A., & Fer, I. (2009). Early Spring Oceanic Heat Fluxes and Mixing Observed from Drift Stations North of Svalbard*. *Journal of Physical Oceanography*, *39*(12), 3049–3069.

Skagseth, Ø., Eldevik, T., Årthun, M., Asbjørnsen, H., Lien, V. S., & Smedsrud, L. H. (2020). Reduced efficiency of the Barents Sea cooling machine. *Nature Climate Change*, *10*(7), 661–666.

Smedsrud, L. H., Ingvaldsen, R., Nilsen, J. E., & Skagseth. (2010). Heat in the Barents Sea: Transport, storage, and surface fluxes. *Ocean Science*, *6*(1), 219–234.

Smedsrud, L. H., Halvorsen, M. H., Stroeve, J. C., Zhang, R., & Kloster, K. (2017). Fram Strait sea ice export variability and September Arctic sea ice extent over the last 80 years. *Cryosphere*, *11*(1), 65–79.

Smith, G. C., Roy, F., Mann, P., Dupont, F., Brasnett, B., Lemieux, J.-F., Laroche, S., & Bélair, S. (2014). A new atmospheric dataset for forcing ice-ocean models: Evaluation of reforecasts using the Canadian global deterministic prediction system. *Quarterly Journal of the Royal Meteorological Society*, *140*(680), 881–894.

Spall, M. A. (2013). On the circulation of Atlantic water in the Arctic Ocean. *Journal of Physical Oceanography*, *43*(11), 2352–2371.

Spreen, G., Kern, S., Stammer, D., & Hansen, E. (2009). Fram Strait sea ice volume export estimated between 2003 and 2008 from satellite data. *Geophysical Research Letters*, *36*(19), 1–6.

Spreen, G., Kwok, R., & Menemenlis, D. (2011). Trends in Arctic sea ice drift and role of wind forcing: 1992-2009. *Geophysical Research Letters*, *38*(19).

Spreen, G., de Steur, L., Divine, D., Gerland, S., Hansen, E., & Kwok, R. (2020). Arctic Sea Ice Volume Export Through Fram Strait From 1992 to 2014. *Journal of Geophysical Research: Oceans*, *125*(6).

Steele, M., Morley, R., & Ermold, W. (2001). PHC: A global ocean hydrography with a high-quality Arctic Ocean. *Journal of Climate*, *14*(9), 2079–2087.

Steele, M., & Boyd, T. (1998). Retreat of the cold halocline layer in the Arctic Ocean. *Journal of Geophysical Research: Oceans*, *103*(C5), 10419–10435.

Steele, M., & Flato, G. M. (2000). Sea Ice Growth , Melt , and Modeling : A Survey. In NATO & ARW (Eds.), *The arctic ocean freshwater budget*.

Steele, M., Morison, J., Ermold, W., Rigor, I. G., Ortmeyer, M., & Shimada, K. (2004). Circulation of summer Pacific halocline water in the Arctic Ocean. *Journal of Geophysical Research C: Oceans*, *109*(2), 1–18.

Steele, M., & Ermold, W. (2004). Salinity trends on the Siberian shelves. *Geophysical Research Letters*, *31*(24), 1–4.

Steele, M., Ermold, W., & Zhang, J. (2008). Arctic Ocean surface warming trends over the past 100 years. *Geophysical Research Letters*, *35*(2), 1–6.

Steele, M., Zhang, J., & Ermold, W. (2010). Mechanisms of summertime upper Arctic Ocean warming and the effect on sea ice melt. *Journal of Geophysical Research: Oceans*, *115*(11), 1–12.

Steele, M., & Dickinson, S. (2016). The phenology of Arctic Ocean surface warming. *Journal of Geophysical Research: Oceans*, *121*(9), 6847–6861.

Stewart, K. D., & Haine, T. W. N. (2013). Wind-driven Arctic freshwater anomalies. *Geophysical Research Letters*, *40*(23), 6196–6201.

Stouffer, R. J., Yin, J., Gregory, J. M., Dixon, K. W., Spelman, M. J., Hurlin, W., Weaver, A. J., Eby, M., Flato, G. M., Hasumi, H., Hu, A., Jungclaus, J. H., Kamenkovich, I. V., Levermann, A., Montoya, M., Murakami, S., Nawrath, S., Oka, A., Peltier, W. R., … Weber, S. L. (2006). Investigating the causes of the response of the thermohaline circulation to past and future climate changes. *86th AMS Annual Meeting*.

Stroeve, J. C., Holland, M. M., Meier, W., Scambos, T., & Serreze, M. C. (2007). Arctic sea ice decline: Faster than forecast. *Geophysical Research Letters*, *34*(9), 1–5.

Stroeve, J. C., Maslanik, J. A., Serreze, M. C., Rigor, I. G., Meier, W., & Fowler, C. (2011). Sea ice response to an extreme negative phase of the Arctic Oscillation during winter 2009/2010. *Geophysical Research Letters*, *38*(2), 1–6.

Stroeve, J. C., Serreze, M. C., Holland, M. M., Kay, J. E., Malanik, J., & Barrett, A. P. (2012). The Arctic's rapidly shrinking sea ice cover: A research synthesis. *Climatic Change*, *110*(3-4), 1005–1027.

Stroeve, J. C., & Notz, D. (2018). Changing state of Arctic sea ice across all seasons. *Environmental Research Letters*, *13*(10).

Stroeve, J. C., Schroder, D., Tsamados, M., & Feltham, D. (2018). Warm winter, thin ice? *Cryosphere*, *12*(5), 1791–1809.

Stroeve, J. C., Liston, G. E., Buzzard, S., Zhou, L., Mallett, R. D., Barrett, A., Tschudi, M. A., Tsamados, M., Itkin, P., & Stewart, J. S. (2020). A Lagrangian Snow Evolution System

for Sea Ice Applications (SnowModel-LG): Part II—Analyses. *Journal of Geophysical Research: Oceans*, *125*(10).

Swart, N. C., Fyfe, J. C., Hawkins, E., Kay, J. E., & Jahn, A. (2015). Influence of internal variability on Arctic sea-ice trends. *Nature Climate Change*, *5*(2), 86–89.

Tamura, T., & Ohshima, K. I. (2011). Mapping of sea ice production in the Arctic coastal polynyas. *Journal of Geophysical Research: Oceans*, *116*(7), 1–20.

Tarasenko, A., Supply, A., Kusse-Tiuz, N., Ivanov, V., Makhotin, M., Tournadre, J., Chapron, B., Boutin, J., Kolodziejczyk, N., & Reverdin, G. (2021). Properties of surface water masses in the Laptev and the East Siberian seas in summer 2018 from in situ and satellite data. *Ocean Science*, *17*(1), 221–247.

Tebaldi, C., Arblaster, J. M., & Knutti, R. (2011). Mapping model agreement on future climate projections. *Geophysical Research Letters*, *38*(23), 1–5.

Thompson, D. W., & Wallace, J. M. (2001). Regional climate impacts of the Northern Hemisphere annular mode. *Science*, *293*(5527), 85–89.

Thompson, D. W., & Wallace, J. M. (1998). The Arctic oscillation signature in the wintertime geopotential height and temperature fields. *Geophysical Research Letters*, *25*(9), 1297–1300.

Thorndike, A. S., Rothrock, D. A., Maykut, G. A., & Colony, R. (1975). The thickness distribution of sea ice. *Journal of Geophysical Research*, *80*(33), 4501–4513.

Thorndike, A. S., & Colony, R. (1982). Sea ice motion in response to geostrophic winds. *Journal of Geophysical Research*, *87*(C8), 5845.

Tietsche, S., Notz, D., Jungclaus, J. H., & Marotzke, J. (2011). Recovery mechanisms of Arctic summer sea ice. *Geophysical Research Letters*, *38*(2), 1–4.

Tilling, R. L., Ridout, A., & Shepherd, A. (2018). Estimating Arctic sea ice thickness and volume using CryoSat-2 radar altimeter data. *Advances in Space Research*, *62*(6), 1203–1225.

Timmermans, M.-L., Toole, J. M., Krishfield, R., & Winsor, P. (2008). Ice-Tethered Profiler observations of the double-diffusive staircase in the Canada Basin thermocline. *Journal of Geophysical Research*, *113*, 1–10.

Timmermans, M.-L., Proshutinsky, A., Krishfield, R. A., Perovich, D. K., Richter-Menge, J. A., Stanton, T. P., & Toole, J. M. (2011). Surface freshening in the Arctic Ocean's Eurasian Basin: An apparent consequence of recent change in the wind-driven circulation. *Journal of Geophysical Research: Oceans*, *116*(7), 1–17.

Timmermans, M.-L., Proshutinsky, A., Golubeva, E., Jackson, J. M., Krishfield, R., McCall, M., Platov, G., Toole, J. M., Williams, W., Kikuchi, T., & Nishino, S. (2014). Mechanisms of Pacific Summer Water variability in the Arctic's Central Canada Basin. *Journal of Geophysical Research: Oceans*, *119*(11), 7523–7548.

Timmermans, M.-L., & Jayne, S. R. (2016). The Arctic Ocean spices up. *Journal of Physical Oceanography*, *46*(4), 1277–1284.

Timmermans, M.-L., Marshall, J., Proshutinsky, A., & Scott, J. (2017). Seasonally derived components of the Canada Basin halocline. *Geophysical Research Letters*, *44*(10), 5008–5015.

Timmermans, M.-L., Toole, J. M., & Krishfield, R. (2018). Warming of the interior Arctic Ocean linked to sea ice losses at the basin margins. *Science Advances*, *4*(8), 1–7.

Timmermans, M.-L., & Labe, Z. (2020). Sea Surface Temperature. *Arctic Report Card 2020*.

Timmermans, M.-L., & Marshall, J. (2020). Understanding Arctic Ocean Circulation: A Review of Ocean Dynamics in a Changing Climate. *Journal of Geophysical Research: Oceans*, *125*(4), 1–35.

Treguier, A. M., Deshayes, J., Le Sommer, J., Lique, C., Madec, G., Penduff, T., Molines, J.-M., Barnier, B., Bourdalle-Badie, R., & Talandier, C. (2014). Meridional transport of salt in the global ocean from an eddy-resolving model. *Ocean Science*, *10*(2), 243–255.

Tsamados, M., Feltham, D. L., Schroeder, D., Flocco, D., Farrell, S. L., Kurtz, N., Laxon, S. W., & Bacon, S. (2014). Impact of Variable Atmospheric and Oceanic Form Drag on Simulations of Arctic Sea Ice*. *Journal of Physical Oceanography*, *44*(5), 1329–1353.

Tschudi, M. A., Meier, W. N., Stewart, J., Fowler, C., & Maslanik, J. A. (2019). Polar Pathfinder Daily 25 km EASE-Grid Sea Ice Motion Vectors, Version 4. [1978-2018].

Tsukernik, M., Deser, C., Alexander, M., & Tomas, R. (2010). Atmospheric forcing of Fram Strait sea ice export: A closer look. *Climate Dynamics*, *35*(7), 1349–1360.

Uttal, T., Curry, J. A., Mcphee, M. G., Perovich, D. K., Moritz, R. E., Maslanik, J. A., Guest, P. S., Stern, H. L., Moore, J. A., Turenne, R., Heiberg, A., Serreze, M. C., Wylie, D. P., Persson, O. G., Paulson, C. A., Halle, C., Morison, J. H., Wheeler, P. A., Makshtas, A., … Grenfeld, T. C. (2002). Surface Heat Budget of the Arctic Ocean. *Bulletin of the American Meteorological Society*, *83*(2), 255–275.

Vavrus, S. (2004). The Impact of Cloud Feedbacks on Arctic Climate under Greenhouse Forcing. *Journal of Climate*, *17*(3), 603–615.

Vinje, T. (2001). Fram Strait Ice Fluxes and Atmospheric Circulation: 1950-2000. *Journal of Climate*, *14*(16), 3508–3517.

Vinje, T., Nordlund, N., & Kvambekk, Å. (1998). Monitoring ice thickness in Fram Strait. *Journal of Geophysical Research: Oceans*, *103*(C5), 10437–10449.

Voldoire, A., Sanchez-Gomez, E., Salas y Mélia, D., Decharme, B., Cassou, C., Sénési, S., Valcke, S., Beau, I., Alias, A., Chevallier, M., Déqué, M., Deshayes, J., Douville, H., Fernandez, E., Madec, G., Maisonnave, E., Moine, M.-P., Planton, S., Saint-Martin, D., … Chauvin, F. (2013). The CNRM-CM5.1 global climate model: description and basic evaluation. *Climate Dynamics*, *40*(9-10), 2091–2121.

Wadhams, P. (1983). Sea ice thickness distribution in Fram Strait. *Nature*, *305*(5930), 108–111.

Wadhams, P., Lange, M. A., & Ackley, S. F. (1987). The ice thickness distribution across the Atlantic sector of the Antarctic Ocean in midwinter. *Journal of Geophysical Research*, *92*(C13), 14535.

Walczowski, W., & Piechura, J. (2006). New evidence of warming propagating toward the Arctic Ocean. *Geophysical Research Letters*, *33*(12), 1–5.

Wang, C., Graham, R. M., Wang, K., Gerland, S., & Granskog, M. A. (2019). Comparison of ERA5 and ERA-Interim near-surface air temperature, snowfall and precipitation over Arctic sea ice: effects on sea ice thermodynamics and evolution. *Cryosphere*, *13*(6), 1661–1679.

Wang, H., Legg, S., & Hallberg, R. (2018). The effect of Arctic freshwater pathways on North Atlantic convection and the Atlantic meridional overturning circulation. *Journal of Climate*, *31*(13), 5165–5188.

Wang, M., Wang, J., Duan, A., Liu, Y., & Zhou, S. (2018). Coupling of the Quasi-Biweekly Oscillation of the Tibetan Plateau Summer Monsoon With the Arctic Oscillation. *Geophysical Research Letters*, *45*(15), 7756–7764.

Wang, Q., Ilicak, M., Gerdes, R., Drange, H., Aksenov, Y., Bailey, D. A., Bentsen, M., Biastoch, A., Bozec, A., Böning, C., Cassou, C., Chassignet, E., Coward, A. C., Curry, B., Danabasoglu, G., Danilov, S., Fernandez, E., Fogli, P. G., Fujii, Y., … Yeager, S. G. (2016). An assessment of the Arctic Ocean in a suite of interannual CORE-II simulations. Part II: Liquid freshwater. *Ocean Modelling*, *99*, 86–109.

Wang, Q., Wekerle, C., Danilov, S., Koldunov, N., Sidorenko, D., Sein, D., Rabe, B., & Jung, T. (2018). Arctic Sea Ice Decline Significantly Contributed to the Unprecedented Liquid Freshwater Accumulation in the Beaufort Gyre of the Arctic Ocean. *Geophysical Research Letters*, *45*(10), 4956–4964.

Wang, Q., Wekerle, C., Danilov, S., Sidorenko, D., Koldunov, N., Sein, D., Rabe, B., & Jung, T. (2019). Recent Sea Ice Decline Did Not Significantly Increase the Total Liquid Freshwater Content of the Arctic Ocean. *Journal of Climate*, *32*(1), 15–32.

Warren, S. G., Rigor, I. G., Untersteiner, N., Radionov, V. F., Bryazgin, N. N., Aleksandrov, Y. I., & Colony, R. (1999). Snow Depth on Arctic Sea Ice. *Journal of Climate*, *12*(6), 1814–1829.

Watanabe, E. (2011). Beaufort shelf break eddies and shelf-basin exchange of Pacific summer water in the western Arctic Ocean detected by satellite and modeling analyses. *Journal of Geophysical Research: Oceans*, *116*(8), 1–16.

Watanabe, E., Wang, J., Sumi, A., & Hasumi, H. (2006). Arctic dipole anomaly and its contribution to sea ice export from the Arctic Ocean in the 20th century. *Geophysical Research Letters*, *33*(23), 2–5.

Watanabe, M., Suzuki, T., O'ishi, R., Komuro, Y., Watanabe, S., Emori, S., Takemura, T., Chikira, M., Ogura, T., Sekiguchi, M., Takata, K., Yamazaki, D., Yokohata, T., Nozawa, T., Hasumi, H., Tatebe, H., & Kimoto, M. (2010). Improved Climate Simulation by MIROC5: Mean States, Variability, and Climate Sensitivity. *Journal of Climate*, *23*(23), 6312–6335.

Weaver, A. J., Sedláček, J., Eby, M., Alexander, K., Crespin, E., Fichefet, T., Philippon-Berthier, G., Joos, F., Kawamiya, M., Matsumoto, K., Steinacher, M., Tachiiri, K., Tokos, K., Yoshimori, M., & Zickfeld, K. (2012). Stability of the Atlantic meridional overturning circulation: A model intercomparison. *Geophysical Research Letters*, *39*(20), 2012GL053763.

Weisheimer, A., Schaller, N., O'Reilly, C., MacLeod, D. A., & Palmer, T. (2017). Atmospheric seasonal forecasts of the twentieth century: multi-decadal variability in predictive skill of the winter North Atlantic Oscillation (NAO) and their potential value for extreme event attribution. *Quarterly Journal of the Royal Meteorological Society*, *143*(703), 917–926.

Wernli, H., & Papritz, L. (2018). Role of polar anticyclones and mid-latitude cyclones for Arctic summertime sea-ice melting. *Nature Geoscience*, *11*(2), 108–113.

Whitefield, J., Winsor, P., McClelland, J., & Menemenlis, D. (2015). A new river discharge and river temperature climatology data set for the pan-Arctic region. *Ocean Modelling*, *88*, 1–15.

Willatt, R., Laxon, S., Giles, K., Cullen, R., Haas, C., & Helm, V. (2011). Ku-band radar penetration into snow cover on Arctic sea ice using airborne data. *Annals of Glaciology*, *52*(57), 197–205.

Williams, J., Tremblay, B., Newton, R., & Allard, R. (2016). Dynamic preconditioning of the minimum september sea-ice extent. *Journal of Climate*, *29*(16), 5879–5891.

Wingham, D., Francis, C., Baker, S., Bouzinac, C., Brockley, D., Cullen, R., de Chateau-Thierry, P., Laxon, S., Mallow, U., Mavrocordatos, C., Phalippou, L., Ratier, G., Rey, L., Rostan, F., Viau, P., & Wallis, D. (2006). CryoSat: A mission to determine the fluctuations in Earth's land and marine ice fields. *Advances in Space Research*, *37*(4), 841–871.

Winsor, P., & Björk, G. (2000). Polynya activity in the Arctic Ocean from 1958 to 1997. *Journal of Geophysical Research: Oceans*, *105*(C4), 8789–8803.

Winton, M. (2006). Amplified Arctic climate change: What does surface albedo feedback have to do with it? *Geophysical Research Letters*, *33*(3), 1–4.

Woodgate, R. A. (2018). Increases in the Pacific inflow to the Arctic from 1990 to 2015, and insights into seasonal trends and driving mechanisms from year-round Bering Strait mooring data. *Progress in Oceanography*, *160*(June 2017), 124–154.

Woodgate, R. A., Aagaard, K., Muench, R. D., Gunn, J., Björk, G., Rudels, B., Roach, A. T., & Schauer, U. (2001). The Arctic Ocean boundary current along the Eurasian slope and the adjacent Lomonosov ridge: Water mass properties, transports and transformations from moored instruments. *Deep-Sea Research Part I: Oceanographic Research Papers*, *48*(8), 1757–1792.

Woodgate, R. A., Weingartner, T., & Lindsay, R. (2010). The 2007 Bering Strait oceanic heat flux and anomalous Arctic sea-ice retreat. *Geophysical Research Letters*, *37*(1), 1–5.

Woodgate, R. A., Weingartner, T. J., & Lindsay, R. (2012). Observed increases in Bering Strait oceanic fluxes from the Pacific to the Arctic from 2001 to 2011 and their impacts on the Arctic Ocean water column. *Geophysical Research Letters*, *39*(24), 2–7.

Woods, C., & Caballero, R. (2016). The role of moist intrusions in winter arctic warming and sea ice decline. *Journal of Climate*, *29*(12), 4473–4485.

Wu, B., Wang, J., & Walsh, J. E. (2006). Dipole anomaly in the winter Arctic atmosphere and its association with sea ice motion. *Journal of Climate*, *19*(1), 210–225.

Yamamoto-Kawai, M., McLaughlin, F. A., & Carmack, E. (2013). Ocean acidification in the three oceans surrounding northern North America. *Journal of Geophysical Research: Oceans*, *118*(11), 6274–6284.

Yang, J., Proshutinsky, A., & Lin, X. (2016). Dynamics of an idealized Beaufort Gyre: 1. The effect of a small beta and lack of western boundaries. *Journal of Geophysical Research: Oceans*, *121*(2), 1249–1261.

Yang, Q., Dixon, T. H., Myers, P. G., Bonin, J., Chambers, D., & Van Den Broeke, M. R. (2016). Recent increases in Arctic freshwater flux affects Labrador Sea convection and Atlantic overturning circulation. *Nature Communications*, *7*.

Zanowski, H., Jahn, A., & Holland, M. M. (2021). Arctic Ocean freshwater in CMIP6 Ensembles: Declining Sea Ice, Increasing Ocean Storage and Export. *Journal of Geophysical Research: Oceans*.

Zhang, J., Rothrock, D., & Steele, M. (2000). Recent changes in Arctic Sea ice: The interplay between ice dynamics and thermodynamics. *Journal of Climate*, *13*(17), 3099–3114.

Zhang, J., & Hibler, W. D. (1997). On an efficient numerical method for modeling sea ice dynamics. *Journal of Geophysical Research: Oceans*, *102*(C4), 8691–8702.

Zhang, J., & Steele, M. (2007). Effect of vertical mixing on the Atlantic Water layer circulation in the Arctic Ocean. *Journal of Geophysical Research: Oceans*, *112*(4), 1–9.

Zhang, J., Lindsay, R., Schweiger, A., & Rigor, I. G. (2012). Recent changes in the dynamic properties of declining Arctic sea ice: A model study. *Geophysical Research Letters*, *39*(20), 1–6.

Zhang, X., Ikeda, M., & Walsh, J. E. (2003). Arctic sea ice and freshwater changes driven by the atmospheric leading mode in a coupled sea ice-ocean model. *Journal of Climate*, *16*(13), 2159–2177.

Zhao, B., & Timmermans, M.-L. (2018). Topographic Rossby Waves in the Arctic Ocean's Beaufort Gyre. *Journal of Geophysical Research: Oceans*, *123*(9), 6521–6530.

Zhao, M., Timmermans, M.-L., Cole, S., Krishfield, R., & Toole, J. M. (2016). Evolution of the eddy field in the Arctic Ocean's Canada Basin, 2005–2015. *Geophysical Research Letters*, *43*(15), 8106–8114.

Zhong, W., Steele, M., Zhang, J., & Zhao, J. (2018). Greater Role of Geostrophic Currents in Ekman Dynamics in the Western Arctic Ocean as a Mechanism for Beaufort Gyre Stabilization. *Journal of Geophysical Research: Oceans*, *123*(1), 149–165.

Zhuang, Y., Jin, H., Cai, W.-j., Li, H., Jin, M., Qi, D., & Chen, J. (2021). Freshening leads to a three-decade trend of declining nutrients in the western Arctic ocean. *Environmental Research Letters*.

Glossary

albedo A measure of the proportion of incoming shortwave radiation that is reflected by the surface of the Earth. 2

Arctic Amplification The phenomenon of enhanced surface air temperature warming in the Arctic region relative to lower latitudes. 136

flaw A lead or polynya is termed a flaw lead or flaw polynya if it forms at the edge of landfast ice. The terms flaw lead and flaw polynya are often used interchangeably. 139

halocline Layer of the ocean characterised by a gradient in salinity; salinity increases downwards. 8

leads Cracks in the pack ice that accommodate sea ice divergence and expose open water to the atmosphere. 139, 181, 186

pack ice Floating sea ice that is mobile, as opposed to landfast. 8, 239

polynyas Areas of open water in otherwise ice-covered ocean. In the Arctic Ocean, polynyas form along coastlines and at the edge of landfast ice. 139

sea ice draft The thickness of sea ice that is below the water surface; the vertical length from surface to ice base. 90